Development of Microstrip Patch Antenna Strain Sensors for Wireless Structural Health Monitoring

A thesis submitted in fulfilment of the requirements for the degree of

Doctor of Philosophy

Ali Daliri
B.Eng.

School of Aerospace, Mechanical & Manufacturing Engineering
College of Science, Engineering and Health

RMIT University
August 2011

Dedicated to

My Parents, Darab and Shayesteh

I would like to express my heartfelt thanks and gratitude to my parents who has encouraged and supported me during the years of my studies and my life. I would not have been able to finish writing this thesis without the support of my parents, and therefore I am deeply indebted to them for all their help.

Declaration

I certify that except where due acknowledgement has been made, the work is that of the author alone; the work has not been submitted previously, in whole or in part, to qualify for any other academic award; the content of the thesis is the result of work which has been carried out since the official commencement date of the approved research program; and, any editorial work, paid or unpaid, carried out by a third party is acknowledged.

Ali Daliri

25 August 2011

Acknowledgement

First, I wish to dedicate my deep down appreciation to my first supervisor, Professor Sabu John of the Royal Melbourne Institute of Technology (RMIT), for his invaluable help and support from the first day of this project as well as his technical guidance, endless forbearance, and constant encouragement. I am grateful for his directness and for a well-organized research environment which led this project to success.

I wish to thank my second supervisor, Professor Chun Wang of RMIT University School of Aerospace Mechanical and Manufacturing Engineering, for his priceless assistance, support and suggestions during the time of this study.

I also wish to thank the following:

- Dr. Wayne Rowe of RMIT University School of Electrical and Computer Engineering for his valuable assistance, support and suggestions during different stages of this research.

- Associate Professor Kamran Ghorbani of RMIT University School of Electrical and Computer Engineering for his valuable assistance and support in different stages of this research.

- Dr. Amir Galehdar of RMIT University School of Electrical and Computer Engineering for his great assistance during this research in simulation of antenna sensors, manufacturing of antenna samples, wireless measurement of strain, preparing the publications and novel ideas.

- Mr. Peter Tkatchyk of RMIT University for his technical support and assistance in the testing of the antenna sensors.

- Mr. Robert Ryan of RMIT University for his assistance in the manufacture of composite test plates at RMIT University composite laboratory.

- Mr. Patrick Wilkins of RMIT University for his assistance in the manufacture of aluminium test plates at RMIT University manufacturing workshop.

Abstract

Current developments in the design and manufacturing of composite materials along with their superior mechanical characteristics have resulted in the extensive use of these materials in advanced structures for aerospace industry. In recent years, several different attempts have been made to develop Structural Health Monitoring (SHM) systems and, as a result, various SHM techniques have been introduced. Currently, however, none of these techniques are capable of monitoring the condition of complex operational aerospace structures.

The number of sensors and its wiring pose significant problems because of the increased signal processing demand and heightened system unreliability, respectively. Current available wireless sensors are not efficient enough to be used in SHM for aerospace structures primarily because of cost and battery power limitations. The aim in this research was to investigate the feasibility of using microstrip patch antennas as a new type of strain sensor and develop the required techniques for wireless strain measurement without these aforementioned problems.

Analytical, computational (finite element analysis) and experimental tests conducted in this research demonstrated that microstrip patch antennas can be used to reliably measure strain. As a result of investigating different microstrip patch antenna configurations in this study, novel antenna sensors were designed, simulated and tested. These antenna sensors (circular, slotted circular and meandered circular microstrip patch antennas) showed good sensitivity with strain with acceptable linearity between strain and the shift in its resonant frequency. In particular, the meandered circular microstrip patch antenna was shown to have localised and omni-directional strain measurement capabilities.

In this research, it was shown that by using carefully selected techniques, the resonant frequency of circular microstrip patch antennas can be detected and measured wirelessly. As a result, the feasibility of wireless strain measurement for different aerospace materials (aluminium, carbon fibre reinforced polymer and glass fibre reinforced polymer) was demonstrated. Several diagnostic-related parameters here were investigated and a pivotal parameter discovered was the distance between the sensor and the reader. With further developments of this technology, it is envisaged that reliable wireless measurement and detection of strain and indeed, damage, will be possible in aerospace and other structures.

Table of Contents

1 Introduction 1

1.1 Background 1

1.2 Objectives and Rational 2

1.3 Methodology 3

1.4 Thesis Outline 4

1.5 List of Publications 6

2 Literature Review: Structural Health Monitoring 8

2.1 Introduction 8

2.2 Background (SHM methods) 11

2.3 Wireless Health Monitoring 14

2.3.1 Wireless structural health monitoring in civil industry 14

2.3.2 Wireless sensors for medical applications 16

2.3.3 Wireless sensors in various applications 17

2.3.4 Sensor networks for wireless structural health monitoring 20

2.3.5 Antennas for wireless health monitoring systems 21

2.4 Microstrip patch antenna strain sensor 21

2.5 Conclusion 28

3 Literature Review: Microstrip Patch Antennas 29

3.1 Introduction 29

3.2 Antennas 29

3.3 Electromagnetic Principles 32

3.3.1 Electromagnetic Wave Equations (Maxwell's Equations) 33

3.3.2 Radio Wave Propagation Mechanisms 35

3.3.2.1 Reflection and Transmission 35

3.3.2.2 Diffraction and Huygens's Principle 37

3.3.2.3 Scattering 37

3.3.3 Media Classification 38

3.3.4 Fundamental Parameters of Antennas 38

3.3.4.1 Radiation Pattern 39

3.3.4.2 Radiation Power Density 40

3.3.4.3 Radiation Intensity 40

3.3.4.4 Beamwidth 41

3.3.4.5 Directivity 41

3.3.4.6 Antenna Efficiency 41

3.3.4.7 Gain 42

3.3.4.8 Bandwidth 43

3.3.4.9 Polarisation 43

3.3.4.10 Input Impedance 44

3.3.4.11 Reflection Coefficient, Return Loss and VSWR 44

3.3.4.12 Scattering Parameters 45

3.4 Microstrip Patch Antennas 46

3.4.1 Radiation Mechanism 47
3.4.2 Various Antenna Configurations....50
3.4.3 Substrate Material 50
3.4.4 Feeding Mechanisms....52
3.4.5 Ground Plane 53
3.4.6 Applications 54
3.5 Conclusion 55
4 Antenna Theory and Evaluation 56
4.1 Introduction....56
4.2 Strain-Frequency Shift Relationship....57
4.2.1 Microstrip Patch Antennas (MPAs)....57
4.2.1.1 Circular Microstrip Patch Antennas (CMPAs) 57
4.2.1.2 Rectangular Microstrip Patch Antennas (RMPAs) 60
4.2.2 Dielectric Resonator Antennas (DRAs) 62
4.2.2.1 Hemispherical DRA....62
4.2.2.2 Cylindrical DRA 64
4.2.2.3 Rectangular DRA....66
4.2.3 Split Ring Resonators (SRRs)....68
4.2.3.1 Edge-Coupled SRR....68
4.2.3.2 Broadside-Coupled SRR....71
4.2.3.3 Nonbianisotropic SRR 72

4.2.3.4 Double-Split SRR 73
4.2.3.5 Spirals 73
4.3 Antenna Design....74
4.3.1 Rectangular Microstrip Patch Antenna 74
4.3.1.1 Antenna dimensions....74
4.3.1.2 Probe feed location....76
4.3.2 Circular Microstrip Patch Antenna 77
4.3.2.1 Antenna dimensions....77
4.3.2.2 Probe feed location....78
4.3.3 Microstrip line feed design 79
4.4 Conclusion 81
5 Finite Element Analysis....82
5.1 Introduction....82
5.2 Background....83
5.2.1 ANSYS™....83
5.2.1.1 Mechanical APDL™....83
5.2.1.2 Workbench™....84
5.2.2 HFSS™ 84
5.2.3 High-Frequency (HF) Electromagnetic Analysis....85
5.3 FEA Method 1 (ANSYS APDL™-FORTRAN™)....87
5.4 New Antenna Designs (HFSS™)....92

5.4.1 Slotted Circular Microstrip Patch Antenna 93

5.4.2 Meandered Circular Microstrip Patch Antenna 94

5.5 STEMCOF Data Processing Protocol (ANSYS Workbench™-HFSS™) 97

5.6 Conclusion 105

6 Experimental Details 106

6.1 Introduction 106

6.2 Manufacturing of Test Samples 106

6.2.1 Antennas 106

6.2.2 Test Plates 109

6.2.2.1 Aluminium plates 109

6.2.2.2 Composite plates 110

6.3 Test Setup 112

6.4 Data Acquisition Devices 114

6.4.1 Network Analyser 114

6.4.2 Strain Indicator and Recorder 117

6.5 Data Analysis 117

6.6 Conclusion 118

7 Results and Discussion 119

7.1 Introduction 119

7.2 Circular Microstrip Patch Antenna 119

7.3 Slotted Circular Microstrip Patch Antenna 127

7.4 Meandered Circular Microstrip Patch Antenna 131

7.5 Comparison of Different Antenna/Sensor Designs 141

7.6 Conclusion 143

8 Wireless Strain Measurement 144

8.1 Introduction 144

8.2 Wireless Reading of Circular Microstrip Patch Antenna Resonant Frequency 144

8.3 Near Field and Far Field Conditions 149

8.4 Finite Element Analysis 153

8.4.1 Modelling of the Horn Antenna 153

8.4.2 Patch Excitation and Strain Measurement 156

8.5 Experimental Wireless Measurement of Strain 162

8.5.1 Wireless Test Setup 162

8.5.2 Strain Measurement and Effect of Important Parameters 167

8.6 High Quality Factor Antennas 198

8.7 Conclusion 200

9 Conclusion 202

9.1 Overview 202

9.2 Theory of Strain-Frequency Shift Relationship 202

9.3 Computational (FEA) Models 203

9.4 Experimental Validation 203

9.5 Circular Microstrip Patch Antenna 203

9.6 Novel Antenna/Sensor Configurations 204

9.7 Wireless Strain Measurement 205

9.8 Future Work 206

Appendix A - MATLAB™ Codes....207

Appendix B - ANSYS™ Codes 227

Appendix C - FORTRAN™ Code 250

Appendix D – ANSYS Workbench™ Instructions for Simulation of Slotted/Meandered Circular Microstrip Patch Antenna 252

Appendix E - HFSS™ Instructions for Simulation of Deformed Shape of Slotted/Meandered Circular Microstrip Patch Antenna 255

References 259

List of Tables

Table 4.1 Rectangular microstrip patch antenna dimensions for operating frequency of 1 to 10 GHz (According to Huang and Boyle (2008) and Balanis (2005)) 75

Table 4.2 Rectangular microstrip patch antenna dimensions for operating frequency of 1 to 10 GHz (According to Volakis (2007)) 75

Table 4.3 Rectangular microstrip patch antenna dimensions for operating frequency of 1 to 10 GHz (According to Garg et al. (2000)) 76

Table 4.4 Circular microstrip patch antenna dimensions for operating frequency of 1 to 10 GHz (According to Balanis (2005) and Volakis (2007)) 77

Table 4.5 Circular microstrip patch antenna dimensions for operating frequency of 1 to 10 GHz (According to Garg et al. (2000)) 78

Table 7.1 Comparison of the amount of shift in the resonant frequency of the circular microstrip patch antenna attached to test plates from different materials. 126

Table 7.2 Comparison between three microstrip patch antennas. 142

List of Figures

Figure 2.1 A shower of foam debris after the impact on Columbia's left wing. The event was not observed in real time (Courtesy: NASA). 9

Figure 2.2 The Columbia shuttle explosion (Courtesy: NASA). 9

Figure 2.3 Advanced composite use in BOEING 787 commercial airplane (Courtesy: BOEING). 10

Figure 2.4 A wireless load bridge monitoring system (Farhey, 2006). 15

Figure 2.5 wireless system for monitoring the cable tension of cable-stayed bridges (Liao, Wang and Huang, 2001) 15

Figure 2.6 Chip-size antenna assembled with an RFCMOS transceiver (Carmo et al., 2006) 17

Figure 2.7 Photograph of fabricated patch type sensor (Matsuzaki and Todoroki, 2007). 17

Figure 2.8 Schematic of a practical structure of a carbon/epoxy composite when an electrical current is applied. (a) Electrical network structures of the fibre in a CFRP laminate. (b) The electrical network is broken with a delamination (Matsuzaki and Todoroki, 2006). 18

Figure 2.9 Evolution of antenna configurations from a dipole to antenna/sensor multifunctional wing structures (Matsuzaki, Melnykowycz and Todoroki, 2009). 19

Figure 2.10 Wireless microsystem architecture (Chaimanonart and Young, 2006). 20

Figure 2.11 Geometry of the fabricated antenna (Zivanovic et al., 2007). 22

Figure 2.12 Illustration of the experimental setup of an inductive coil in an LC circuit (Butler et al., 2002). 23

Figure 2.13 Fabricated planar spiral inductor and test setup (Jia et al., 2006). 24

Figure 2.14 The response of 2nd harmonic signal (Tan et al., 2008). 24

Figure 2.15 A plan view micrograph of the fabricated sensor with on-chip antennas (Melik et al., 2008). 25

Figure 2.16 An array of split ring resonators under compression test (Melik et al., 2009). 25

Figure 2.17 The microstrain vs. Resonant frequency of split ring resonator array (Melik et al., 2009)...26

Figure 2.18 Fabricated patch antenna (Tata et al., 2009).....26

Figure 2.19 Test Setup and patch antenna attached to a metal plate (Deshmukh et al., 2009).....27

Figure 2.20 Experimental setup for fatigue test (Deshmukh et al., 2009). 27

Figure 3.1 Antenna as a transition device (Balanis, 2005). 30

Figure 3.2 A typical radio system (Huang and Boyle, 2008).....31

Figure 3.3 (a) Impedance and (b) admittance representations of an antenna (Volakis, 2007).....31

Figure 3.4 Plane wave reflection and transmission, and its analogous transmission line (Huang and Boyle, 2008).....36

Figure 3.5 Radio wave diffraction over a knife-edge obstacle (Huang and Boyle, 2008).....37

Figure 3.6 Radio wave scattering (Huang and Boyle, 2008). 37

Figure 3.7 The 3D radiation pattern of an electrically short current element (Huang and Boyle, 2008)..39

Figure 3.8 The E-plane and H-plane patterns of an electrically short current element (Huang and Boyle, 2008). 39

Figure 3.9 Reference terminals and losses of an antenna (Balanis, 2005).....41

Figure 3.10 Antenna input impedance model (Huang and Boyle, 2008; Balanis, 2005).....44

Figure 3.11 The equivalent 2-port network of a transmitting-receiving antenna system (Huang and Boyle, 2008).....45

Figure 3.12 (a) Rectangular microstrip patch antenna and (b) circular microstrip patch antenna (Huang and Boyle, 2008; Balanis, 2005; Volakis, 2007). 46

Figure 3.13 Fringing effect on edges of the patch (Balanis, 2005). 48

Figure 3.14 Charge distribution and current density creation on microstrip patch (Balanis, 2005). 48

Figure 3.15 Field configurations (modes) for rectangular microstrip patch (Balanis, 2005). 49

Figure 3.16 Various shapes of microstrip patch elements (Huang and Boyle, 2008; Balanis, 2005; Garg et al., 2000). 50

Figure 3.17 Feeding mechanisms for microstrip patch antennas (Balanis, 2005; Volakis, 2007; Garg et al., 2000; James and Hall, 1989). 52

Figure 3.18 Equivalent circuits for typical feeds of microstrip patch antennas (Balanis, 2005). 53

Figure 4.1 Circular microsttrip patch antenna (Balanis, 2005). 57

Figure 4.2 Analytical relationship of strain and normalised frequency shift for CMPA. 60

Figure 4.3 Rectangular microstrip patch antenna (Balanis, 2005). 60

Figure 4.4 Analytical relationship of strain and normalised frequency shift for RMPA. 62

Figure 4.5 Hemispherical DRA (Petosa, 2007). 62

Figure 4.6 Analytical relationship of strain and normalised frequency shift for H-DRA. 64

Figure 4.7 Cylindrical DRA (Petosa, 2007). 64

Figure 4.8 Analytical relationship of strain and normalised frequency shift for C-DRA. 66

Figure 4.9 Rectangular DRA (Petosa, 2007). 66

Figure 4.10 Analytical relationship of strain and normalised frequency shift for R-DRA. 68

Figure 4.11 Edge-coupled SRR (Marques, Martin and Sorolla, 2008). 69

Figure 4.12 Analytical relationship of strain and normalised frequency shift for EC-SRR. 71

Figure 4.13 Broadside-coupled SRR (Marques, Martin and Sorolla, 2008).....72

Figure 4.14 Nonbianisotropic SRR (Marques, Martin and Sorolla, 2008). 72

Figure 4.15 Double-split SRR (Marques, Martin and Sorolla, 2008).....73

Figure 4.16 Two-turn spiral resonator (Marques, Martin and Sorolla, 2008).....74

Figure 4.17 Feeding microstrip patch antennas directly with microstrip line (Balanis, 2005). 79

Figure 4.18 Feeding microstrip patch antennas with microstrip line using a quarter-wavelength transformer (Balanis, 2005). 79

Figure 5.1 Schematic of design and modification process for micrsotrip patch antenna sensors. 82

Figure 5.2 Typical finite element shapes for CEM (Volakis, 2007). 86

Figure 5.3 SOLID186 element geometry and coordinate system (ANSYS® Academic Research, 2010d). 88

Figure 5.4 HF120 element geometry and coordinate system (ANSYS® Academic Research, 2010e). ..88

Figure 5.5 Schematic of the procedure used in FEA method 1. 90

Figure 5.6 Contour of strain after 10mm displacement at the centre of aluminium plate at 0° orientation for circular microstrip patch antenna (half of the structure is modelled).....91

Figure 5.7 Contour of electric field magnitude after 10mm displacement at the centre of aluminium plate at 0° orientation for circular microstrip patch antenna (half of the structure is modelled). 92

Figure 5.8 Surface current distribution for a circular patch and a slotted circular patch. 93

Figure 5.9 Dimensions of the slotted circular microstrip patch antenna.....94

Figure 5.10 Simulated resonant frequency of the slotted circular microstrip patch antenna. 94

Figure 5.11 Measured resonant frequency of a short-circuited circular microstrip patch against the slot length (Wong, 2000). 95

Figure 5.12 Surface current distribution for a circular patch and a meandered circular patch. 95

Figure 5.13 Dimensions of the meandered circular microstrip patch antenna. 96

Figure 5.14 Measured and simulated resonant frequency of the meandered circular microstrip patch antenna. 97

Figure 5.15 Schematic of the project in ANSYS Workbench™ 98

Figure 5.16 Contour of strain after 10mm displacement at the centre of aluminium plate at 0° orientation for slotted circular microstrip patch antenna. 98

Figure 5.17 Contour of strain after 10mm displacement at the centre of aluminium plate at 0° orientation for meandered circular microstrip patch antenna. 99

Figure 5.18 Schematic of the procedure used in STEMCOF Data Processing Protocol. 100

Figure 5.19 Contour of electric field magnitude after 10mm displacement at the centre of aluminium plate at 0° orientation for slotted circular microstrip patch antenna. 101

Figure 5.20 Contour of electric field magnitude after 10mm displacement at the centre of aluminium plate at 0° orientation for meandered circular microstrip patch antenna. 101

Figure 5.21 Contour of strain for meandered circular patch antenna after 10mm displacement at the centre of plate at 0° orientation, attached to an aluminium plate with the diameter of the central hole being 2.5 mm. 102

Figure 5.22 Contour of strain for meandered circular patch antenna after 10mm displacement at the centre of plate at 0° orientation, attached to an aluminium plate with the diameter of the central hole being 5 mm. 103

Figure 5.23 Contour of strain for meandered circular patch antenna after 10mm displacement at the centre of plate at 0° orientation, attached to an aluminium plate with the diameter of the central hole being 7.5 mm. 103

Figure 5.24 Contour of strain for meandered circular patch antenna after 10mm displacement at the centre of plate at 0° orientation, attached to an aluminium plate with the diameter of the central hole being 10 mm. 104

Figure 5.25 Contour of strain for meandered circular patch antenna after 10mm displacement at the centre of plate at 0° orientation, attached to an aluminium plate with the diameter of the central hole being 12.5 mm. 104

Figure 5.26 Contour of strain for meandered circular patch antenna after 10mm displacement at the centre of plate at 0° orientation, attached to an aluminium plate with the diameter of the central hole being 15 mm. 105

Figure 6.1 Schematic of etching process (James and Hall, 1989). 108

Figure 6.2 Strain gauge locations at the back of the aluminium plate. 109

Figure 6.3 Strain gauge locations at the back of the octagon aluminium plate.....110

Figure 6.4 Strain gauges attached to the back of the carbon fibre composite plate. 111

Figure 6.5 Strain gauges attached to the back of the fibre glass composite plate. 111

Figure 6.6 Circular microstrip patch antenna attached to three different materials: (a) carbon fibre composite, (b) fibre glass composite, and (c) aluminum. 112

Figure 6.7 Slotted circular microstrip patch antenna attached to a carbon fobre composite plate on a wooden jig.....112

Figure 6.8 Final setup for the 3-point bend test. 113

Figure 6.9 Rectangular slot in the wooden jig to avoid the contact between wood and the meandered circular microstrip patch antenna.....114

Figure 6.10 The VNA used for experimental tests. 115

Figure 6.11 Architecture of a typical VNA (Huang and Boyle, 2008). 115

Figure 6.12 Calibration kit used for antenna measurement. 116

Figure 6.13 Vishay Micro-Measurements™ strain indicator and recorder (Model P3™) (Vishay, 2011).117

Figure 7.1 Bending directions; and E-plane and H-plane orientations for circular microstrip patch antenna. 120

Figure 7.2 Shift in the resonant frequency of the circular microstrip patch antenna sensor at 0° orientation (attached to the aluminium plate). 120

Figure 7.3 Comparison of strain and frequency shift relationship in three different materials at 0° orientation (Circular microstrip patch antenna). 121

Figure 7.4 Comparison of strain and frequency shift relationship in three different materials at 90° orientation (Circular microstrip patch antenna). 121

Figure 7.5 Strain and frequency shift relationship at 45° orientation (Circular microstrip patch antenna).....122

Figure 7.6 Strain and frequency shift relationship at 1st and 2nd resonant frequencies of the patch at 0° orientation (Circular microstrip patch antenna). 123

Figure 7.7 Strain and frequency shift relationship at 1st and 2nd resonant frequencies of the patch at 90° orientation (Circular microstrip patch antenna). 123

Figure 7.8 Comparison of measured and FEA results of strain and frequency shift (Circular microstrip patch antenna). 124

Figure 7.9 Comparison of measured and theoretical results of strain and frequency shift (Circular microstrip patch antenna).....125

Figure 7.10 Test results of strain and frequency shift at 0° orientation for circular patch (Strain gauge 1 is 14 cm away from the edge of the plate, and strain gauge 2 is 7 cm away from the edge of the plate).125

Figure 7.11 Test results of strain and frequency shift at 90° orientation for circular patch (Strain gauge 3 is 14 cm away from the edge of the plate, and strain gauge 4 is 7 cm away from the edge of the plate). 126

Figure 7.12 Bending directions; and E-plane and H-plane orientations for slotted circular microstrip patch antenna. 127

Figure 7.13 Shift in the resonant frequency of the slotted circular microstrip patch antenna sensor at 0° orientation (attached to the aluminium plate). 128

Figure 7.14 Experimental strain-frequency shift relationship for carbon fibre panel (Strain gauge 1 at 0° orientation and strain gauge 3 at 90° orientation). 128

Figure 7.15 Experimental Strain-frequency shift relationship for aluminium panel (Strain gauge 1 at 0°orientation and strain gauge 3 at 90° orientation). 129

Figure 7.16 Comparison of FEA and experimental results in 0° orientation. 130

Figure 7.17 Comparison of FEA and experimental results in 90° orientation. 130

Figure 7.18 Effect of strain intensity in 0° orientation.....131

Figure 7.19 Effect of strain intensity in 90° orientation.....131

Figure 7.20 Shift in the resonant frequency of the meandered antenna sensor at 45° orientation (attached to the aluminium plate).....132

Figure 7.21 Bending directions; and E-plane and H-plane orientations for meandered circular microstrip patch antenna. 132

Figure 7.22 Comparison of measured and FEA results of strain and frequency shift relationship at 0° orientation for meandered patch. 133

Figure 7.23 Comparison of measured and FEA results of strain and frequency shift relationship at 90° orientation for meandered patch. 134

Figure 7.24 Comparison of measured and FEA results of strain and frequency shift relationship at 45° orientation for meandered patch. 134

Figure 7.25 Comparison of experimental results of normalized frequency shift at different steps of bending at three different orientations for meandered patch. 135

Figure 7.26 Comparison of experimental results of normalized frequency shift at different steps of bending at 90° orientation for circular and meandered patch. 136

Figure 7.27 Comparison of measured results of normalized frequency shift at different steps of bending at four different orientations for meandered patch sample number 1 (hole diameter: 2.5 mm). 136

Figure 7.28 Comparison of measured results of normalized frequency shift at different steps of bending at four different orientations for meandered patch sample number 2 (hole diameter: 5 mm). 137

Figure 7.29 Comparison of measured results of normalized frequency shift at different steps of bending at four different orientations for meandered patch sample number 3 (hole diameter: 7.5 mm). 137

Figure 7.30 Comparison of measured results of normalized frequency shift at different steps of bending at four different orientations for meandered patch sample number 4 (hole diameter: 10 mm). 138

Figure 7.31 Comparison of measured results of normalized frequency shift at different steps of bending at four different orientations for meandered patch sample number 5 (hole diameter: 12.5 mm). 138

Figure 7.32 Comparison of measured results of normalized frequency shift at different steps of bending at four different orientations for meandered patch sample number 6 (hole diameter: 15 mm). 139

Figure 7.33 Comparison of measured results of normalized frequency shift at different steps of bending at -45° orientations for meandered patch samples number 1 to 6. 139

Figure 7.34 Comparison of measured results of normalized frequency shift at different steps of bending at 0° orientations for meandered patch samples number 1 to 6. 140

Figure 7.35 Comparison of measured results of normalized frequency shift at different steps of bending at 45° orientations for meandered patch samples number 1 to 6. 140

Figure 7.36 Comparison of measured results of normalized frequency shift at different steps of bending at 90° orientations for meandered patch samples number 1 to 6. 141

Figure 7.37 Cross slotted circular microstrip patch antenna. 142

Figure 8.1 Two horn configuration for wireless measurement of CMPA resonant frequency. 145

Figure 8.2 Final setup for wireless measurement using the two horn configuration. 146

Figure 8.3 Resonant frequency of CMPA attached to three plates with different materials (measured by connecting a coaxial cable to the CMPA). 147

Figure 8.4 Transmision coeficeint of two horn antennas in front of CMPA/CMPA_back. 147

Figure 8.5 Transmision coeficeint of two horn antennas in front of CMPA/Aluminium plate. 148

Figure 8.6 Transmision coeficeint of two horn antennas in front of CMPA/CFRP plate. 148

Figure 8.7 Transmision coeficeint of two horn antennas in front of CMPA/GFRP plate. 149

Figure 8.8 Three regions of electromagnetic field in the surrounding space of an antenna (Balanis, 2005). 150

Figure 8.9 The amplitude pattern of an antenna in three different electromagnetic field regions (Balanis, 2005). 151

Figure 8.10 Variation in the magnitude of electric and magnetic field of an antenna against the normalised distance from the antenna (Huang, 2008). 152

Figure 8.11 The Autodesk Photo Scene Editor™ environment. 154

Figure 8.12 The final model of the horn antenna (View 1). 155

Figure 8.13 The final model of the horn antenna (View 2). 155

Figure 8.14 The final model of the horn antenna (View 3). 155

Figure 8.15 The gain of the horn antenna (faced toward free space). 157

Figure 8.16 The gain of the horn antenna (faced toward an aluminium plate). 157

Figure 8.17 The gain of the horn antenna (faced toward an FR4 substrate attached to an aluminium plate). 158

Figure 8.18 The gain of the horn antenna (faced toward a CMPA attached to an aluminium plate).....158

Figure 8.19 Contour of electric field on CMPA surface (excited by horn antenna). 159

Figure 8.20 Return loss of the horn antenna for, H: Horn antenna facing free space; HP: Horn antenna facing aluminium plate; HPS: Horn antenna facing substrate attached to aluminium plate; and HPSP: Horn antenna facing CMPA attached to aluminium plate. 160

Figure 8.21 Simplified strain configuration used for FEA. 161

Figure 8.22 Shift in the resonant frequency of the CMPA after applying simplified strain (FEA). 162

Figure 8.23 The final setup used for wireless strain measurement. 164

Figure 8.24 The interrogation distance between CMPA sensor and horn antenna (10 cm).....164

Figure 8.25 The horn antenna in front of the CMAP sensor at relative angle of 45°. 165

Figure 8.26 The horn antenna in front of a CFRP plate at 0° orientation. 165

Figure 8.27 The horn antenna in front of a GFRP plate at 90° orientation. 165

Figure 8.28 The horn location at the reference distance of 0 cm. 166

Figure 8.29 The horn location at the offset distance of 5 cm. 166

Figure 8.30 The horn location at the offset distance of -5 cm. 166

Figure 8.31 Effect of interrogation distance on the return loss of the horn antenna at the resonant frequency of the CMPA, attached to an aluminium plate at 0° orientation. 167

Figure 8.32 Effect of interrogation distance on the return loss of the horn antenna at the resonant frequency of the CMPA, attached to an aluminium plate at 45° orientation. 168

Figure 8.33 Effect of interrogation distance on the return loss of the horn antenna at the resonant frequency of the CMPA, attached to an aluminium plate at 90° orientation. 168

Figure 8.34 Effect of horn antenna orientation on the resonant frequency of the CMPA attached to an aluminium plate for the interrogation distance of 1 cm. 169

Figure 8.35 Effect of horn antenna orientation on the resonant frequency of the CMPA attached to an aluminium plate for the interrogation distance of 5 cm. 169

Figure 8.36 Effect of horn antenna orientation on the resonant frequency of the CMPA attached to an aluminium plate for the interrogation distance of 10 cm. 170

Figure 8.37 Shift in the resonant frequency of the CMPA attached to an aluminium plate at interrogation distance of 1 cm and 0° orientation. 171

Figure 8.38 Shift in the resonant frequency of the CMPA attached to an aluminium plate at interrogation distance of 1 cm and 45° orientation. 171

Figure 8.39 Shift in the resonant frequency of the CMPA attached to an aluminium plate at interrogation distance of 1 cm and 90° orientation. 172

Figure 8.40 Normalised shift in the resonant frequency of the CMPA attached to an aluminium plate against the applied strain for three different horn orientations at interrogation distance of 1 cm. 173

Figure 8.41 Normalised shift in the resonant frequency of the CMPA attached to an aluminium plate against the applied strain for three different horn orientations at interrogation distance of 2 cm. 173

Figure 8.42 Normalised shift in the resonant frequency of the CMPA attached to an aluminium plate against the applied strain for three different horn orientations at interrogation distance of 3 cm. 174

Figure 8.43 Normalised shift in the resonant frequency of the CMPA attached to an aluminium plate against the applied strain for three different horn orientations at interrogation distance of 4 cm. 174

Figure 8.44 Normalised shift in the resonant frequency of the CMPA attached to an aluminium plate against the applied strain for three different horn orientations at interrogation distance of 5 cm. 175

Figure 8.45 Normalised shift in the resonant frequency of the CMPA attached to an aluminium plate against the applied strain for three different horn orientations at interrogation distance of 6 cm.....175

Figure 8.46 Normalised shift in the resonant frequency of the CMPA attached to an aluminium plate against the applied strain for three different horn orientations at interrogation distance of 7 cm.....176

Figure 8.47 Normalised shift in the resonant frequency of the CMPA attached to an aluminium plate against the applied strain for three different horn orientations at interrogation distance of 8 cm.....176

Figure 8.48 Normalised shift in the resonant frequency of the CMPA attached to an aluminium plate against the applied strain for three different horn orientations at interrogation distance of 9 cm.....177

Figure 8.49 Normalised shift in the resonant frequency of the CMPA attached to an aluminium plate against the applied strain for three different horn orientations at interrogation distance of 10 cm.....177

Figure 8.50 Shift in the resonant frequency of the CMPA attached to a CFRP plate at interrogation distance of 1 cm and 0° orientation.....178

Figure 8.51 Shift in the resonant frequency of the CMPA attached to a CFRP plate at interrogation distance of 1 cm and 45° orientation.....179

Figure 8.52 Shift in the resonant frequency of the CMPA attached to a CFRP plate at interrogation distance of 1 cm and 90° orientation.....179

Figure 8.53 Normalised shift in the resonant frequency of the CMPA attached to a CFRP plate against the applied strain for three different horn orientations at interrogation distance of 1 cm. 180

Figure 8.54 Normalised shift in the resonant frequency of the CMPA attached to a CFRP plate against the applied strain for three different horn orientations at interrogation distance of 5 cm. 180

Figure 8.55 Normalised shift in the resonant frequency of the CMPA attached to a CFRP plate against the applied strain for three different horn orientations at interrogation distance of 10 cm. 181

Figure 8.56 Shift in the resonant frequency of the CMPA attached to a GFRP plate at interrogation distance of 1 cm and 0° orientation.....182

Figure 8.57 Shift in the resonant frequency of the CMPA attached to a GFRP plate at interrogation distance of 1 cm and 45° orientation.....182

Figure 8.58 Shift in the resonant frequency of the CMPA attached to a GFRP plate at interrogation distance of 1 cm and 90° orientation.....183

Figure 8.59 Normalised shift in the resonant frequency of the CMPA attached to a GFRP plate against the applied strain for three different horn orientations at interrogation distance of 1 cm. 183

Figure 8.60 Normalised shift in the resonant frequency of the CMPA attached to a GFRP plate against the applied strain for three different horn orientations at interrogation distance of 5 cm. 184

Figure 8.61 Normalised shift in the resonant frequency of the CMPA attached to a GFRP plate against the applied strain for three different horn orientations at interrogation distance of 10 cm. 184

Figure 8.62 Comparison of the relationship between applied strain and the normalised shift in the resonant frequency of the CMPA for different interrogation distances at 0° orientation. 185

Figure 8.63 Comparison of the relationship between applied strain and the normalised shift in the resonant frequency of the CMPA for different interrogation distances at 45° orientation. 186

Figure 8.64 Comparison of the relationship between applied strain and the normalised shift in the resonant frequency of the CMPA for different interrogation distances at 90° orientation. 186

Figure 8.65 Comparison of the relationship between applied strain and the normalised shift in the resonant frequency of the CMPA attached to an aluminium plate for interrogation distances of 1 cm, 5 cm and 10 cm at 0° orientation. 187

Figure 8.66 Comparison of the relationship between applied strain and the normalised shift in the resonant frequency of the CMPA attached to an aluminium plate for interrogation distances of 1 cm, 5 cm and 10 cm at 45° orientation. 187

Figure 8.67 Comparison of the relationship between applied strain and the normalised shift in the resonant frequency of the CMPA attached to an aluminium plate for interrogation distances of 1 cm, 5 cm and 10 cm at 90° orientation. 188

Figure 8.68 Comparison of the relationship between applied strain and the normalised shift in the resonant frequency of the CMPA attached to a CFRP plate for interrogation distances of 1 cm, 5 cm and 10 cm at 0° orientation. 188

Figure 8.69 Comparison of the relationship between applied strain and the normalised shift in the resonant frequency of the CMPA attached to a CFRP plate for interrogation distances of 1 cm, 5 cm and 10 cm at 45° orientation. 189

Figure 8.70 Comparison of the relationship between applied strain and the normalised shift in the resonant frequency of the CMPA attached to a CFRP plate for interrogation distances of 1 cm, 5 cm and 10 cm at 90° orientation. 189

Figure 8.71 Comparison of the relationship between applied strain and the normalised shift in the resonant frequency of the CMPA attached to a GFRP plate for interrogation distances of 1 cm, 5 cm and 10 cm at 0° orientation. 190

Figure 8.72 Comparison of the relationship between applied strain and the normalised shift in the resonant frequency of the CMPA attached to a GFRP plate for interrogation distances of 1 cm, 5 cm and 10 cm at 45° orientation. 190

Figure 8.73 Comparison of the relationship between applied strain and the normalised shift in the resonant frequency of the CMPA attached to a GFRP plate for interrogation distances of 1 cm, 5 cm and 10 cm at 90° orientation. 191

Figure 8.74 Comparison of strain-normalised frequency shift relationship at interrogation distance of 1 cm and 0° orientation for reference and offset locations of horn antenna. 192

Figure 8.75 Comparison of resonant frequency of CMPA at interrogation distance of 1 cm and 0° orientation for reference and offset locations of horn antenna.....192

Figure 8.76 Comparison of resonant frequency of CMPA attached to three different plates at interrogation distance of 1 cm and 0° orientation. 193

Figure 8.77 Comparison of strain-normalised frequency shift relationship at interrogation distance of 1 cm and 0° orientation for three different plates. 194

Figure 8.78 Comparison of strain-normalised frequency shift relationship at interrogation distance of 1 cm and 45° orientation for three different plates. 194

Figure 8.79 Comparison of strain-normalised frequency shift relationship at interrogation distance of 1 cm and 90° orientation for three different plates. 195

Figure 8.80 Comparison of strain-normalised frequency shift relationship at interrogation distance of 5 cm and 0° orientation for three different plates. 195

Figure 8.81 Comparison of strain-normalised frequency shift relationship at interrogation distance of 5 cm and 45° orientation for three different plates. 196

Figure 8.82 Comparison of strain-normalised frequency shift relationship at interrogation distance of 5 cm and 90° orientation for three different plates. 196

Figure 8.83 Comparison of strain-normalised frequency shift relationship at interrogation distance of 10 cm and 0° orientation for three different plates. 197

Figure 8.84 Comparison of strain-normalised frequency shift relationship at interrogation distance of 10 cm and 45° orientation for three different plates. 197

Figure 8.85 Comparison of strain-normalised frequency shift relationship at interrogation distance of 10 cm and 90° orientation for three different plates. 198

Abbreviations and Acronyms

2D	Two Dimensional
2-SR	Two-Turn Spiral Resonator
2-SRR	Double-Split Split Ring Resonator
3D	Three Dimensional
ABC	Absorbing Boundary Condition
APDL	ANSYS Parametric Design Language
BC-SRR	Broadside-Coupled Split Ring Resonator
BI	Boundary Integral
C-DRA	Cylindrical Dielectric Resonator Antenna
CEM	Computational Electromagnetics
CFRP	Carbon Fibre Reinforced Polymer
CH	Cluster Head
cm	Centimetre
CMPA	Circular Microstrip Patch Antenna
CPU	Central Processing Unit
CSV	Comma Separated Values
dB	Decibel
DBS	Direct Broadcast Service
DOF	Degree of Freedom
DRA	Dielectric Resonator Antenna
e.g.	Example
EC-SRR	Edge-Coupled Split Ring Resonator
edn	Edition
et al.	And others
FD-TD	Finite Difference Time Domain
FE	Finite Element
FEA	Finite Element Analysis
FIT	Finite Integration Technique
FNBW	First-Null Beamwidth
FR4	Flame Retardant 4
GA	Genetic Algorithm
GFRP	Glass Fibre Reinforced Polymer

GHz	Gigahertz
GIS	Gas Insulation Switchgear
GPS	Global Positioning System
GUI	Graphical User Interface
H-DRA	Hemispherical Dielectric Resonator Antenna
HF	High Frequency
HPBW	Half-Power Beamwidth
i.e.	That is
KHz	Kilohertz
kN	Kilo Newton
MHz	Megahertz
mm	Millimetre
MMIC	Monolithic Microwave Integrated Circuit
MoM	Method of Moments
MPA	Microstrip Patch Antenna
NA	Network Analyser
NB-SRR	Nonbianisotropic Split Ring Resonator
NN	Neural Network
no.	Number
ohm	ohm (unit of electric resistance)
PCB	Printed Circuit Board
PEC	Perfect Electric Conductor
PMC	Perfect Magnetic Conductor
PML	Perfectly Matched Layer
pp.	Pages
PTFE	Polytetrafluoroethylene
R-DRA	Rectangular Dielectric Resonator Antenna
RF CMOS	Radio Frequency Complementary Metal-Oxide-Semiconductor
RF	Radio Frequency
RMIT	Royal Melbourne Institute of Technology
RMPA	Rectangular Microstrip Patch Antenna
SAR	Specific Absorption Rate
SHM	Structural Health Monitoring
SMA	Sub-Miniature version A
SMN	Station Management Node

SN	Sensor Node
SNA	Scalar Network Analyser
SRR	Split Ring Resonator
TD-FE	Time Domain Finite Element
TD-IE	Time Domain Integral Equation
TRC	Time Reversal Concept
UHF	Ultra High Frequency
UV	Ultraviolet
VNA	Vector Network Analyser
vol.	Volume
vs.	Versus
VSWR	Voltage Standing Wave Ratio
WLAN	Wireless Local Area Network

List of Symbols

ω	Angular frequency of the wave
Y	Antenna input admittance
I_{in}	Antenna input current
Z	Antenna input impedance
V_{in}	Antenna input voltage
G_{loss}	Antenna loss conductance
R_{loss}	Antenna loss resistance
G_{rad}	Antenna radiation conductance
R_{rad}	Antenna radiation resistance
I_0	Antenna source current
V_0	Antenna source voltage
ε_s	Applied strain
C	Capacitance SRR
Z_T	Characteristic impedance of a quarter-wavelength transformer
Z_1	Characteristic impedance of medium 1
Z_2	Characteristic impedance of medium 2
ρ	Charge density
G_1	Conductance
G_c	Conduction conductance
e_c	Conduction efficiency of an antenna
σ	Conductivity
c_1	Constant number 1
c_2	Constant number 2
$\nabla\times$	Curl operator
J	Current density
$\vec{J}_b$	Current density at the bottom surface of the patch

$\vec{J}_t$	Current density at the top surface of the patch
J_z	Current density of the patch at z direction
dB	Decibel
d	Depth of Rectangular dielectric resonator antenna
G_d	Dielectric conductance
e_d	Dielectric efficiency of an antenna
D	Directivity of an antenna
r	Distance from the antenna
$\nabla \bullet$	Divergence operator
$TE_{01\delta}$	Dominant electric mode of cylindrical dielectric resonator antenna
$TM_{01\delta}$	Dominant magnetic mode of cylindrical dielectric resonator antenna
$HE_{11\delta}$	Dominant magnetic-electric mode of cylindrical dielectric resonator antenna
TE_{111}	Dominant mode of hemispherical dielectric resonator antenna
$TE^{x}_{\delta 11}$	Dominant mode of Rectangular dielectric resonator antenna
L_{EC}	EC-SRR self inductance
L_{eff}	Effective length of the rectangular microstrip patch antenna
ε_e	Effective permittivity
a_e	Effective radius of circular microstrip patch antenna
a_{es}	Effective radius of circular microstrip patch antenna after applying strain
ε_{reff}	Effective relative permittivity
E	Electric field
E_z	Electric field at z direction
E_ϕ	Electric field component at azimuth direction
E_θ	Electric field component at inclination direction
E_r	Electric field component at radial direction
D'	Electric flux density
X	Equivalent reactance of the antenna
B	Equivalent susceptance of the antenna
$J(x)$	First-order Bessel function

k_0	Free-space wave number
λ_0	Free-space wavelength
ω_0	Frequency of resonance of the EC-SRR
f_{wave}	Frequency of the wave
G	Gain of an antenna
h_c	Height of Cylindrical dielectric resonator antenna
h	Height of dielectric substrate
h_r	Height of Rectangular dielectric resonator antenna
ε''	Imaginary part of permittivity
Z_L	Impedance at the edge of microstrip patch antenna
Z_C	Impedance of microstrip feed line
Z_0	Impedance of the transmission line
E_i	Incident electric field
a_1	Input at Port 1
a_2	Input at Port 2
Z_a	Input impedance of an antenna
E'	Instantaneous electric field intensity
H'	Instantaneous magnetic field intensity
D	Largest dimension of the antenna
L_T	Length of a quarter-wavelength transformer
L	Length of rectangular microstrip patch antenna
L_s	Length of slot in circular microstrip patch antenna
$\tan\delta$	Loss tangent
H	Magnetic field
B'	Magnetic flux density
r	Mean radius of the EC-SRR
$\mu\varepsilon$	Micro-strain
G_{12}	Mutual conductance
F	Normalised frequency of Rectangular dielectric resonator antenna
Ω	Ohm
b_1	Output at Port 1

b_2	Output at Port 2
k_p	Patch geometry factor
C_{pul}	Per unit length capacitance of SRR along the slot between the rings
μ	Permeability
μ_0	Permeability of free space
ε	Permittivity
ε_0	Permittivity of free space
z	Perpendicular direction to the circular patch
ν	Poisson's ration
S_{11}	Port 1 reflection coefficient
S_{21}	Port 1 to Port 2 transmission coefficient
S_{22}	Port 2 reflection coefficient
S_{12}	Port 2 to Port 1 transmission coefficient
E_r	Radiated electric field
P_{rad}	Radiated power
η_e	Radiation efficiency factor of the antenna
U	Radiation intensity
U_0	Radiation intensity of an isotropic source
W_{rad}	Radiation power density (instantaneous Poynting vector)
a	Radius of circular microstrip patch antenna
R	Radius of circular microstrip patch antenna
a_c	Radius of cylindrical dielectric resonator antenna
a_h	Radius of hemispherical dielectric resonator antenna
ε'	Real part of permittivity
e_r	Reflection (mismatch) efficiency of an antenna
Γ	Reflection coefficient
ε_r	Relative permittivity
R_{in}	Resonance input resistance
f	Resonant frequency
f_r	Resonant frequency of circular microstrip patch antenna
f_{rs}	Resonant frequency of circular microstrip patch antenna after applying strain

f_0	Resonant frequency of the EC-SRR
L_{RT}	Return loss of an antenna
S	Scattering parameter
TM_{101}	Second order mode of hemispherical dielectric resonator antenna
∇f	Shift in the resonant frequency of circular microstrip patch antenna
P	Signal power
S_i	Sine integral
TM^z	Supported mode by circular microstrip patch antenna
R	The distance from an antenna to its far-field region
TM_{110}	The dominant mode of circular microstrip patch antenna
Q_c	The quality factor of the antenna due to conductive losses
Q_d	The quality factor of the antenna due to dielectric losses
Q_{rad}	The quality factor of the antenna due to radiation losses
Q_{sw}	The quality factor of the antenna due to surface waves
R_2	The radius of the radiating near-field region boundary
R_1	The radius of the reactive near-field region boundary
J_n	The nth order Bessel function
S_n	The nth order Struve function
Q_t	The total quality factor of the antenna
t_p	Thickness of metallic patch
t	Time
G_t	Total conductance
e_0	Total efficiency of an antenna
P_{in}	Total input power accepted by the antenna
P_t	Total radiated power
T	Transmission coefficient
E_t	Transmitted electric field
∇	Vector operator
c	Velocity of light in vacuum
V	Voltage

$VSWR$	Voltage standing wave ratio
v	Wave velocity
λ	Wavelength
w_0	Width of microstrip feed line
w_r	Width of Rectangular dielectric resonator antenna
w	Width of rectangular microstrip patch antenna
ΔL	Difference between actual and effective length of rectangular microstrip patch antenna at one edge of the patch
TM^x_{002}	Second order mode of rectangular microstrip patch antenna in the direction of its width
TM^x_{020}	Second order mode of rectangular microstrip patch antenna in the direction of its length
$H^{(2)}(x)$	Second-order Hankel function
TM^x_{010}	The dominant mode of rectangular microstrip patch antenna in the direction of its length
TM^x_{001}	The dominant mode of rectangular microstrip patch antenna in the direction of its width
k_0	Phase constant for free space
y_0	Feed distance from the edge of rectangular microstrip patch antenna
$\acute{\rho}$	Distance from the centre of circular microstrip patch antenna
ρ_0	Feed distance from the centre of circular microstrip patch antenna
k	Wave phase constant
y	Distance from the edge of rectangular microstrip patch antenna

CHAPTER 1

Introduction

1.1 Background

There have been significant developments in aerospace, marine and civil industries during the past few decades. These developments include new design methods and tools like computational software packages, new manufacturing techniques and new materials. One of the major advances especially in aerospace industry is the utilization of highly developed composite materials. These materials have several advantages over conventional aerospace materials such as aluminium alloys. They have superior strength-to-weight ratio which help the manufacture of more fuel efficient aircrafts. Their electromagnetic properties, also, make them suitable for multifunctional applications in both commercial and military airplanes. However, composite structures have introduced new complications in health and usage monitoring for aerospace, marine and civil structures. These shortcomings include new types of damages such as delamination, debonding and fibre breakage which enhanced the need for more accurate and reliable damage monitoring techniques.

In recent years, new structural health monitoring (SHM) systems has been developed to detect various types of damages in both metallic and composite structures. SHM techniques are in their initial stages of development and require more advanced technologies to be able to implement them in real structures. These requirements include wireless sensors, reliable damage detection mechanisms, robust sensor networks, and improved signal processing techniques. Wireless sensors are of interest because of their potential to eliminate complex wiring networks in SHM systems which may result in more reliable and practical monitoring techniques for new and old structures. Wireless monitoring techniques may help in the development of real time monitoring of damage in aerospace structures to avoid consequential catastrophic events. However, design and manufacturing of compact, accurate

and reliable wireless sensors that could be integrated into composite structures to detect miniature defects introduces new areas of research.

1.2 Objectives and Rational

Although a huge amount of work has been done regarding wireless sensors and their applications in SHM, all these technologies have major problems. These drawbacks include the need for a battery which has a limited life time, need for a separate sensor and antenna which increases the complexity, size and weight of the sensory unit, need for specialist sensor fabrication technology which make them costly and finally need for a wireless sensor network which need complicated software and data acquisition units. Therefore, present technologies do not seem feasible for most industries. All of these complications could be solved if the sensor itself acts as a communication device.

The aim of this research is to investigate the feasibility of wireless strain measurement using microstrip patch antennas. The main question is whether the resonant frequency of microstrip patch antennas changes with a change in its physical dimensions as a result of the applied strain. The relationship between strain and antenna frequency shift needs to be investigated. Also, the possibility of using this type of antenna for measuring strain in composite materials is of interest. The final question targets the requirements of wireless strain measurement.

The key objective of this research is to study different antenna sensor configurations in order to investigate the sensitivity and directionality of the antenna strain sensor and enable the wireless strain measurement technology. The proposed antenna sensors should be able to detect strain as well as its directions. These sensors are required to be comparable in size to conventional strain gauges. The final objective is to develop design tools and methodologies which can be used for further development of these sensors including Finite Element procedures. Alternative electromagnetic configurations which may be suitable for this purpose should be proposed for future research.

If this type of antenna could be used as a wireless strain sensor, wireless detection of damage in SHM systems may be possible and as a result, weight, cost and complexity of the SHM system will decrease. In addition, more sensors could be embedded in a structure which results in better performance and increases the reliability of the monitoring system. This leads to safer and less expensive structures for aerospace, marine and civil applications.

1.3 Methodology

In order to achieve the objectives of the proposed research, first a comprehensive literature review on structural health monitoring techniques with an emphasis on wireless sensors has been conducted to identify the current gaps in this area. The literature review was in a direction to find the requirements for a breakthrough in current use of antennas in wireless sensor technologies. The author has made the effort to narrow down the scope of the research to the use of microstrip patch antennas and similar electromagnetic structures in wireless structural health monitoring.

After identifying the current problems with regard to the use of microstrip patch antennas in SHM, a comprehensive study on electromagnetic principles especially microstrip patch antennas has been performed. This study was necessary to gain knowledge about the characteristics and operation mechanisms of microstrip patch antennas. In this stage, several major antenna handbooks were used to obtain important properties of microstrip patch antennas and similar electromagnetic structures. This led to a more detailed study of the relationship between strain and resonant frequency of these structures. As a result, a theoretical relationship between strain and normalised frequency shift of circular microstrip patch antennas has been derived. This was followed by numerical studies on strain measurement capability of different electromagnetic structures using MATLAB™ software.

To further investigate the linear relationship between strain and frequency shift Finite Element Analysis (FEA) has been carried out. This was after a comprehensive study on two software packages, ASNSY™ and HFSS™, for mechanical/high-frequency electromagnetic and high-frequency electromagnetic analysis, respectively. During this stage, two different FEA methods have been developed to be used for further study on different antenna configurations. The developed FEA methods could be used in the future for more precise design of antenna sensors as well as optimisations. Whilst the FEA results confirmed the theoretical study in the previous stage, new antenna configurations with better sensitivity and directionality have been designed.

In the next stage, for each antenna sensor design, the antennas as well as test plates were fabricated to verify the theoretical and computational results. Conventional strain gauges were used to measure the applied strain induced by the test machine. Three-point bend test

was used to bend the antennas attached to the test plates. These tests were performed at RMIT University's Material Testing Laboratory.

Final stage of this study includes a combination of different approaches to enable wireless measurement of strain. Primary experimental investigations followed by theoretical studies on electromagnetic wave propagation and antenna field regions resulted in proposing a new technique to measure the resonant frequency of circular microstrip patch antennas wirelessly. This study was followed by further finite element analysis to accurately model the wireless strain measurement environment. Finally, experimental tests were used to evaluate the proposed technique and to demonstrate wireless strain measurement for different aerospace materials.

1.4 Thesis Outline

Chapter 1: Introduction

This chapter presents a brief background of structural health monitoring, the objectives and rationale of the research, the research methodology, the outline of the thesis, and a list of publications.

Chapter 2: Literature Review: Structural Health Monitoring

A comprehensive literature review on structural health monitoring techniques with an emphasis on wireless sensors is available in this chapter. The reader will gain the knowledge about the current use of antennas in wireless sensor technologies. The author has made the effort to narrow down the scope of the research to the use of microstrip patch antennas and similar electromagnetic structures in wireless structural health monitoring.

Chapter 3: Literature Review: Microstrip Patch Antennas

In this chapter, a comprehensive literature review on microstrip patch antennas is provided. First, basic electromagnetic concepts are explained and then important antenna parameters required to understand the principle of operation of microstrip patch antennas are described. After that, microstrip patch antenna radiation mechanisms, different components, various configurations and their applications are discussed.

Chapter 4: Antenna Theory and Evaluation

The theory of using microstrip patch antennas for strain measurement is first introduced in this chapter. The theoretical study of strain-frequency shift relationship for circular microstrip patch antennas is discussed. This is followed by analytical evaluation of the proposed theory for circular microstrip patch antennas. In addition, other possible antenna and resonator configurations which may be used as a strain sensor are studied analytically. At the end, antenna design procedures including the design of different feeding mechanisms are provided. The computer codes used in this chapter are written in MATLAB™ and are provided in Appendix A.

Chapter 5: Finite Element Analysis

Finite element analysis is required to validate the proposed theory and is vital for future designs of antenna sensors. This chapter explains two different finite element methods which are developed for microstrip patch antenna sensor study. First method utilizes ANSYS APDL™ and FORTRAN™ software and the second one employs ANSYS Workbench™ and HFSS™ software. Also, the design of two novel antenna configurations, to overcome the shortcomings of simple circular microstrip patch antenna sensor, which is based on simulations using HFSS™ software are provided. The codes and simulation instructions for this chapter are provided in Appendixes B, C, D and E.

Chapter 6: Experimental Details

In order to validate theoretical results as well as finite element analysis provided in previous chapters, experimental tests are required. The detail description of these tests including sample manufacturing (antennas and test plates); test setup configuration, and data acquisition devices used in this research are presented in this chapter.

Chapter 7: Results and Discussion

The results derived from theoretical, analytical, computational and experimental studies are gathered in this chapter. The reader can find detail discussions about three different antenna sensor configurations which are the subject of this research, in this chapter. The effect of loading direction, test plate material and other parameters are discussed.

Chapter 8: Wireless Strain Measurement

This chapter includes the study on required techniques for wireless measurement of strain. The appropriate technique for wireless strain measurement is chosen and finite element analysis using HFSS™ software is used to enhance the study which is further evaluated by experimental tests. Effects of important parameters on wireless strain measurement are also investigated.

Chapter 9: Conclusion

This chapter finally presents a summary of the outcomes of the work conducted in this study including some suggestions for future work.

1.5 List of Publications

Journal Papers

- Daliri, A., Galehdar, A., John, S., Rowe, W.S.T., Ghorbani, K. 2010, 'Circular microstrip patch antenna strain sensor for wireless structural health monitoring', *Journal of Lecture Notes in Engineering and Computer Science,* 2184(1), pp. 1173-1178.

- Daliri, A., Galehdar, A., Rowe, W.S.T., Ghorbani, K., John, S., 'Utilising microstrip patch antenna strain sensors for structural health monitoring', *Journal of Intelligent Material Systems and Structures* (Accepted for publication on 14 November 2011).

Conference Papers

- Daliri, A., Galehdar, A., John, S., Rowe, W.S.T., Ghorbani, K. 2010, 'Circular microstrip patch antenna strain sensor for wireless structural health monitoring,' in: *Proceedings of the World Congress on Engineering (WCE 2010),* London, U.K., Jun-Jul, 2010.

- Daliri, A., John, S., Galehdar, A., Rowe, W.S.T., Ghorbani, K. 2010, 'Strain measurement in composite materials using microstrip patch antennas,' in: *Proceedings of the ASME 2010 Conference on Smart materials, Adaptive structures*

and Intelligent Systems (SMASIS 2010), Philadelphia, Pennsylvania, USA, Sep-Oct, 2010.

- Daliri, A., Galehdar, A., John, S., Rowe, W.S.T., Ghorbani, K. 2011, 'Slotted circular microstrip patch antenna application in strain based structural health monitoring,' in: *Proceedings of the 7th DSTO International Conference on Health & Usage Monitoring (HUMS 2011)*, Melbourne, Australia, Feb-March, 2011.

- Daliri, A., Galehdar, A., Rowe, W.S.T., John, S., Ghorbani, K., Wang, C.H. 2011, 'Multidirectional circular microstrip patch antenna strain sensor,' in: *Proceedings of the ASME 2011 Conference on Smart materials, Adaptive structures and Intelligent Systems (SMASIS 2011)*, Phoenix, Arizona, USA, Sep, 2011.

Conference Abstract Presentations

- Daliri, A., Galehdar, A., John, S., Rowe, W.S.T., Ghorbani, K. 2011, 'Microstrip patch antenna strain sensors,' in: *Proceedings of Twelfth Australian Symposium on Antennas (ASA12)*, Sydney, Australia, Feb, 2011.

CHAPTER 2

Literature Review: Structural Health Monitoring

2.1 Introduction

Science and technology have been developing from the beginning of recorded human history to help mankind for a better and more comfortable life. As a result, numerous amounts of structures have been designed and manufactured that form different areas of science and technology. Recent developments include airplanes and cars for transporting human and goods, giant ships and submarines for various purposes, space shuttles and satellites for communication and discovery and civil structures such as bridges and high-rise buildings.

Despite of the state of the art progress in engineering and technology which lead to a better life, there are still several concerns regarding these cutting edge technologies. Two main challenges in front of engineers are safety and cost (Staszewski, 2000; Mancini, Tumino and Gaudenzi, 2006; Auweraer and Peeters, 2003). The importance of these issues is well known to everyone and there is no need to be discussed further. The accident that has happened to the space shuttle Columbia is a case in point (Figures 2.1 and 2.2).

To ensure structural integrity and safety and also to reduce structural costs such as repair and maintenance costs, health and usage monitoring techniques are developed in many engineering areas (Staszewski, Boller and Tomlinson, 2004; Tanner et al., 2003). These techniques help predict structural failures in early stages and therefore inspection intervals can be adjusted to real needs and special overhauls could be performed (Staszewski, Boller and Tomlinson, 2004; Mancini, Tumino and Gaudenzi, 2006). As a result, engineers can avoid catastrophic events and maintenance costs can be lowered. However, these techniques

are in there early stages and more research needs to be done in the area of monitoring the health of structures.

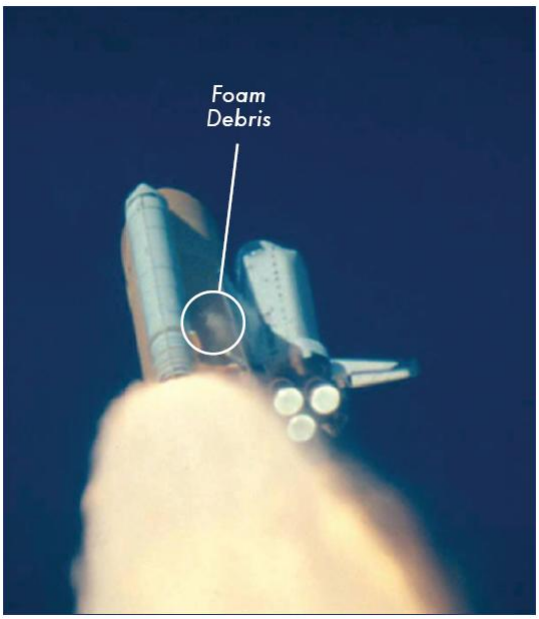

Figure 2.1 A shower of foam debris after the impact on Columbia's left wing. The event was not observed in real time (Courtesy: NASA).

Figure 2.2 The Columbia shuttle explosion (Courtesy: NASA).

Structural health monitoring (SHM) is of critical importance to different industries, e.g. Aerospace, Marine and Civil industries, especially for composite structures (Chang, Flatau and Liu, 2003; Auweraer and Peeters, 2003). Applications of composite materials in these industries are growing everyday and the need for online monitoring of such structures grows consequently. This is because of their advantages over conventional metals, apart from major disadvantages such as delamination (Kesavan, John and Herszberg, 2008a, 2008b). Mechanical properties of these materials which results in light weight-structures attracts aerospace industries to apply them in commercial airplanes like BOEING 787 which half of

its structure is made of composite materials (Figure 2.3) (BOEING, 2011a). As a Result, this airplane “will use 20 percent less fuel for comparable missions than today's similarly sized airplane” (BOEING, 2011b). Apart from huge amount of work in the literature, there is still a gap in Structural Health Monitoring (SHM) systems for the detection of different types of defects in composite materials.

Figure 2.3 Advanced composite use in BOEING 787 commercial airplane (Courtesy: BOEING).

A good deal of work has been accomplished on SHM which all indicate its value. A comprehensive list of different international research programs on this subject could be found in (Auweraer and Peeters, 2003). Being sure about the safety of a structure is a vital concern. This matter is not only for the safety but also is for better performance, increasing lifetime and on time overhaul of the structure. Several different methods have been used for SHM while new approaches could be investigated to improve reliability and application of SHM.

Currently, SHM techniques are based on life safe design and periodic inspections. Moreover, flight parameters and non-destructive testings are used in practice (Staszewski, Boller and Tomlinson, 2004; Mancini, Tumino and Gaudenzi, 2006). Available and developing methods in SHM and various sensor technologies will be discussed in the

following section to provide a general view of them. A more comprehensive literature review about SHM techniques can be found in (Mehdizadeh, 2009).

2.2 Background (SHM methods)

From a damage detection point of view, SHM methods could be divided into two general categories. First category includes methods which can only determine whether or not damage is present in the entire structure. These methods are referred to as ‘‘global health monitoring’’ methods. Second category includes techniques to measure the state of stress, locate damage and evaluate its size. These methods are ‘‘local health monitoring’’ methods (Chang, Flatau and Liu, 2003).

At present, traditional non-destructive techniques including visual inspection, radiography and eddy current are used to inspect aerospace structures. Acousto-Ultrasonics and guided Ultrasonic waves are developed recently by the use of optical fibre and piezoelectric sensors for damage detection (Staszewski, Boller and Tomlinson, 2004; Chang, Flatau and Liu, 2003). These techniques need the large mass and power required to have an effective damage monitoring system for aerospace vehicles (Mancini, Tumino and Gaudenzi, 2006; Chang, Flatau and Liu, 2003). Other methods are based on magnetic field, X-ray or thermal principles (Auweraer and Peeters, 2003). Tap tests are also used in civil infrastructure, which include bridges and buildings, to determine if voids or de-bonding exist in the structure. However, tap tests are limited to finding voids near the surface, de-bonding of wraps and significant cracks (Chang, Flatau and Liu, 2003). These technologies are followed by advanced signal processing technologies like neural networks or wavelets which make the damage detection easier. The advantages of these methods include reduced life cycle costs, reduced inspection/maintenance effort, improved performance, improved high rate operator availability, extended life of structures and improved safety (Staszewski, Boller and Tomlinson, 2004).

Traditional methods are time consuming and expensive (Staszewski, Boller and Tomlinson, 2004; Chang, Flatau and Liu, 2003). They also need human interaction and sometimes factors like loss of alertness or fatigue of operator affect the results (Staszewski, Boller and Tomlinson, 2004). In addition these human-based inspection processes are very costly (Auweraer and Peeters, 2003). Therefore, the need for a structural health monitoring system which can reliably and accurately locate the damage in a structure and specify its size and

location still exists. Such an in-situ monitoring system should be smart and functional while the structure is in service to alert the operator in the early stages of damage. Such methods which are based on new sensor technologies are in development stages (Staszewski, 2000).

One of these emerging methods is based on strain distribution in the structure (Kesavan, John and Herszberg, 2008a, 2008b). Strain is one of the most important mechanical parameters in SHM systems. By monitoring strain changes in structures, factors that could cause structural failures such as excessive loading, vibration, foundation damages, crack development and environmental aging can be detected (Tata et al., 2009). Different types of sensors are used for detecting strain distribution in structures , for example, strain gauges (Kesavan, John and Herszberg, 2008a, 2008b) or fibre Bragg grating strain sensors (Silva-Munoz and Lopez-Anido, 2009; Li et al., 2006). There are several significant researches about strain-based methods in SHM. Different structural configurations especially T-joint structures have been investigated because of their use in maritime structures (Silva-Munoz and Lopez-Anido, 2009). Different types of defects have been investigated in composite structures using this technique, such as delamination (Kesavan, John and Herszberg, 2008a, 2008b; Zhou and Sim, 2009), crack (Silva-Munoz and Lopez-Anido, 2009) and de-bonding (Li et al., 2006). On the other hand, the importance of an optimized strain sensor network is noticeable (Kesavan, John and Herszberg, 2008a, 2008b; Silva-Munoz and Lopez-Anido, 2009; Tata et al., 2009).

Vibration based method is another relatively new and emerging area of research within SHM. Great deal of work with several different approaches has been done using this method. These works include both traditional methods and modern methods (Oruganti et al., 2008). Traditional methods have different disadvantages such as dependence on experiments for measuring mode shape and damping, dependence on the properties of individual structures and not being sensitive to initial damage (Yan et al., 2007). On the other hand, modern-type methods including Wavelet analysis, Genetic algorithm (GA) and Artificial Neural Network (NN) have their own disadvantages. For example, reliance on environmental excitation, being sensitive to noise and not having a specific damage index (Yan et al., 2007). Therefore, more research is needed to make the use of these techniques in aerospace structures possible. Although these methods are more reliable than other techniques, a practical SHM system which could be able to monitor a structure during work and detect its defects precisely needs more developed techniques.

On the other hand, several works have been done regarding Time-Reversal Concept (TRC) and its applications in different areas of study especially in medical purposes (Wang, Rose and Chang, 2004; Fink, 1999). There are also few researches regarding the use of TRC in monitoring the structure online (Wang, Rose and Chang, 2004; Fink, 1999). Piezoelectric transducers are being used in SHM methods like TRC because of their ability to act as both sensor and actuator (Wang, Rose and Chang, 2004; Mancini, Tumino and Gaudenzi, 2006). However, there are several complications for using TRC in SHM such as determining the exact size of defect (Wang, Rose and Chang, 2004) which is an important issue in SHM. A significant effort should be done to improve its reliability and extend its applications. Furthermore, there is a need for optimizing the number of sensors (/actuators) and their configuration in the structure. Overcoming such problems could help to develop the use of TRC in monitoring the health of aerospace structures.

Optical fibre and piezoelectric sensors are suitable for embedded monitoring systems (Staszewski, 2000). Optical fibre sensor arrays have the ability to both monitor crack growth and delamination under a bonded repair (Jones and Galea, 2002). However, an experimental, analytical and FE modelling has been done on the effect of embedded optical fibres on strength of carbon epoxy composites (Hadzic, John and Herszberg, 1999) which shows that optical fibres reduce the strength of material if their positional spatial density goes beyond a certain amount. In addition, optical fibres need expensive interrogation equipment, have limited strain range, are brittle and it is difficult to replace or repair a fibre (Mancini, Tumino and Gaudenzi, 2006; Chuang, Thomson and Bridges, 2005).

According to Staszewski (2000), none of the damage monitoring techniques will alone be able of meeting all the specification requirements for monitoring aerospace structures. Even if all the benefits of existing methods are considered, there are still major issues to be solved. These techniques are costly, complicated, in some cases they need complex signal processing and require advanced technology for manufacturing them, and could not locate initial damage in all cases. Most importantly, all the techniques mentioned above use wired sensors. These sensors have many disadvantages such as the need for installation during construction. Wires also limit structure's functionality; increase the system complexity and the overall weight of the structure. Therefore, the number of sensors that could be applied is limited (Chang, Flatau and Liu, 2003; Choi, Choi and Cha, 2008; Jia et al., 2006). Hence, a structural health monitoring system able to work wirelessly is required to achieve a comprehensive and practical monitoring technology.

2.3 Wireless Health Monitoring

One important part of any SHM system is the sensor which is used to detect the damage and is common in most of the techniques, where as the damage detection method is different from one system to another. Many of the sensors available for SHM are wired and therefore have practical limitations in order to be embedded into the structures, like strain gauges, piezoelectric transducers, fibre optic sensors, and micro-fibre composite actuators. The initial setup and cabling of sensors is a very time consuming process especially when the number of sensors increases.

Wireless sensors can eliminate the wiring problem of the traditional SHM systems and reduce the maintenance costs associated with it (Wu et al., 2009; Tanner et al., 2003; Spencer, Ruiz-Sandoval and Kurata, 2004). Wiring is especially difficult for rotating composite components such as helicopter blades, rotor shafts, and wind turbine blades (Matsuzaki, Melnykowycz and Todoroki, 2009). An introduction to smart sensing technology, its opportunities and some of its associated challenges is provided in (Spencer, Ruiz-Sandoval and Kurata, 2004). A wireless sensor reduces the weight of the structure and its complexity; thus, practical SHM systems could be developed. However, wireless sensors currently available in the market use batteries as an energy source which has a limited lifetime and increases the sensor size and weight; therefore, could not be used widely in the structure. In some cases where the sensor receives its energy through an antenna the sensory unit is too complicated.

There are several significant researches in this field in recent years which all indicate the need for a wireless sensing system and its importance. However, most of the works in the literature investigate the feasibility of applying a wireless communication device to existing sensors to transfer information or power to and from sensors. A brief description of some recent developments in this area is provided here.

2.3.1 Wireless structural health monitoring in civil industry

One of the major areas of SHM is civil industry and monitoring the condition of concrete is of critical importance for bridges and other structures. Several works has been done to make wireless detection of damage possible in concrete. Figure 2.4 shows a computer-controlled integrated instrumentation and monitoring system for wireless load bridge monitoring (Farhey, 2006).

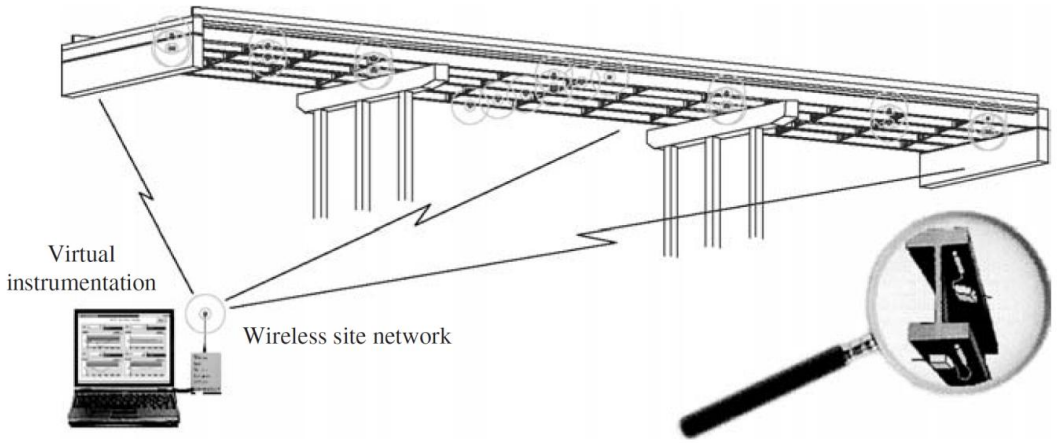

Figure 2.4 A wireless load bridge monitoring system (Farhey, 2006).

The principles, feasibility, and configuration of the wireless system for monitoring the cable tension of cable-stayed bridges are investigated using piezoelectric film sensors in (Liao, Wang and Huang, 2001) (Figure 2.5). In (Chacon et al., 2009) conventional pre-wired gauges and a wirelessly connected strain-measuring system for monitoring steel girders in bridges are compared.

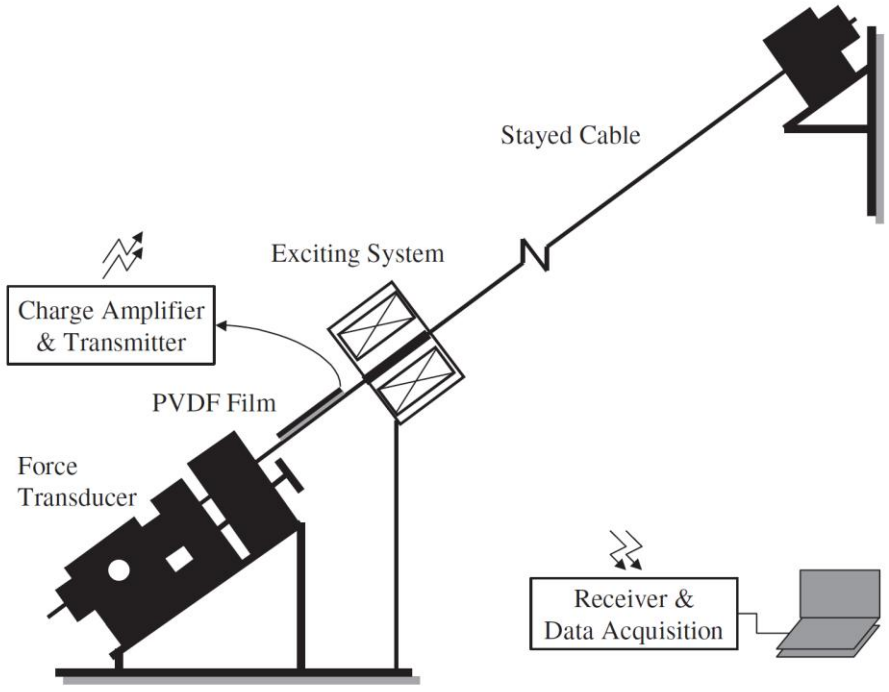

Figure 2.5 wireless system for monitoring the cable tension of cable-stayed bridges (Liao, Wang and Huang, 2001).

Several works has been done regarding embedding an antenna into concrete for use as a communication device between embedded sensor and receiver (Bernhard et al., 2003;

Shams, Ali and Miah, 2006). Different characteristics of microstrip patch antennas with regard to concrete dielectric constant, loss tangent and air-gap has been studied (Shams, Ali and Miah, 2006). In a recent work, the feasibility of sending wireless power to a buried microstrip patch antenna within concrete and effects of moisture, air-gap and thickness has been studied (Shams and Ali, 2007). In all these works antenna has been used as a communication device.

In (Chuang, Thomson and Bridges, 2005) a conducting coaxial electromagnetic cavity that is embedded in or bonded to the concrete structure has been used as a strain sensor. When the structure's dimensions change the dimensions of the cavity change subsequently and as a result the resonant frequency of the cavity changes. A simple loop antenna has been used to determine the cavity resonant frequency remotely. The presented strain sensor is a passive device and requires no power to operate.

A bolted frame structure was tested under load condition by using a coupled commercially available micro electro-mechanical system sensors and a wireless telemetry unit with damage detection firmware (Tanner et al., 2003). This system uses an on-chip antenna to communicate wirelessly; however, it uses a battery pack for its power consumption which increases size and weight of the sensory unit and hence limits its application for aerospace structures where size and weight are two important factors.

2.3.2 Wireless sensors for medical applications

Significant works, regarding wireless sensing for medical applications, have also been reported. A wireless passive strain sensor system which could be fabricated from biocompatible materials is proposed to monitor fractured bones (Umbrecht et al., 2005). However, the sensor is based on volume deformation of a liquid and is not applicable to other applications. A compact stair shaped DRA (Dielectric resonator antenna) sensor for microwave breast cancer detection has been introduced in (Huang and Kishk, 2007). In a recent work microstrip patch antennas has been tested for wearable sensors, which show that resonant frequency shift is dependent on the type of antenna (Conway et al., 2008). A chip-size microstrip patch antenna, assembled with a low-power, low-voltage RF CMOS transceiver was presented for the implementation of wireless nodes in a wireless sensors network mounted in an electronic shirt that monitors the cardio-respiratory functions (Figure 2.6) (Carmo et al., 2006).

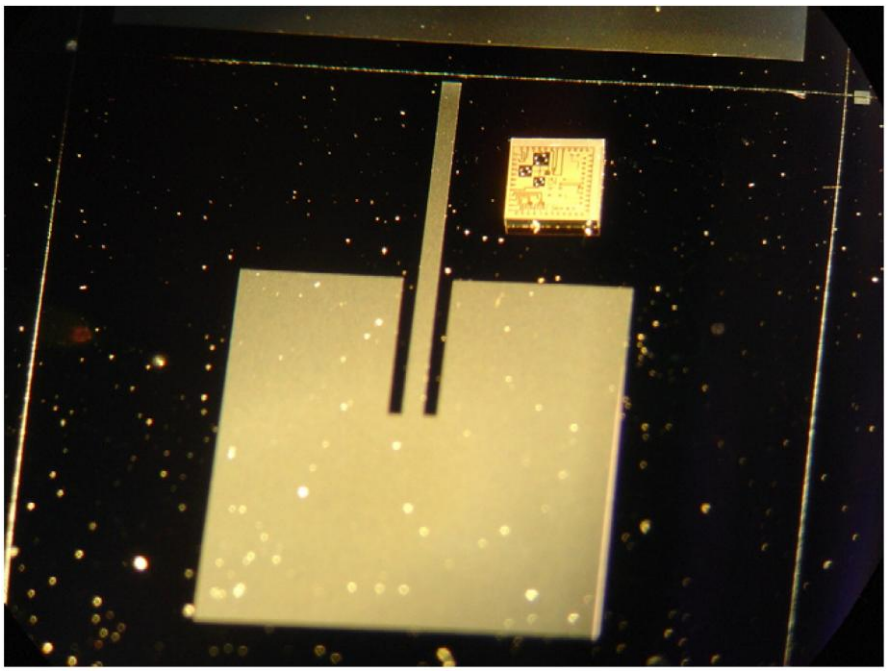

Figure 2.6 Chip-size antenna assembled with an RFCMOS transceiver (Carmo et al., 2006)

2.3.3 Wireless sensors in various applications

A flexible patch type sensor which is composed of the sensor capacitance, reference capacitance, a buffer, and a transmitting antenna is presented for measuring strain in automobile tires (Matsuzaki and Todoroki, 2007). The antenna used is located outside of tire and is attached to sensor using wires. The overall size of sensor and antenna limits its applications. The sensor without the transmitting antenna and signal generator is shown in Figure 2.7.

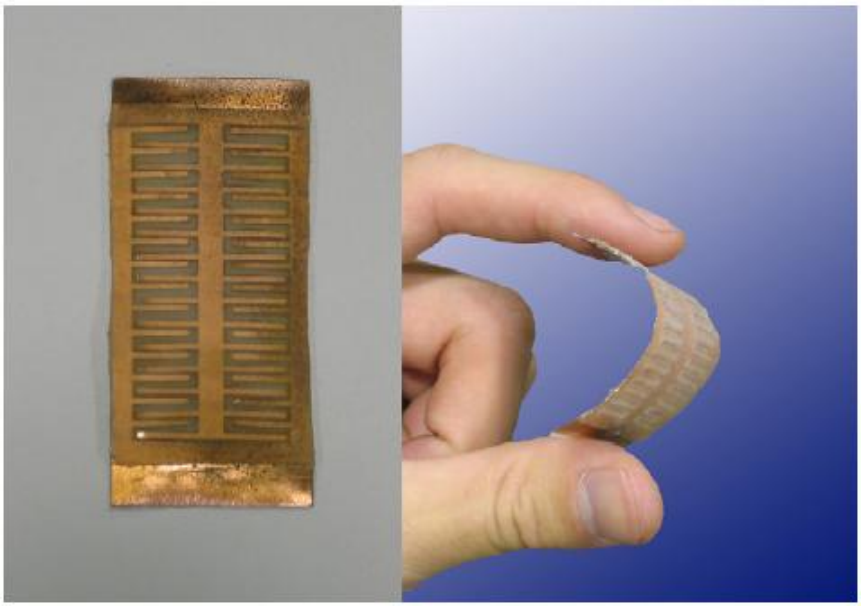

Figure 2.7 Photograph of fabricated patch type sensor (Matsuzaki and Todoroki, 2007).

Multifunctional composites are also attracted some attention to be used in wireless health monitoring systems. Electrical resistance properties of CFRPs (Carbon Fibre Reinforced Polymers) have been used to find delamination cracks (Figure 2.8) (Matsuzaki and Todoroki, 2006). The change in electrical resistance changes the frequency of oscillating circuit and this change is wirelessly sent to another location using an antenna. However, additional techniques are needed to eliminate environmental effects such as temperature change. In addition, the sensing unit still utilises wires.

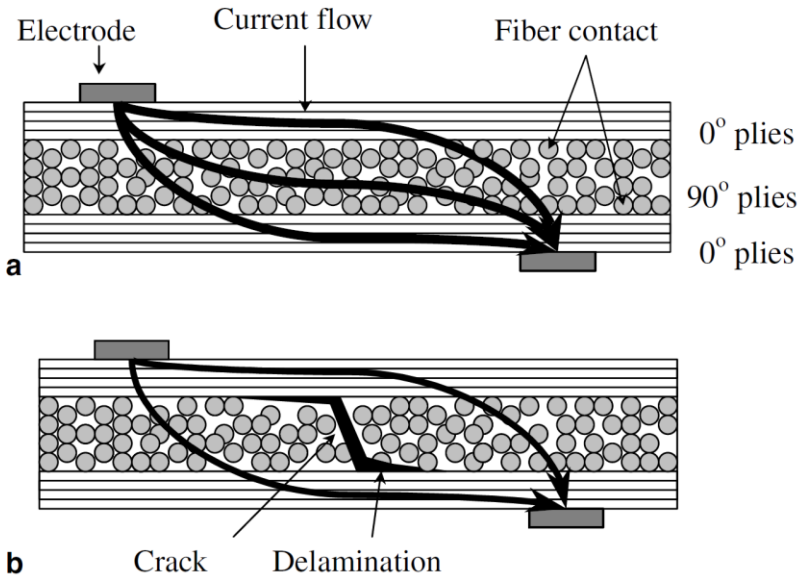

Figure 2.8 Schematic of a practical structure of a carbon/epoxy composite when an electrical current is applied. (a) Electrical network structures of the fibre in a CFRP laminate. (b) The electrical network is broken with a delamination (Matsuzaki and Todoroki, 2006).

In a recent work (Matsuzaki, Melnykowycz and Todoroki, 2009), the electrical conductivity of carbon fibre has been used to model a CFRP structure as a dipole antenna (Figure 2.9). A wing structure or a rotating blade could be modelled in this way and when a crack or delamination occurs, the fibre breakage changes the antenna properties. As the resonant frequency of dipole antenna depends on its length, when a crack occurs this frequency increases and therefore the presence of damage and its location could be identified wirelessly. However, this innovative approach is able to detect one type of damage and only in lateral direction, if the crack already reaches a critical length and therefore could not avoid catastrophic failure. In addition, mentioned techniques could only be applied to one type of material and their damage detection capabilities are limited.

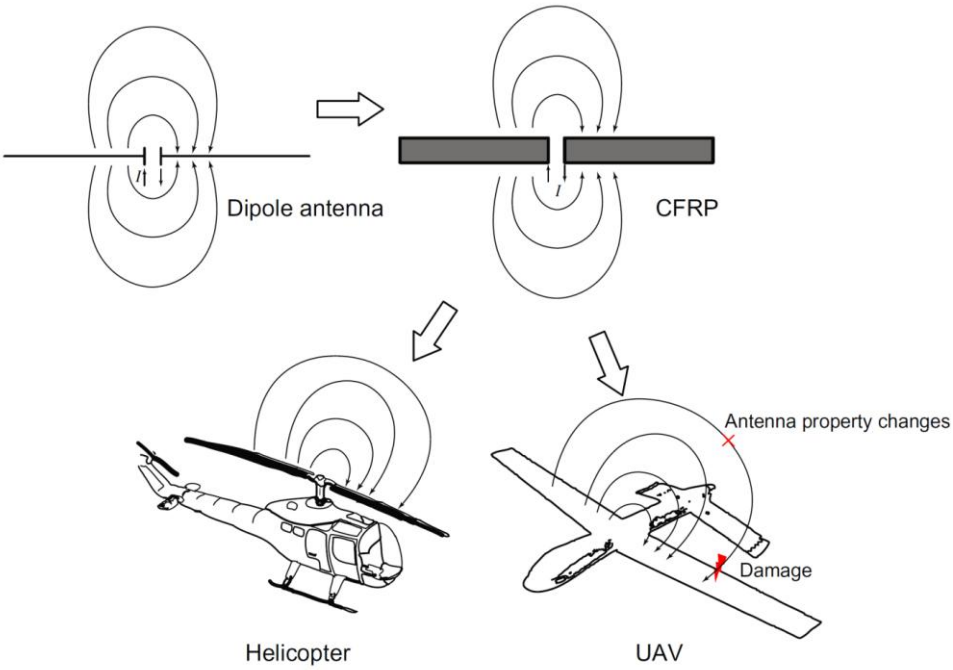

Figure 2.9 Evolution of antenna configurations from a dipole to antenna/sensor multifunctional wing structures (Matsuzaki, Melnykowycz and Todoroki, 2009).

The effort to achieve a wireless sensor has been followed in different industries for various applications. For example, a temperature threshold sensor has been designed for monitoring the temperature at the base of the gaps between the thermal protection tiles on the Space Shuttle (Watters et al., 2007). A rectangular microstrip patch antenna sensor is designed to monitor GIS (gas insulation switchgear) partial discharge UHF signals (Ju et al., 2007). A disk patch microstrip antenna is used for moisture measurements by measuring the magnitudes of microwave reflection (Ghretli et al., 2007b) and the effect of temperature has been eliminated (Ghretli et al., 2007a). A mine-detection sensor using two microstrip patch array antennas has been investigated which show mutual coupling can influence the performance of microstrip antennas and arrays (Zainud-Deen et al., 2006).

In (Choi, Choi and Cha, 2008) several improvements have been made to strain gauge enabled wireless sensor nodes for use in SHM. In a recent study (Takao et al., 2007), the concept and experimental results of RF-powered silicon micro sensors with two types of sensors (A fuse type strain sensor and a moisture sensor) has been investigated. Power source of these micro sensors are provided by remote RF-electromagnetic wave received by a small antenna such as loop-antenna. The maximum distance from sensor nodes and source depends on the emission power, directivity of the antenna, and environment around the chip which limits its applications. In (Chaimanonart and Young, 2006) an external radio

frequency (RF) power source has been used to drive a coil loop, which couples the RF energy into an implanted miniature coil through magnetic coupling to power the microelectronics wirelessly. However, the distance between these two loops is short (Figure 2.10).

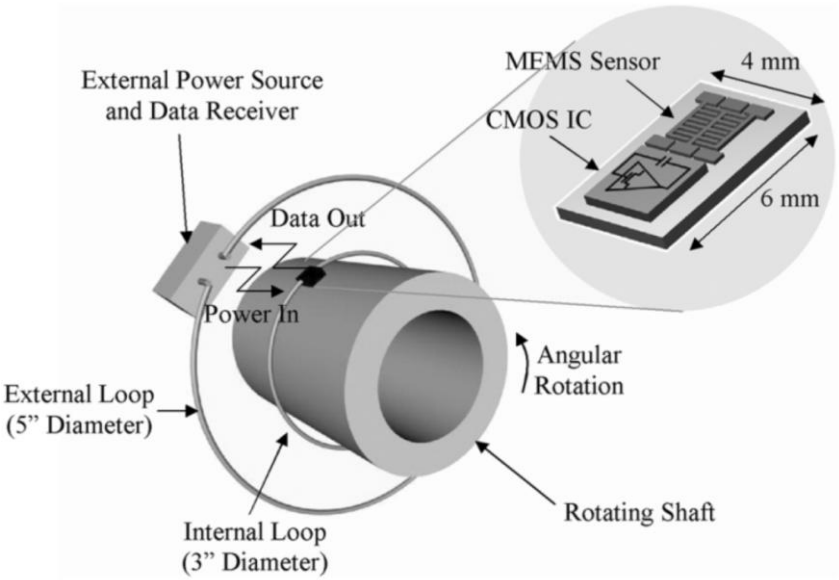

Figure 2.10 Wireless microsystem architecture (Chaimanonart and Young, 2006).

2.3.4 Sensor networks for wireless structural health monitoring

In SHM, sensor networks are deployed in specific locations to collect information about stress, stain, pressure, etc and report to a remote central station. The sensor network consists of the following types of nodes: Sensor Nodes (SN), Cluster Heads (CH), and Station Management Node (SMN). The design of the wireless sensor node includes three modules: sensor input unit, processing core, and wireless communication (Wu et al., 2009). There are several works regarding wireless sensor networks which investigate the optimum number of sensors (Kucuk, Kavak and Yigit, 2007), the location estimation problems of sensor nodes (Kucuk et al., 2008), a topology discovery algorithm for wireless sensor networks (Khedr and Osamy, 2006) and multi-agent wireless sensor networks (Wu et al., 2009). Regardless of these, there are still many complications to be solved so the sensory network with present sensors and wireless nodes attached to them can become practical. Overcoming this problem needs a lot of effort and the resulted networks need complicated hardware and software (Each sensor node is equipped with memory and processing capabilities, multiple sensing modalities and communication capabilities (Khedr and Osamy, 2006)), which could be time consuming and costly.

2.3.5 Antennas for wireless health monitoring systems

One of the major elements in a wireless health monitoring system is the communication device. There is a huge amount of work regarding design and optimization of antennas for wireless sensory applications (Pires et al., 2008; Fu et al., 2009; Fallah-Rad and Shafai, 2008). In (Cheng, 2007) a novel concept is introduced for the antenna designs at high frequencies. In this work the human body surface along with a single straight notch antenna is used to get the maximum antenna gain. In (Kakoyiannis and Constantinou, 2008) feasible reduction on the size of the ground plane for printed antennas has been investigated. A double-folded structure based on multiple-stacked substrates presented which result in further antenna size reduction with the added benefit of dual-band operation for wireless sensor networks (Mendes et al., 2004). A dipole antenna pair coupled sensor unit is introduced in (Yang et al., 2008) and its response to the radiation field measured by the voltage in the readout electronics, which could be used for wireless sensing.

Although a huge amount of work has been done regarding wireless sensors and their applications in SHM, all these technologies have major problems. These drawbacks include the need for a battery which has a limited life time; need for a separate sensor and antenna which increases the complexity, size and weight of the sensory unit; need for a costly technology to fabricate sensor nodes which make them costly; and finally need for a wireless sensor network which need complicated software and data acquisition units. Therefore, present technologies cannot be used for practical applications especially in aerospace industry. However, all of these complications could be solved if the sensor itself acts as a communication device. This matter will be discussed in the following section.

2.4 Microstrip patch antenna strain sensor

There are many types of strain sensors such as resistive and capacitive strain gauges and fibre optic sensors. Resistive strain gauges work based on the principle where the resistance of an electrical conductor changes upon an externally applied load, whether tensile or compressive. On the other hand, capacitive strain gauges are based on the change of separation distance between two parallel conductor plates, which alters the capacitance of the sensor. Optical fibres measure strain based on the change in their length and a resultant reflected wave (Staszewski, Boller and Tomlinson, 2004; Tan et al., 2008). A detailed study on current existing sensors for SHM (including piezoelectric sensors, optical fibre sensors,

resistance strain gauges and shape memory alloys) is available in (Kesavan, 2006; Mehdizadeh, 2009).

As mentioned in previous sections these sensors need a wiring system. Meanwhile, advances in microstrip antennas raise an idea to use these types of antennas as sensors. Therefore, many problems of available wireless strain sensors could be solved. There are few works in the literature which demonstrates the possibility of using these antennas as sensors as a result of changes in their characteristics with different parameters.

Only few significant works have been done recently which show the effect of different parameters on the shift in the resonant frequencies of microstrip patch antennas, such as paint cover (Pell et al., 2008) or adhesive bonds in multi-layer composite antennas (Kim, You and Hwang, 2009). In (Boufrioua and Benghalia, 2006) effects of uniaxial anisotropy in the substrate on the resonant frequency of the rectangular microstrip patch antenna are investigated. It shows that the permittivity in one direction has more effect on the resonant frequency than other directions. In a recent work (Ourir et al., 2009), it has been shown that in cavity antennas a decrease in the value of the capacitance of the metamaterial causes a shift in the resonance toward higher frequencies. Kumar and Pourush (2009) investigated the effect of anisotropy on the resonant frequency of the antenna. It has been found that patch resonant frequencies vary significantly with change of bias field. Conway et al. (2008) show that the resonant frequency shift is dependent on the antenna type and construction. Zivanovic et al. (2007) demonstrated that the use of an air cavity reduces the dielectric constant of the material and changing its position increases the resonant frequency of a rectangular patch antenna (Figure 2.11). The effect of integrating aperture-coupled microstrip antennas in a composite sandwich structure, and sandwich geometry on antenna's electrical properties has been studied using transmission line theory (You and Hwang, 2007).

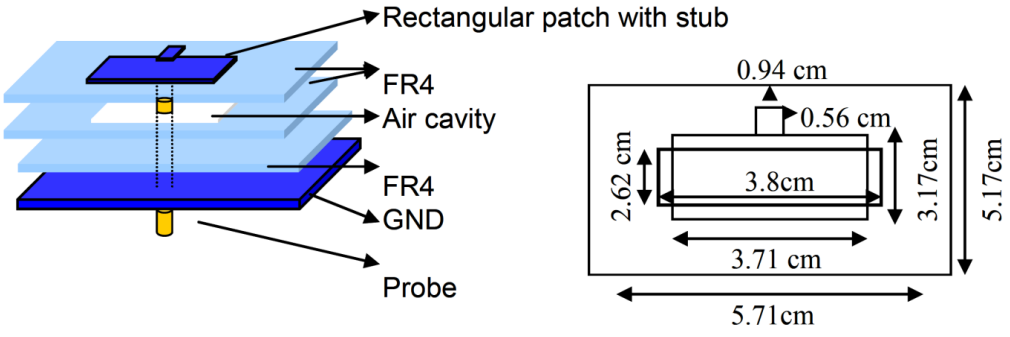

Figure 2.11 Geometry of the fabricated antenna (Zivanovic et al., 2007).

A microstrip patch antenna has been used in an automatic sprinkler control system (Soontornpipit, 2006). The antenna senses the moisture of the soil and transmits this information to an external control system. In this work, genetic algorithm has been used to optimise two different bands of antenna for sensing and communication. This method could be used for designing antenna for different damage types.

Butler et al. (2002) show that strain could be detected in a composite material using an inductive coil in an LC circuit. When the profile of the inductor changes because of strain, its inductance changes subsequently and as a result the resonant frequency shifts which could be detected wirelessly (Figure 2.12). Index of this change in shape is the inductor cross sectional area. The main problem of this system is that the distance between sensor and detector is about 1.43 cm which is very short and therefore makes its applications limited. This system is also sensitive to sensor position and could not detect strain in all directions. Finally, the relationship between strain and frequency is not linear; hence, it is very difficult to estimate strain from measured shift in frequency.

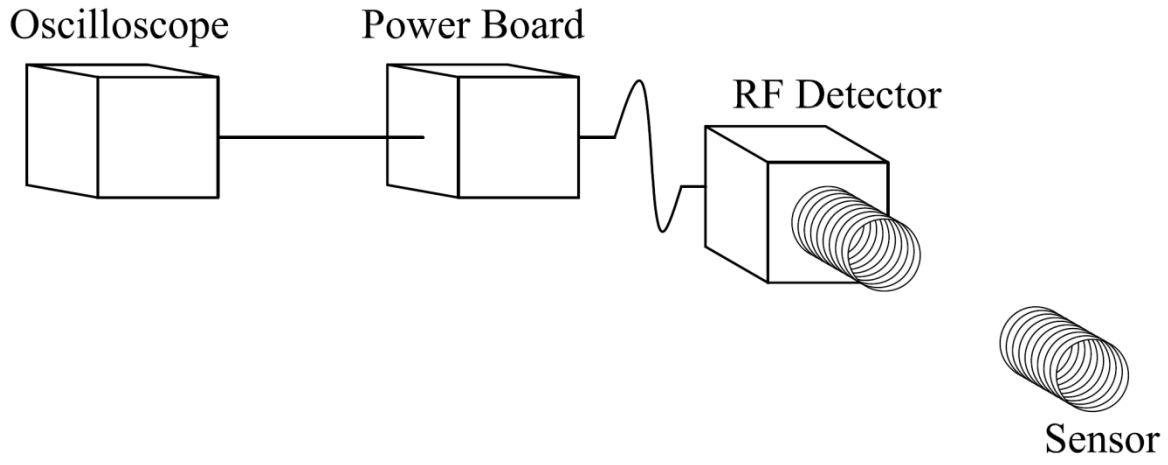

Figure 2.12 Illustration of the experimental setup of an inductive coil in an LC circuit (Butler et al., 2002).

A strain sensor consists of an LC resonant circuit is proposed in (Figure 2.13) (Jia et al., 2006). The planar spiral inductor acts as a passive power source and communication device, whilst the capacitor works as a sensing unit. When electrodes in the capacitor and gaps between them deform, the capacitance and the resonant frequency of the circuit change subsequently. This sensor could be activated by electromagnetic waves, and by applying an oscillating signal using a single loop antenna the frequency response of the voltage across the circuit could be monitored. However, the sensitivity of this sensor depends on the

direction of electrodes of the capacitor. In addition, the magnitude of the frequency response changes with the relative position of the reader antenna. Most importantly, the distance between the senor and reader is limited (less than 120 mm) and the sensor is too large.

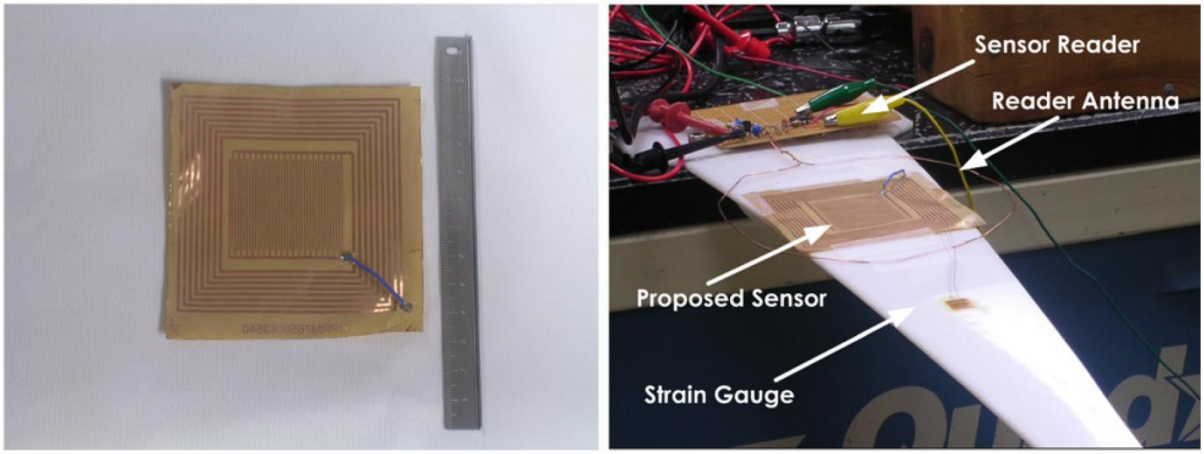

Figure 2.13 Fabricated planar spiral inductor and test setup (Jia et al., 2006).

A strain sensor base on the horizontal shift of the 2nd harmonic spectrum of a magnetically soft material has been proposed in (Tan et al., 2008). This sensor consists of a magnetically soft element and a deformable material. By putting the sensor over a permanent magnetic element, strain could be measured wirelessly. When dimensions of the deformable layer changes, the distance between two magnetic materials will change and results in a shift in higher order harmonic field. Although the relationship between this shift and strain is linear, it is very sensitive to the distance between sensor and detector (Figure 2.14). This sensor is large in size and could be used to evaluate strain in only one direction. Therefore, its application to aerospace structures for online monitoring does not seem feasible.

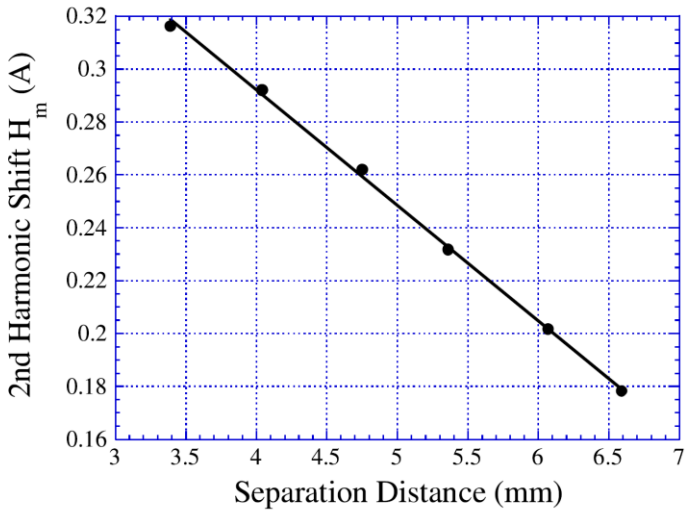

Figure 2.14 The response of 2nd harmonic signal (Tan et al., 2008).

Another recent effort to obtain a wireless strain sensor is done by (Melik et al., 2008). In this work a strain sensor based on the change in the capacitance of a resonator is proposed. Applied load changes the area of a film between metal and substrate material which lead to a change in the capacitance. As a result, the resonant frequency of the sensor shifts. However, two additional antennas are needed for wireless communication (Figure 2.15). The relationship between strain and resonant frequency shift is not linear which makes it impractical for SHM applications.

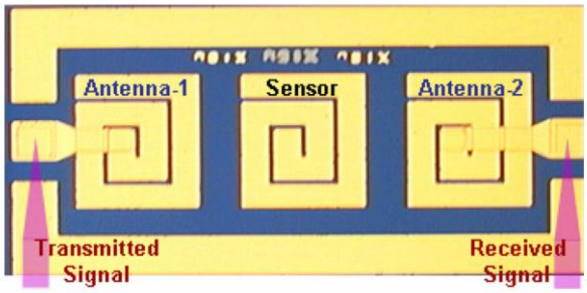

Figure 2.15 A plan view micrograph of the fabricated sensor with on-chip antennas (Melik et al., 2008).

Following this work, a meta-material based wireless strain sensor consisting of an 5×5 array of split ring resonators has been proposed recently (Melik et al., 2009) and seen in Figure 2.16. The principle of this sensor is same as the sensor in (Melik et al., 2008); however, a better sensitivity and a good linearity between strain and frequency shift has been achieved (Figure 2.17).

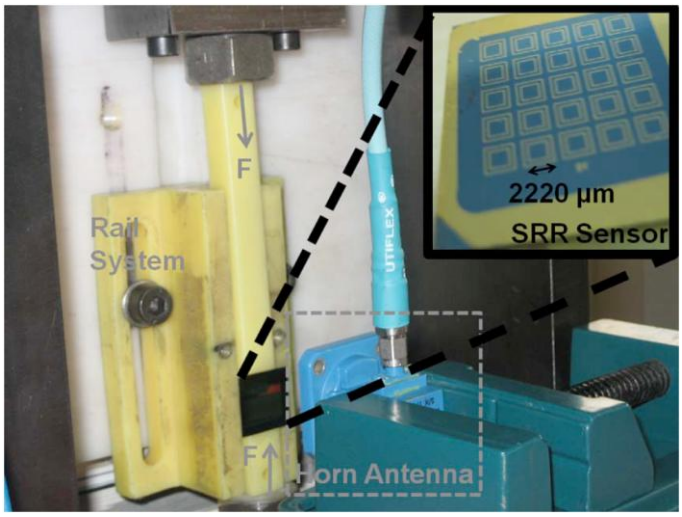

Figure 2.16 An array of split ring resonators under compression test (Melik et al., 2009).

This sensor is suitable for medical application where the short distance between sensor and receiver is not a problem. However, for industrial applications such as SHM the effect of

embedding sensor in the structure especially composites structures should be investigated. The effect of distance from reader needs attention and the ability to locate damage and its size is still not proven. Also, the effect of temperature should be taken into account.

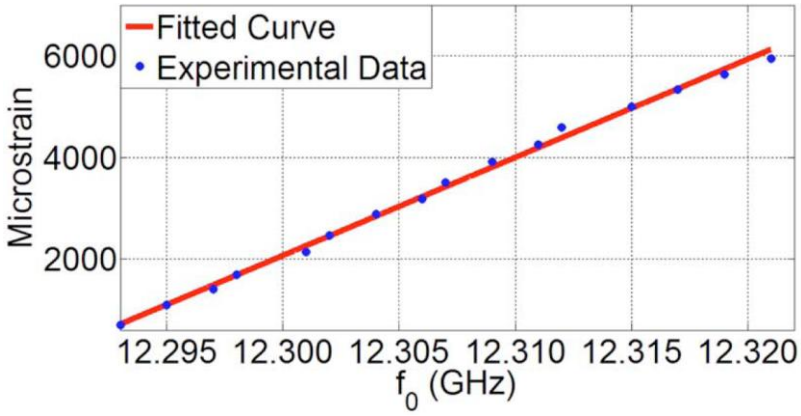

Figure 2.17 The microstrain vs. Resonant frequency of split ring resonator array (Melik et al., 2009).

Meanwhile, Tata et al. (2009) show that microstrip patch antennas could be used not only for communication between sensor and receiver, but also, as a strain sensor itself (Figure 2.18). This work assumes that Poisson's ratio of the antennas' substrate and the metallic patch are equal. Then, from rectangular microstrip patch antennas' resonant frequency formulation a relationship between strain and resonant frequency shift is derived. As frequency shift only depends on the substrate material and antenna dimensions, when these dimensions change the resonant frequency will change which could be detected wirelessly. However, in this work the concept of wireless detection has not been discussed. Also, it is not clear if the shift in the resonant frequency of the antenna is affected by the changes in the microstrip line feed dimensions. The resonant frequency of a microstrip patch antenna could be changed; solely, by changing the dimensions of the microstrip line feed.

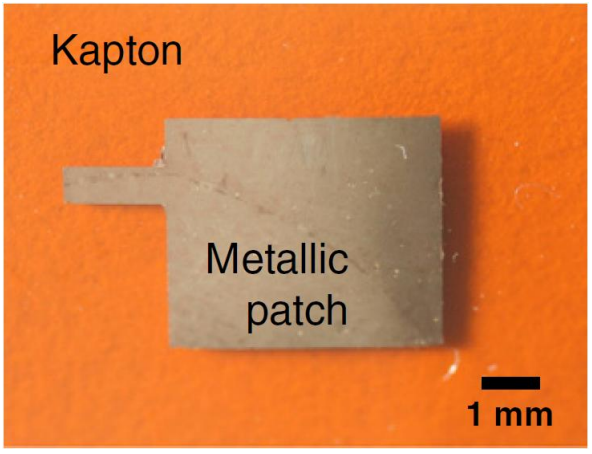

Figure 2.18 Fabricated patch antenna (Tata et al., 2009).

Deshmukh et al. (2009) have extended the above work by providing wireless power supply through an external antenna (Figure 2.19). The same rectangular patch antenna was investigated. It was explained that when there is a crack under the patch, the electrical current path moves around the crack and hence the electrical length increases and thus reduces the frequency. In this work, the experimental test to detect crack and wireless reading test are performed separately (Figures 2.19 and 2.20). The ability of the antenna to detect cracks in different directions is not mentioned and it is not clear if the crack is in the antenna or the structure. Moreover, the structure is used as the ground plane which makes this technique impractical for composite materials.

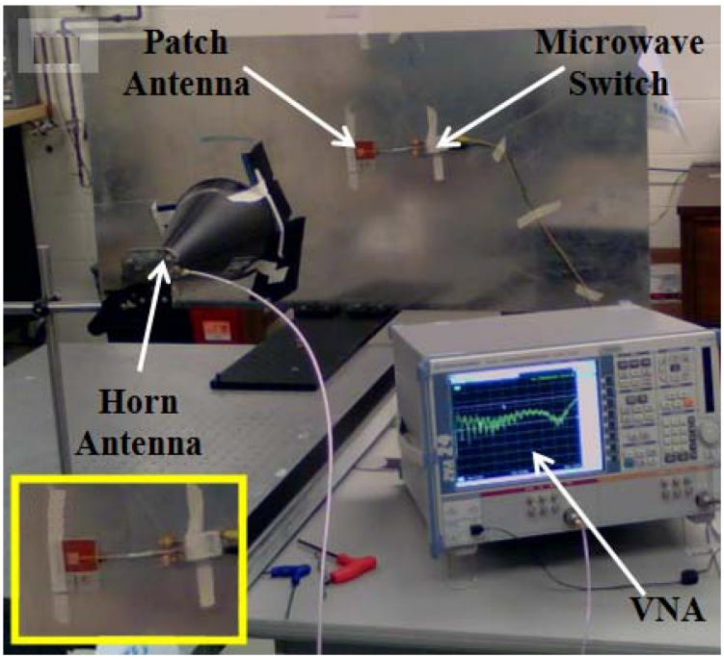

Figure 2.19 Test Setup and patch antenna attached to a metal plate (Deshmukh et al., 2009).

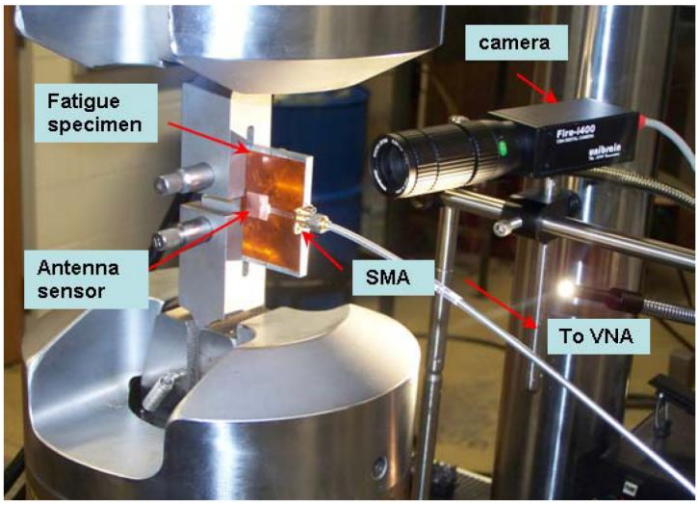

Figure 2.20 Experimental setup for fatigue test (Deshmukh et al., 2009).

2.5 Conclusion

By developing wireless antenna/sensors for strain measurement in aerospace structures especially composite materials the shortcomings of current sensor technologies (e.g. wiring, limited number of sensors, directionality) could be solved. In order to achieve this goal a comprehensive study on microstrip patch antennas and the feasibility of strain measurement using this type of antenna is required. There is no work available in literature regarding a passive wireless strain sensor based on antennas' theory which could detect and locate the damage. To the author's knowledge, use of microstrip patch antennas in SHM is a new area which needs further research.

CHAPTER 3

Literature Review: Microstrip Patch Antennas

3.1 Introduction

In recent years microstrip antennas have been widely used in microwave frequencies and are integrated in many electronic devices (Boufrioua and Benghalia, 2006; Soontornpipit et al., 2006). This popularity is because of their compact, adaptable size, inexpensive printed circuit board technology, and ease of integration with related electronics (Soontornpipit et al., 2006).

A microstrip antenna is fabricated by printing a specifically shaped metallic patch on a grounded dielectric material. At low frequencies, the analysis for this structure can be done by using either the transmission model or a cavity model (Boufrioua and Benghalia, 2006).

In the following section, first basic electromagnetic concepts are explained and then important antenna parameters required to understand the principle of operation of microstrip patch antennas are described. After that, microstrip patch antenna radiation mechanisms, different components, various configurations and their applications are discussed.

3.2 Antennas

The history of antennas dates back to James Clerk Maxwell who unified the theories of electricity and magnetism, and expressively represented their relations through a set of profound equations best known as Maxwell's Equations (Balanis, 2005). His work was first published in 1873 (Balanis, 2005). He also showed that light is electromagnetic wave and that both light and electromagnetic waves travel by wave disturbances of the same speed (Balanis, 2005). In 1886, the German physicist Professor Heinrich Rudolph Hertz demonstrated the first wireless electromagnetic system (Huang and Boyle, 2008; Balanis,

2005). The original intention of his experiment was to demonstrate the existence of electromagnetic radiation (Huang and Boyle, 2008).

An antenna is defined by Webster's Dictionary as "a usually metallic device (as a rod or wire) for radiating or receiving radio waves" (Balanis, 2005). The IEEE Standard Definitions of Terms for Antennas (IEEE Std. 145–1983) defines the antenna as "a means for radiating or receiving radio waves." In other words the antenna is the transitional structure between free-space and a guiding device (Figure 3.1) (Balanis, 2005).

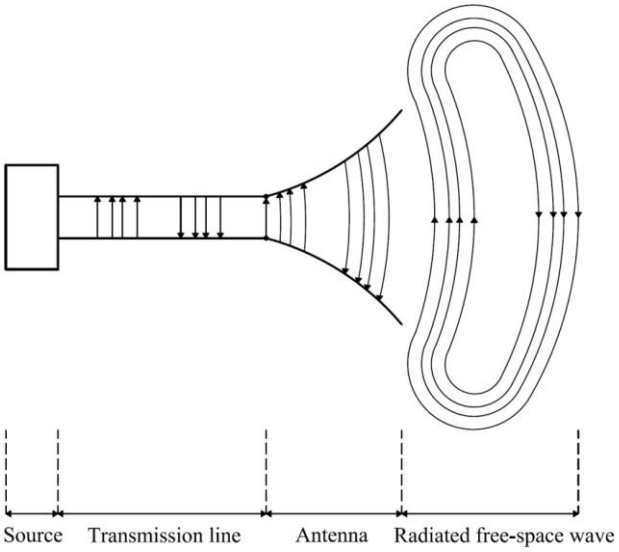

Figure 3.1 Antenna as a transition device (Balanis, 2005).

Antennas are key components of any wireless communication system (e.g. radio broadcasting, communication or radar system) and are defined as a device which can radiate and receive electromagnetic energy (Huang and Boyle, 2008; Volakis, 2007). They are the devices that allow for the transfer of a signal (in a wired system) to waves that, in turn, propagate through space (in an efficient and desired manner) and can be received by another antenna (Huang and Boyle, 2008; Volakis, 2007). The receiving antenna is responsible for the reciprocal process, i.e., that of turning an electromagnetic wave into a signal or voltage at its terminals that can subsequently be processed by the receiver (Volakis, 2007). The receiving and transmitting functionalities of the antenna structure itself are fully characterized by Maxwell's equations (Volakis, 2007). It is normally made of metal, but other materials may also be used (Huang and Boyle, 2008). For example, ceramic materials have been employed to make dielectric resonator antennas (DRAs) (Huang and Boyle, 2008). A radio system is generally considered to be an electronic system which employs radio waves,

a type of electromagnetic wave up to GHz frequencies (Huang and Boyle, 2008). A typical radio communication system is shown in Figure 3.2.

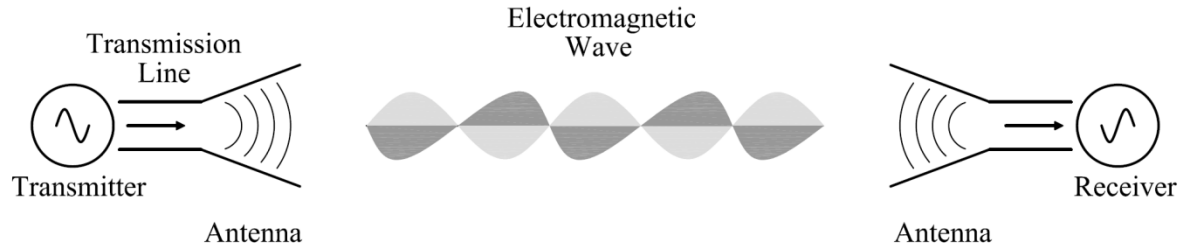

Figure 3.2 A typical radio system (Huang and Boyle, 2008).

The dipole antenna (a straight wire, fed at the centre by a two-wire transmission line) was the first antenna ever used and is also one of the best understood (Volakis, 2007).

If the antenna is a two-terminal circuit, equivalent network parameters are employed to describe the antenna behaviour within the context of an electromagnetic circuit (Volakis, 2007). Accordingly, the antenna may be replaced by equivalent circuit models such as those given in Figure 3.3, where the antenna is characterized by its input impedance (Z) and a source voltage (V_0) or its input admittance (Y) and a source current (I_0). In the transmitting mode, V_0 or I_0 is zero, and V_{in} or I_{in} is the input voltage or current that drives the antenna. Part of the source power is dissipated in the loss resistance (R_{loss}) or loss conductance (G_{loss}). The power associated with the radiation resistance (R_{rad}) or radiation conductance (G_{rad}) is responsible for the radiated wave that escapes from the antenna to the surrounding space. The quantities X and B refer to the equivalent reactance and susceptance of the antenna, respectively (Volakis, 2007).

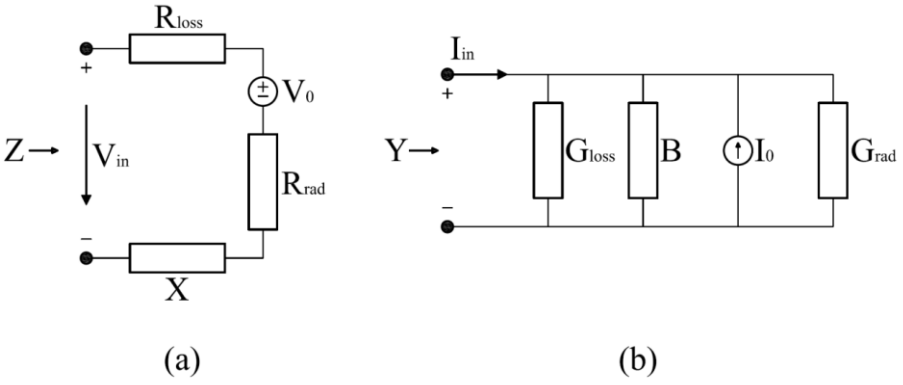

Figure 3.3 (a) Impedance and (b) admittance representations of an antenna (Volakis, 2007).

Common types of antennas include (Balanis, 2005):

- Wire Antennas
- Aperture Antennas
- Microstrip Antennas
- Array Antennas
- Reflector Antennas
- Lens Antennas

3.3 Electromagnetic Principles

The wave velocity (v), the frequency of the wave (f_{wave}) and the wavelength (λ) are related to each other with the following equation (Huang and Boyle, 2008):

$$v = \frac{\lambda}{f_{wave}} \tag{3.1}$$

The wave velocity can be obtained by using the permitivity and permeability of the medium. Therefore for free space (Huang and Boyle, 2008):

$$v = \frac{1}{\sqrt{\mu_0 \varepsilon_0}} \tag{3.2}$$

where

μ_0 is the permeability of free space;

and

ε_0 is the permittivity of free space.

The velocity of electromagnetic waves is equal to the velocity of light in free space ($c = 2.99792458 \times 10^8 \, m/s$) which is constant. Therefore, a higher frequency wave has a shorter wavelength.

Because the magnitude of RF (Radio Frequency) signals change significantly (e.g. over 1000 times) the logarithmic scales are commonly used in this area. The signal power is normally expressed in dB and is defined as (Huang and Boyle, 2008):

$$P(dBW) = 10\log_{10}\frac{P(W)}{1W} \tag{3.3}$$

or

$$P(dBm) = 10\log_{10}\frac{P(W)}{1mW} \tag{3.4}$$

The voltage can be converted to dBV by (Huang and Boyle, 2008):

$$V(dBV) = 20\log_{10}\frac{V(V)}{1V} \tag{3.5}$$

3.3.1 Electromagnetic Wave Equations (Maxwell's Equations)

As it is mentioned before, the antenna receiving and transmitting characteristics could be fully formulated using the Maxwell's equations (Volakis, 2007). They are a set of equations congregated for the first time by James Clerk Maxwell in the second half of nineteenth century (Huang and Boyle, 2008). These set of mathematical equations are (Huang and Boyle, 2008):

$$\begin{aligned} \nabla \times E &= -\frac{dB'}{dt} \\ \nabla \times H &= J + \frac{dD'}{dt} \\ \nabla \bullet D' &= \rho \\ \nabla \bullet B' &= 0 \end{aligned} \tag{3.6}$$

where

ρ is the charge density;

$\nabla = \frac{\partial}{\partial x}\hat{x} + \frac{\partial}{\partial y}\hat{y} + \frac{\partial}{\partial z}\hat{z}$ is a vector operator;

$\nabla \times$ is the curl operator;

and

$\nabla \bullet$ is the divergence operator.

These set of equations express the interrelationship between electric fields, magnetic fields, electric charge and electric current (Huang and Boyle, 2008).

Faraday's Law of Induction

The following equation is Faraday's law of induction which says the induced electromotive force is proportional to the rate of change of the magnetic flux through a coil (Huang and Boyle, 2008).

$$\nabla \times E = \frac{dB'}{dt} \tag{3.7}$$

Ampere's Circuital Law

This equation is Ampere's circuital law which says a magnetic field appears during the charge or discharge of a capacitor (Huang and Boyle, 2008). Maxwell modified this equation by adding the displacement current $\frac{dD'}{dt}$ (Huang and Boyle, 2008).

$$\nabla \times H = J + \frac{dD'}{dt} \tag{3.8}$$

Gauss's Law for Electric Fields

The electrostatic application of Gauss's generalised theorem (giving the equivalence relation between any fluxes) which says forming a closed loop is not possible for electric fields is (Huang and Boyle, 2008):

$$\nabla \bullet D' = \rho \tag{3.9}$$

Gauss's Law for Magnetic Fields

This equation states that the divergence of the magnetic field ($\nabla \bullet B$) is zero, which means that the magnetic field lines form closed loops; and therefore, the integral of B over a close surface is zero (Huang and Boyle, 2008).

$$\nabla \bullet B' = 0 \tag{3.10}$$

Rewriting the Maxwell's equations for a time-harmonic electromagnetic field gives us the following set of equations (Huang and Boyle, 2008):

$$\begin{aligned}
&\nabla \times E = -j\omega\mu H \\
&\nabla \times H = J + j\omega\varepsilon E = j\omega\varepsilon\left(1 - j\frac{\sigma}{\omega\varepsilon}\right)E \\
&\nabla \bullet E = \rho/\varepsilon \\
&\nabla \bullet H = 0
\end{aligned} \tag{3.11}$$

where

ω is the angular frequency of the wave;

μ is the permeability of the medium;

σ is the conductivity (S/m) of the medium;

and

ε is the electric permittivity (dielectric constant) of the medium.

Combining Maxwell's equations gives us the wave equation (Huang and Boyle, 2008):

$$\nabla^2 E - \gamma^2 E = 0 \tag{3.12}$$

where

$\gamma = \sqrt{j\omega\mu(\sigma + j\omega\varepsilon)}$.

One of the possible solutions in free space is (Huang and Boyle, 2008):

$$E = \hat{x}E_0 e^{j\omega t - \gamma z} \tag{3.13}$$

3.3.2 Radio Wave Propagation Mechanisms

3.3.2.1 Reflection and Transmission

When a plane wave is incident on the surface between two media (Figure 3.4), the wave will be partially reflected back to medium 1 and partially transmitted (refracted) into medium 2 (Huang and Boyle, 2008). Refraction occurs because of the change in the direction of the transmitted wave due to the change in wave velocity from one medium to another (Huang and Boyle, 2008).

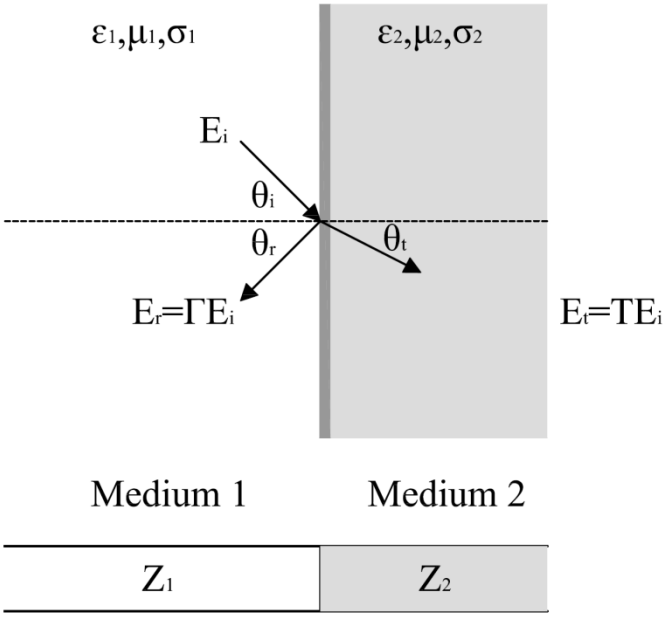

Figure 3.4 Plane wave reflection and transmission, and its analogous transmission line (Huang and Boyle, 2008).

The ratio of the reflected wave to the incident wave is the reflection coefficient, which is (Huang and Boyle, 2008):

$$\Gamma = \frac{E_r}{E_i} \tag{3.14}$$

Likewise, the ratio of the transmitted wave to the incident wave is the transmission coefficient, which is (Huang and Boyle, 2008):

$$\mathrm{T} = \frac{E_t}{E_i} \tag{3.15}$$

If we look at these two media as two transmission lines, then the reflection coefficient and the transmission coefficient between these two transmission lines (at the boundary between two media) are (Huang and Boyle, 2008):

$$\Gamma = \frac{Z_2 - Z_1}{Z_2 + Z_1} \tag{3.16}$$

and

$$\mathrm{T} = 1 + \Gamma = \frac{2Z_2}{Z_2 + Z_1} \tag{3.17}$$

where

Z_1 and Z_2 are the characteristic impedances of the two media.

As the reflection coefficient and transmission coefficient represent the ratios of electric field strengths and because the sum of reflected and transmitted powers equals the incident power, it is obvious that (Huang and Boyle, 2008):

$$|\Gamma|^2 + |T|^2 = 1 \tag{3.18}$$

3.3.2.2 Diffraction and Huygens's Principle

Diffraction is when any type of wave (sound waves, water waves, electromagnetic waves, etc.) meet an obstacle and as a result of that bends or spreads (Huang and Boyle, 2008). Figure 3.5 shows the diffraction of an electromagnetic wave over a knife-edge obstacle.

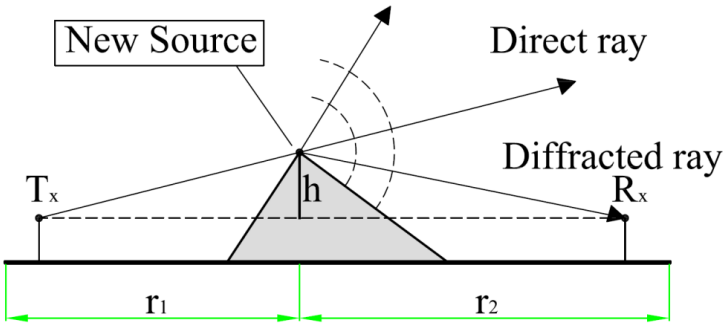

Figure 3.5 Radio wave diffraction over a knife-edge obstacle (Huang and Boyle, 2008).

3.3.2.3 Scattering

Scattering is when a portion of the incident wave is diffused in all directions by an obstacle (with a comparable to or smaller size than the wavelength) in a medium with a different permittivity (dielectric constant) (Huang and Boyle, 2008). This is illustrated in Figure 3.6.

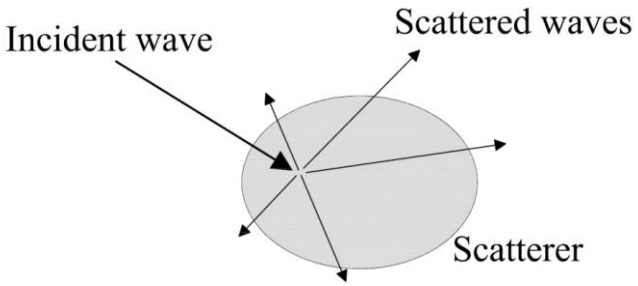

Figure 3.6 Radio wave scattering (Huang and Boyle, 2008).

3.3.3 Media Classification

From an electromagnetic point of view, materials can be classified as conductive, semi-conductive or dielectric (Huang and Boyle, 2008). However, the electromagnetic properties of materials are frequency dependent. In order to categorise different materials the complex permittivity and the loss tangent of the material should be defined. The complex permittivity (which means the material has some loss) is (Huang and Boyle, 2008):

$$\varepsilon = \varepsilon' - j\varepsilon'' \tag{3.19}$$

where

ε' and ε'' are real and imaginary part of the permittivity (ε), respectively.

The loss tangent is defined by (Huang and Boyle, 2008):

$$\tan\delta = \frac{\varepsilon''}{\varepsilon'} = \frac{\sigma}{\omega\varepsilon} \tag{3.20}$$

Therefore, different materials are categorised by the following definitions:

- Conductor: $\tan\delta > 100$
- Semi-conductor: $0.01 < \tan\delta < 100$
- Dielectric: $\tan\delta < 0.01$

3.3.4 Fundamental Parameters of Antennas

To describe the performance of any antenna, definitions of various antenna parameters are essential (Balanis, 2005). The most important parameters of any antenna include the radiation pattern, beamwidth, directivity, gain, efficiency factor, effective aperture, polarization and the bandwidth (Huang and Boyle, 2008; Balanis, 2005; Volakis, 2007). Most of these parameters are related to the far-field region of an antenna. The distance from an antenna to its far-field depends on the antenna size which is (Volakis, 2007):

$$R = \frac{2D^2}{\lambda} \tag{3.21}$$

where

D is the largest dimension of the antenna.

3.3.4.1 Radiation Pattern

The antenna radiation pattern is a mathematical function or a graphical representation of the radiating/receiving properties of the antenna as a function of space coordinates (the angle at a fixed distance) in the far-field region (Huang and Boyle, 2008; Balanis, 2005; Volakis, 2007). The 3D radiation pattern of an electrically short current element is illustrated in Figure 3.7.

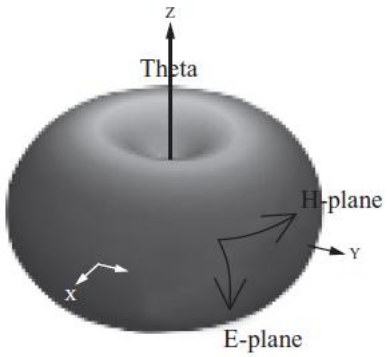

Figure 3.7 The 3D radiation pattern of an electrically short current element (Huang and Boyle, 2008).

The pattern of an antenna which is in a plane parallel to the **E** field vector is the **E** plane pattern. Similarly, the pattern which is in a plane parallel to the **H** field vector is the **H** plane pattern (Figure 3.8). These are the most important patterns for an antenna (Huang and Boyle, 2008; Volakis, 2007).

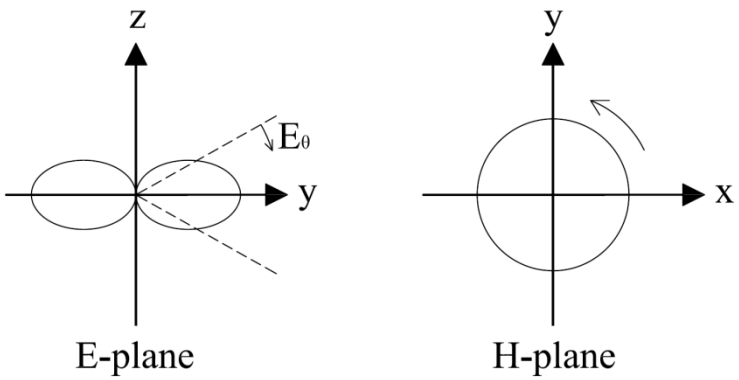

Figure 3.8 The E-plane and H-plane patterns of an electrically short current element (Huang and Boyle, 2008).

Among many different types of antenna radiation patterns, the most common are (Volakis, 2007):

● Omni-directional (circular pattern)

● Pencil beam (highly directive pattern)

● Fan beam (narrow in one direction and wide in the other)

● Shaped beam (adapted to the requirements of a particular application)

3.3.4.2 Radiation Power Density

The quantity to express the power/energy coupled with an electromagnetic wave which transports data through a wireless medium or a guiding structure, from one point to the other is called the radiation power density (Balanis, 2005):

$$W_{rad} = E' \times H' \tag{3.22}$$

where

W_{rad} is the instantaneous Poynting vector W/m^2;

E' is the instantaneous electric-field intensity V/m;

and

H' is the instantaneous magnetic-field intensity A/m.

3.3.4.3 Radiation Intensity

Another far-field parameter is the radiation intensity which is defined as "the power radiated from an antenna per unit solid angle" and can be calculated with the following equation (Balanis, 2005):

$$U = r_a{}^2 W_{rad} \tag{3.23}$$

where

U is the radiation intensity ($W/unit\ solid\ angle$);

W_{rad} is the radiation density (W/m^2);

and

r_a is the distance from the antenna (m).

The radiation intensity of an isotropic source is (Balanis, 2005):

$$U_0 = \frac{P_{rad}}{4\pi} \tag{3.24}$$

3.3.4.4 Beamwidth

In an antenna pattern, the angular distance between any two identical points on opposite sides of the pattern maximum is defined as the beamwidth (Balanis, 2005). Therefore, different beamwidths can be defined for a single pattern to describe different antenna characteristics (Balanis, 2005). For example, the Half-Power Beamwidth (HPBW) is the angle between the two directions in which the radiation intensity is one-half value of the beam (Balanis, 2005). First-Null Beamwidth (FNBW) is another important measure, which is the angle between the first nulls of the pattern (Balanis, 2005).

3.3.4.5 Directivity

Directivity of an antenna is a measure of the concentration of radiated power in a particular direction (the most important quantitative information from the field point of view) (Huang and Boyle, 2008; Volakis, 2007). It is defined as the ratio of the radiation intensity in a given direction from the antenna to the radiation intensity averaged over all directions. The average radiation intensity is equal to the total radiated power divided by 4π (Huang and Boyle, 2008; Balanis, 2005). For a non-isotropic source, directivity can be defined as the ratio of its radiation intensity in a given direction over that of an isotropic source (Balanis, 2005):

$$D = \frac{U}{U_0} = \frac{4\pi U}{P_{rad}} \tag{3.25}$$

3.3.4.6 Antenna Efficiency

The losses at the input terminals and the structure of the antenna are because of reflection loss as a reason of mismatch between the transmission line and the antenna, and conduction and dielectric losses (Figure 3.9) (Balanis, 2005). The total antenna efficiency is a representative of these losses (Balanis, 2005).

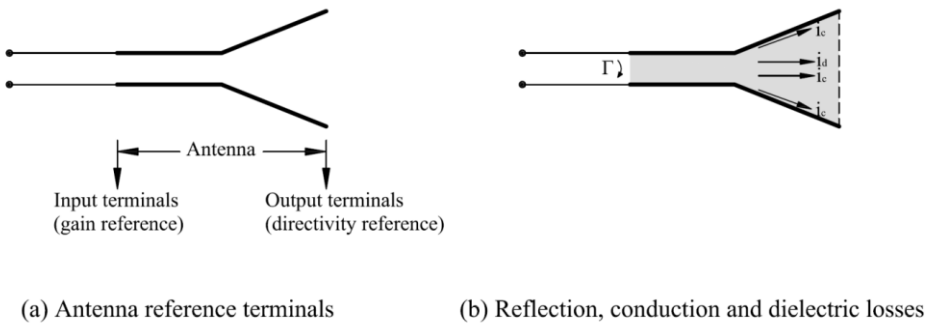

Figure 3.9 Reference terminals and losses of an antenna (Balanis, 2005).

The overall efficiency is (Balanis, 2005):

$$e_0 = e_r e_c e_d \tag{3.26}$$

where

e_0 is total efficiency (dimensionless);

$e_r = 1 - |\Gamma|^2$ is reflection (mismatch) efficiency (dimensionless);

e_c is conduction efficiency (dimensionless);

e_d is dielectric efficiency (dimensionless);

Γ is voltage reflection coefficient at the input terminals of the antenna (defined by Equations 3.14 & 3.16);

and

$VSWR = \frac{1+|\Gamma|}{1-|\Gamma|}$ is voltage standing wave ratio.

3.3.4.7 Gain

Gain of an antenna is a parameter which defines the efficiency and the directional capabilities of it at the same time, against the directivity which only describes properties of the antenna (Huang and Boyle, 2008; Balanis, 2005).

It is defined as the ratio of the radiation intensity, in a given direction, to the total power accepted by the antenna (Huang and Boyle, 2008; Balanis, 2005). Gain is a dimensionless parameter and can be calculated using the following equation (Huang and Boyle, 2008; Balanis, 2005):

$$G = \frac{4\pi U}{P_{in}} \tag{3.27}$$

where

U is the radiation intensity ($W/unit\ solid\ angle$);

and

P_{in} is the total input power accepted by the antenna (W).

The relationship between gain and directivity is defined as (Huang and Boyle, 2008):

$$G = \frac{P_t}{P_{in}} D = \eta_e D \tag{3.28}$$

where

η_e is the radiation efficiency factor of the antenna;

and

P_t is the total radiated power.

3.3.4.8 Bandwidth

The bandwidth of an antenna is defined as the range of frequencies within which the antenna characteristics (such as input impedance, pattern, beamwidth, polarization, gain, beam direction, radiation efficiency) conforms to a specified standard (Balanis, 2005).

From the circuit point of view, the antenna bandwidth is defined as the frequency bandwidth with $L_{RT} > 10\,dB$ or $VSWR < 2$ (Huang and Boyle, 2008). It is a very important parameter because it should be considered from both the circuit point of view ($VSWR$ or L_{RT}) and the field point of view (radiation pattern) (Huang and Boyle, 2008).

3.3.4.9 Polarisation

Polarisation is defined for a radiated electromagnetic wave as well as an antenna (transmitting or receiving) (Huang and Boyle, 2008; Balanis, 2005; Volakis, 2007). Polarisation of a single-frequency electromagnetic wave describes the direction and relative magnitude of the electric-field vector as a function of time (Balanis, 2005; Volakis, 2007). If the electric field is observed along the propagation direction then the polarisation is the curve traced by the end point of the arrow representing the instantaneous electric field (Balanis, 2005). Polarisation of an antenna is the polarisation of the radiated wave by the antenna in a given direction (Balanis, 2005).

Depending on the current moves in the antenna there are three types of polarisation: linear, circular, or elliptical (Huang and Boyle, 2008; Balanis, 2005). If the current travels along one axis then polarisation is linear and if two orthogonal currents with 90 degree phase offset are created on the antenna then polarisation is circular (Huang and Boyle, 2008).

3.3.4.10 Input Impedance

The input impedance (Z_a) of an antenna is the impedance presented by an antenna at its terminals or the ratio of the voltage to current at its terminals (Figure 3.10). The input impedance is (Huang and Boyle, 2008; Balanis, 2005):

$$Z_a = \frac{V_{in}}{I_{in}} \tag{3.29}$$

where V_{in} and I_{in} are the input voltage and current of the antenna, respectively.

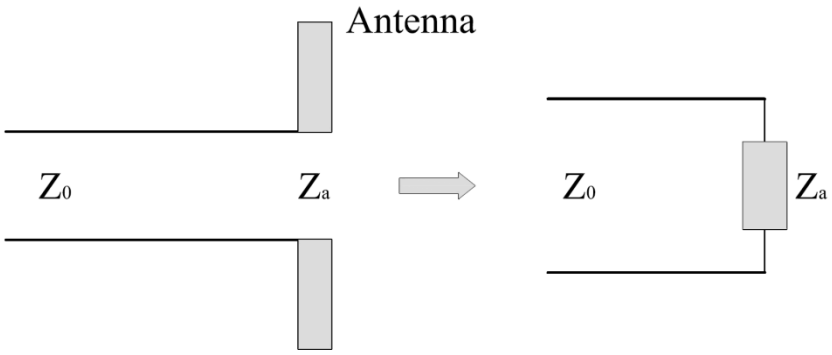

Figure 3.10 Antenna input impedance model (Huang and Boyle, 2008; Balanis, 2005).

3.3.4.11 Reflection Coefficient, Return Loss and VSWR

When designing an antenna a special care must be taken for the impedance matching. This is because the antenna is a load to the transmission line and if the input impedance of the antenna is not matched to the impedance of the transmission line (e.g. a $50\,\Omega$ coaxial cable) then a portion of the transmitted wave is reflected back at the antenna input terminals Antenna input impedance model (Huang and Boyle, 2008); and therefore, affects the antenna efficiency. Impedance matching could be expressed in terms of reflection coefficient (Γ), return loss (L_{RT}) and voltage standing wave ratio ($VSWR$), which are interlinked (Huang and Boyle, 2008).

Reflection coefficient (a complex number) is (Huang and Boyle, 2008):

$$\Gamma = \frac{Z_a - Z_0}{Z_a + Z_0} \tag{3.30}$$

Return loss (expressed in dB) is (Huang and Boyle, 2008):

$$L_{RT} = -20\log_{10}(|\Gamma|) \tag{3.31}$$

And *VSWR* (a ratio between 1 and infinity) is (Huang and Boyle, 2008):

$$VSWR = \frac{1+|\Gamma|}{1-|\Gamma|} \tag{3.32}$$

3.3.4.12 Scattering Parameters

Scattering parameter or S-Parameter is a measurement for reflection coefficient and transmission coefficient in a one port or two port network (Figure 3.11) (Huang and Boyle, 2008).

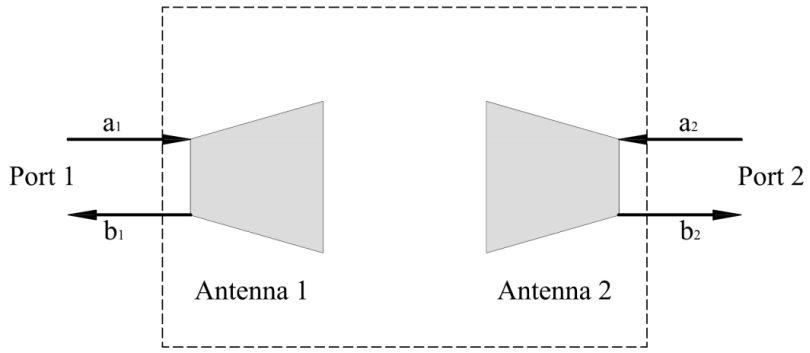

Figure 3.11 The equivalent 2-port network of a transmitting-receiving antenna system (Huang and Boyle, 2008).

$$[S] = \begin{bmatrix} S_{11} & S_{12} \\ S_{21} & S_{22} \end{bmatrix} \tag{3.33}$$

Scattering parameter links the input to the output by the following equation to the equivalent 2-port network of a transmitting-receiving antenna system (Huang and Boyle, 2008):

$$\begin{bmatrix} b_1 \\ b_2 \end{bmatrix} = \begin{bmatrix} S_{11} & S_{12} \\ S_{21} & S_{22} \end{bmatrix} \begin{bmatrix} a_1 \\ a_2 \end{bmatrix} \tag{3.34}$$

where

S_{11} is Port 1 reflection coefficient (b_1/a_1);

S_{12} is Port 2 to Port 1 transmission coefficient (b_1/a_2);

S_{21} is Port 1 to Port 2 transmission coefficient (b_2/a_1);

and

S_{22} is Port 2 reflection coefficient (b_2/a_2).

3.4 Microstrip Patch Antennas

Microstrip patch antennas were first introduced by Munson in early 1970s and became popular primarily for space-borne applications (Balanis, 2005; Volakis, 2007). They are widely used in the microwave frequency region because of their simplicity, compatibility with printed-circuit technology, and ease of manufacturing (Volakis, 2007). A simple microstrip patch antenna consists of a very thin ($t_p << \lambda_0$, where λ_0 is the free-space wavelength) metallic patch on top of a dielectric substrate ($h << \lambda_0$, usually $0.003\lambda_0 < h < 0.05\lambda_0$) attached to a metallic ground plane (Figure 3.12) (Huang and Boyle, 2008; Balanis, 2005; Volakis, 2007). For a rectangular patch, the length (L) of the element is usually in the region of $\lambda_0/3 < L < \lambda_0/2$ (Balanis, 2005). Their radiation efficiency depends on the substrate permittivity and thickness (Volakis, 2007).

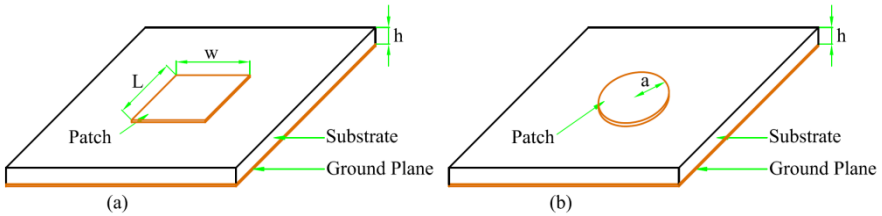

Figure 3.12 (a) Rectangular microstrip patch antenna and (b) circular microstrip patch antenna (Huang and Boyle, 2008; Balanis, 2005; Volakis, 2007).

Microstrip patch antennas have several advantages which make them attractive for many applications. They cover a broad frequency range from almost 100 MHz to almost 100 GHz (Garg et al., 2000). These advantages include (Huang and Boyle, 2008; Balanis, 2005; Volakis, 2007; Garg et al., 2000):

- Light weight, low volume;
- Low profile;
- Conformable to planar and non-planar surfaces (with thin substrates);
- Low fabrication cost due to modern printed-circuit technology;
- Mechanically robust when mounted on rigid surfaces;
- Versatile in terms of resonant frequency, polarisation, pattern and impedance;
- Linear and circular polarisations are possible with simple feed;
- Dual-frequency and dual-polarisation antennas can be easily made;
- No cavity backing is required;

- Easily can be integrated with MMIC (monolithic microwave integrated circuit);
- Simultaneous fabrication of antenna structure, feed lines and matching network;

On the other hand, they have some major disadvantages including (Huang and Boyle, 2008; Balanis, 2005; Volakis, 2007; Garg et al., 2000):

- Low radiation efficiency (conducting, dielectric and especially surface wave losses);
- Low power handling capability;
- Poor polarisation purity;
- Poor scan performance;
- Spurious feed radiation;
- Very narrow frequency bandwidth (typically only a fraction of a percent or at most a few percent);
- Somewhat lower gain compare to conventional microwave antennas;
- Most microstrip patch antennas radiate into half-space;
- Complex feed structures required for high-performance arrays;
- Poor end-fire radiator (except tapered slot antennas);
- Excitation of surface waves;

3.4.1 Radiation Mechanism

Among many different methods of analysis for microstrip patch antennas the most popular models are the transmission-line (the easiest of all which gives good physical insight, but is less accurate and it is more difficult to model coupling), cavity, and full wave (which include primarily integral equations/Moment Method) (Balanis, 2005).

Using the cavity model, the microstrip patch and the ground plane together form a resonant cavity (filled with the substrate material). The cavity is lossy, due to the material loss (conductor and dielectric) as well as the (desirable) radiation into space (Balanis, 2005; Volakis, 2007).

The transmission-line method models the microstrip patch antenna by an array of two radiating narrow apertures, separated by a low-impedance Z_c transmission line of length L (Balanis, 2005). To be a resonant antenna, the length L should be around half of the wavelength (Huang and Boyle, 2008). Therefore, the antenna can be considered a $\lambda/2$ transmission line resonant cavity with two open ends where the fringing fields from the

patch to the ground are exposed to the upper half space and create the radiation (Huang and Boyle, 2008). The finite dimensions of the patch along its length and width cause the fields at the edges of the patch to undergo fringing (Figure 3.13) (Balanis, 2005). The distance between fringing fields at the ends is $\lambda/2$, which means that they are 180 degrees out of phase but are equal in magnitude (Huang and Boyle, 2008).

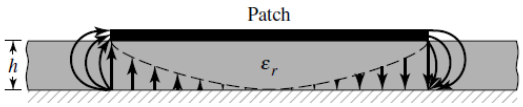

Figure 3.13 Fringing effect on edges of the patch (Balanis, 2005).

The amount of fringing is a function of patch dimensions and substrate height (Balanis, 2005). For the principal E-plane fringing is a function of the ratio of the length of the patch L to the height h of the substrate (L/h) as well as the relative permittivity ε_r of the substrate (Balanis, 2005). Although for microstrip patch antennas fringing is reduced (due to $L/h >> 1$), its influences on the resonant frequency of the antenna must be taken into account (Balanis, 2005).

An alternative to describe microstrip patch antenna radiation instead of field distribution of patch metallisation and ground plate is surface current distribution on the patch metallisation (Garg et al., 2000). Consider a microstrip patch antenna that is energized by a microwave source. As a result, a charge distribution is established on the upper and lower surfaces of the patch, as well as on the surface of the ground plane (Figure 3.14) (Balanis, 2005; Garg et al., 2000).

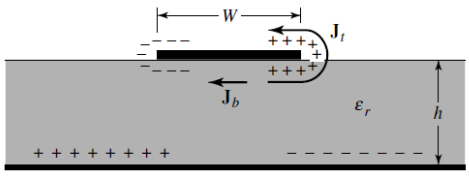

Figure 3.14 Charge distribution and current density creation on microstrip patch (Balanis, 2005).

The nature of the charge distribution arises because the patch is about a half-wave long at the dominant mode (Garg et al., 2000). The charge distribution is controlled by two mechanisms: an attractive and a repulsive mechanism (Balanis, 2005). The attractive mechanism is between the corresponding opposite charges on the bottom side of the patch and the ground plane, which tends to maintain the charge concentration on the bottom of the

patch (Balanis, 2005; Garg et al., 2000). The repulsive mechanism is between like charges on the bottom surface of the patch, which tends to push some charges from the bottom surface of the patch, around its edges, to its top surface (Balanis, 2005; Garg et al., 2000). The movement of these charges creates corresponding current densities $\vec{J}_b$ and $\vec{J}_t$, at the bottom and top surfaces of the patch, respectively (Balanis, 2005; Garg et al., 2000).

The dominant mode of antenna resonance is the mode with the lowest order resonant frequency (Balanis, 2005). To determine the order of the modes of operation the resonant frequencies should be placed in an ascending order (Balanis, 2005). For all rectangular microstrip patch antennas $h<L$ and $h<W$. If $L>W>h$, the dominant mode is the TM^{x}_{010}. If $W>L>h$, the dominant mode is the TM^{x}_{001} while if $W>W/2>L>h$ the second order mode is the TM^{x}_{002} (Balanis, 2005). The distribution of the tangential electric field along the side walls of the substrate for the TM^{x}_{010}, TM^{x}_{001}, TM^{x}_{020} and TM^{x}_{002} are shown in Figure 3.15.

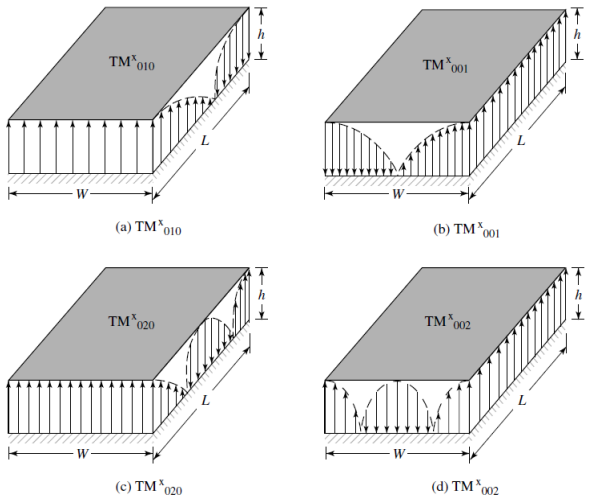

Figure 3.15 Field configurations (modes) for rectangular microstrip patch (Balanis, 2005).

The modes supported by the circular microstrip patch antenna can be found by treating the patch, ground plane, and the substrate as a circular cavity (Balanis, 2005). Similar to rectangular patch, the modes that are supported primarily by a circular microstrip patch antenna whose substrate height is small ($h>>\lambda$) are TM^{z} where z is the perpendicular direction to the patch (Balanis, 2005). For the rectangular microstrip patch antenna, there are two degrees of freedom to control (length and width). Thus, the order of the modes can be changed by changing the relative dimensions of the width and length of the patch. However, for the circular patch there is only one degree of freedom to control (radius of the patch).

Changing the radius does not change the order of the modes; however, it does change the absolute value of the resonant frequency (Balanis, 2005).

3.4.2 Various Antenna Configurations

The radiating elements and the feed lines of the microstrip patch antenna (/array of microstrip patch antennas) are photo-etched on the dielectric substrate and can take various forms to meet different design requirements (Huang and Boyle, 2008; Balanis, 2005; Garg et al., 2000). The patch can exist in several different configurations (Figure 3.16). The most common shapes are rectangular, square, dipole, circular, and circular ring because of their attractive characteristics such as low cross polarisation radiation (Huang and Boyle, 2008; Balanis, 2005).

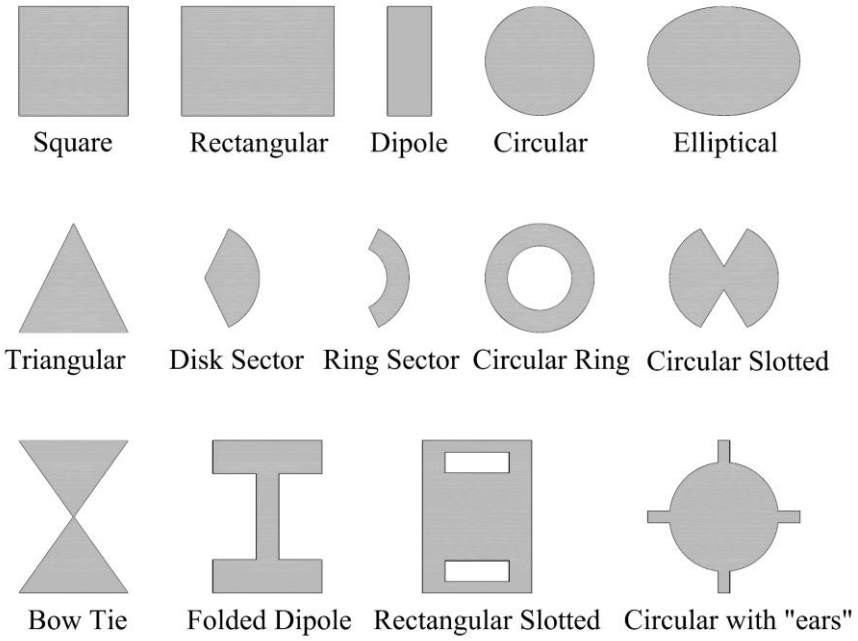

Figure 3.16 Various shapes of microstrip patch elements (Huang and Boyle, 2008; Balanis, 2005; Garg et al., 2000).

3.4.3 Substrate Material

Because substrate material properties play an important role in antenna design, production and finished product performance, special care should be taken in choosing the right material for the required application (James and Hall, 1989). Some of the important factors to be considered include ability to measure and control critical properties (e.g. relative permittivity and dissipation factor), the possible adverse effects of necessary processing steps or environment in the final application (James and Hall, 1989).

For a material to be completely characterised from electrical point of view, permittivity ε, permeability μ, and conductivity σ at the desirable frequency must be specified (Volakis, 2007). For the substrates suitable for microstrip patch antenna design, permeability equals that of free space ($4\pi \times 10^{-7}\ H/\mathrm{m}$), and permittivity is a complex number (Volakis, 2007):

$$\varepsilon = \varepsilon' - j\varepsilon'' = \varepsilon'(1 - j\tan\delta) \tag{3.35}$$

and is usually expressed as the relative permittivity (Huang and Boyle, 2008):

$$\varepsilon_r = \frac{\varepsilon}{\varepsilon_0} \tag{3.36}$$

where $\varepsilon_0 = 8.85419 \times 10^{-12}\ F/m$ is the permittivity of free space.

Among the numerous substrates available for the design of microstrip patch antennas (with the dielectric constant of $2.2 \le \varepsilon_r \le 12$) the most suitable ones for good antenna performance are thick substrates with a lowest dielectric constant (Balanis, 2005; Volakis, 2007). This is because they provide better efficiency, larger bandwidth, loosely bound fields for radiation into space (at the expense of larger size) (Balanis, 2005). Thin substrates with higher dielectric constants (desirable for microwave circuitry) have greater losses and are less efficient and have relatively smaller bandwidths (Balanis, 2005).

Generally, there is no ideal substrate material because the material selection depends on the application (Garg et al., 2000). For example, flexible substrates are suitable for conformal antenna applications; whereas, high dielectric constants are required for low-frequency applications (Garg et al., 2000). There are a large number of substrate materials available such as PTFE (polytetrafluoroethylene), polystyrene, polyolefin, polyphenylene, alumina, sapphire, quartz, ferromagnetic, and semiconductor substrates which makes choosing the substrate more flexible (Garg et al., 2000). The various substrates can be grouped in five categories (Garg et al., 2000):

- Ceramic;
- Semiconductor;
- Ferromagnetic;
- Synthetic;
- Composite.

3.4.4 Feeding Mechanisms

There are four common feeding techniques for microstrip patch antennas including (Huang and Boyle, 2008; Balanis, 2005; Volakis, 2007; Garg et al., 2000; James and Hall, 1989):

- Coaxial probe feed (the most common feed for a stand-alone element)
- Microstrip line (coplanar) feed (common for array applications)
- Proximity coupled microstrip feed (requires multilayer fabrication, but reduces spurious radiation from the feed line)
- Aperture coupled microstrip feed (eliminates feed-line radiation at the expense of some back radiation from the aperture; also allows for relatively thick substrates)

The schematic illustration of these feeding mechanisms is shown in Figure 3.17.

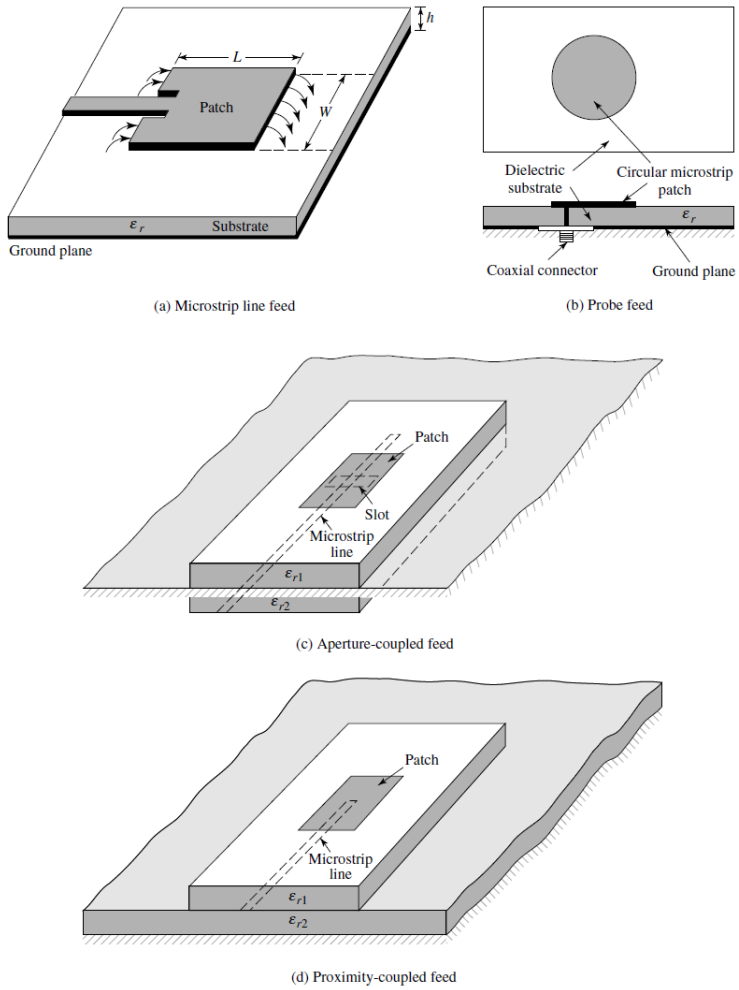

Figure 14.3 Typical feeds for microstrip antennas.

Figure 3.17 Feeding mechanisms for microstrip patch antennas (Balanis, 2005; Volakis, 2007; Garg et al., 2000; James and Hall, 1989).

The coaxial connector outer conductor is attached to the ground plane and the coaxial centre conductor after passing through the substrate is soldered to the patch (Garg et al., 2000; James and Hall, 1989). Based on the interested mode, the location of the feed point determines how much the impedance of the transmission line is matched to the antenna impedance (Garg et al., 2000; James and Hall, 1989). Coupling between the feed J_z current and the E_z field excites the patch (Garg et al., 2000). This feeding technique is easy to fabricate and match, difficult to model, and has low spurious radiations and low bandwidth (Balanis, 2005; James and Hall, 1989).

The microstrip line is a conducting strip with a much smaller width compared to the patch. It is easy to fabricate, simple to match with the patch impedance by controlling the inset position, and rather simple to model. However, it has spurious feed radiations, which limits its bandwidth (Balanis, 2005).

The most difficult to fabricate is the aperture coupling which also has narrow bandwidth (Balanis, 2005). However, it is easier to model and has less spurious radiations (Balanis, 2005; James and Hall, 1989). This feeding technique consists of two substrates separated by a ground plane. The microstrip line is at the bottom of the lower substrate and its energy is coupled to the patch through a slot on the ground plane which is between the two substrates (Balanis, 2005; James and Hall, 1989).

The equivalent circuits for each of these four feeding mechanisms are shown in Figure 3.18.

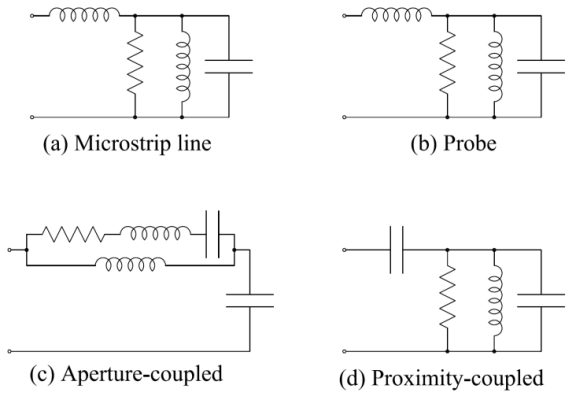

Figure 3.18 Equivalent circuits for typical feeds of microstrip patch antennas (Balanis, 2005).

3.4.5 Ground Plane

Ground plane is an important part of a microstrip patch antenna. The ground plane should be infinite in theory; however, because of practical limitations it should be as small as possible

(Huang and Boyle, 2008). The minimum size of the ground plane is related to the thickness of the substrate because the radiation of a microstrip patch antenna is generated by the fringing field between the patch and the ground plane (Figure 3.13). As a general guideline, the ground plane edges should be extended $\lambda/4$ from the edges of patch (Huang and Boyle, 2008).

3.4.6 Applications

Microstrip patch antennas may have some disadvantages (e.g. low gain); however, their characteristics such as low cost of manufacturing (low cost of substrate material and mature fabrication technology), ease of fabrication, ease of installation, low profile (when there is a limited space for antenna aperture), conformal profile (for multifunctional antenna applications), aerodynamic profile, small size, and low weight as well as some of the disadvantages which could be an advantage for specific applications (e.g. narrow bandwidth for government security systems) make them a suitable replacement for conventional antennas (Balanis, 2005; Volakis, 2007; Garg et al., 2000).

Some of their remarkable applications include (Balanis, 2005; Volakis, 2007; Garg et al., 2000):

- Government security systems;
- Military or commercial aircrafts and satellites;
- Military command and control systems, missiles, and rockets (stick-on sensors and weapon fusing);
- Commercial and military radio, wireless communication systems, and direct broadcast services (DBS);
- Commercial or military cars;
- Commercial devices such as cell phones, pagers, WLAN networking cards, Personal digital assistants, and GPS receivers;
- Doppler and other radars;
- Biomedical radiators and intruder alarms.

3.5 Conclusion

In this chapter, the principles of electromagnetic waves which are necessary to understand the operation of microstrip patch antennas, are discussed. Also, microstrip patch antennas are introduced and their radiation mechanism is discussed. Different configurations for microstrip patch antennas, possible feeding techniques, suitable materials for substrates and potential applications are also introduced. Using the principal of operation of these antennas a theoretical approach can be developed to investigate the relationship between antenna resonant frequency and strain. This is discussed in detail in the next chapter and is used to investigate the application of microstrip patch antennas for strain measurement.

CHAPTER 4

Antenna Theory and Evaluation

4.1 Introduction

In this chapter the possibility of using microstrip patch antennas (especially circular microstrip patch antenna) is investigated based on the analytical formulae for antenna resonant frequencies. The relationship between strain (applied to the antenna) and the shift in the resonant frequency of the circular microstrip patch antenna is derived theoretically. This relationship is also investigated analytically using MATLAB™ programming software. Comparing these two different approaches has motivated the author to study this relationship using different methods which will be discussed in the next two chapters.

In addition, other potential electromagnetic structures that could be used for strain measurement are introduced here and the analytical relationship between strain and their resonant frequency is investigated. These structures include rectangular microstrip patch antenna, dielectric resonator antennas (DRAs) and split ring resonators (SRRs).

Next, the design procedures for two aforementioned microstrip patch antenna configurations including the feeding designs are provided. These procedures are used for the initial design of the circular microstrip patch antenna. All the MATLAB™ codes written for this chapter are available in Appendix A which could be used in the future to further investigate the strain measurement capability of the potential structures.

4.2 Strain-Frequency Shift Relationship

4.2.1 Microstrip Patch Antennas (MPAs)

4.2.1.1 Circular Microstrip Patch Antennas (CMPAs)

A typical circular microstrip patch antenna (Coaxial probe feed) is shown in Figure 4.1. The antenna consists of a very thin layer of copper as a patch, a layer of substrate, and the ground plane (A thin layer of copper). The thickness of the patch is very small compared to the free-space wavelength ($t_a << \lambda_0$). Substrate thickness is usually between 0.003 and 0.05 of free-space wavelength and their dielectric constant is usually between 2.2 and 12 (Balanis, 2005). For the application of sensor, the substrate thickness should be small and the dielectric constant should be large enough so that the antenna becomes narrowband. As a result, any shift in the resonant frequency of the antenna will become more clear, and easy to measure.

For the antenna sensor application, the coaxial probe feed is chosen to isolate the results from physical changes in the feed. This is because any change in the dimensions of the antenna structure changes the dimension of the microstrip line and as a result, the impedance of the feed and also the frequency of the antenna will change.

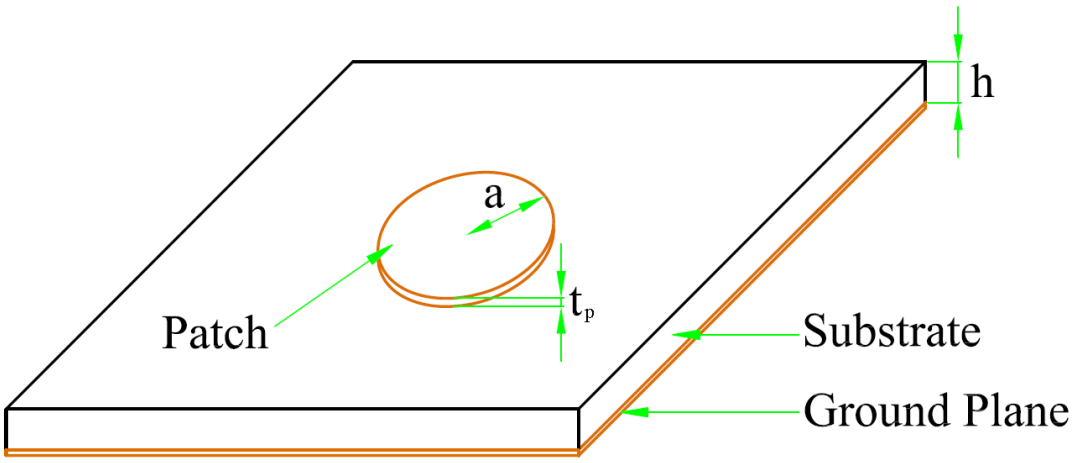

Figure 4.1 Circular microsttrip patch antenna (Balanis, 2005).

According to Balanis (2005), the resonant frequency of a circular patch antenna with the radius of a, substrate thickness of h and relative permittivity of ε_r, in its dominant mode (TM_{110}) is:

$$(f_r)_{110} = \frac{1.2412c}{2\pi a_e \sqrt{\varepsilon_r}} \tag{4.1}$$

where

$$c = \frac{1}{\sqrt{\mu_0 \varepsilon_0}} \tag{4.2}$$

is the speed of light in free space;

and

$$a_e = a\left\{1 + \frac{2h}{\pi a \varepsilon_r}\left[\ln(\frac{\pi a}{2h}) + 1.7726\right]\right\}^{1/2} \tag{4.3}$$

is the effective radius of the antenna.

If we consider that $\varepsilon_s^{1/2} << \varepsilon_s$ (where ε_s is the applied strain) then we could conclude that after applying tensile strain the following statement does not change significantly and therefore it could be considered constant:

$$\left\{1 + \frac{2h}{\pi a \varepsilon_r}\left[\ln(\frac{\pi a}{2h}) + 1.7726\right]\right\}^{1/2} = c_1 \tag{4.4}$$

thus, from Equations 4.3 and 4.4 we have:

$$a_e = c_1 a \tag{4.5}$$

and from Equation 4.1:

$$f_r = \frac{c_2}{a_e} \tag{4.6}$$

where

$$c_2 = \frac{1.2412c}{2\pi\sqrt{\varepsilon_r}} \tag{4.7}$$

after applying strain, effective radius of antenna is:

$$a_{es} = a_e(1 + \varepsilon_s) \tag{4.8}$$

thus, from Equations 4.6 and 4.8, resonant frequency of the antenna is:

$$f_{rs} = \frac{c_2}{a_{es}} = \frac{c_2}{a_e(1+\varepsilon_s)} \tag{4.9}$$

hence, the frequency shift is:

$$\Delta f = f_{rs} - f_r = \frac{c_2}{a_e}\left(\frac{1}{1+\varepsilon_s} - 1\right) \tag{4.10}$$

thus

$$\frac{\Delta f}{f_{rs}} = \left(\frac{\frac{1}{1+\varepsilon_s} - 1}{\frac{1}{1+\varepsilon_s}}\right) = -\varepsilon_s \tag{4.11}$$

The equations 4.4 to 4.11 were derived by the author of this thesis. As we can see, in a circular microstrip patch antenna, the percentage of frequency shift has a linear relationship with strain. Without using the above assumption and by calculating the resonant frequency using Equations 4.1, 4.2, and 4.3 in MATLAB™, the same results are obtained (Figure 4.2). The antenna used for analytical calculations has the resonant frequency of 1.5 GHz, patch radius of 27.1 mm, substrate thickness of 1.5 mm, and the substrate is FR4 Epoxy with the permittivity of 4.5 and Poisson ratio of 0.12. The applied strain is up to 3000 micro-strain in steps of 500 micro-strain. These results are based on pure tension and with the assumption that the change in the radius of the antenna in the direction of the E-plane has the most important impact on the resonant frequency of the antenna. This is because the effective electrical length of the antenna is dependent on the physical size of the antenna in the direction of the E-plane.

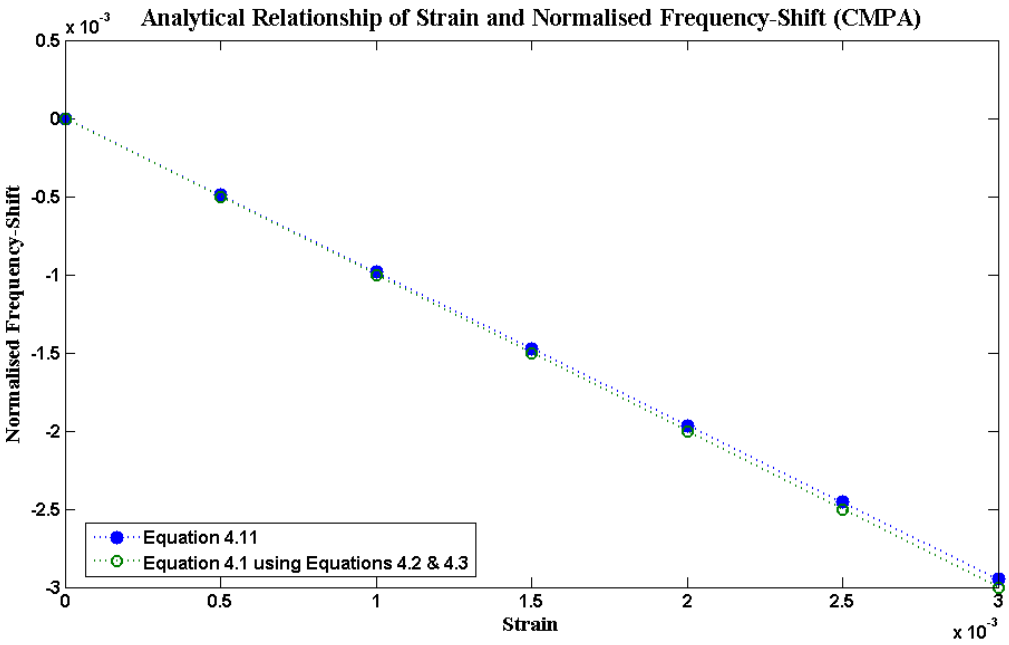

Figure 4.2 Analytical relationship of strain and normalised frequency shift for CMPA.

4.2.1.2 Rectangular Microstrip Patch Antennas (RMPAs)

A typical rectangular microstrip patch antenna (Coaxial probe feed) is shown in Figure 4.3.

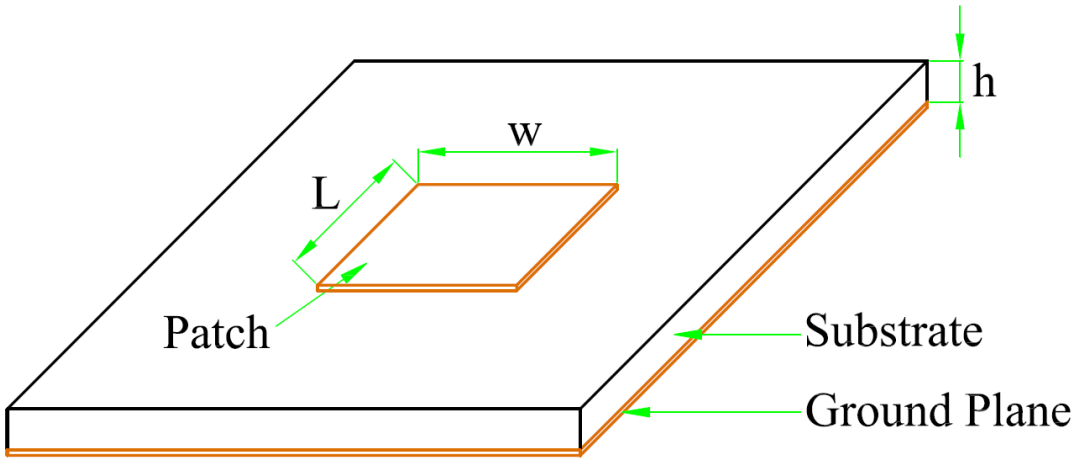

Figure 4.3 Rectangular microstrip patch antenna (Balanis, 2005).

Resonant frequency of a rectangular microstrip patch antenna for its dominant mode (TM_{010}) is (Balanis, 2005):

$$f = \frac{c}{2L_{eff}\sqrt{\varepsilon_{reff}}} \tag{4.12}$$

where

c is the velocity of light in free-space;

L_{eff} is the effective length of the patch:

$$L_{eff} = L + 2\Delta L \tag{4.13}$$

where L is the patch length;

and

$$\Delta L = 0.412h\frac{\left(\varepsilon_{reff} + 0.3\right)\left(\frac{w}{h} + 0.264\right)}{\left(\varepsilon_{reff} - 0.258\right)\left(\frac{w}{h} + 0.8\right)} \tag{4.14}$$

and ε_{reff} is the effective permittivity:

$$\text{for } w/h > 1 \quad \varepsilon_{reff} = \frac{\varepsilon_r + 1}{2} + \frac{\varepsilon_r - 1}{2}\left[1 + 12\frac{h}{w}\right]^{-1/2} \tag{4.15}$$

where ε_r, w and h are permittivity, width and thickness of the substrate, respectively.

The analytical relationship between strain and normalised frequency-shift is investigated using MATLAB™ (Figure 4.4). The results show that the shift in the antenna frequency when strain is applied in the direction of antenna length is same as the circular microstrip patch antenna with the same material and operating frequency. However, when the strain is applied in the direction of antenna width, the amount of shift is much smaller and in the opposite direction. The length and width of the patch are 46.9 mm and 60.3 mm, respectively.

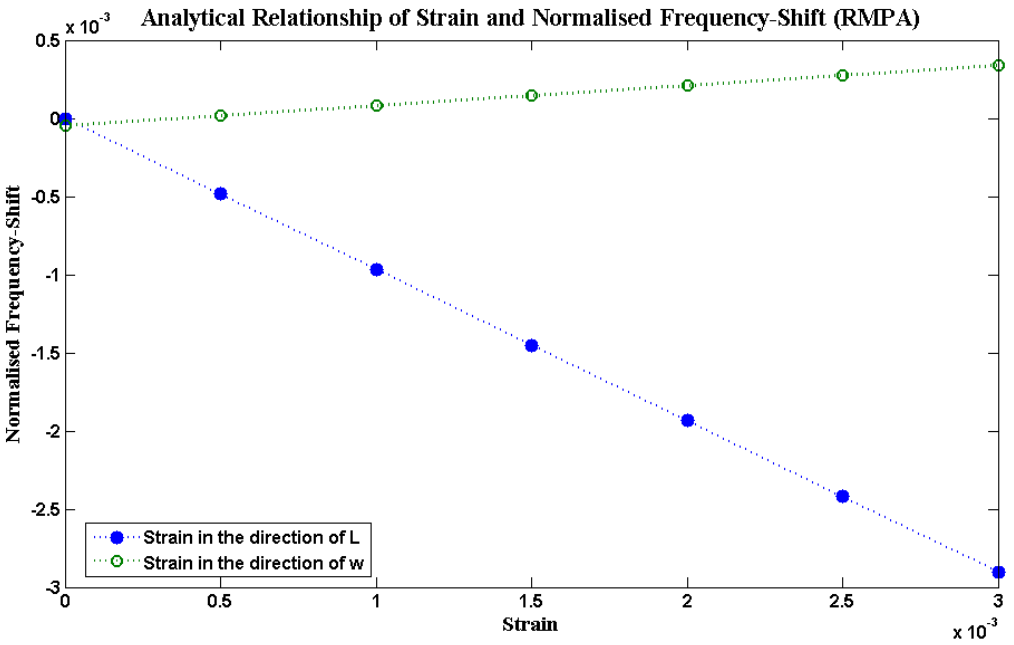

Figure 4.4 Analytical relationship of strain and normalised frequency shift for RMPA.

4.2.2 Dielectric Resonator Antennas (DRAs)

Dielectric resonator antennas (DRAs) are un-metallised radiators with several different applications in printed circuit integration such as filters and oscillators. One of the main advantages of DRAs is their high degree of flexibility, allowing for a wide range of designs to suit different physical or electrical requirements (Petosa, 2007).

4.2.2.1 Hemispherical DRA

A hemispherical DRA is characterized by its radius a and permittivity ε_r (Figure 4.5) (Petosa, 2007).

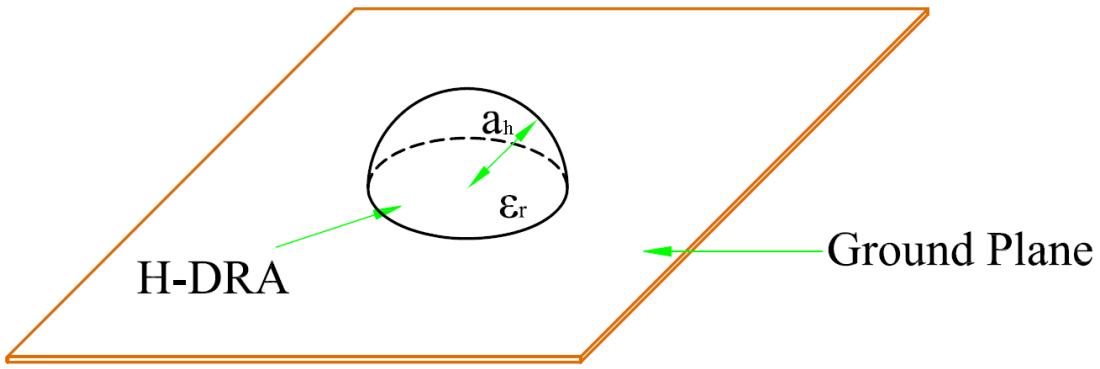

Figure 4.5 Hemispherical DRA (Petosa, 2007).

The resonant frequency of the DRA is (Petosa, 2007):

$$f = \frac{4.7713\,\mathrm{Re}(k_0 a_h)}{a_h} \tag{4.16}$$

where

f is the resonant frequency in GHz;

a_h is the radius of the DRA in cm;

and

k_0 is the free-space wave number and can be obtained from (Petosa, 2007):

$$\frac{J_{1/2}\left(\sqrt{\varepsilon_r}k_0 a_h\right)}{J_{3/2}\left(\sqrt{\varepsilon_r}k_0 a_h\right)} = \frac{H^{(2)}_{1/2}(k_0 a_h)}{\sqrt{\varepsilon_r}H^{(2)}_{3/2}(k_0 a_h)} \tag{4.17}$$

where

$J(x)$ is the first-order Bessel function;

and

$H^{(2)}(x)$ is the second-order Hankel function.

For the hemispherical DRA the fundamental dominant mode is the TE_{111} mode (Petosa, 2007). The real part of $(k_0 a_h)$ for this mode can be obtained from (Petosa, 2007):

$$\mathrm{Re}(k_0 a_h) = 2.8316\varepsilon_r^{-0.47829} \tag{4.18}$$

Second important mode of the hemispherical DRA is TM_{101} (Petosa, 2007). The real part of $(k_0 a_h)$ for this mode can be obtained from (Petosa, 2007):

$$\mathrm{Re}(k_0 a_h) = 4.47226\varepsilon_r^{-0.505} \tag{4.19}$$

The analytical relationship between strain and normalised frequency-shift is investigated using MATLAB™ for both mode of an H-DRA (Figure 4.6). The results show that the shift in the antenna frequency of an H-DRA is almost the same as the circular microstrip patch antenna when the DRA material is same as the CMPA substrate. The radius of the DRA used to calculate the results is 50 mm and therefore the resonant frequency of TE_{111} and TM_{101} modes are 1.3161 GHz and 1.9967 GHz, respectively. The amount of shift is same for these two different modes as it is expected from Equation 4.16 (because $\mathrm{Re}(k_0 a_h)$ is

constant for a specific dielectric material); however, the TE_{111} mode can be used to fabricate a smaller antenna sensor for the same operating frequency compared to the TM_{101} mode.

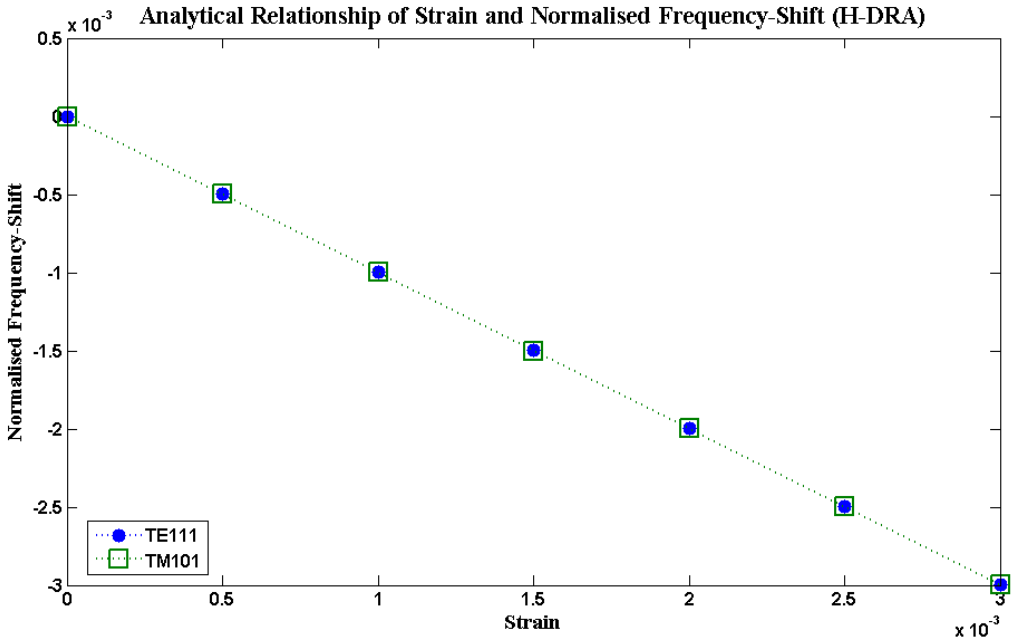

Figure 4.6 Analytical relationship of strain and normalised frequency shift for H-DRA.

4.2.2.2 Cylindrical DRA

A cylindrical DRA is characterized by its height h_c, radius a_c and permittivity ε_r (Figure 4.7) (Petosa, 2007).

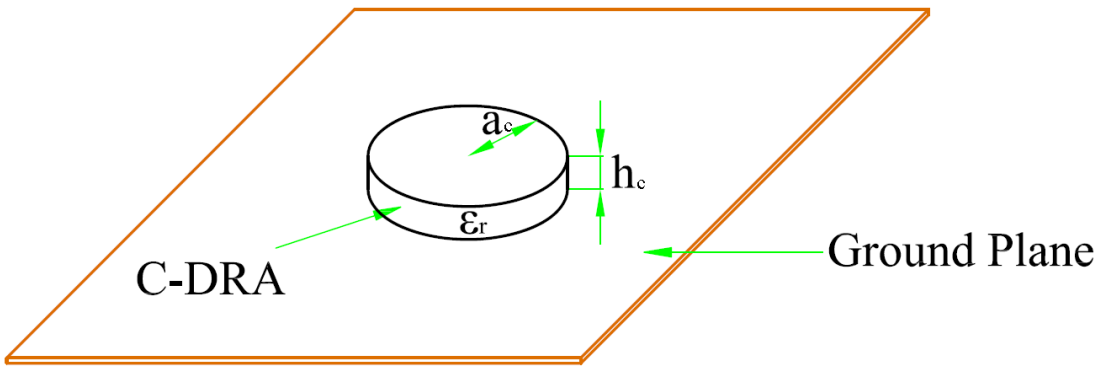

Figure 4.7 Cylindrical DRA (Petosa, 2007).

The cylindrical DRA has one degree of freedom more than the hemispherical DRA which is the aspect ratio a_c/h_c (usually less than 5) (Petosa, 2007). For a given permittivity, this

ratio determines the value of $(k_0 a_c)$. The resonant frequency of the DRA can be determined from equation 4.16 (Petosa, 2007). The modes which are most commonly used for radiating applications are the $TM_{01\delta}$, $TE_{01\delta}$ and $HE_{11\delta}$ modes (Petosa, 2007). The value of δ depends on the dielectric constant and is between 0 and 1 (Petosa, 2007).

The real part of $(k_0 a_c)$ for $TE_{01\delta}$ mode can be obtained from (Petosa, 2007):

$$\mathrm{Re}(k_0 a_c) = \frac{2.327}{\sqrt{\varepsilon_r + 1}} \left\{ 1 + 0.2123 \frac{a_c}{h_c} - 0.00898 \left(\frac{a_c}{h_c} \right)^2 \right\} \tag{4.20}$$

The real part of $(k_0 a_c)$ for $TM_{01\delta}$ mode is (Petosa, 2007):

$$\mathrm{Re}(k_0 a_c) = \frac{\sqrt{3.83^2 + \left(\frac{\pi a_c}{2h_c} \right)^2}}{\sqrt{\varepsilon_r + 2}} \tag{4.21}$$

The real part of $(k_0 a_c)$ for $HE_{11\delta}$ mode can be calculated from (Petosa, 2007):

$$\mathrm{Re}(k_0 a_c) = \frac{6.324}{\sqrt{\varepsilon_r + 2}} \left\{ 0.27 + 0.36 \frac{a_c}{2h_c} + 0.02 \left(\frac{a_c}{2h_c} \right)^2 \right\} \tag{4.22}$$

Again, the analytical relationship between strain and normalised frequency-shift is investigated using MATLAB™ for three principal modes of a C-DRA (Figure 4.8). The results show that the shift in the antenna frequency of a C-DRA ($TE_{01\delta}$ mode) is almost half of the CMPA when the DRA material is same as the CMPA substrate. For two other modes the shift is almost negligible. The radius ad height of the DRA used to calculate the results are 50 mm and 10 mm, respectively. Therefore the resonant frequency of $TE_{01\delta}$, $TM_{01\delta}$, and $HE_{11\delta}$ modes are 1.7394 GHz, 3.2706 GHz and 3.0653 GHz, respectively. The $TE_{01\delta}$ mode also has a lower operating frequency compared to the other two modes.

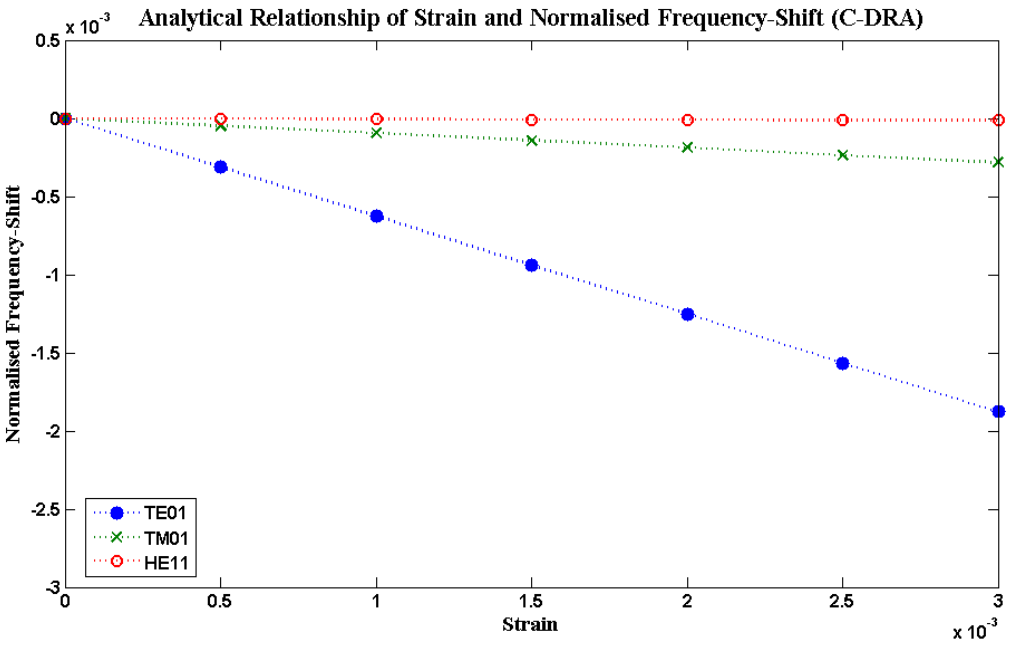

Figure 4.8 Analytical relationship of strain and normalised frequency shift for C-DRA.

4.2.2.3 Rectangular DRA

A rectangular DRA is characterized by its height h_r, width w_r, depth d and permittivity ε_r (Figure 4.9) (Petosa, 2007).

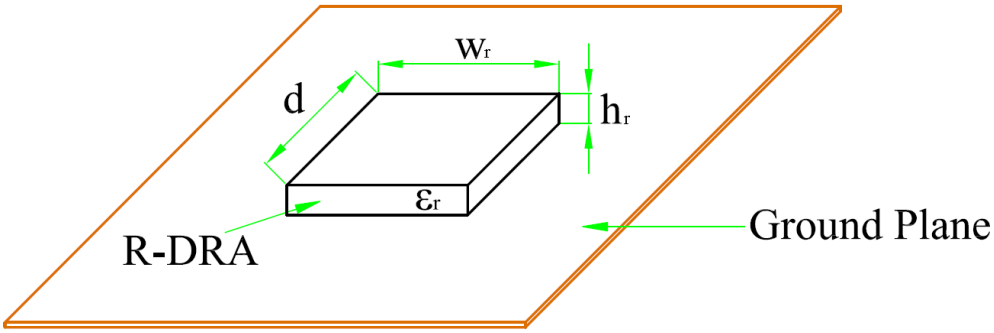

Figure 4.9 Rectangular DRA (Petosa, 2007).

The rectangular DRA has two degrees of freedom more than the hemispherical DRA which are the aspect ratios w_r/h_r and w_r/d (Petosa, 2007). The lowest order mode for a rectangular DRA, if $w_r > d > 2h_r$, is the $TE^x_{\delta 11}$ mode (Petosa, 2007). The resonant frequency of the DRA for this mode is (Petosa, 2007):

$$f = \frac{15F}{w_r \pi \sqrt{\varepsilon_r}} \tag{4.23}$$

where

f is the resonant frequency in GHz;

w_r is the width of the DRA in cm;

and

F is the normalised frequency and can be obtained from (Petosa, 2007):

$$F = a_0 + a_1\left(w_r / 2h_r\right) + a_2\left(w_r / 2h_r\right)^2 \tag{4.24}$$

where

$$a_0 = 2.57 - 0.8\left(d/2h_r\right) + 0.42\left(d/2h_r\right)^2 - 0.05\left(d/2h_r\right)^3 \tag{4.25}$$

$$a_1 = 2.71\left(d/2h_r\right)^{-0.282} \tag{4.26}$$

and

$$a_2 = 0.16 \tag{4.27}$$

Figure 4.10 shows the analytical relationship between strain and normalised frequency-shift an R-DRA for its dominant mode ($TE^x_{\delta 11}$) when strain is separately applied in two different directions. The results show that shift in the frequency of an R-DRA ($TE^x_{\delta 11}$ mode) is almost negligible (compared to the CMPA), when the DRA material is same as the CMPA substrate. The width, depth and height of the DRA used to calculate the results are 50 mm, 50 mm and 10 mm, respectively. The resonant frequency of $TE^x_{\delta 11}$ mode is 3.8921 GHz.

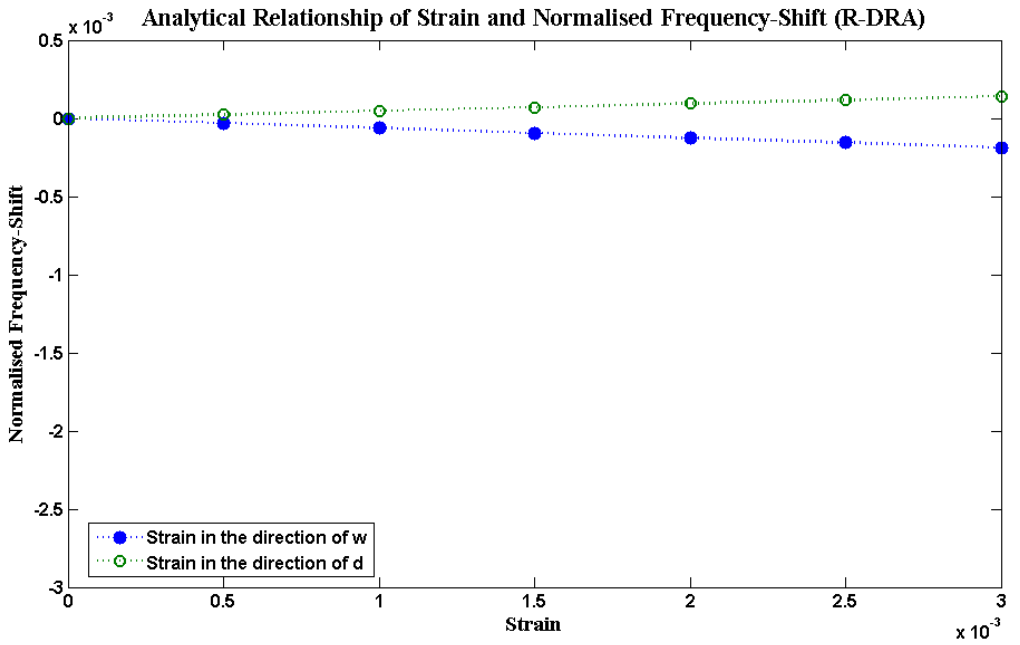

Figure 4.10 Analytical relationship of strain and normalised frequency shift for R-DRA.

4.2.3 Split Ring Resonators (SRRs)

A standard procedure for the design of artificial media with negative parameters at microwave frequencies makes use of a system of metallic wires and/or plates to obtain the negative dielectric permittivity (Marques, Martin and Sorolla, 2008). A system of split ring resonators is used to obtain the negative magnetic permeability. Split Ring Resonator (SRR) is proposed by Pendry et al. (1999), using this design it is possible to manufacture large series of small loops, of very high and negative polarizability, by using standard planar photo-etching techniques.

4.2.3.1 Edge-Coupled SRR

Edge-coupled SRR of EC-SRR is consists of two concentric metallic split rings, printed on a microwave dielectric circuit board (Marques, Martin and Sorolla, 2008). When it is excited by a time-varying external magnetic field directed along the z-axis, the cuts on each ring (which are placed on opposite sides of the EC-SRR) force the electric current to flow from one ring to another across the slots between them, taking the form of a strong displacement current (Marques, Martin and Sorolla, 2008). The slots between the rings therefore behave as a distributed capacitance, and the whole EC-SRR has the equivalent circuit shown in Figure 4.11, where L_{EC} is the EC-SRR self inductance and C is the capacitance associated with each EC-SRR half. The capacitance is $C = \pi r C_{pul}$, where r is the mean radius of the

EC-SRR ($r = r_{ext} - c - d/2$), and C_{pul} is the per unit length capacitance along the slot between the rings (Marques, Martin and Sorolla, 2008).

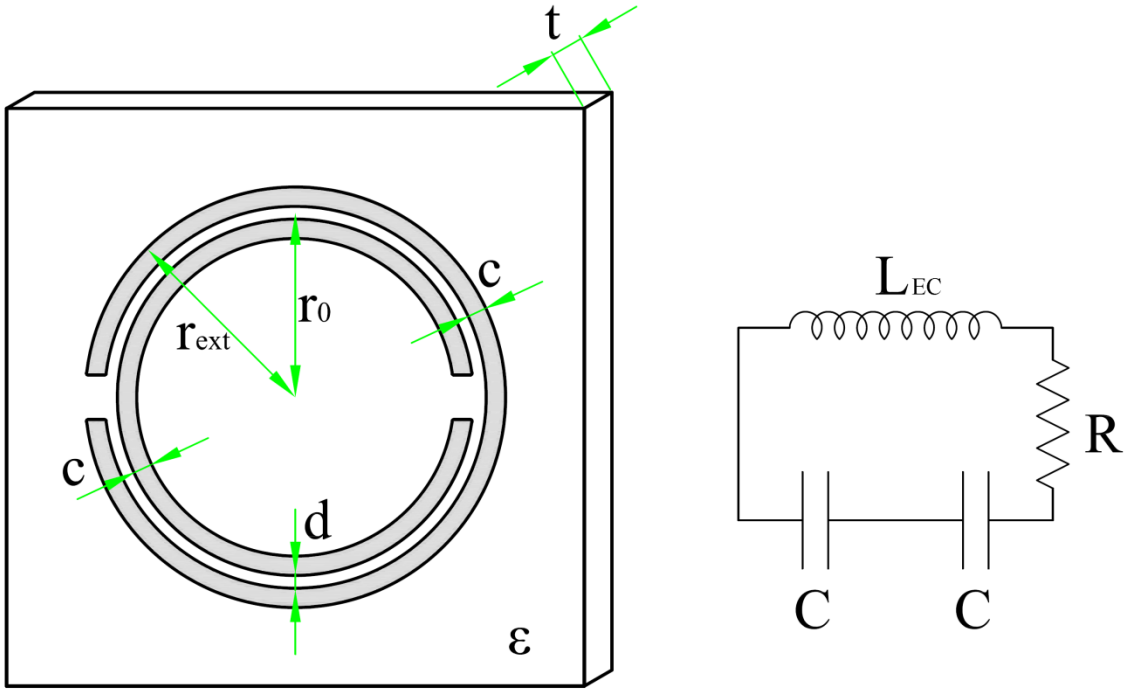

Figure 4.11 Edge-coupled SRR (Marques, Martin and Sorolla, 2008).

The frequency of resonance, ω_0, of the EC-SRR is (Marques, Martin and Sorolla, 2008):

$$\omega_0^{\,2} = \frac{2}{L_{EC}C} = \frac{2}{\pi r C_{pul} L_{EC}} \tag{4.28}$$

Therefore,

$$f_0 = \frac{1}{2\pi}\sqrt{\frac{2}{L_{EC}C}} \tag{4.29}$$

The self inductance of the ring is (Marques, Martin and Sorolla, 2008):

$$L_{EC} = \frac{\mu_0 \pi^3}{4c^2}\int_0^{\infty} \frac{1}{k^2}\left(b\beta(kb) - a\beta(ka)\right)^2 dk \tag{4.30}$$

Where c is the width of the ring, $a = r - c/2$, $b = r + c/2$ and function $\beta(x)$ is defined as

$$\beta(x) = S_0(x)J_1(x) - S_1(x)J_0(x) \tag{4.31}$$

Where S_n and J_n are the nth order Struve and Bessel functions respectively.

The per unit length capacitance of the EC-SRR can be calculated using (Marques, Martin and Sorolla, 2008):

$$C_{pul} = \varepsilon_0 \varepsilon_e F(k) \tag{4.32}$$

where

$$\varepsilon_e = 1 + \frac{\varepsilon - \varepsilon_0}{2\varepsilon_0} \frac{F(k)}{F(k_1)} \tag{4.33}$$

$$k = a/b\,,\ a = d/2\,,\ b = d/2 + c \tag{4.34}$$

$$k_1 = \frac{\sinh(\pi a/2t)}{\sinh(\pi b/2t)} \tag{4.35}$$

$$F(k) = \begin{cases} \dfrac{1}{\pi}\ln\left(2\dfrac{1+\sqrt{k'}}{1-\sqrt{k'}}\right) & 0 \le k \le 0.7 \\ \pi\left\{\ln\left(2\dfrac{1+\sqrt{k}}{1-\sqrt{k}}\right)\right\}^{-1} & 0.7 \le k \le 1 \end{cases} \tag{4.36}$$

where $k' = \sqrt{1-k^2}$.

The EC-SRR electrical size, although small, cannot be reduced in practice to values much smaller than $\lambda/10$, where λ is the free-space wavelength (Marques, Martin and Sorolla, 2008).

Figure 4.12 shows the analytical relationship between strain and normalised frequency-shift of an EC-SRR. The results show that shift in the frequency of an EC-SRR is same as the CMPA when the SRR substrate material is same as the CMPA substrate. The resonant frequency of the SRR used for analytical calculation is 5.1711 GHz (twice as the CMPA frequency) whilst its radius is 2.54 mm (1/10 of CMPA radius). The thickness of the SRR substrate, its relative permittivity, the separation distance between rings and width of strips are 0.49 mm, 2.43, 0.17 mm and 0.19 mm, respectively. This reduction in size may be used to measure more localised strain compared to CMPA.

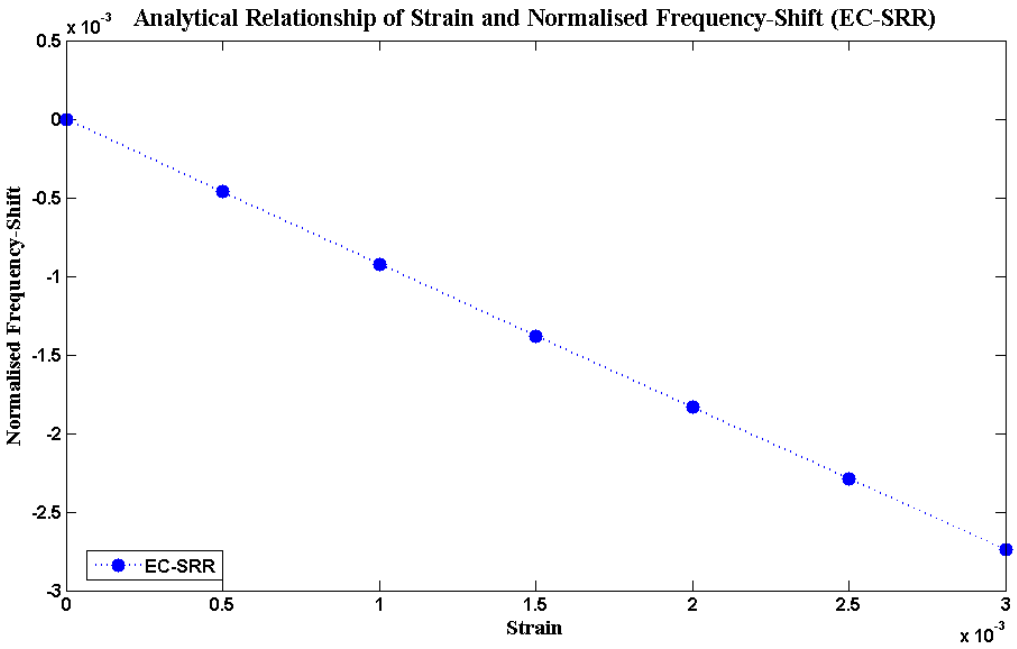

Figure 4.12 Analytical relationship of strain and normalised frequency shift for EC-SRR.

4.2.3.2 Broadside-Coupled SRR

The Broadside-coupled SRR (BC-SRR) is proposed by Marques, Medinaand and Rafi-El-Idrissi (2002) and has the advantage of a potentially much smaller electrical size (Marques et al., 2003b) as well as the inversion symmetry. The BC-SRR is shown in Figure 4.13. In BC-SRR, both rings are printed at both sides of the dielectric board (compared to EC-SRR); therefore, the per unit length capacitance, C_{pul}, of the BC-SRR is the capacitance of the broadside-coupled strips (Marques, Martin and Sorolla, 2008). The equivalent circuit for the BC-SRR is the same as for the EC-SRR (Marques, Martin and Sorolla, 2008).

The resonant frequency of the BC-SRR can be calculated using the same formula for the EC-SRR. The only difference is in per unit length capacitance which can be obtained from (Marques, Martin and Sorolla, 2008):

$$C_{pul} = 1/2\,\varepsilon_0\varepsilon_e\left(\frac{2c}{t} + 1.393 + 0.667\ln\left(\frac{2c}{t} + 1.444\right)\right) \tag{4.37}$$

where

$$\varepsilon_e = \frac{\varepsilon + \varepsilon_0}{2\varepsilon_0} + \frac{\varepsilon - \varepsilon_0}{2\varepsilon_0}\left(1 + \frac{6t}{c}\right)^{-1} \tag{4.38}$$

and t is the thickness of the dielectric substrate.

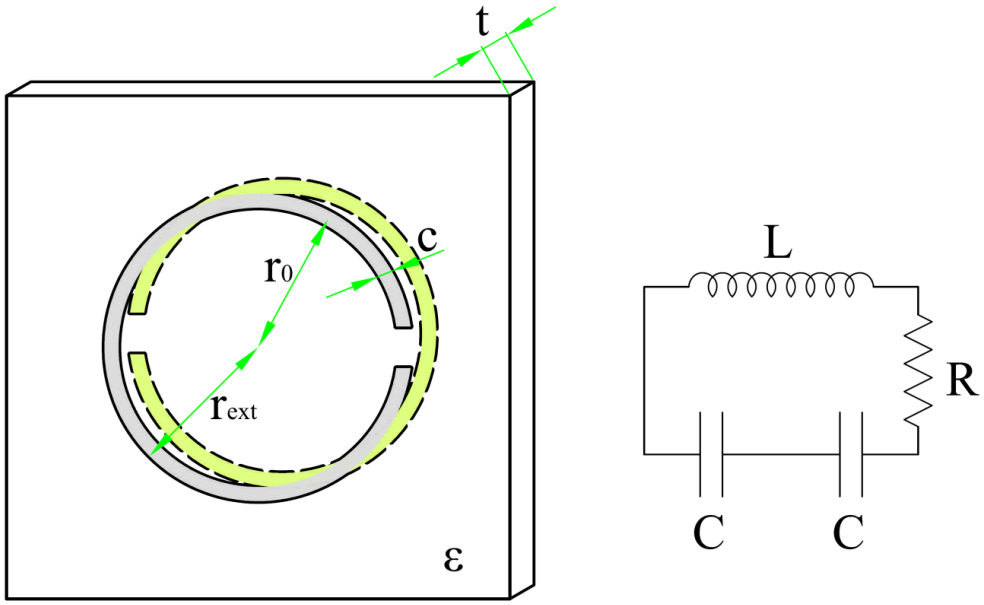

Figure 4.13 Broadside-coupled SRR (Marques, Martin and Sorolla, 2008).

BC-SRR with smaller sizes than EC-SRR can be made by using thin substrates of high permittivity (Marques, Martin and Sorolla, 2008). This could be used as an advantage for sensor applications.

4.2.3.3 Nonbianisotropic SRR

The Nonbianisotropic SRR (NB-SRR) is initially proposed by (Marques et al., 2003a) and is illustrated in Figure 4.14. It has the same resonant frequency as the EC-SRR with similar dimensions. The advantage of NB-SRR over EC-SRR is the inversion symmetry with regards to its centre (Marques, Martin and Sorolla, 2008). This symmetry may results in more symmetrical strain measurement while used as a strain sensor.

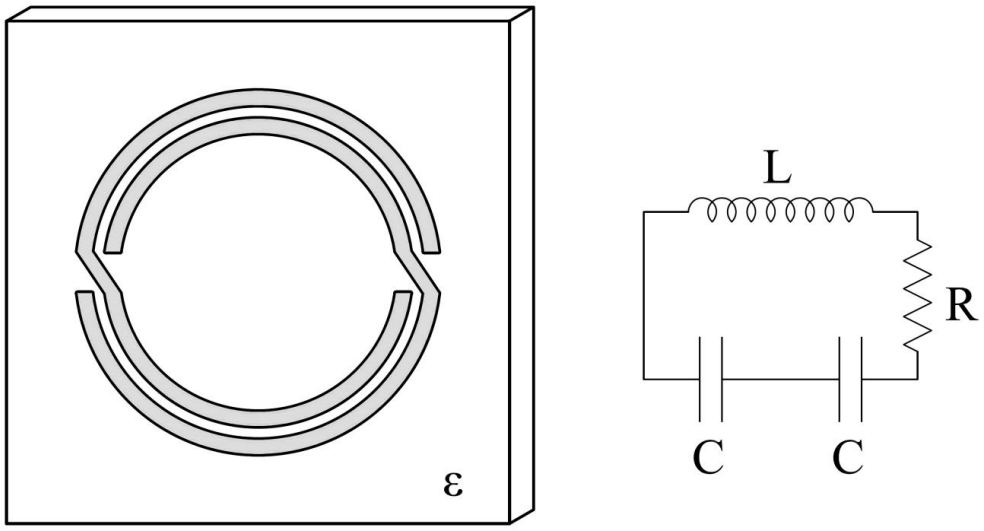

Figure 4.14 Nonbianisotropic SRR (Marques, Martin and Sorolla, 2008).

4.2.3.4 Double-Split SRR

The Double-split SRR (2-SRR) (Marques et al., 2003a) and its equivalent circuit is shown in Figure 4.15. It is another SRR design which solves the symmetry problem in EC-SRR. However, for the same dimensions, the capacitance of the 2-SRR is $C = \pi C_{pul}/2$ which results in a resonant frequency twice as the EC-SRR or NB-SRR (Marques, Martin and Sorolla, 2008). This is a disadvantage for 2-SRR if used as a strain measurement device; however, the difference in the structure of 2-SRR may results in different sensitivity or directionality compared to EC-SRR.

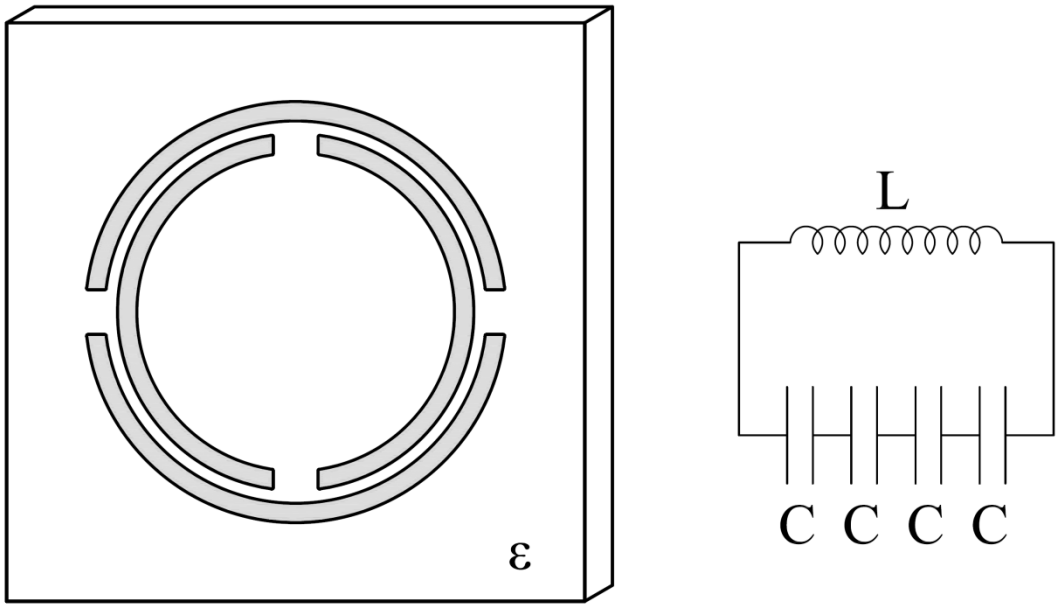

Figure 4.15 Double-split SRR (Marques, Martin and Sorolla, 2008).

4.2.3.5 Spirals

A two-turn spiral resonator (2-SR) (Baena et al., 2004) and its equivalent circuit are shown in figure 4.16. From the equivalent circuit, it is obvious that the resonant frequency of 2-SR is half the frequency of the EC-SRR or NB-SRR with the same dimensions. The electrical size of the spiral can be reduced more by increasing the number of turns (Marques, Martin and Sorolla, 2008). This is a great advantage over EC-SRR and consequently circular microstrip patch antennas.

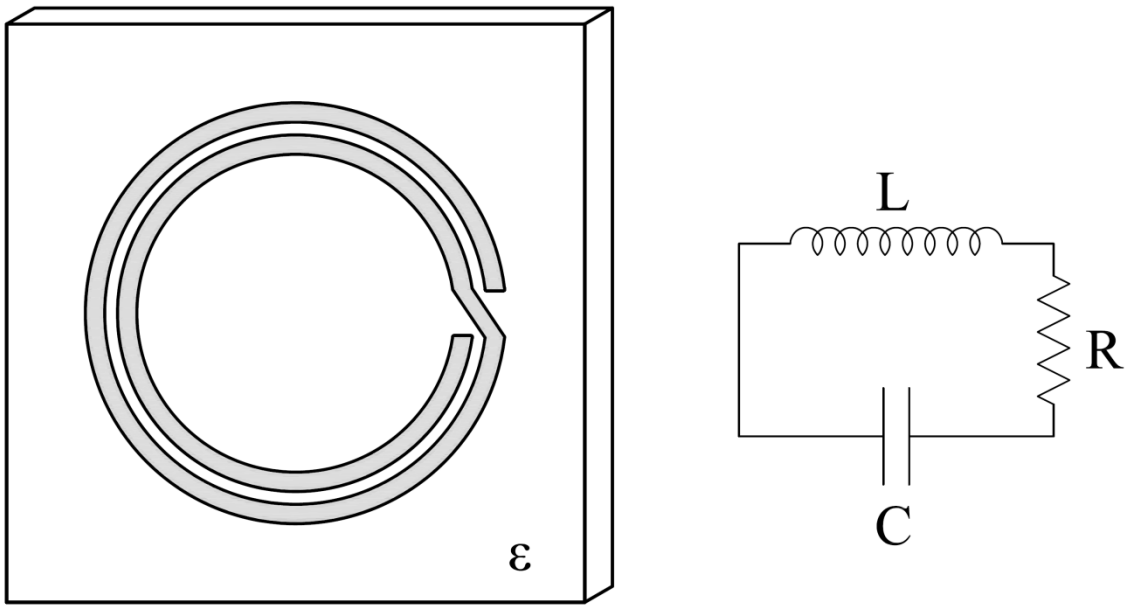

Figure 4.16 Two-turn spiral resonator (Marques, Martin and Sorolla, 2008).

4.3 Antenna Design

In this section, the design procedure for two different configurations of microstrip patch antennas as well as two different feeding methods is provided. The formulae used are extracted from different sources to compare the differences in design results. The design used for further study is based on working frequency of 1.5 GHz (highlighted in the tables 4.1 to 4.5). MATLAB™ software is used to design a rectangular and circular microstrip patch antennas which are further analysed using FEA packages and finally are fabricated for experimental tests. The MATLAB™ codes used here are available in Appendix A.

4.3.1 Rectangular Microstrip Patch Antenna

4.3.1.1 Antenna dimensions

According to Huang and Boyle (2008) and Balanis (2005):
For $^{w}/_{h} > 1$:

$$\varepsilon_{reff} = \frac{\varepsilon_r+1}{2} + \frac{\varepsilon_r-1}{2}\left[1 + 12\frac{h}{w}\right]^{-1/2} \quad (4.39)$$

$$\Delta L = 0.412h\frac{\left(\varepsilon_{reff}+0.3\right)\left(\frac{w}{h}+0.264\right)}{\left(\varepsilon_{reff}-0.258\right)\left(\frac{w}{h}+0.8\right)} \quad (4.40)$$

$$L_{eff} = L + 2\Delta L \quad (4.41)$$

For TM_{010} mode:

$$(f_r)_{010} = \frac{c}{2L_{eff}\sqrt{\varepsilon_{reff}}} \tag{4.42}$$

where $c = \frac{1}{\sqrt{\mu_0 \varepsilon_0}}$ is the velocity of light in free-space.

For an efficient radiator:

$$w = \frac{c}{2f_r}\sqrt{\frac{2}{\varepsilon_r+1}} \tag{4.43}$$

Table 4.1 Rectangular microstrip patch antenna dimensions for operating frequency of 1 to 10 GHz (According to Huang and Boyle (2008) and Balanis (2005))

Microstrip Patch Antenna Dimensions ($\varepsilon_r = 4.5$ & $thickness = 1.5\ mm$)																			
fr(GHz)	1	1.5	2	2.5	3	3.5	4	4.5	5	5.5	6	6.5	7	7.5	8	8.5	9	9.5	10
w(mm)	90.5	60.3	45.2	36.2	30.2	25.8	22.6	20.1	18.1	16.4	15.1	13.9	12.9	12.1	11.3	10.6	10.0	9.5	9.0
L(mm)	70.6	46.9	35.1	28.0	23.2	19.8	17.3	15.3	13.7	12.3	11.3	10.3	9.5	8.8	8.2	7.7	7.2	6.8	6.4
y_0(mm)	26.2	17.5	13.0	10.4	8.6	7.4	6.4	5.7	5.1	4.6	4.2	3.8	3.5	3.3	3.0	2.8	2.7	2.5	2.4

y_0: Feed distance from the edge of the patch

According to Volakis (2007):

For $^{w}/_{h} > 1$:

$$\varepsilon_{reff} = \frac{\varepsilon_r+1}{2} + \frac{\varepsilon_r-1}{2}\left[1 + 10\frac{h}{w}\right]^{-1/2} \tag{4.44}$$

$$\Delta L = 0.412h\frac{\left(\varepsilon_{reff}+0.3\right)\left(\frac{w}{h}+0.264\right)}{\left(\varepsilon_{reff}-0.258\right)\left(\frac{w}{h}+0.8\right)} \tag{4.45}$$

$$L_{eff} = L + 2\Delta L \tag{4.46}$$

For TM_{010} mode:

$$(f_r)_{010} = \frac{c}{2L_{eff}\sqrt{\varepsilon_r}} \tag{4.47}$$

where $c = \frac{1}{\sqrt{\mu_0 \varepsilon_0}}$ is the velocity of light in free-space.

Table 4.2 Rectangular microstrip patch antenna dimensions for operating frequency of 1 to 10 GHz (According to Volakis (2007))

Microstrip Patch Antenna Dimensions ($\varepsilon_r = 4.5$ & $thickness = 1.5\ mm$)																			
fr(GHz)	1	1.5	2	2.5	3	3.5	4	4.5	5	5.5	6	6.5	7	7.5	8	8.5	9	9.5	10
w(mm)	90.5	60.3	45.2	36.2	30.2	25.8	22.6	20.1	18.1	16.4	15.1	13.9	12.9	12.1	11.3	10.6	10.0	9.5	9.0
L(mm)	69.3	45.8	34.0	26.9	22.2	18.8	16.3	14.3	12.8	11.5	10.4	9.5	8.8	8.1	7.5	7.0	6.5	6.1	5.8
y_0(mm)	25.8	17.0	12.6	10.0	8.2	7.0	6.0	5.3	4.7	4.2	3.8	3.5	3.2	3.0	2.8	2.6	2.4	2.2	2.1

y_0: Feed distance from the edge of the patch

According to Garg et al. (2000):

For $^{w}/_{h} > 1$:

$$\varepsilon_{reff} = \frac{\varepsilon_r+1}{2} + \frac{\varepsilon_r-1}{2}\left[1 + 12\frac{h}{w}\right]^{-1/2} \quad (4.48)$$

$$\Delta L = 0.412h\frac{\left(\varepsilon_{reff}+0.3\right)\left(\frac{w}{h}+0.264\right)}{\left(\varepsilon_{reff}-0.258\right)\left(\frac{w}{h}+0.813\right)} \quad (4.49)$$

$$L_{eff} = L + 2\Delta L \quad (4.50)$$

For TM_{010} mode:

$$(f_r)_{010} = \frac{c}{2L_{eff}\sqrt{\varepsilon_{reff}}} \quad (4.51)$$

where $c = \frac{1}{\sqrt{\mu_0\varepsilon_0}}$ is the velocity of light in free-space.

Table 4.3 Rectangular microstrip patch antenna dimensions for operating frequency of 1 to 10 GHz (According to Garg et al. (2000))

Microstrip Patch Antenna Dimensions ($\varepsilon_r = 4.5$ & $thickness = 1.5\ mm$)																			
fr(GHz)	1	1.5	2	2.5	3	3.5	4	4.5	5	5.5	6	6.5	7	7.5	8	8.5	9	9.5	10
w(mm)	90.5	60.3	45.2	36.2	30.2	25.8	22.6	20.1	18.1	16.4	15.1	13.9	12.9	12.1	11.3	10.6	10.0	9.5	9.0
L(mm)	70.5	46.9	35.1	28.0	23.2	19.8	17.3	15.3	13.7	12.3	11.3	10.3	9.5	8.8	8.2	7.7	7.2	6.8	6.4
y_0(mm)	26.2	17.5	13.0	10.4	8.6	7.4	6.4	5.7	5.1	4.6	4.2	3.8	3.5	3.3	3.0	2.9	2.7	2.5	2.4

y_0: Feed distance from the edge of the patch

4.3.1.2 Probe feed location

According to Balanis (2005), the probe feed location for a rectangular microstrip patch antenna for $50\,\Omega$ matching can be calculated using the following equations:

$$50\ (ohms) = R_{in}(y = y_0) = R_{in}(y = 0)\cos^2\left(\frac{\pi}{L}y_0\right)$$

$$R_{in} = \frac{1}{2(G_1 \pm G_{12})} \quad (4.52)$$

where R_{in} is the resonant input resistance;

and

+ is used for modes with odd resonant voltage distribution beneath the patch and between the slots, and – is used for modes with even resonant voltage distribution beneath the patch and between the slots. For TM_{010} mode + should be used.

Conductance is:

$$G_1 = \frac{2P_{rad}}{|V_0|^2} = \frac{I_1}{120\pi^2} \quad (4.53)$$

$$I_1 = \int_0^{\pi} \left[\frac{\sin\left(\frac{k_0 w}{2}\cos\theta\right)}{\cos\theta}\right]^2 \sin^3\theta \, d\theta = -2 + \cos X + X S_i(X) + \frac{\sin X}{X} \qquad (4.54)$$

where

$$X = k_0 w \qquad where: k_0 = \frac{2\pi}{\lambda_0}$$

$$k_0 = Phase\ constant\ for\ free\ space$$

$$S_i(x) = \int_0^x \frac{\sin y}{y} dy \qquad (4.55)$$

Mutual conductance is:

$$G_{12} = \frac{1}{120\pi^2} \int_0^{\pi} \left[\frac{\sin\left(\frac{k_0 w}{2}\cos\theta\right)}{\cos\theta}\right]^2 J_0(k_0 L \sin\theta) \sin^3\theta \, d\theta \qquad (4.56)$$

4.3.2 Circular Microstrip Patch Antenna

4.3.2.1 Antenna dimensions

According to Balanis (2005) and Volakis (2007), based on cavity model, the dominant mode is TM_{110}:

$$a_e = a\left\{1 + \frac{2h}{\pi a \varepsilon_r}\left[\ln\frac{\pi a}{2h} + 1.7726\right]\right\}^{1/2} \qquad (4.57)$$

$$(f_r)_{110} = \frac{1.8412c}{2\pi a_e \sqrt{\varepsilon_r}} \qquad (4.58)$$

where $c = \frac{1}{\sqrt{\mu_0 \varepsilon_0}}$ is the velocity of light in free-space.

Table 4.4 Circular microstrip patch antenna dimensions for operating frequency of 1 to 10 GHz (According to Balanis (2005) and Volakis (2007))

Microstrip Patch Antenna Dimensions ($\varepsilon_r = 4.5$, $thickness = 1.5\ mm$)																			
fr(GHz)	1	1.5	2	2.5	3	3.5	4	4.5	5	5.5	6	6.5	7	7.5	8	8.5	9	9.5	10
a(mm)	40.9	27.1	20.2	16.1	13.4	11.4	9.9	8.8	7.9	7.1	6.5	6.0	5.6	5.2	4.8	4.5	4.3	4.0	3.8
ρ_0 (mm)	13.8	7.8	5.3	4.0	3.2	2.6	2.2	1.9	1.7	1.5	1.4	1.2	1.1	1.0	1.0	0.9	0.9	0.8	0.8

ρ_0: Feed distance from the centre of the patch

According to Garg et al. (2000):

Based on cavity model, the dominant mode is TM_{110}:

By using disk capacitance:

$$a_e = a\left\{1 + \frac{2h}{\pi a \varepsilon_r}\left[\ln\frac{a}{2h} + (1.41\varepsilon_r + 1.77) + \frac{h}{a}(0.268\varepsilon_r + 1.65)\right]\right\}^{1/2} \qquad (4.59)$$

$$(f_r)_{110} = \frac{1.84118c}{2\pi a_e\sqrt{\varepsilon_r}} \quad (4.60)$$

where $c = \frac{1}{\sqrt{\mu_0\varepsilon_0}}$ is the velocity of light in free-space.

Table 4.5 Circular microstrip patch antenna dimensions for operating frequency of 1 to 10 GHz (According to Garg et al. (2000))

Microstrip Patch Antenna Dimensions ($\varepsilon_r = 4.5$, $thickness = 1.5\ mm$)																			
fr(GHz)	1	1.5	2	2.5	3	3.5	4	4.5	5	5.5	6	6.5	7	7.5	8	8.5	9	9.5	10
a(mm)	40.3	26.5	19.7	15.5	12.8	10.8	9.4	8.2	7.3	6.6	6.0	5.4	5.0	4.6	4.3	4.0	3.7	3.5	3.3
ρ_0 (mm)	13.6	7.7	5.2	3.9	3.0	2.5	2.1	1.8	1.6	1.4	1.2	1.1	1.0	0.9	0.9	0.8	0.7	0.7	0.6

ρ_0: Feed distance from the centre of the patch

4.3.2.2 Probe feed location

According to Balanis (2005), the probe feed location for a circular microstrip patch antenna for $50\,\Omega$ matching can be calculated using the following equations:

$$50\ (ohms) = R_{in}(\acute{\rho} = \rho_0) = R_{in}(\acute{\rho} = a_e)\frac{{J_1}^2(k\rho_0)}{{J_1}^2(ka_e)} \quad (4.61)$$

$$R_{in}(\acute{\rho} = a_e) = \frac{1}{G_t} \quad (4.62)$$

$$G_t = G_{rad} + G_c + G_d \quad (4.63)$$

$$G_{rad} = \frac{(k_0a_e)^2}{480}\int_0^{\frac{\pi}{2}}\left[{J_{02}^{\acute{}}}^2 + \cos^2\theta\,{J_{02}}^2\right]\sin\theta\,d\theta \quad (4.64)$$

$where: J_{02}^{\acute{}} = J_0(k_0a_e\sin\theta) - J_2(k_0a_e\sin\theta)\ \&\ J_{02} = J_0(k_0a_e\sin\theta) + J_2(k_0a_e\sin\theta)$

$$G_c = \frac{\epsilon_{m0}\pi(\pi\mu_0f_r)^{-3/2}}{4h^2\sqrt{\sigma}}[(ka_e)^2 - m^2] \quad (4.65)$$

$where: \epsilon_{m0} = 2\ for\ m = 0\ \&\ \epsilon_{m0} = 1\ for\ m \neq 0\ \rightarrow for\ TM_{110}\ mode\ \epsilon_{m0} = 1$

$\&\ k = k_0\sqrt{\varepsilon_r}\ is\ wave\ phase\ constant$

$\&\ \mu_0 = 4\pi \times 10^{-7}\ is\ permeability\ of\ free\ space$

$\&\ \sigma\ is\ the\ conductivity\ of\ the\ conductors\ associated\ with\ the\ patch\ and\ ground\ plane$

$$G_d = \frac{\epsilon_{m0}\tan\delta}{4\mu_0hf_r}[(ka_e)^2 - m^2] \quad (4.66)$$

$where: \tan\delta\ is\ the\ loss\ tangent\ of\ the\ substrate$

4.3.3 Microstrip line feed design

In order to use a microstrip line instead of the coaxial probe to feed the antenna two different approaches can be used. One method is to connect a $50\,\Omega$ directly to the antenna. In this case, the microstrip line should be connected to the antenna using an inset (Equation 4.52 or 4.62) to be matched to $50\,\Omega$ transmission line (Figure 4.17) (Huang and Boyle, 2008; Balanis, 2005; Volakis, 2007).

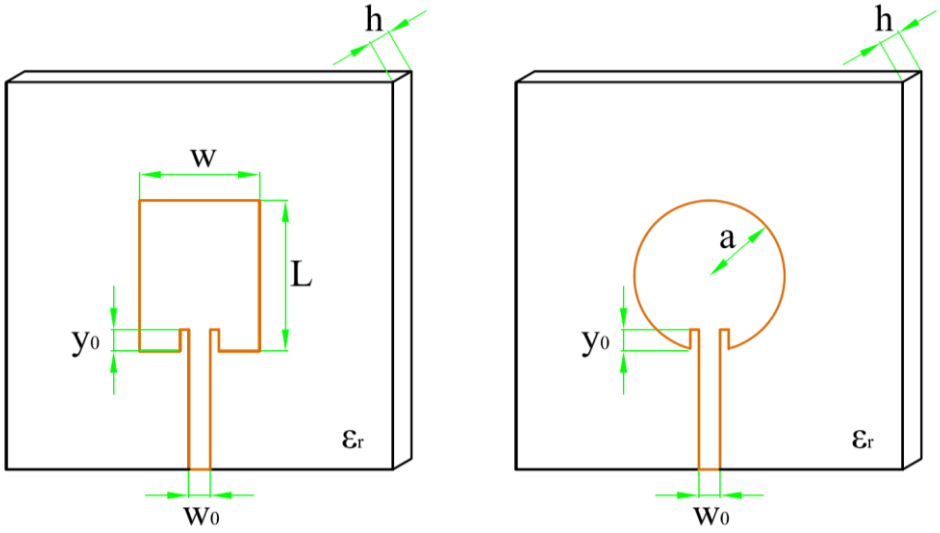

Figure 4.17 Feeding microstrip patch antennas directly with microstrip line (Balanis, 2005).

Another method is to connect the microstrip line to the edge of the antenna. In this case, a quarter-wavelength transformer must be placed between the microstrip line and the antenna for impedance matching (Figure 4.18) (Huang and Boyle, 2008; Balanis, 2005; Volakis, 2007).

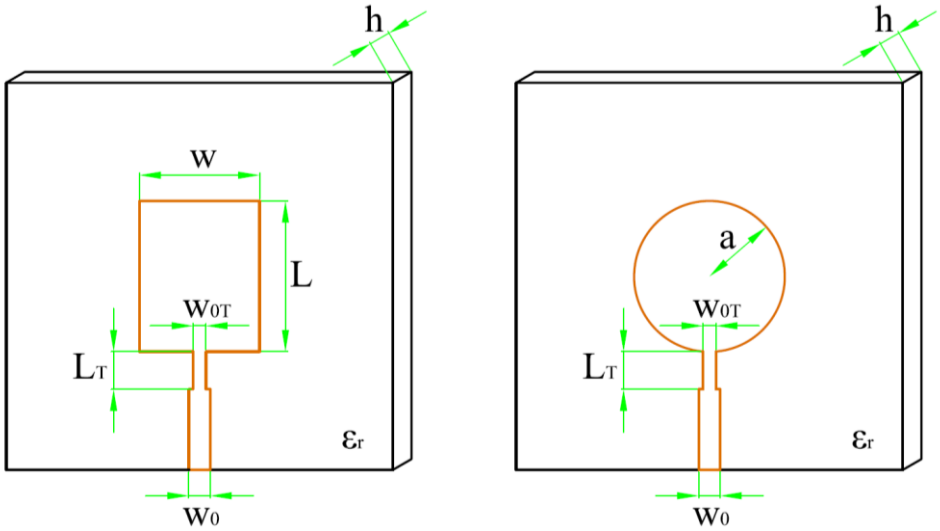

Figure 4.18 Feeding microstrip patch antennas with microstrip line using a quarter-wavelength transformer (Balanis, 2005).

For both methods the width of a $50\,\Omega$ microstrip line should be calculated. In the later, the width and length of the transformer should also be calculated.

The characteristic impedance of a quarter-wavelength transformer is (Huang and Boyle, 2008):

$$Z_T = \sqrt{Z_C Z_L} \tag{4.67}$$

where

Z_C is the impedance of microstrip line;

and

Z_L is the impedance of patch edge.

The characteristic impedance of a microstrip line is (Balanis, 2005):

$$Z_C = \begin{cases} \dfrac{60}{\sqrt{\varepsilon_{reff}}} \ln\left[\dfrac{8h}{w_0} + \dfrac{w_0}{4h}\right] & \dfrac{w_0}{h} \le 1 \\ \dfrac{120\pi}{\sqrt{\varepsilon_{reff}}\left[\dfrac{w_0}{h} + 1.393 + 0.667\ln(\dfrac{w_0}{h} + 1.444)\right]} & \dfrac{w_0}{h} > 1 \end{cases} \tag{4.68}$$

where

w_0 is the width of microstrip line;

h is the thickness of the substrate;

and

ε_{reff} is the effective permittivity of the substrate, which can be calculated using (if w_0 is available) (Balanis, 2005):

$$\varepsilon_{reff} = \frac{\varepsilon_r + 1}{2} + \frac{\varepsilon_r - 1}{2}\left[1 + 12\frac{h}{w_0}\right]^{-1/2} \tag{4.69}$$

or using the following equation (if w_0 is not available) (Volakis, 2007), to be used as the first input for an iterative design:

$$\varepsilon_{reff} \approx \frac{\varepsilon_r + 1}{2} \tag{4.70}$$

Finally, the length of the transformer can be calculated using (Volakis, 2007):

$$L_T = \frac{\lambda}{4} = \frac{\lambda_0}{4\sqrt{\varepsilon_{reff}}} \tag{4.71}$$

A program has been written in MATLAB™ to calculate the width of a $50\,\Omega$ microstrip line and dimensions of a quarter-wavelength transformer (Appendix A). The program uses the substrate permittivity to calculate the first order approximation of the effective permittivity using 4.70. It uses the effective permittivity, thickness of the substrate and first order approximation of microstrip line width (thickness of the substrate) to calculate the width of the microstrip line and effective permittivity using 4.68 and 4.69. The length of the transformer can now be calculated using 4.71 by having the operating frequency. Because the microstrip patch antenna is already designed, its impedance is known. Therefore, using 4.67 the impedance of the transformer is calculated. Then using equations 4.68 and 4.69, and the same iterative procedure, the width of the transformer is calculated.

4.4 Conclusion

Theoretical study of a circular microstrip patch antenna frequency equations show that there is a linear relationship between normalised shift in the resonant frequency of the antenna and the applied strain. This relationship can be used to measure strain using this type of antenna. Further investigations on strain measurement capability of this antenna and experimental validations are discussed in the following chapters.

In addition, other electromagnetic configurations with potential strain measurement capability (RMPA, DRAs and SRRs) are discussed and the relationship between strain and their resonant frequency is studied analytically using MATLAB™ software. As the focus of this research is on the circular microstrip patch antenna because of its physical and electromagnetic characteristics, and ease of fabrication, other configurations are compared to it. Each electromagnetic configuration has its own advantages and disadvantages; however, further investigations are required to understand their strain measurement quality.

CHAPTER 5

Finite Element Analysis

5.1 Introduction

Theoretical study of the resonant frequency of a circular microstrip patch antenna along with the analytical calculations using MATLAB™ software show that there is a linear relationship between strain and frequency shift of the antenna. Before investigating this relationship using experimental tests, finite element analysis (FEA) is used to validate the strain measurement capability of this type of antenna. Also, to improve the sensitivity and directionality of the antenna sensor, new antennas are designed using FEA packages and their strain measurement capability is studied. The entire procedure of antenna sensor design and improvement is a combination of analytical studies, FEA and experimental tests as illustrated in Figure 5.1.

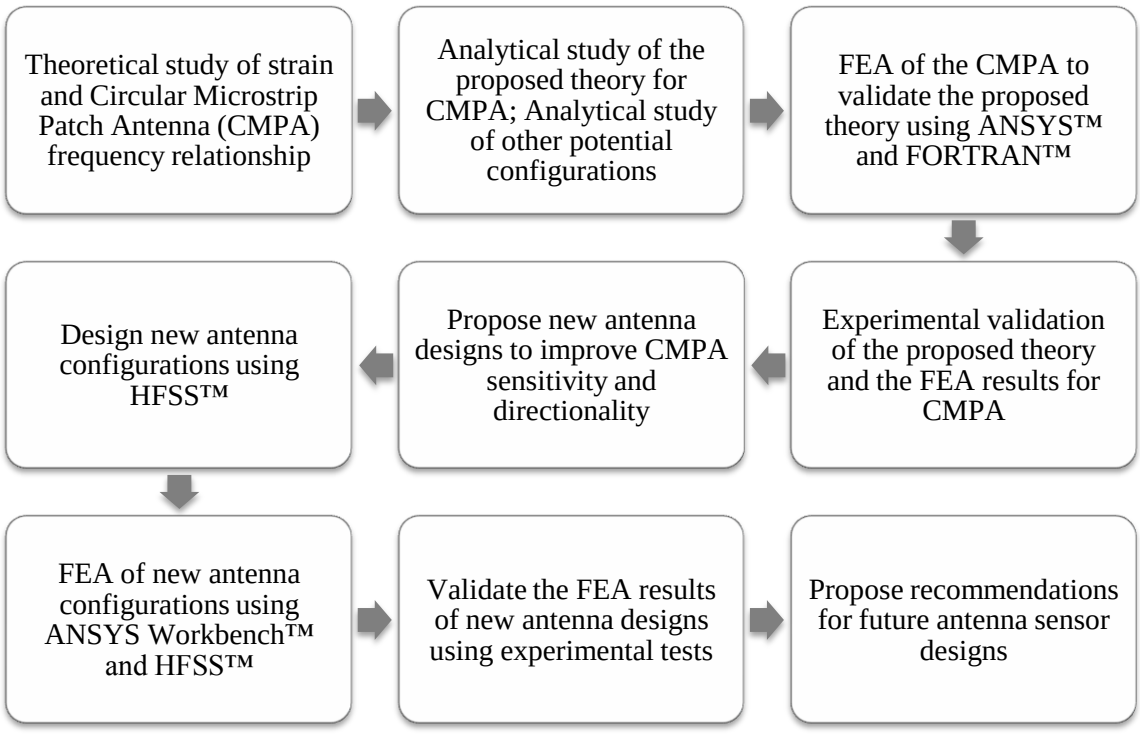

Figure 5.1 Schematic of design and modification process for micrsotrip patch antenna sensors.

In this chapter, the FEA software packages are introduced and two different FEA methods are discussed in detail. Also the design considerations for new antenna sensor configurations are described.

5.2 Background

5.2.1 ANSYS™

Founded in 1970, ANSYS™ is a finite element analysis engineering simulation software with several features to predict how product designs will operate and how manufacturing processes will behave in real-world environments. ANSYS™ is a unified and customizable simulation platform that allows users to efficiently perform complex simulations involving the interaction of multiple physics (ANSYS, 2011a).

5.2.1.1 Mechanical APDL™

APDL™ stands for ANSYS Parametric Design Language™, a scripting language that can be used to automate common tasks or to build a parametric model. All ANSYS™ commands can be used as part of the scripting language; however, the APDL™ commands include a wide range of other features such as repeating a command, macros, if-then-else branching, do-loops, and scalar, vector and matrix operations (ANSYS® Academic Research, 2010a).

APDL™ is the foundation for sophisticated ANSYS™ features such as design optimization and adaptive meshing. Some of the advantages of using APDL™ are provided below (ANSYS® Academic Research, 2010a):

- Ability to add frequently used ANSYS™ functions or macros to the ANSYS™ toolbar by defining abbreviations.
- Using parameters (variables); ANSYS™ has two types of parameters: scalar and array.
- Using APDL™ Math for matrix manipulations.
- Creating macros to record frequently used sequences of ANSYS™ commands.
- Interfacing with the GUI (Graphical User Interface).
- Encrypting macros.

5.2.1.2 Workbench™

ANSYS Workbench™ has the power of both core product solvers and project management tools (necessary to manage the project workflow). In ANSYS Workbench™, analyses are defined as systems, which can be combined together to form a project. The project is a schematic workflow that controls the correlations between different systems. Using the schematic, both applications that are native to ANSYS Workbench™ (Project Schematic, Engineering Data, and Design Exploration) and applications that are data-integrated with ANSYS Workbench™ (Mechanical APDL™, ANSYS FLUENT™, ANSYS CFX™, the Mechanical Application) can be connected together (ANSYS® Academic Research, 2010b).

Projects in ANSYS Workbench™ are built by adding and connecting systems. Each system is displayed in the Project Schematic as a block of cells. You complete your analyses by working through each cell in order. In general, data flows from the top to bottom within systems and from left to right between systems. Output data from upstream cells is provided as input data to downstream cells. For example, the geometry from the Geometry cell in one system can be the input for the Mesh cell in another system or the Solution cell from a Fluid Flow system can provide input for the Setup cell of a Static Structural system (ANSYS® Academic Research, 2010b).

5.2.2 HFSS™

HFSS™ is an industry-standard simulation tool for 3D full-wave electromagnetic field simulation which can be used for the design of high-frequency electromagnetic devises such as antennas. HFSS™ has multiple solver technologies based on the proven finite element method (ANSYS, 2011b).

HFSS™ can be used to extract scattering parameters (S_{11}), visualize 3D electromagnetic fields (near- and far-field) and generate Full-Wave SPICE™ models that link to circuit simulations. Also, it can be used in signal integrity engineering to evaluate signal quality, including transmission path losses, reflection loss due to impedance mismatches, parasitic coupling and radiation (ANSYS, 2011c).

5.2.3 High-Frequency (HF) Electromagnetic Analysis

High-frequency electromagnetic analysis calculates the propagation properties of electromagnetic fields in a given structure (ANSYS® Academic Research, 2010c). Such an analysis is usually used for one of the following (ANSYS® Academic Research, 2010c):

- Power flow carried by electromagnetic waves
- Wave scattering properties such as transmission, reflection and diffraction
- Frequency dependent parameters
- Power loss due to dielectric loss or finite conductivity

There are various methods available in computational electromagnetics (CEM) to simulate the antenna structures. A brief description of each method is provided below (they are categorised in two major groups) (Volakis, 2007; Jin and Riley, 2009):

- TIME-DOMAIN METHODS
  - Finite Difference-Time Domain (FD-TD) Method:

    With this method differential operators are approximated using difference operators resulting in both the electric and magnetic field as a function of time.
  - Time Domain-Integral Equation (TD-IE) Method:

    The time domain-integral equation method solves integral equations directly in the time-domain.
  - Time Domain-Finite Element (TD-FE) Method:

    This method solves the partial differential equations using a finite element procedure rather than finite differences. The field quantities are functions of both time and space.

- FREQUENCY-DOMAIN METHODS
  - Method of Moments (MoM):

    Integral equations formulated and solved in the frequency-domain, are referred to as the Method of Moments (MoM).
  - Finite Element (FE) Method:

    The finite element (FE) method provides one of the most powerful formulations for antenna modelling provided that the antenna has a dielectric load. The finite element method is an approach for solving Maxwell's equation by solving the vector wave equation. Most implementations of the finite element method for

electromagnetics primarily differ in the elements used to expand the unknown field (and usually the testing functions as well since these are similar) and the method to enforce the boundary conditions. The most popular elements for solution of the finite element equations are the brick, right prism, and tetrahedron (Figure 5.2).

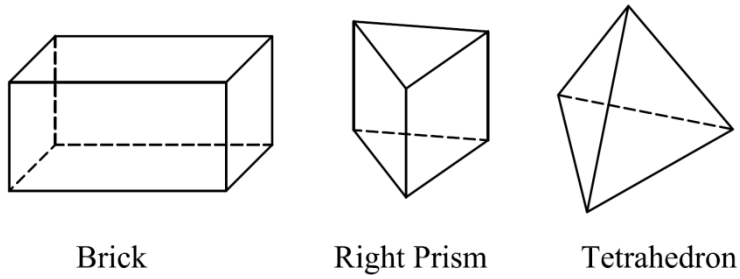

Figure 5.2 Typical finite element shapes for CEM (Volakis, 2007).

COMMERCIAL CODES

A list of the most popular commercial CEM codes is provided below (Volakis, 2007):

- WWW.ANSOFT.COM: The Ansoft™ Corporation (part of ANSYS Corporation™) offers a variety of CEM solutions for antenna design, electromagnetic compatibility, and other applications. The computer codes offered by Ansoft™ utilize the finite element method, the method of moments, and circuit simulators. These computer programs are some of the most powerful in the industry and are widely used.
- WWW.CST.COM: Computer Simulation Technology™ offers widely used CEM tools based on the finite integration technique (FIT) and the method of moments. Both time-domain and frequency-domain solvers are available.
- WWW.REMCOM.COM: Remcom™ offers a finite difference-time domain method computer program that can be used for antenna design, scattering analysis, and specific absorption rate (SAR) calculations.
- WWW.SONNETUSA.COM: Sonnet Software™ offers a suite of full-wave electromagnetic design tools based on a frequency-domain method of moments for planar geometries.
- WWW.WIPL-D.COM: WIPL-D™ is a powerful antenna design program capable of modelling antennas (and other structures) comprised of both metal and dielectric materials.

- WWW.ANSYS.COM: ANSYS Multiphysics™ provide low-frequency and high-frequency electromagnetic simulation capabilities. This software is based on the finite element method and can be used for coupled field analysis where two or more physics are available.

5.3 FEA Method 1 (ANSYS APDL™-FORTRAN™)

Finite Element Analysis (FEA) reduces costs of experiments by simulating the performance of the antenna under experimental test conditions and helps predict the actual results. FEA can also be used in the future to further optimise the antenna sensor performance. From various FEA packages available, ANSYS Multiphysics™ was chosen because of its ability to perform both structural and electromagnetic simulations. However, it is not possible to perform both analyses at the same time or even connect them to each other using basic tools in the software for high frequency electromagnetic analysis (1 GHz and above). In order to perform simultaneous analyses, a program using the ANSYS Parametric Design Language™ (APDL) from ANSYS™, and FORTRAN™ is written; thus, enabling the coupling of structural and high frequency electromagnetic analyses.

The detail of the experimental setup which is modelled in this section is provided in chapter 6. The antenna sensor modelled using this FEA method is a circular microstrip patch antenna which is designed in chapter 4, section 4.3.2. The antenna is designed to work in 1.5 GHz and the substrate material properties are provided in Table 4.4. The material used in FEA for the test plate that the antenna is attached to is aluminium.

The antenna structure and the plate behind it are modelled using SOLID186 element to simulate bending. SOLID186 element was chosen because it has the same shape topology as HF120 element and it could be used for all types of structural analysis, required for future investigations.

SOLID186 is a higher order 3D 20-node solid element that exhibits quadratic displacement behaviour (Figure 5.3). This element is defined by 20 nodes having three degrees of freedom per node (translations in the nodal x, y, and z directions). This element supports plasticity, hyperelasticity, creep, stress stiffening, large deflection, and large strain capabilities. It also has mixed formulation capability for simulating deformations of nearly incompressible elastoplastic materials, and fully incompressible hyperelastic materials (ANSYS® Academic Research, 2010d).

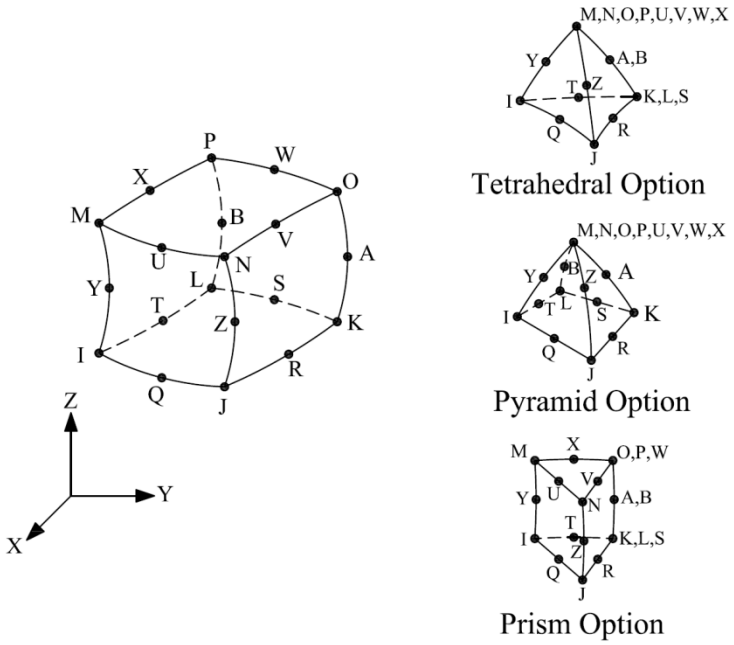

Figure 5.3 SOLID186 element geometry and coordinate system (ANSYS® Academic Research, 2010d).

HF120 (Figure 5.4) is a high-frequency brick element which models 3D electromagnetic fields and waves governed by the full set of Maxwell's equations in linear media. It is based on a full-wave formulation of Maxwell's equations in terms of the time-harmonic electric field. It is defined by up to 20 geometric nodes with AX DOF on element edges and faces and inside the volume. The physical meaning of the AX DOF in this element is a projection of the electric field on edges and faces (ANSYS® Academic Research, 2010e).

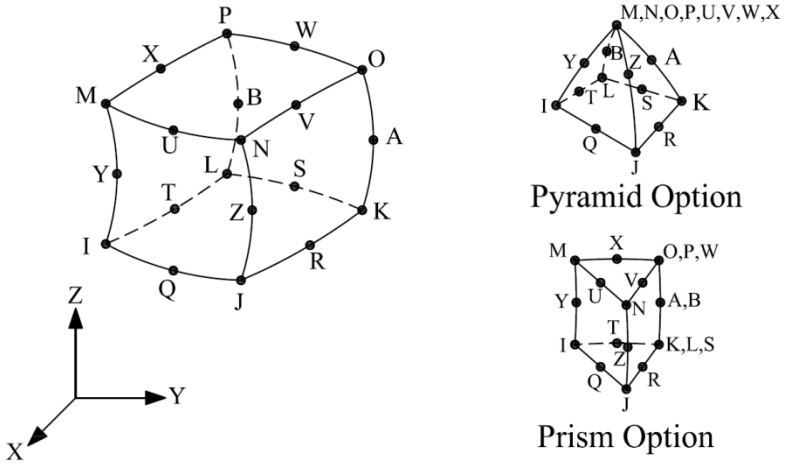

Figure 5.4 HF120 element geometry and coordinate system (ANSYS® Academic Research, 2010e).

After performing the structural analysis, SOLID186 elements were replaced with HF120 elements to perform scattering parameter analysis on the deformed shape of the antenna. HF120 element is chosen for high frequency electromagnetic analysis because of its

accuracy as well as its shape which is required for transferring nodes and elements from structural analysis. For this analysis, first order element option (one AX DOF on each edge) for HF120 elements is used. FORTRAN™ software is used to solve the formatting problem while transferring nodes from one analysis to another. The schematic of the procedure used in the program is illustrated in Figure 5.5. The ANSYS APDL™ and FORTRAN™ codes are provided in Appendix B and Appendix C, respectively. The results are discussed in chapter 7 along with the experimental results.

The frequency sweep was in the region of 1 GHz to 2 GHz with the step of 100 kHz. In order to reduce the simulation time and computational domain, half of the structure has been modelled due to mechanical and electromagnetic symmetry of the structure. A perfect magnetic conductor (PMC) condition must be used as the symmetry condition. Adaptive meshing could not be used with HF120 element; therefore, different configurations were checked to achieve the best mesh for both analyses. For patch, ground plane, and inner conductor of the coaxial feed a perfect electric conductor (PEC) condition is used.

A complete surface must cover the antenna structure to truncate the computational domain (ANSYS® Academic Research, 2010c). The following three methods are the most popular mesh termination conditions (Volakis, 2007; Jin and Riley, 2009):

- Absorbing boundary conditions (ABC):
  Widely used since it is particularly easy to implement; needs a larger computational domain; the distance from the radiating structures required is dependent on the particular ABC and on the problem.
- Perfectly matched layers (PML):
  A PML is an artificial material that is theoretically defined to create no reflections at the truncated boundaries of an electromagnetic simulation environment. It generally requires less stand-off distance from the radiating structure than ABCs. PML must be backed by PEC (Perfect Electric Conductor).
- A boundary integral (BI):
  A boundary integral (BI), is a global rather than local condition. It requires no stand-off distance; however, the resulting matrix is partially full due to the BI, and as a result, the demand for memory and solution time can be quite high.

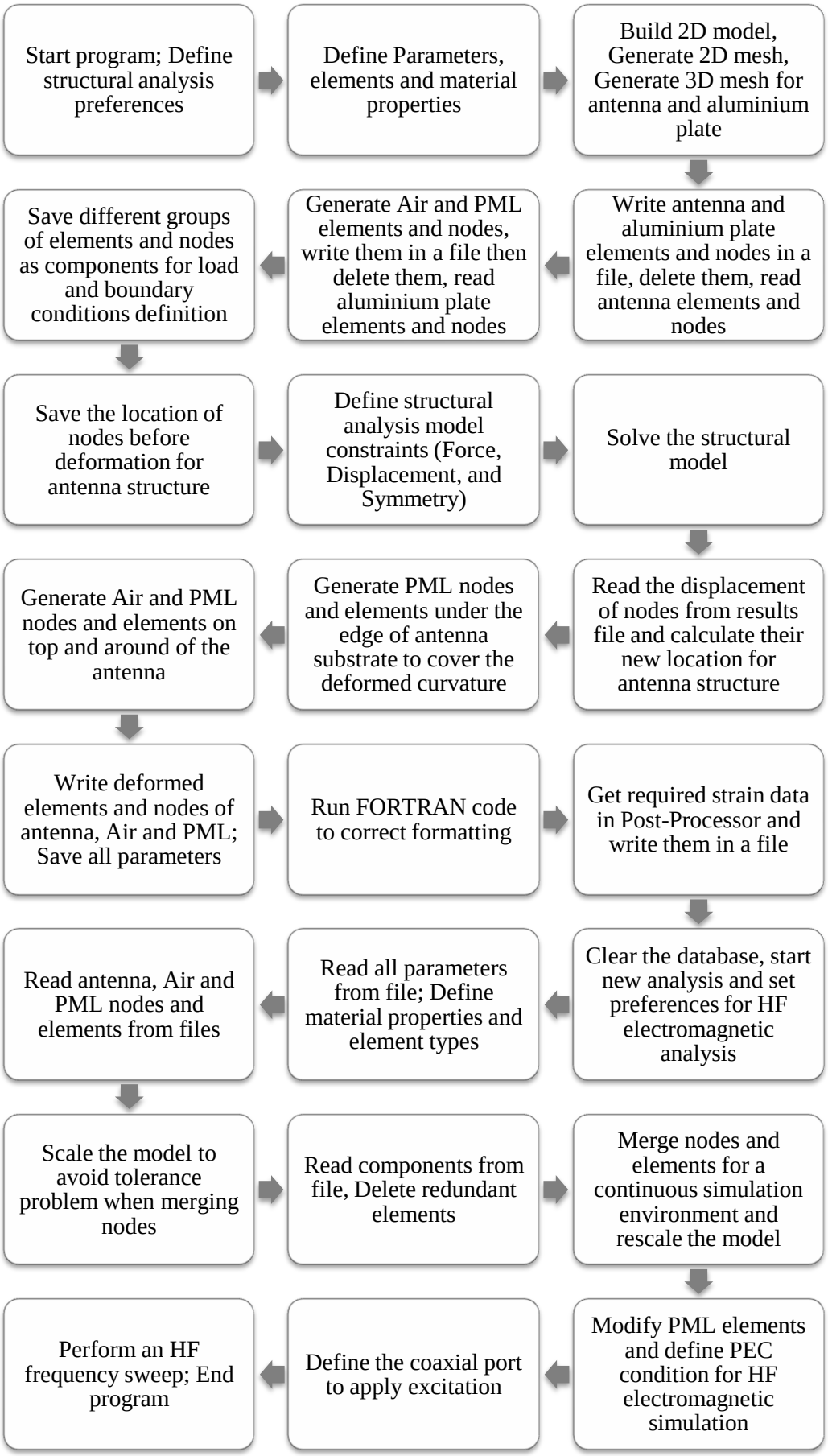

Figure 5.5 Schematic of the procedure used in FEA method 1.

In the electromagnetic analysis PML (Perfectly Matched Layer) elements were used to model the radiation boundary and minimize the computational domain (PML elements inner and outer boundaries must be aligned to axes of coordinate system). At the same time, a thin layer of air was generated above the antenna structure to work as buffer elements. PML and air elements were used only around and above the antenna while behind the ground plane was left empty. This is because the ground plane acts as the symmetry plane and there is no need to simulate that area. As a result, the coaxial feed used was simulated as an external port with the dimensions of a commercial SMA connector. For a coaxial port, the port region is the dielectric region between the inner and outer conductors (ANSYS® Academic Research, 2010c).

The assembly was subjected to a 3-point bend configuration similar to the physical tests. The maximum deformation at the centre of the plate was set to 10 mm with an increment of 0.5 mm while the strain and the scattering parameter (S_{11}) of the antenna were derived at each stage. Figure 5.6 shows the strain distribution in the assembly after 10 mm displacement in the centre of the aluminium plate. The corresponding contour of electric field at 1.5 GHz is depicted in Figure 5.7.

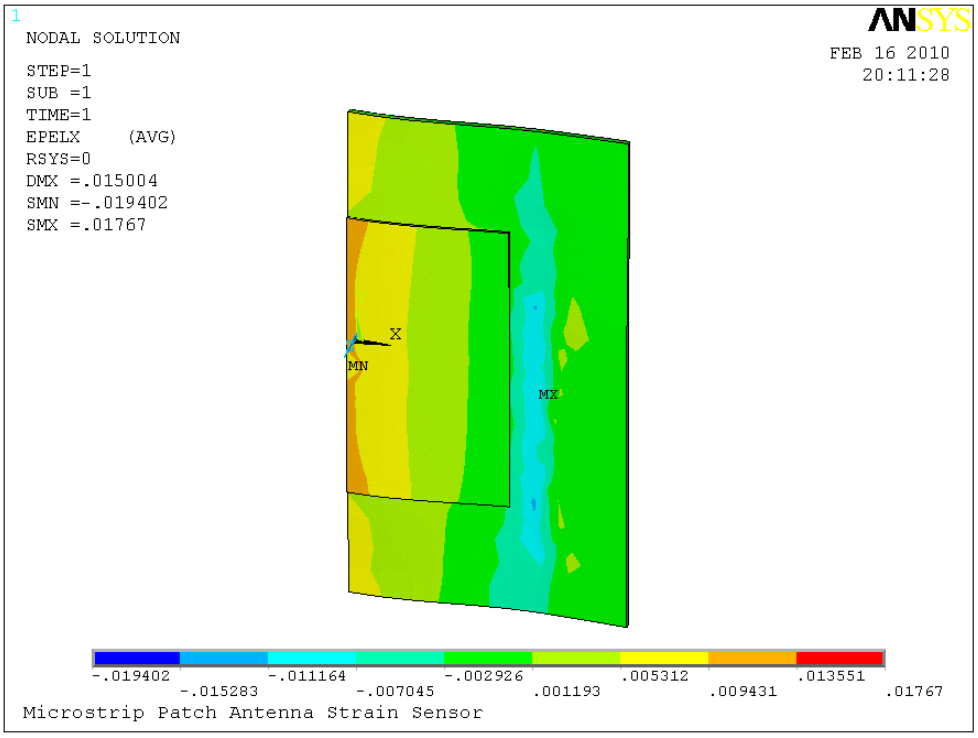

Figure 5.6 Contour of strain after 10mm displacement at the centre of aluminium plate at 0° orientation for circular microstrip patch antenna (half of the structure is modelled).

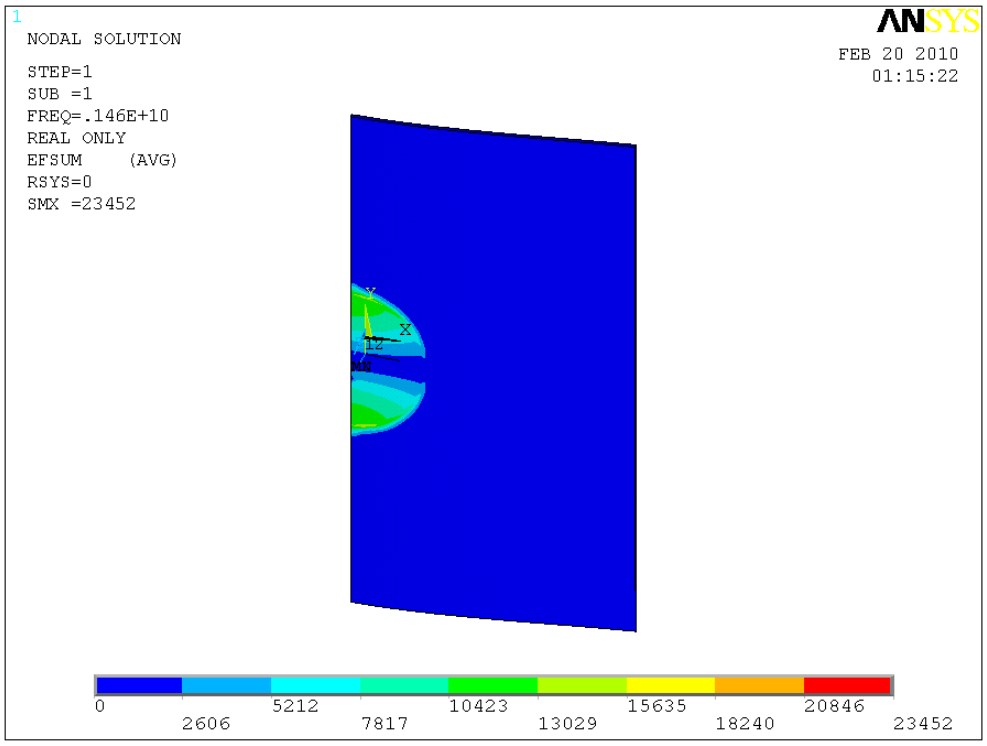

Figure 5.7 Contour of electric field magnitude after 10mm displacement at the centre of aluminium plate at 0° orientation for circular microstrip patch antenna (half of the structure is modelled).

5.4 New Antenna Designs (HFSS™)

The feasibility of using circular microstrip patch antenna as a strain sensor has been established in the previous section. In order to increase the sensitivity and improve the directionality of circular microstrip patch antennas, some modifications need to be applied to a simple circular configuration. Because the formulas available in antenna handbooks about antenna resonant frequencies and other antenna characteristics are limited to simple structures as discussed in the previous chapters, these new designs require advanced FEA software that could simulate the antenna behaviour. ANSYS Multiphysics™ adaptive meshing is not powerful enough to generate accurate results for more complicated shapes; therefore, more specialised software must be used. Here, the author used HFSS™ software because of its capabilities in high frequency electromagnetic analysis for antennas such as adaptive meshing and different types of frequency sweep. Therefore, the new antenna configurations are designed to work in desirable frequencies to achieve the predefined goals. The description of each design is provided in the following sections.

5.4.1 Slotted Circular Microstrip Patch Antenna

As it is described in chapter 3 section 3.4.1, one method to describe microstrip patch antenna performance is the surface current distribution on the metallic patch. Surface current distribution determines the electrical length of the microstrip patch antenna. As it is shown in Figure 5.8, introducing a rectangular slot in the metallic patch changes the surface current distribution by forcing the electrons to go around the slot which increases the electrical length of the patch. At the same time, some of the electromagnetic energy travels over the slot which causes a new radiation frequency. This radiation depends on the width and length of the slot, making the antenna to be more sensitive in one direction than the other. This is because the resonant frequency of the slot is more sensitive to its length. This feature can be used to detect the direction of the applied strain in addition to its presence by further developing this concept.

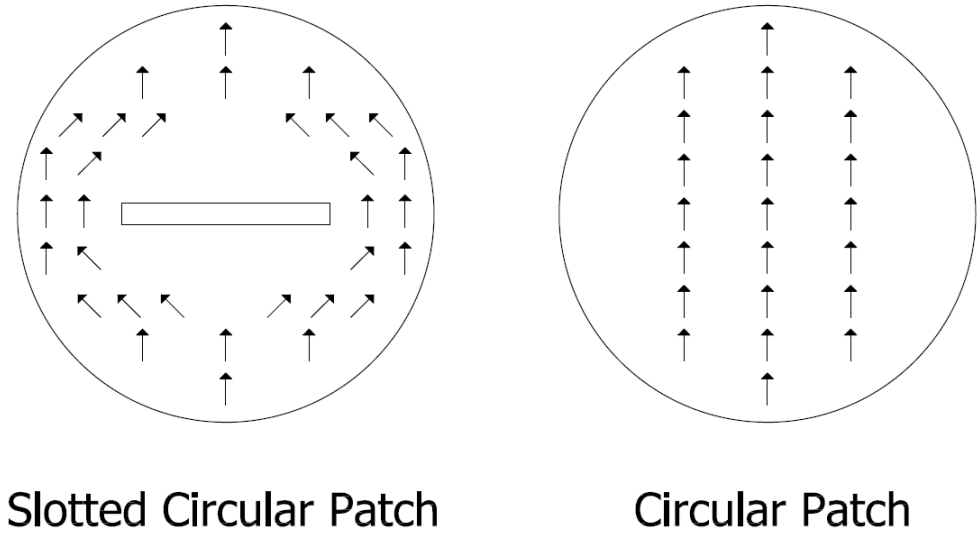

Figure 5.8 Surface current distribution for a circular patch and a slotted circular patch.

In order to design the antenna sensor with a slot in the middle of the circular patch the HFSS™ software is used. The optimisation feature of the software is used to find the best length and width of the slot; therefore, a slot with a very narrow bandwidth is designed. The location of the feed point is selected for the best impedance matching of the slot resonant frequency rather than the patch frequency. The final dimensions of the designed antenna along with the bending orientations are shown in Figure 5.9. The simulated resonant frequency of the antenna is illustrated in Figure 5.10.

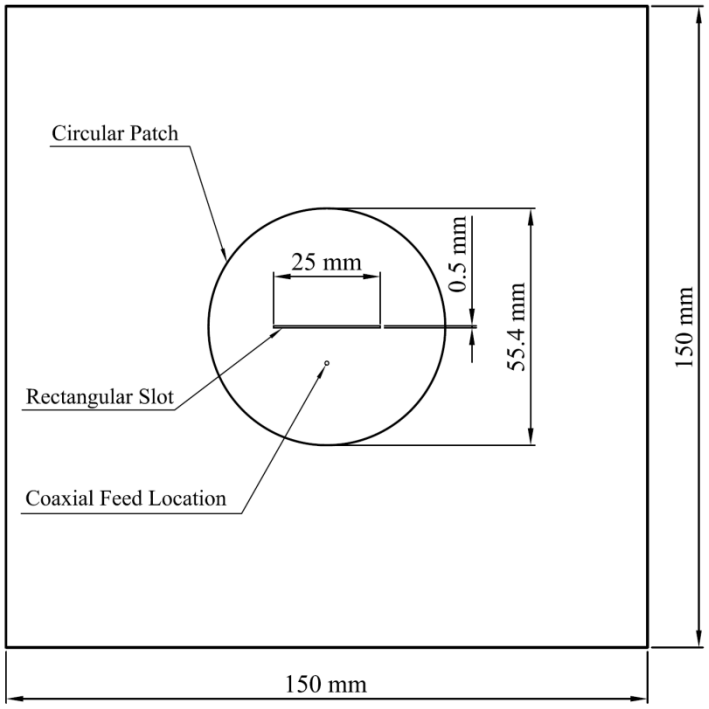

Figure 5.9 Dimensions of the slotted circular microstrip patch antenna.

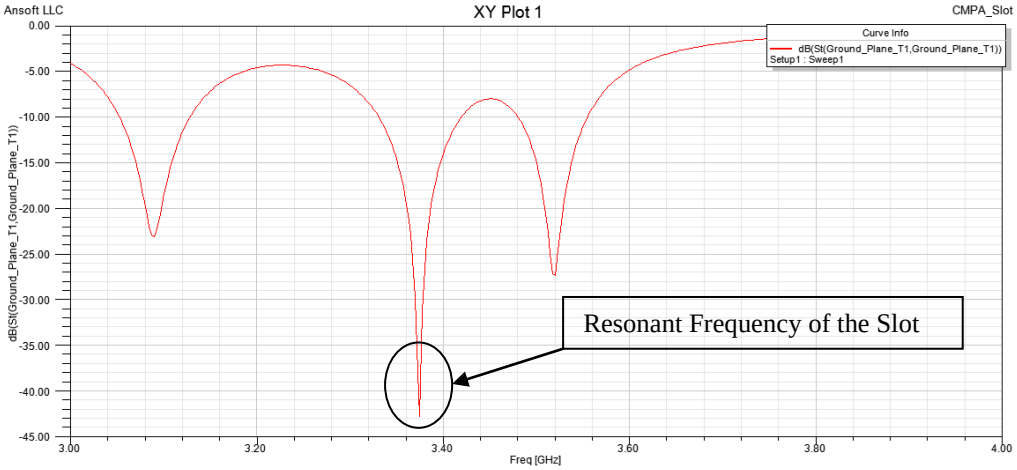

Figure 5.10 Simulated resonant frequency of the slotted circular microstrip patch antenna.

5.4.2 Meandered Circular Microstrip Patch Antenna

One of the methods for compact operation of microstrip antennas is to meander the radiating patch. This kind of patch-meandering technique is achieved mainly by loading several meandering slots at the non-radiating edges of a rectangular patch or at the boundary of a circular patch. The narrow slots increase the effective electrical length of the patch and therefore decrease its resonant frequency (Wong, 2002).

Figure 5.11 shows the measured resonant frequency of a short-circuited circular microstrip patch against the slot length (Wong, 2002). It is obvious that, with increasing slot length, the resonant frequency of the meandered patch decreases. This is because the electrical length of the patch increases when the slot length increases. Also, by increasing the slot length, the rate of change in frequency relative to the change in slots length increases. Likewise, an increase in the slot width results in an increase in the electrical length of the patch and therefore the resonant frequency decreases. Figure 5.12 shows the surface current distribution for a simple circular patch and a meandered circular patch.

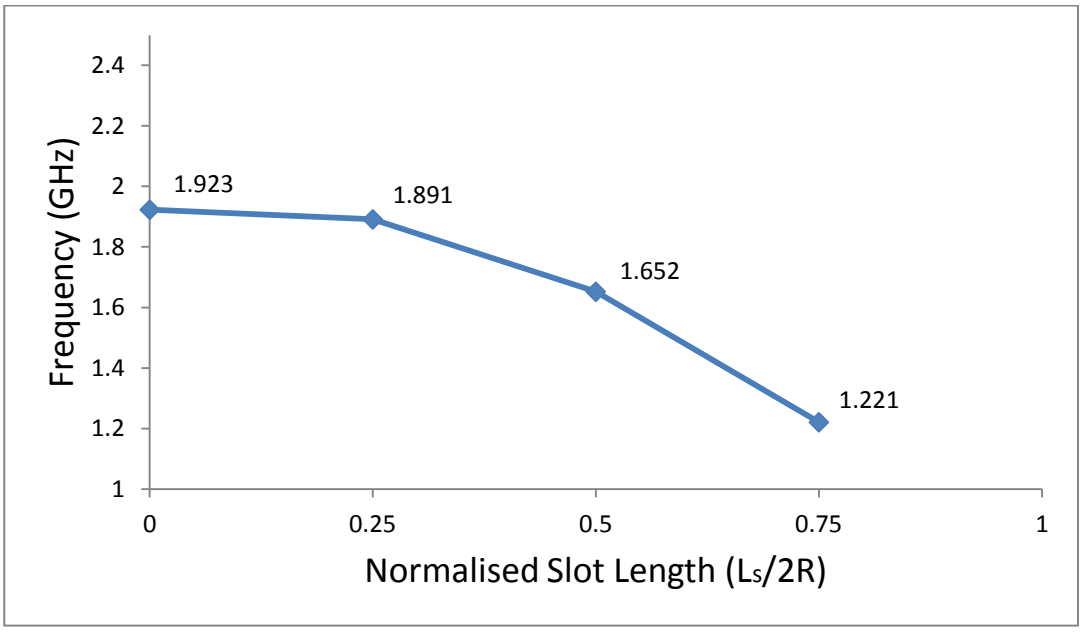

Figure 5.11 Measured resonant frequency of a short-circuited circular microstrip patch against the slot length (Wong, 2000).

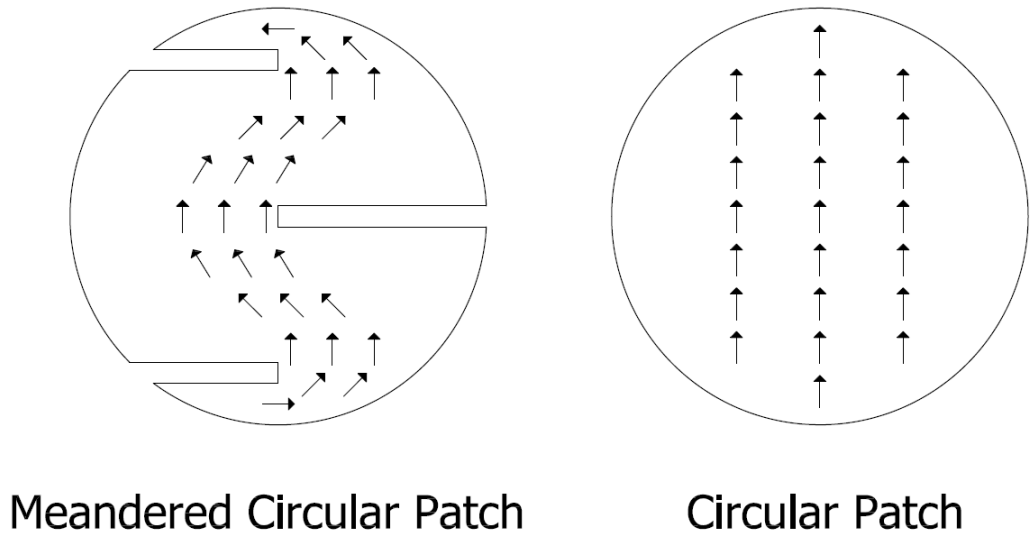

Figure 5.12 Surface current distribution for a circular patch and a meandered circular patch.

Therefore, by introducing narrow slots in a circular microstrip patch antenna two simultaneous results could be achieved. Firstly, a smaller microstrip patch antenna can be made to measure more localised strain while keeping the operating frequency of the patch low. Secondly, compared to a simple circular patch the shift in the resonant frequency can be increased. This is because by decreasing size of the patch, the resonant frequency increases and according to Equation (4.11), with the same amount of strain, the shift in the frequency should increase with the same rate. If the frequency of the normal circular patch increases from 1.5 GHz to 3.5 GHz then the amount of shift will increase from 100 KHz to 233 KHz (according to Equation (4.11)). However, for a simple patch, the size of the antenna sensor will reduce by the factor of 2.33 whereas the size of the meandered patch (for the 3.5GHz) would be five times smaller. This means more sensitivity for more localised strain.

As a consequence of the above discussion, a meandered circular microstrip patch antenna is designed using the HFSS™ software to work at 3.5 GHz. In order to increase the sensitivity of the patch, seven slots are introduced in the patch, which have the same length as the patch radius. The overall dimensions of this antenna sensor along with the bending orientations are illustrated in Figure 5.13. The thickness of the substrate is 0.2 mm and its dielectric constant is 4. The simulated and measured resonant frequencies of the antenna are illustrated in Figure 5.14.

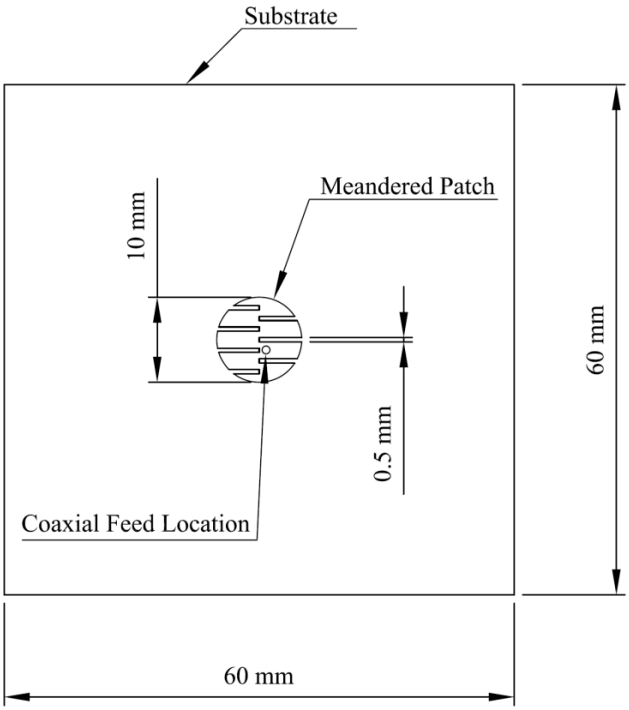

Figure 5.13 Dimensions of the meandered circular microstrip patch antenna.

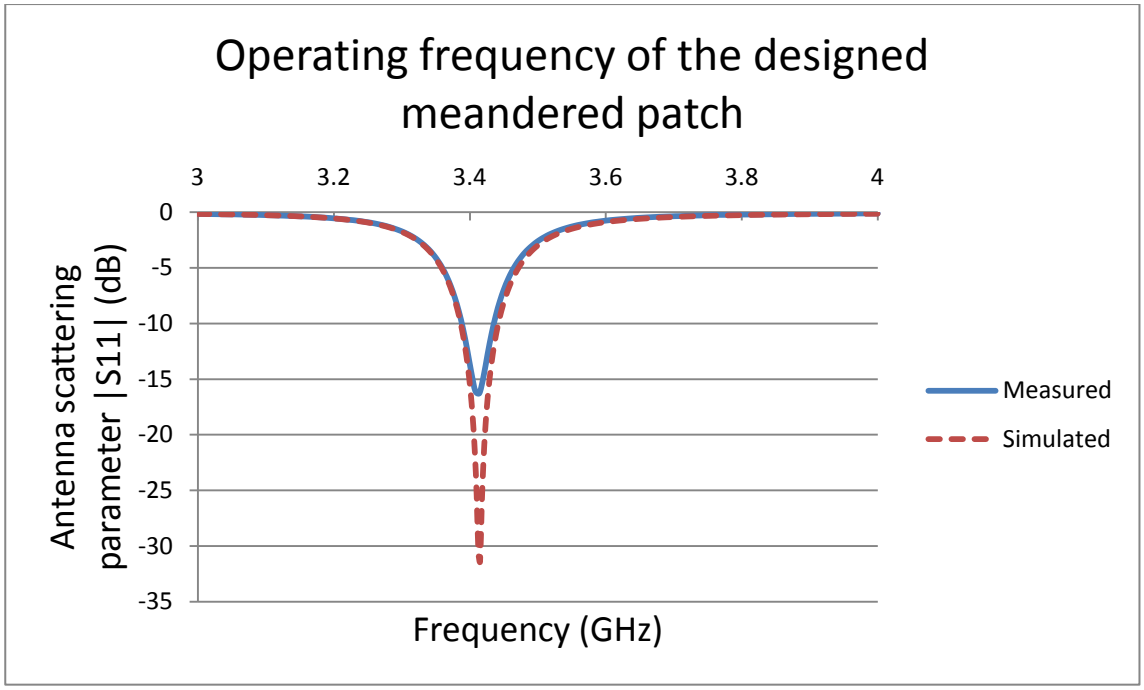

Figure 5.14 Measured and simulated resonant frequency of the meandered circular microstrip patch antenna.

5.5 STEMCOF Data Processing Protocol (ANSYS Workbench™-HFSS™)

The new proposed antenna designs for improving circular microstrip patch antenna sensor capabilities cannot be simulated with ANSYS Multiphysics™. Because the adaptive meshing capability in the HFSS™ software is a powerful tool that could be used in antenna design, the combination of ANSYS™ and HFSS™ is used to simulate the slotted and meandered circular microstrip patch antennas to investigate the relationship between the applied strain and the resonant frequency of each antenna. Therefore, a new method named Structural-Electromagnetic Coupled Field (STEMCOF) data processing protocol was introduced which is described in this subsection. In this method, ANSYS Workbench™ is used for static structural analysis because of its capability to connect different types of analysis to the ANSYS Finite Element Modeler™; whilst, HFSS™ software is used for high frequency electromagnetic analysis.

First, the antenna is simulated with the ANSYS™ software under 3-point bend loading, similar to that used in experimental tests. The antenna is attached to an aluminium plate for FEA and is bent up to 10 mm in 5 mm steps of displacement for the slotted patch and 1 mm of displacement for the meandered patch. After extracting strain in four locations according

to the location of strain gauges attached to test plates (same as circular patch shown in Figure 6.2) after each step of bending, the deformed shape of the antenna is transferred to ANSYS Finite Element Modeler™ to be saved as a Parasolid format. In order to do this, an APDL™ code (available in Appendix A) must be inserted between the static structural analysis and Finite Element Modeler™ to prepare the structure for deformed shape extraction. Also, external surfaces must be selected as "name selections" as well as "shared topology" option in Design Modeler™, prior to structural analysis. The schematic of the project in ANSYS Workbench™ is shown in Figure 5.15; whilst, the detailed instructions for static structural analysis and manual modifications in Finite Element Modeler™ are provided in Appendix D. Figures 5.16 and 5.17 depict the strain distribution in the antenna and aluminium plate after the 10 mm bend at 0° orientation for slotted and meandered antennas, respectively.

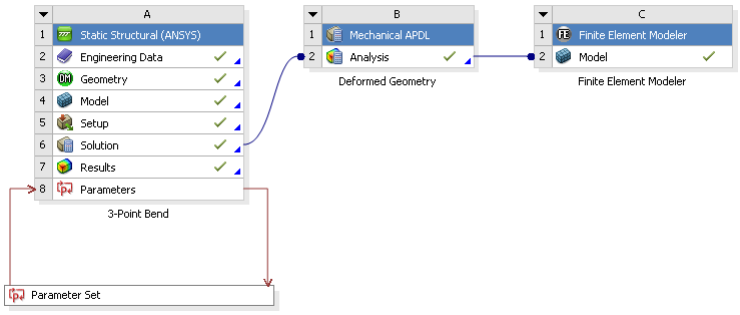

Figure 5.15 Schematic of the project in ANSYS Workbench™.

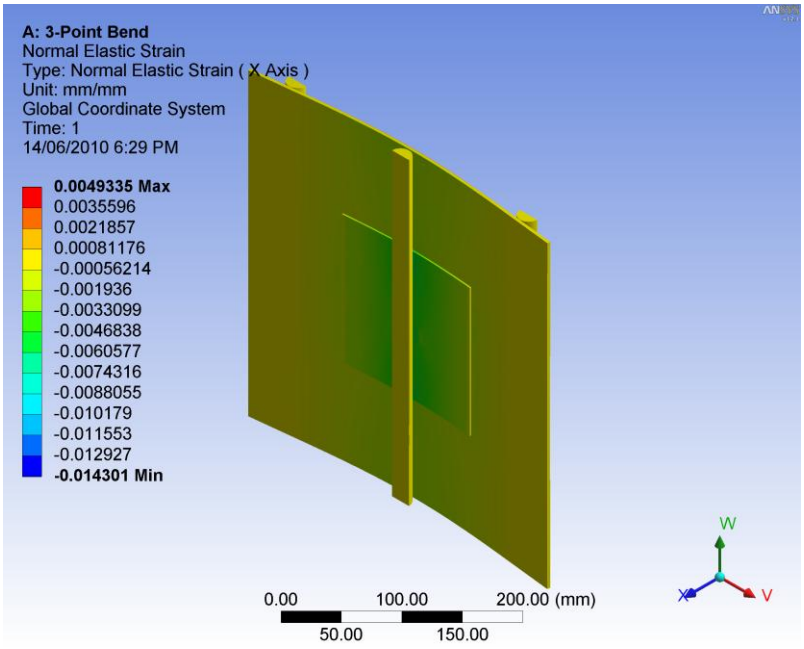

Figure 5.16 Contour of strain after 10mm displacement at the centre of aluminium plate at 0° orientation for slotted circular microstrip patch antenna.

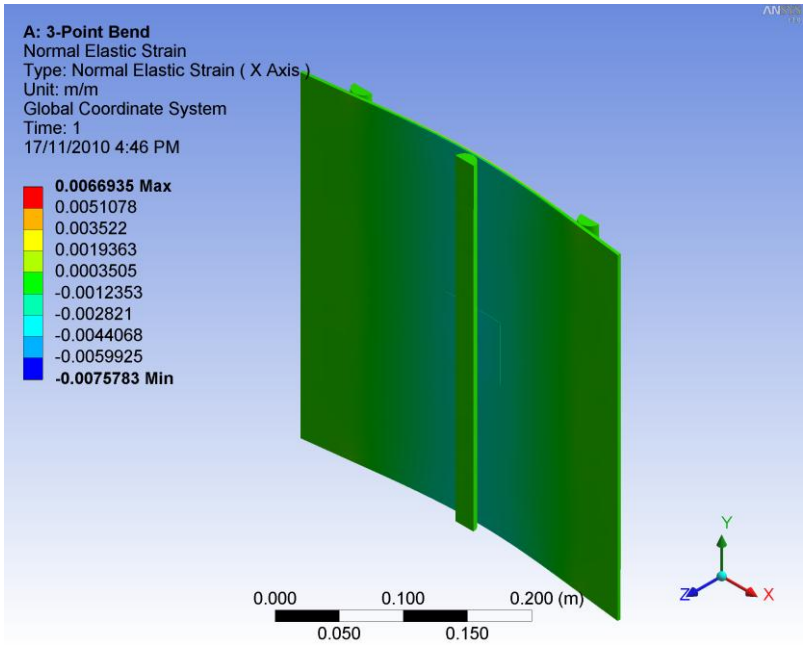

Figure 5.17 Contour of strain after 10mm displacement at the centre of aluminium plate at 0° orientation for meandered circular microstrip patch antenna.

Then the deformed shape of the antenna is imported into HFSS™ software, where additional air layers and PML elements are added to the model. Finally, the antenna was simulated in HFSS™ to obtain the resonant frequency of the antenna. In order to see the shift in the resonant frequency a very fine mesh and very strict settings should be used in HFSS™. The detailed instructions for simulations in HFSS™ to obtain accurate results are described in Appendix E. The schematic of the overall procedure used in this method is illustrated in Figure 5.18.

The corresponding contours of electric field at 3.5 GHz for slotted and meandered antennas (aluminium was used as the material for the plate at 0° orientation) are shown in Figures 5.19 and 5.20 (where air box and PML elements around the antenna are hidden for clarity), respectively.

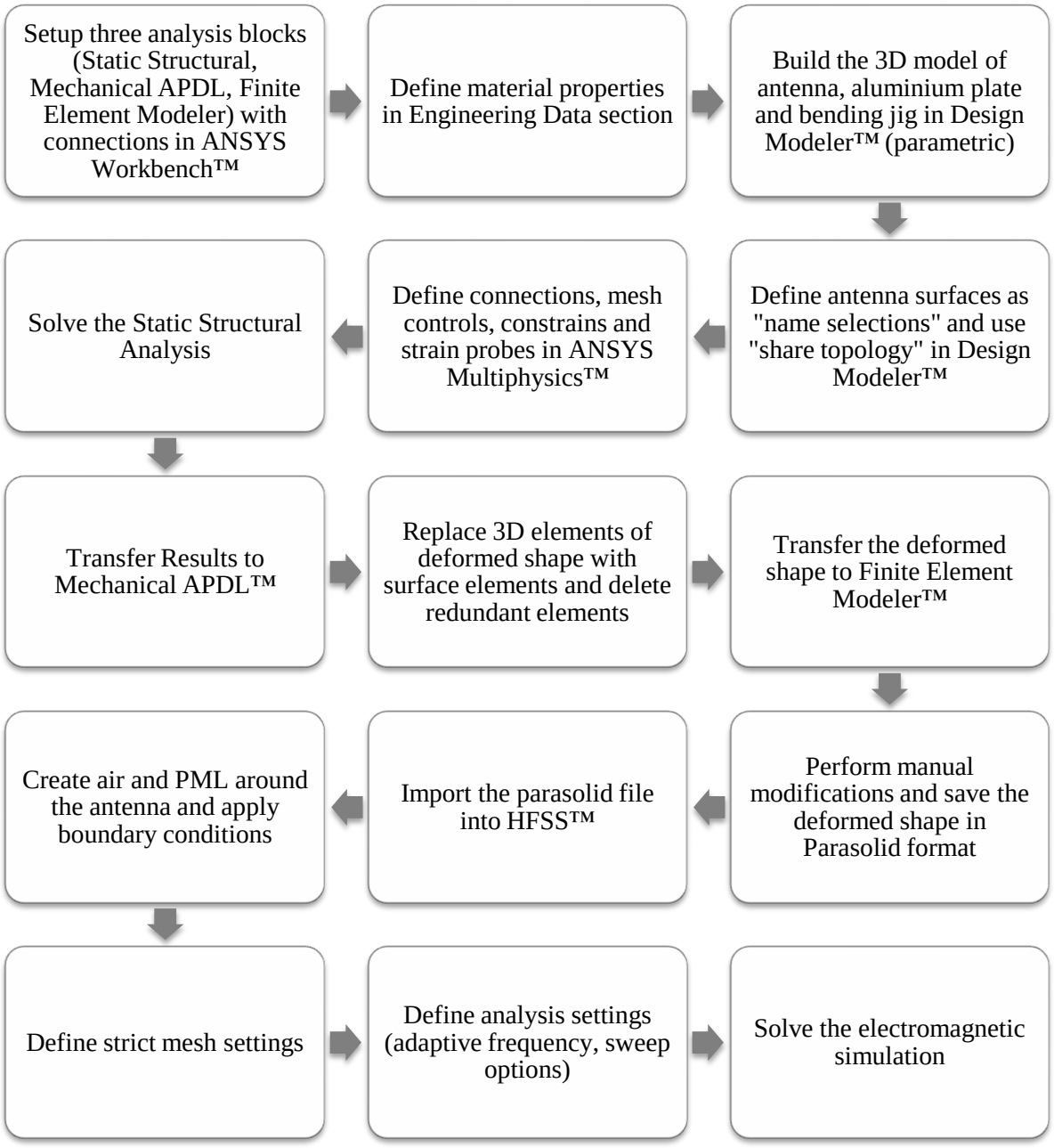

Figure 5.18 Schematic of the procedure used in STEMCOF Data Processing Protocol.

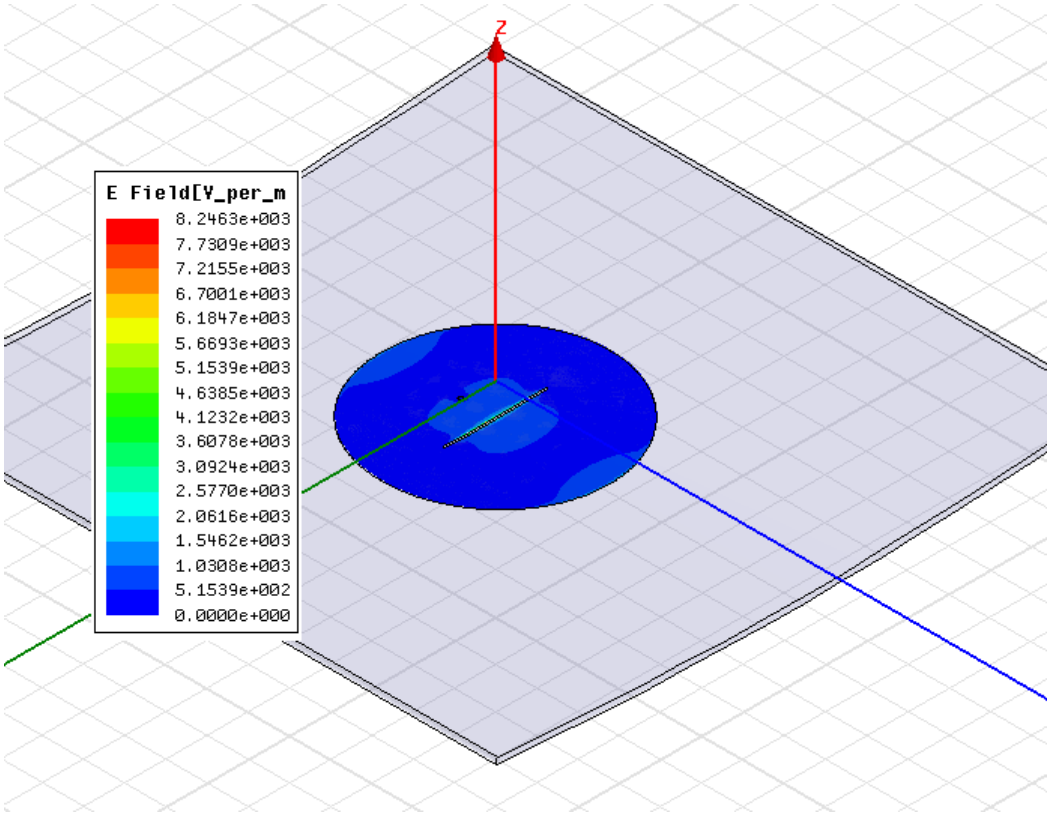

Figure 5.19 Contour of electric field magnitude after 10mm displacement at the centre of aluminium plate at 0° orientation for slotted circular microstrip patch antenna.

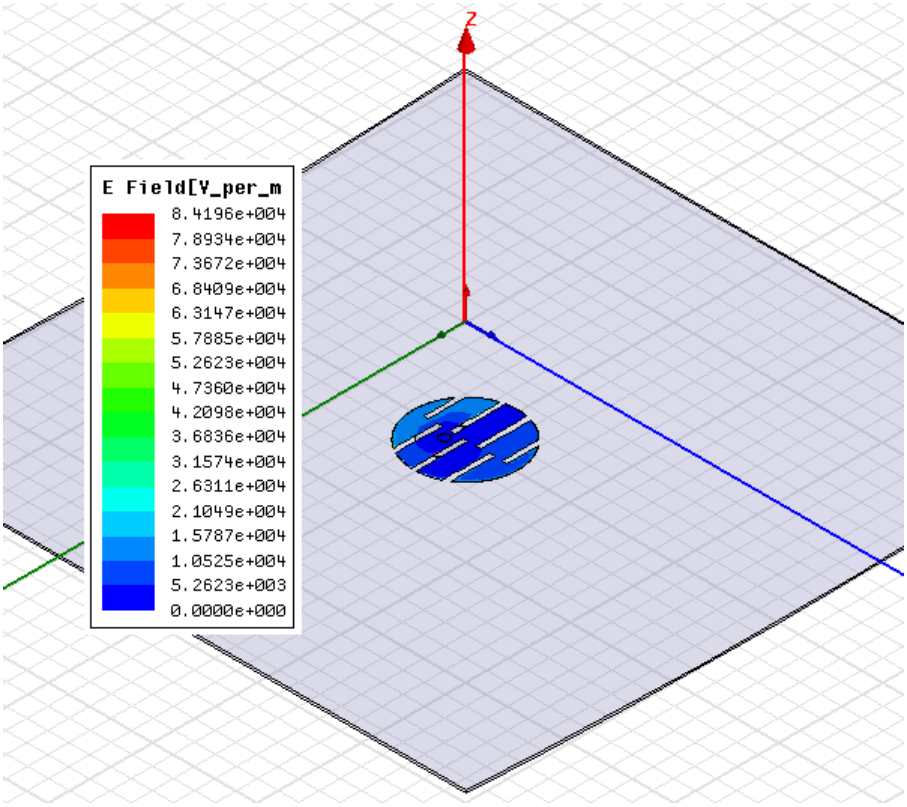

Figure 5.20 Contour of electric field magnitude after 10mm displacement at the centre of aluminium plate at 0° orientation for meandered circular microstrip patch antenna.

In order to connect the coaxial cable to the SMA connector at the back of the antenna, a hole is drilled in the back of the sample plates used for experimental tests. This hole is simulated in all the Analyses described in this chapter. In order to investigate the effect of hole in the performance of the meandered circular microstrip patch antenna, six samples with different hole's diameter are tested (see Chapter 6). These samples are simulated in ANSYS Workbench™ to study the difference in strain distribution in different samples. Figures 5.21 to 5.26 depict the strain distribution in the meandered antenna attached to an aluminium plate with a central hole with six different diameters (2.5 mm, 5 mm, 7.5 mm, 10 mm, 12.5 mm and 15 mm) after the 10 mm bend at 0° orientation.

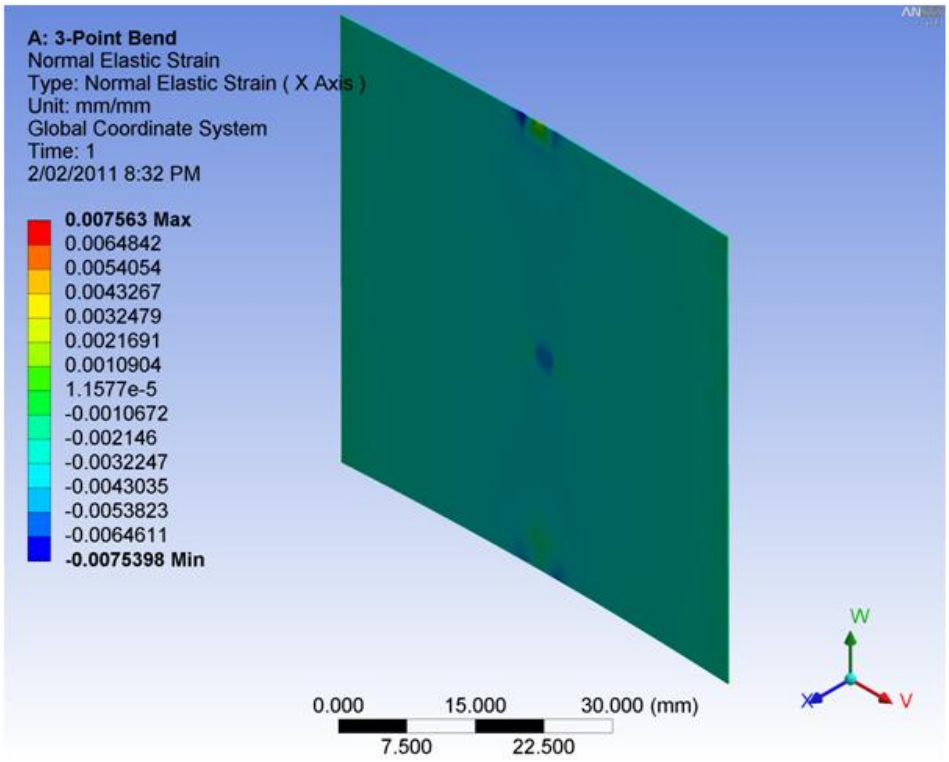

Figure 5.21 Contour of strain for meandered circular patch antenna after 10mm displacement at the centre of plate at 0° orientation, attached to an aluminium plate with the diameter of the central hole being 2.5 mm.

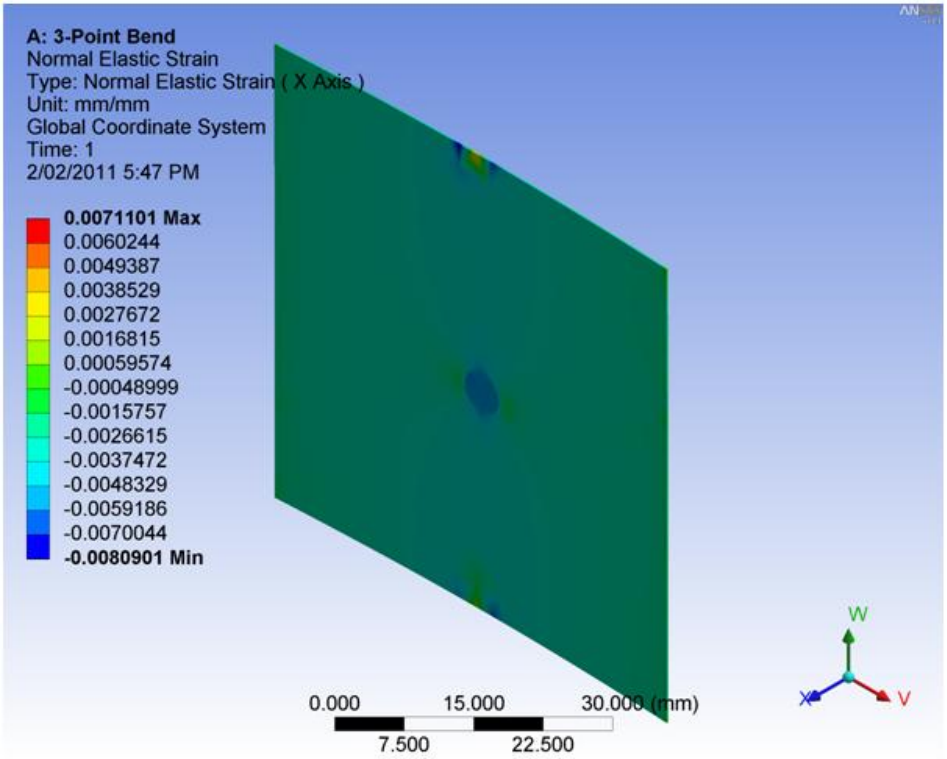

Figure 5.22 Contour of strain for meandered circular patch antenna after 10mm displacement at the centre of plate at 0° orientation, attached to an aluminium plate with the diameter of the central hole being 5 mm.

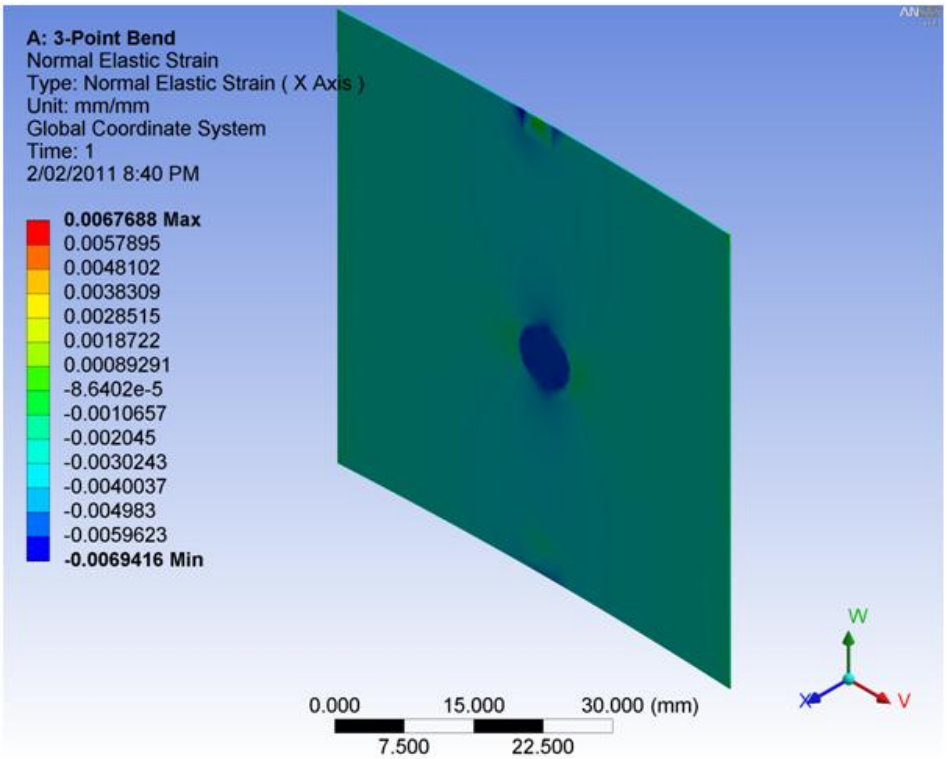

Figure 5.23 Contour of strain for meandered circular patch antenna after 10mm displacement at the centre of plate at 0° orientation, attached to an aluminium plate with the diameter of the central hole being 7.5 mm.

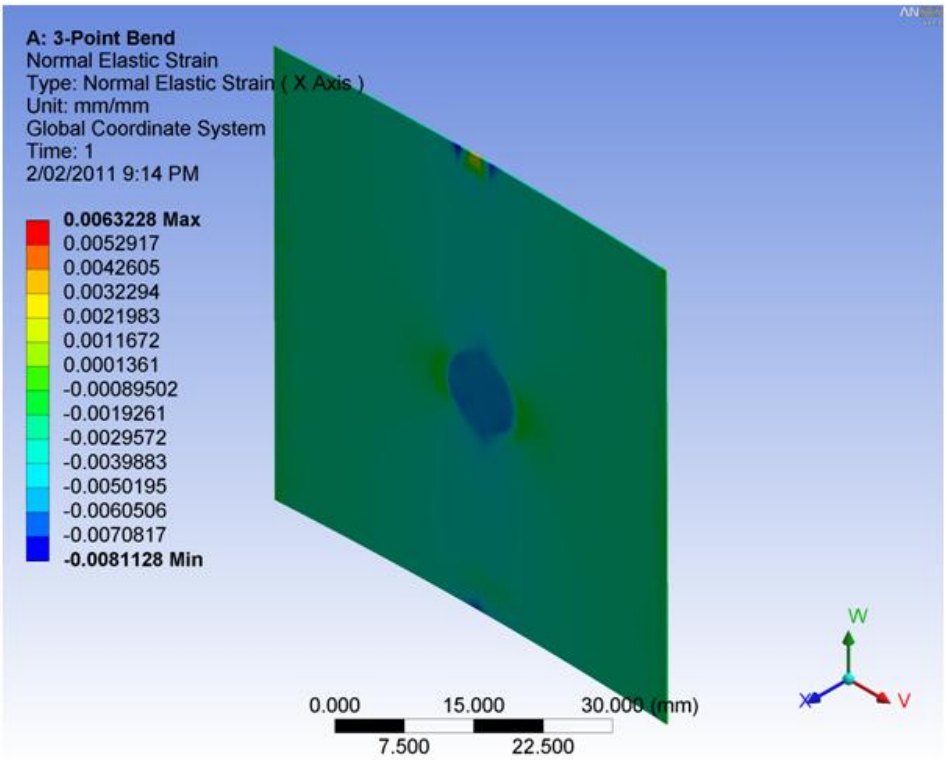

Figure 5.24 Contour of strain for meandered circular patch antenna after 10mm displacement at the centre of plate at 0° orientation, attached to an aluminium plate with the diameter of the central hole being 10 mm.

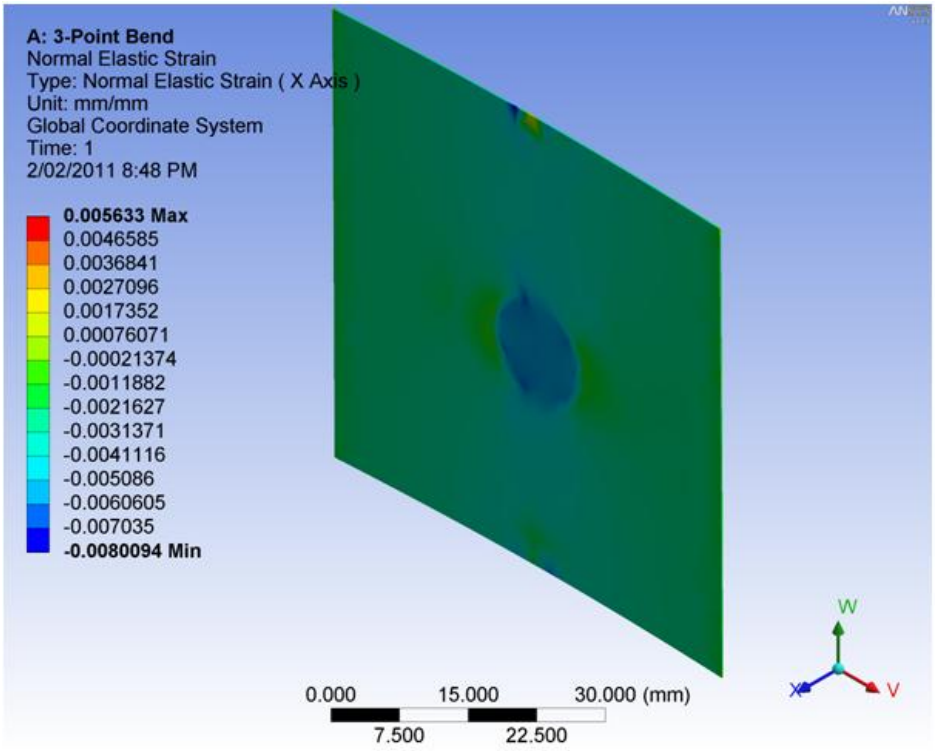

Figure 5.25 Contour of strain for meandered circular patch antenna after 10mm displacement at the centre of plate at 0° orientation, attached to an aluminium plate with the diameter of the central hole being 12.5 mm.

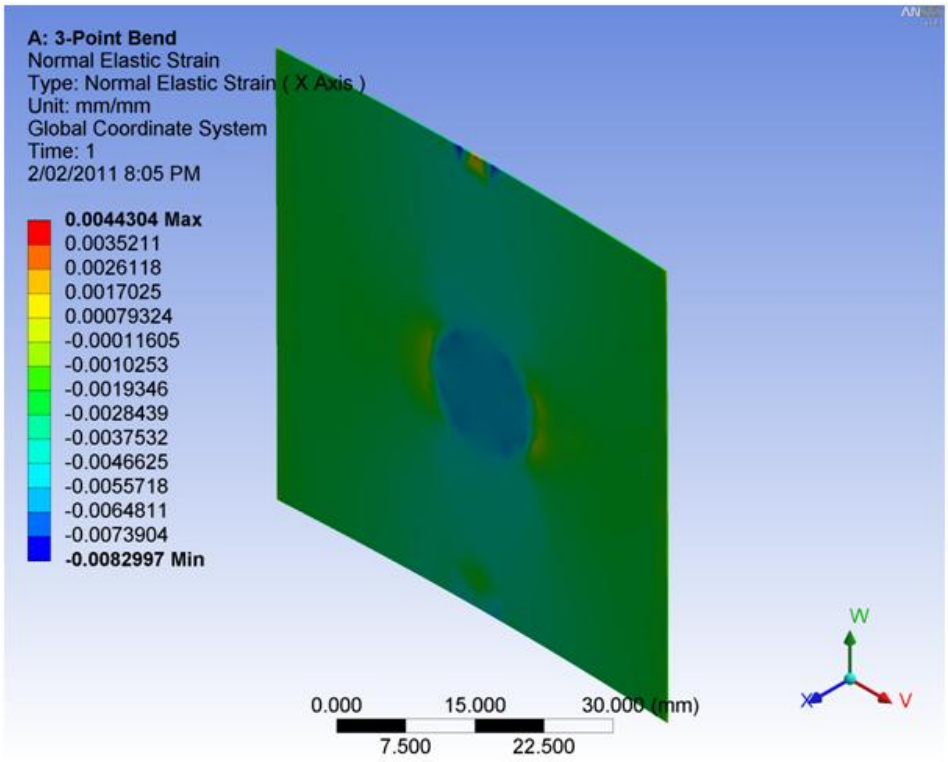

Figure 5.26 Contour of strain for meandered circular patch antenna after 10mm displacement at the centre of plate at 0° orientation, attached to an aluminium plate with the diameter of the central hole being 15 mm.

5.6 Conclusion

Two different data processing protocols used for evaluation and design of the antenna sensors have been described in this chapter. As a result of the second method (STEMCOF protocol), two new antenna sensors are designed for increased sensitivity and multidirectional behaviour. In order to evaluate the FEA results, experimental tests are required which are described in the next chapter. Therefore, the FEA results from this chapter, along with the experimental results from Chapter 6, are presented in Chapter 7.

CHAPTER 6

Experimental Details

6.1 Introduction

In order to validate theoretical results as well as FEA methods which are described in the last two chapters, experimental tests are performed for each antenna sensor configuration. The manufacturing process for antennas and test plates fabrication are explained in detail in the following sections. This is followed by description of the 3-point bend test setup which is also used for the FEA. The devices used for data acquisition include a vector network analyser and a strain indicator and recorder. The characteristics of these devices are provided at the end, followed by the data analysis technique.

6.2 Manufacturing of Test Samples

6.2.1 Antennas

In order to validate the FEA results, three circular microstrip patch antennas were designed and fabricated to work at 1.5 GHz. The antennas utilize a fibre glass (FR4) commercial substrate with the thickness of 1.5 mm, relative permittivity of 4.5, and loss tangent of 0.02. The antennas are probe-fed with a 50 ohm SMA coaxial probe. Two slotted circular microstrip patch antennas are manufactured using the same substrate material used for the circular microstrip patch antennas. The operating frequency of the circular patch is 1.5 GHz while the operating frequency of the slot in the slotted circular patch is 3.4 GHz.

The meandered circular microstrip patch antenna was designed and fabricated to work at 3.5 GHz using the same process as circular and slotted antennas (seven samples). The antenna is made of a fibre glass (Modified FR4) commercial substrate with the thickness of 0.2 mm, relative permittivity of 4.0, and loss tangent of 0.025. The thickness of the substrate is reduced compared to the circular patch and slotted circular patch so that the bandwidth is

narrower. In addition, the operating frequency is increased from 1.5 GHz to 3.5 GHz compared to the circular patch which makes the design of the meandered antenna easier and increases the clarity of the shift in the resonant frequency. As a result, any shift in the resonant frequency of the antenna will become more discernible, and easy to measure.

All the antenna samples used in experimental tests were fabricated using the standard PCB photolithography process (etching) at RMIT University laboratories. The etching process is schematically illustrated in Figure 6.1 as described below (James and Hall, 1989):

1. The substrate consists of a layer of dielectric material sandwiched between two layers of copper. The thickness of copper can be selected from available options. Some commercially available substrates have a layer of photo-resist material coated on both sides of the substrate. If this coating does not exist on substrate then the substrate is dipped into a photo-resist solution. Then it is pulled out at a constant speed. The thickness of the layer depends on the withdrawal speed and the viscosity of the photo-resist. After deposition, the photo-resist must be cured at a high temperature.
2. The negative image of the antenna (metallic patch must be in black) on a transparent paper. The negative is also called "mask". The photographic mask is then vacuum-pressed on the structure
3. Then the structure should be exposed to UV radiation.
4. Next, the substrate is dipped into a chemical to remove the photo-resist layer from locations where the copper needs to be etched.
5. Then the substrate is exposed to an acid that dissolves the metal but does not affect the remaining photo-resist.
6. Finally, the remaining photo-resist is removed with a solvent or a concentrated alkaline solution.

All the steps in the procedure must be carefully separated by rinsing and cleaning operations, sometimes followed by drying in an oven. Drying is particularly critical for some plastic substrates, which tend to absorb water (James and Hall, 1989).

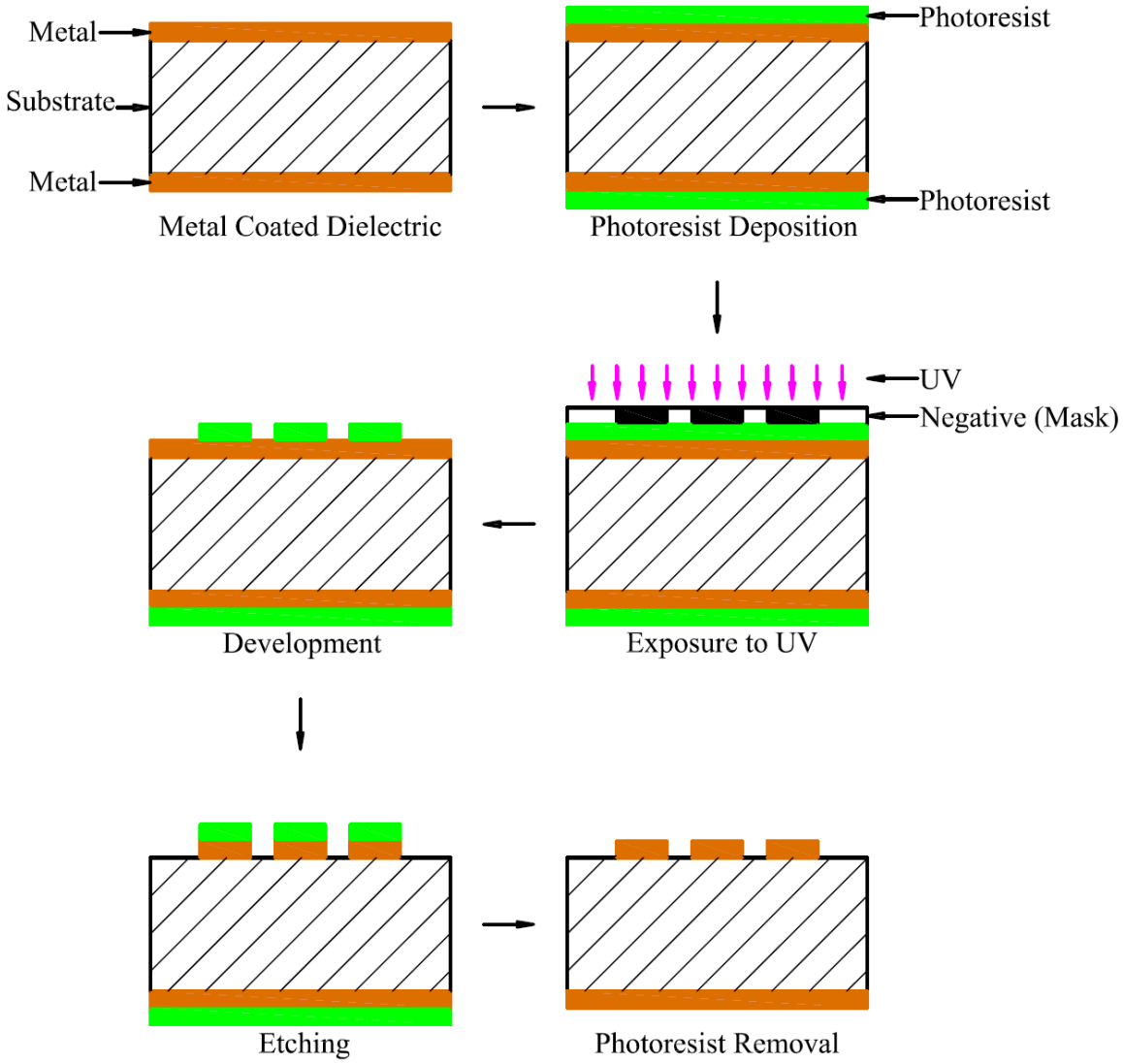

Figure 6.1 Schematic of etching process (James and Hall, 1989).

The following considerations must be made when selecting the chemicals to be used in the process for photo-resist, resist removal and etching (Garg et al., 2000):

- The substrate must be non-reactant, non-absorbent and chemically inert to the materials being used in the process.
- Chemicals or water used in the process must not be trapped in the substrate.
- Also, chemicals being used for etching must not degrade the bond between metal layer and the substrate.

By following the substrate manufacturer's recommendation about the suitable chemicals these problems are avoided.

When the substrate is ready a hole with the size of the inner conductor of the coaxial cable is drilled at the location of feed. Then the SMA connector is soldered to the back of the antenna (ground plane); whilst, the inner conductor is soldered to the metallic patch at the other side of the substrate. The manufactured antenna is now ready for the tests.

6.2.2 Test Plates

6.2.2.1 Aluminium plates

Two types of aluminium plates are manufactured for testing of antenna sensors during this research. The first type is an $35 \times 35\,\text{cm}$ aluminium plate with the thickness of 3 mm in a square shape. A $2\,\text{cm}$ diameter hole is drilled in the centre of the aluminium plate (Figure 6.2); therefore, the antenna can be attached to the plate and the coaxial cable can be connected to the antenna through the back of the plate. Three samples are manufactured with this configuration for testing the circular microstrip patch antenna, slotted circular microstrip patch antenna and meandered circular microstrip patch antenna.

Next, antenna samples are attached to the plates using a standard adhesive. Then four strain gauges were attached to the back of the plate in two directions (two in each direction) in order to measure strain close to the hole and far from the hole (see Figure 6.2). Strain gauges are placed at the axis crossing the centre of plates (14 cm and 7 cm away from the edge); therefore, maximum strain at each direction is obtained.

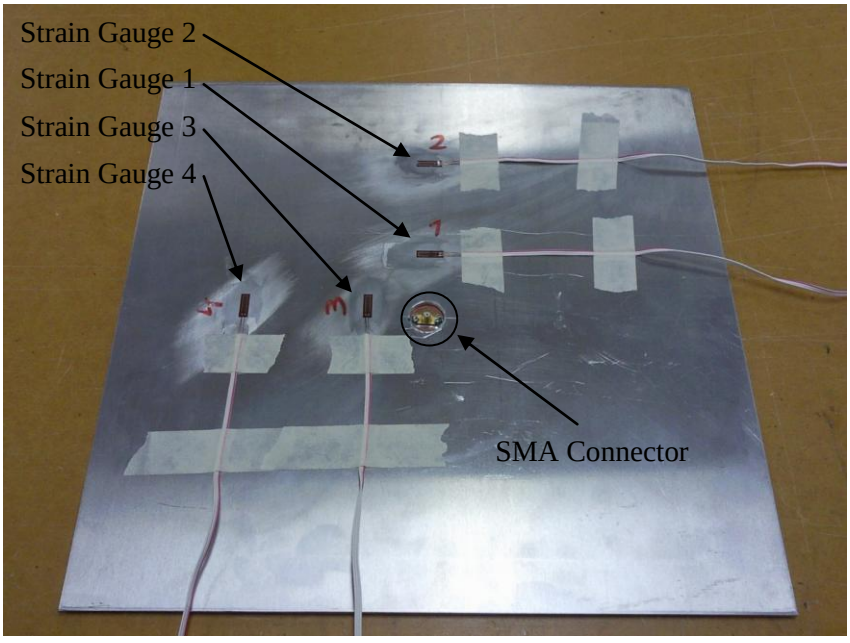

Figure 6.2 Strain gauge locations at the back of the aluminium plate.

Second type of aluminium plate is an octagon with the edge length of 17.5 cm and the thickness of 3 mm (Figure 6.3). The diameter of the hole in the centre of the plates varies from 2.5 mm (sample 1) to 15 mm (sample 6) in 2.5 mm steps to study the effect of hole size in meandered antenna sensor performance. This could be used for further study of the sensor performance with microstrip line feed instead of coaxial cable. By eliminating the hole in the structure the antenna sensor could be used to study damage detection capabilities of it. After attaching antennas to test plates, four strain gauges are attached to the back of each plate in four directions (Figure 6.3). Strain gauges are placed at the axis crossing the centre of plates (15 cm away from the edge); therefore, maximum strain at each direction is obtained. The SMA connector is attached to the antenna samples using a flexible coaxial cable to make the variation in the hole diameter possible.

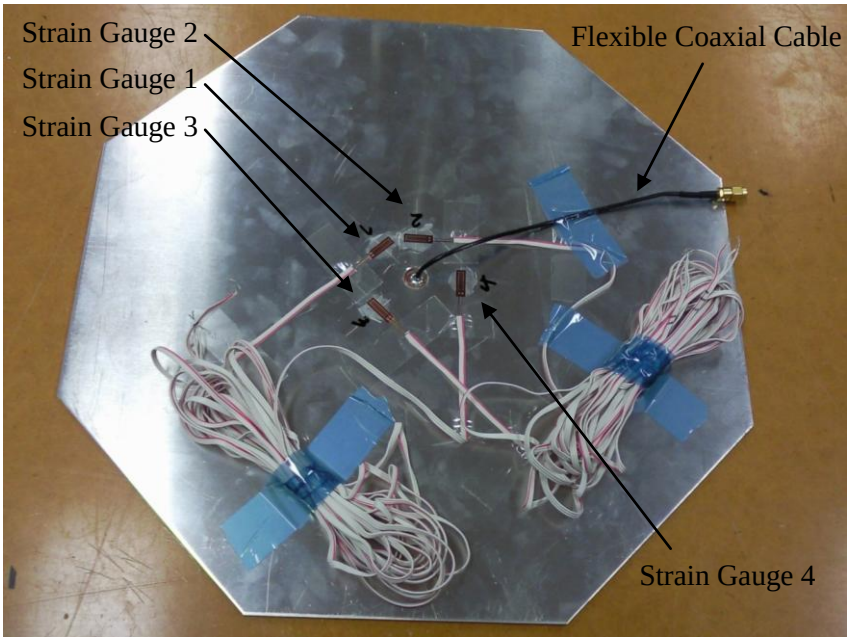

Figure 6.3 Strain gauge locations at the back of the octagon aluminium plate.

6.2.2.2 Composite plates

In order to study the effect of test plate material on the performance of the antenna sensor, two composite plates (two carbon fibre plates and one fibre glass plate) are also manufactured. Each plate is an 35×35 cm square with the thickness of 2 mm. Circular microstrip patch antenna is attached to three different materials; whilst, slotted circular microstrip patch antenna is attached to aluminium and carbon fibre plates, and meandered circular microstrip patch antenna is tested only with the aluminium plate.

The carbon fibre composite plate is made of 8 layer of woven carbon fibre reinforced epoxy with the stacking sequence of $[(0/90)_2]_s$, using the wet hand layup technique. The fibre glass composite plate is made of 10 layers of woven fibre glass, using the wet hand layup technique. After attaching the antenna sensors to composite plates, four strain gauges were attached to the back of each plate in two directions (two in each direction) in order to measure strain close to the hole and far from the hole (Figures 6.4 and 6.5).

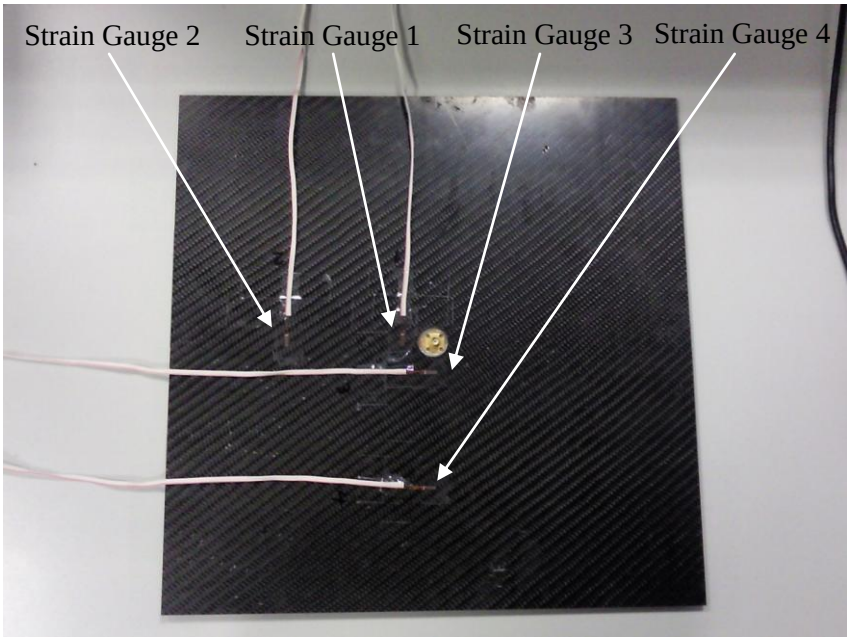

Figure 6.4 Strain gauges attached to the back of the carbon fibre composite plate.

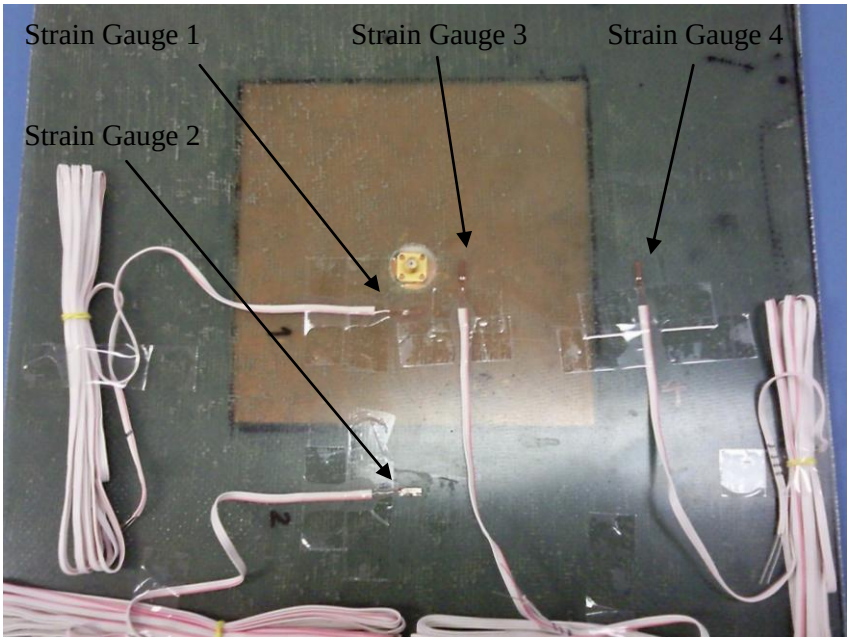

Figure 6.5 Strain gauges attached to the back of the fibre glass composite plate.

Figure 6.6 shows three circular microstrip patch antennas attached to three plates of different materials (carbon fibre composite and aluminium) to investigate the effect of each material on the resonant frequency shift of the antenna.

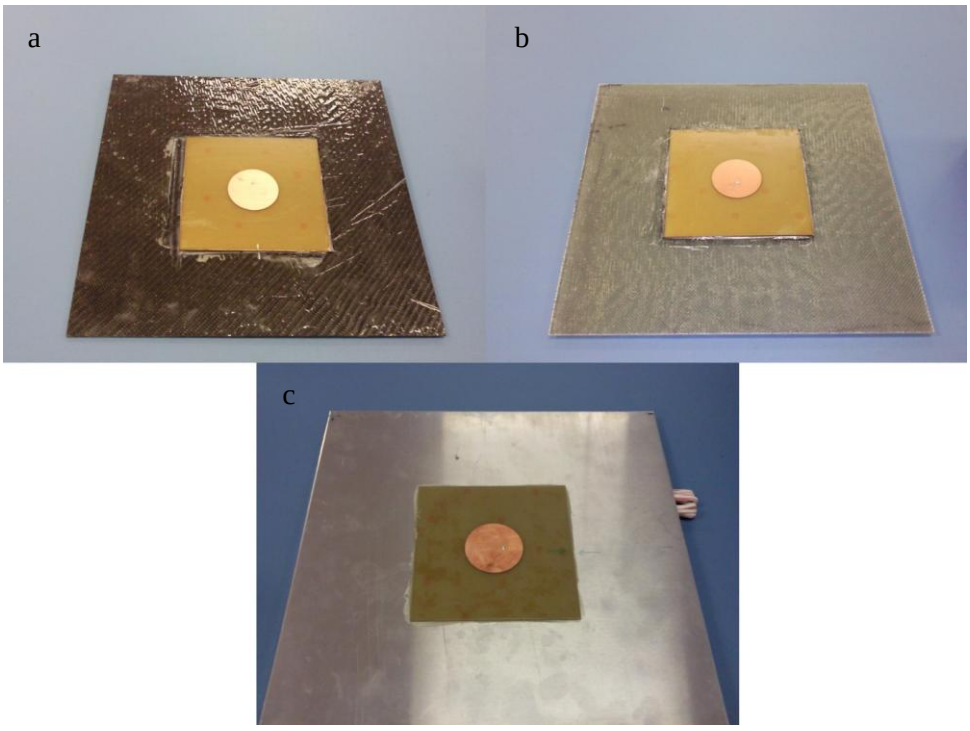

Figure 6.6 Circular microstrip patch antenna attached to three different materials: (a) carbon fibre composite, (b) fibre glass composite, and (c) aluminum.

6.3 Test Setup

After preparing the samples, in order to avoid direct contact between antenna and the metal jig and also to reduce the effect of metal materials in close proximity of the antenna, they are placed on a wooden jig (Figure 6.7).

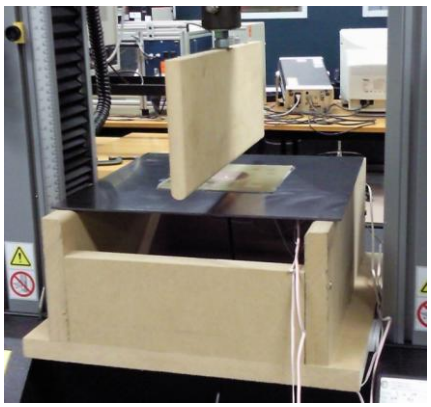

Figure 6.7 Slotted circular microstrip patch antenna attached to a carbon fobre composite plate on a wooden jig.

The assembly (wooden jig, test plate and antenna) has been placed on a 50 kN INSTRON™ test machine for a 3-point bend test. Figure 6.8 shows the final setup including a network analyser which is connected to the SMA connector at the back of the antenna using a coaxial cable to measure the scattering parameter (S_{11}) of the antenna.

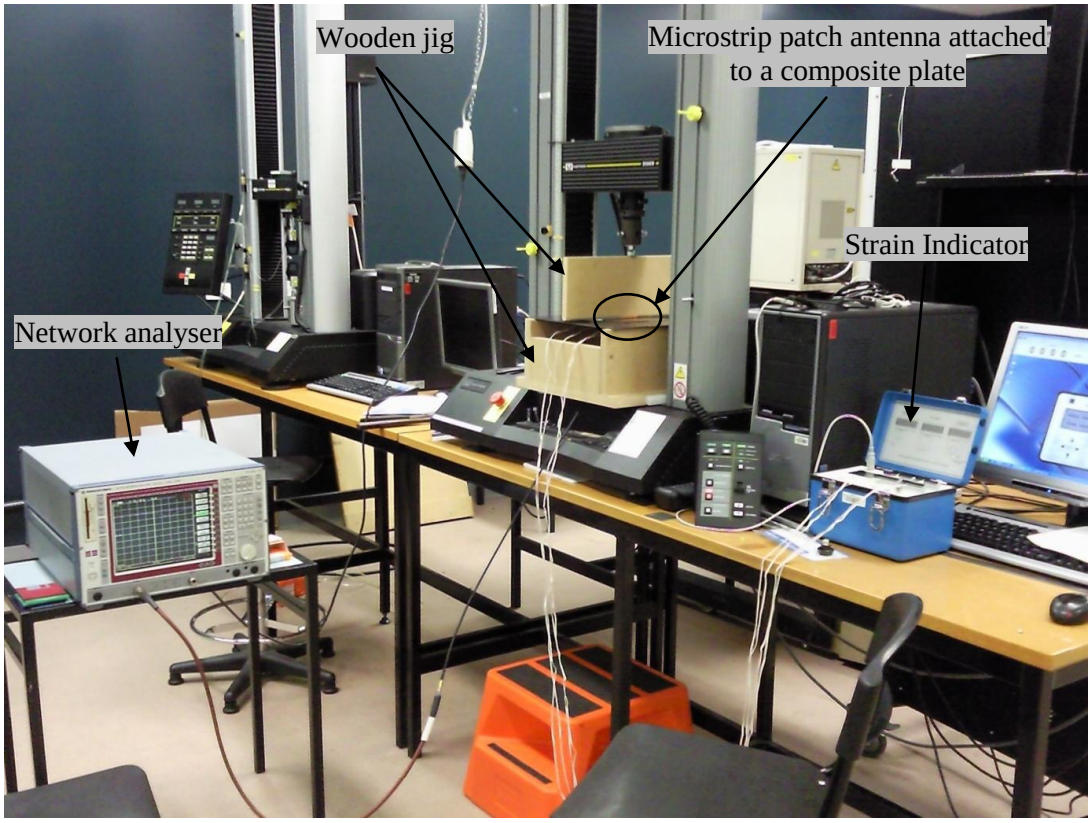

Figure 6.8 Final setup for the 3-point bend test.

The assembly was bent up to 10 mm (central axis of the plate) in steps of 0.5 mm in displacement using a 50 kN INSTRON™ machine. After each step of bending, the resonant frequency of the antenna is measured whereas the strain data from strain gauges is collected separately. To study the effect of strain direction on the antenna resonant frequency the experiment was repeated at three different orientations (0°, 45° and 90°) for circular microstrip patch antenna and meandered circular microstrip patch antenna (attached to square plate), two different orientations (0° and 90°, when the maximum strain is in the direction of slot length and sloth width, respectively) for slotted circular microstrip patch antenna, and four different orientations (-45°, 0°, 45° and 90°) for meandered circular microstrip patch antenna (attached to octagon plate).

In order to test the slotted and meandered antennas, the same experimental configuration and procedure as the circular patch antenna is used. In addition, a rectangular slot is cut in

the middle of the wooden jig to avoid the effect of wood on the resonant frequency of the antennas (Figure 6.9).

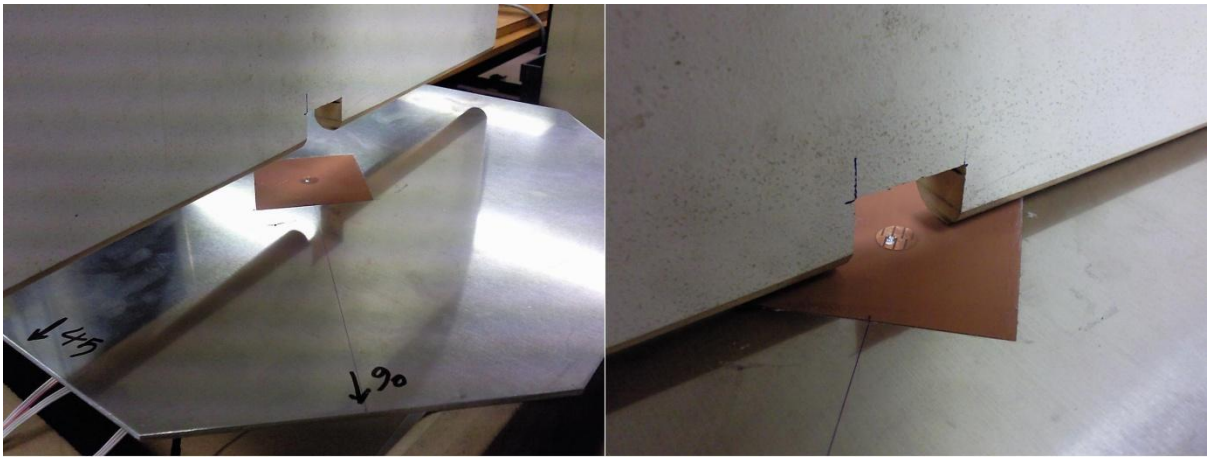

Figure 6.9 Rectangular slot in the wooden jig to avoid the contact between wood and the meandered circular microstrip patch antenna.

6.4 Data Acquisition Devices

6.4.1 Network Analyser

For antenna measurements, the most useful and important piece of equipment is the network analyser (NA), which is basically a combination of a transmitter and a receiver. Normally it has two ports and the signal can be generated or received from either port. The VNA is frequency-domain equipment (it can obtain the signal in the time domain using Fourier transforms) (Huang and Boyle, 2008). There are two types of network analyser (Huang and Boyle, 2008):

- Scalar network analyser (SNA) which measures the amplitude of the parameters of a network.
- Vector network analyser (VNA) which measures both the amplitude and phase of the parameters of a network.

The VNA is much more powerful than the SNA; in addition to the parameters which can be measured by the SNA, it can also measure some very important parameters such as the complex impedance, which is essential for antenna measurements (Huang and Boyle, 2008). The VNA used for experimental tests of this project is shown in Figure 6.10. The architecture of a typical VNA is illustrated in Figure 6.11. The source signal can be transmitted from either Port 1 or Port 2 to the antenna, which is controlled by a switch. Part

of the signal from the source is provided directly to the reference R, which will be compared with the received signal by the central processing unit (CPU).

Figure 6.10 The VNA used for experimental tests.

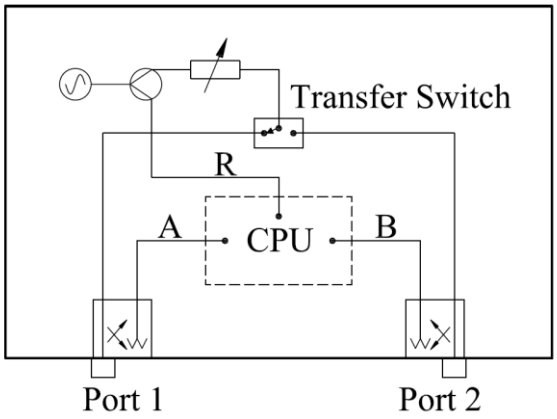

Figure 6.11 Architecture of a typical VNA (Huang and Boyle, 2008).

For antenna measurements, the typical parameters that can be measured by a VNA include (Huang and Boyle, 2008):

Transmission measurements:

- Gain
- Insertion loss
- Insertion phase
- Transmission coefficients
- Electrical length

- Electrical delay
- Deviation from linear phase
- Group delay

Reflection measurements:

- Return loss
- Reflection coefficients
- Reflection coefficients vs. distance
- Impedance
- VSWR

In order to remove the effects of the cable and connectors (attenuation and phase shift), they must be calibrated (Huang and Boyle, 2008). The standard calibration needs three terminations for one-port calibration (short, open and load/matched) (Huang and Boyle, 2008). After connecting each terminator to the cable, one frequency sweep in the frequency range of measurement must be performed. The calibration kit used in this research is shown in Figure 6.12.

Figure 6.12 Calibration kit used for antenna measurement.

Various errors that may be introduced into the measurement include (Huang and Boyle, 2008):

- System errors (can be removed by calibration)
- Random errors
- Drift errors

6.4.2 Strain Indicator and Recorder

The digital data logger used to Measure strain from strain gauges is Vishay Micro-Measurements™ strain indicator and recorder (Model P3™), which is a portable, battery-operated instrument capable of simultaneously accepting four inputs from quarter-, half-, and full-bridge strain-gauge circuits, including strain-gauge-based transducers (Figure 6.13) (Vishay, 2011).

Figure 6.13 Vishay Micro-Measurements™ strain indicator and recorder (Model P3™) (Vishay, 2011).

6.5 Data Analysis

In order to study the relationship between the strain and the shift in the resonant frequency of the antenna the following equation is used to calculate the normalised frequency shift.

$$\text{normalised frequency shift} = \frac{\Delta f}{f_{rs}} = \frac{f_{rs} - f_r}{f_{rs}} \qquad (6.1)$$

Where f_r is the resonant frequency of the antenna before 3-point bend test and f_{rs} is the resonant frequency of the antenna after applying strain.

The scattering parameter of the antenna are saved by the network analyser on a disk using the *.CSV file format (Comma-Separated Values file format). The scattering parameter after each step of bending is saved in a separate file. In order to combine all the results in one file for further processing using Microsoft Excel™, a program is written in MATLAB™ software which is available in Appendix A.

6.6 Conclusion

In this chapter, the photolithography technique used for fabrication of antennas and the manufacturing procedure for composite plates as well as aluminium plates are described. The setup for experimental tests is described and the procedures for the tests are explained in details. Also, the operation of VNA which is used for antenna measurements is presented. The procedures presented in this chapter were used to evaluate the results from FEA. These results are presented in the next chapter where detailed discussion is provided.

CHAPTER 7

Results and Discussion

7.1 Introduction

The theoretical study of the resonant frequency of circular microstrip patch antennas followed by analytical study of strain and normalised frequency shift lead the research to finite element analysis of the circular microstrip patch antenna. Also, experimental tests confirmed the proposed theory of strain measurement using microstrip patch antennas. Detail discussion of these results for circular microstrip patch antennas are presented in this chapter. This is followed by a separate discussion on slotted circular microstrip patch antenna and meandered circular microstrip patch antenna FEA and experimental results. Finally, a comparison between these three antenna sensors is given.

7.2 Circular Microstrip Patch Antenna

Theoretical study of the resonant frequency of circular microstrip patch antennas (Equation 4.11) shows that there is a linear relationship between applied strain and the shift in the resonant frequency of the antenna. This theoretical study is discussed in detail in Chapter 4 and is validated with analytical study using MATLAB™ software. FEA modelling and experimental tests (described in Chapter 5 and 6, respectively) show that the resonant frequency of a circular microstrip patch antenna shifts by bending the antenna attached to a plate.

When the bending angle is 0° and 90°, the structure is bent at an axis parallel to the E-plane and H-plane of the antenna, respectively (Figure 7.1). The E-plane is defined as “the plane, containing the electric-field vector and the direction of maximum radiation”, and the H-plane as “the plane, containing the magnetic-field vector and the direction of maximum radiation”. The shift in the resonant frequency of the antenna after bending is shown in

Figure 7.2. The arrow in Figure 7.2 shows the direction of the shift in the resonant frequency of the antenna. The amount of frequency shift after each step (0.5 mm) is 100 kHz.

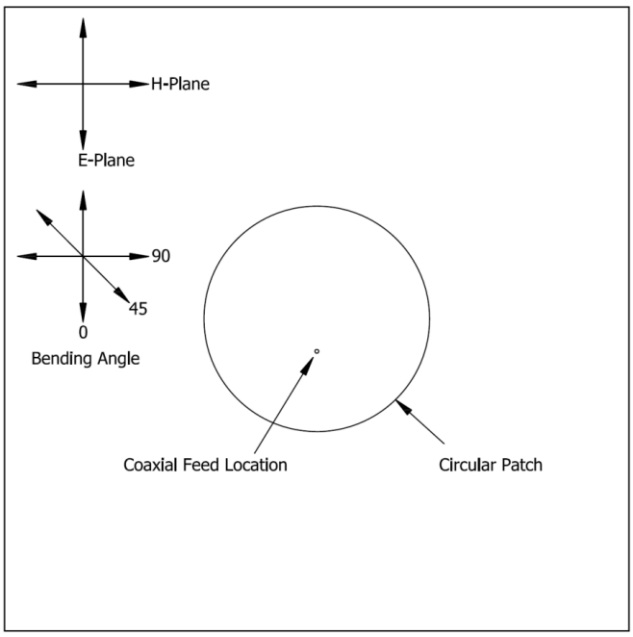

Figure 7.1 Bending directions; and E-plane and H-plane orientations for circular microstrip patch antenna.

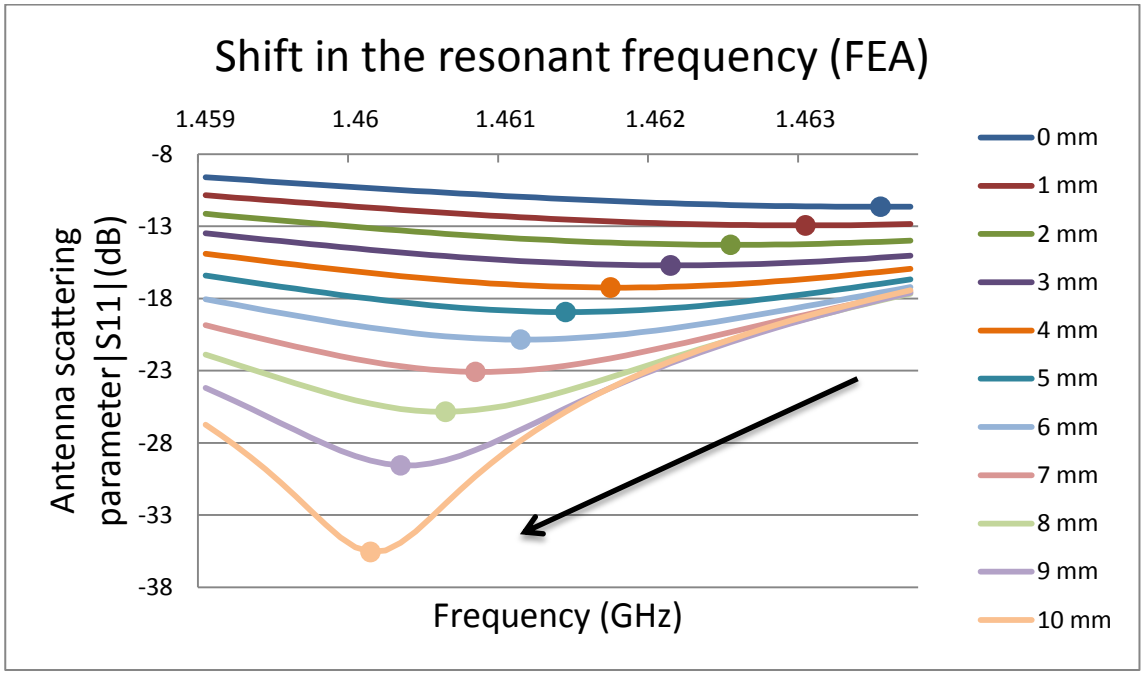

Figure 7.2 Shift in the resonant frequency of the circular microstrip patch antenna sensor at 0° orientation (attached to the aluminium plate).

The results derived from the experimental study show that when the antenna is attached to a carbon fibre plate or an aluminium plate, the percentage of the shift in resonant frequency of the antenna is close to theoretical model. However, when the antenna is attached to a fibre

glass plate there is a negligible shift in the resonant frequency of the antenna (Figures 7.3 and 7.4). This could be because of the relatively low electrical conductivity of the fibre glass (compared to aluminium and carbon fibre), especially when these plate materials are designed to act as an infinite ground plane.

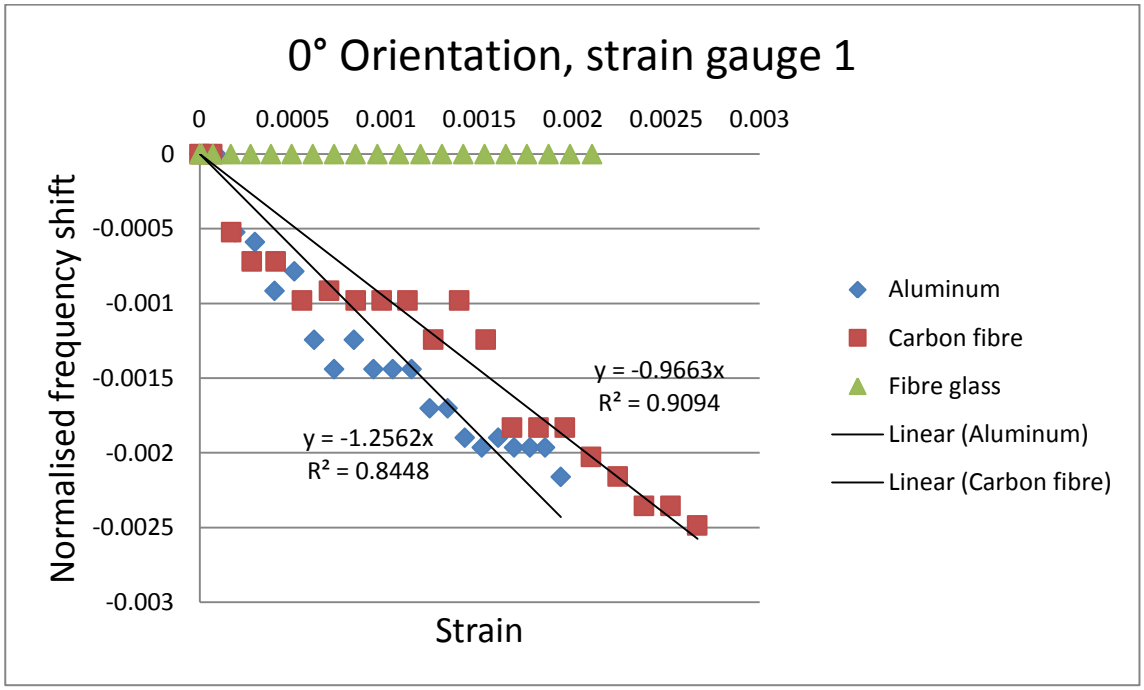

Figure 7.3 Comparison of strain and frequency shift relationship in three different materials at 0° orientation (Circular microstrip patch antenna).

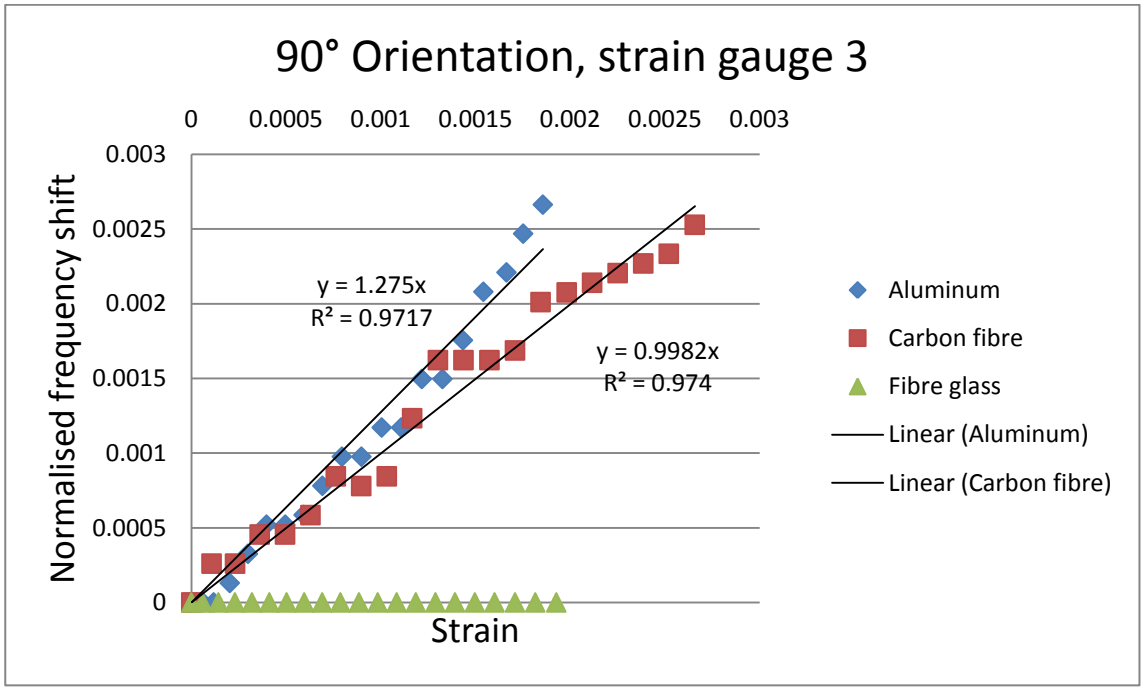

Figure 7.4 Comparison of strain and frequency shift relationship in three different materials at 90° orientation (Circular microstrip patch antenna).

The resonant frequency of the antenna shifts toward lower frequencies, if the assembly is bent in 0° orientation; therefore, we have minus sign in Equation 4.11 (Figure 7.3). If the bending angle is 90°, the resonant frequency shifts toward higher frequencies. This is because the applied strain is in H-plane of the antenna (Figure 7.4); therefore, the effective length (radius) of the patch (E-plane direction) decreases. The effective electrical length of the antenna is a function of the resultant overall shape of the antenna after deformation in both the E and H planes (or 0^0 & 90^0 loading orientations, respectively). Figures 7.3 and 7.4 show that rate of change of the shift in frequency is the same for 0° and 90° orientations; though, the shift is in different directions. The plateau regions in Figures 7.3 and 7.4 are because of low sensitivity of the antenna to strain; resulted from nonlinearity in the material, antenna physical size and the imperfection of the bond between the antenna and two plates. This is a shortcoming for the circular microstrip patch antenna.

Figure 7.5 shows the relationship between strain and frequency shift after bending in 45° orientation for carbon fibre plate. There are small variations in the shift; however there is no overall relationship with strain. The reason is when the antenna is bent at 45° the magnitude of strain is similar in both directions (E-plane and H-plane) and as a result the shift from each direction neutralises the shift from another direction. This is a significant shortcoming for a sensor and this will be discussed later in this chapter.

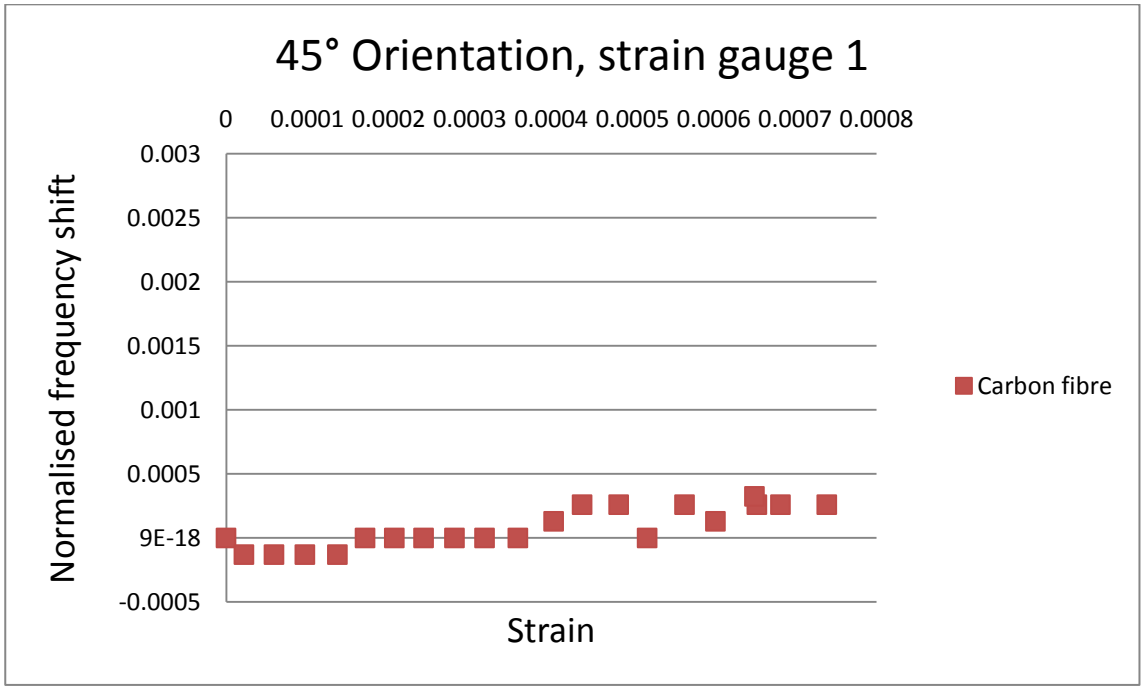

Figure 7.5 Strain and frequency shift relationship at 45° orientation (Circular microstrip patch antenna).

The test was also repeated for the second resonant frequency of the circular microstrip patch antenna. Figures 7.6 and 7.7 show the comparison between results from the first and the second resonant frequency of the antenna attached to the carbon fibre plate. There is no significant shift in the second resonant frequency of the antenna after bending.

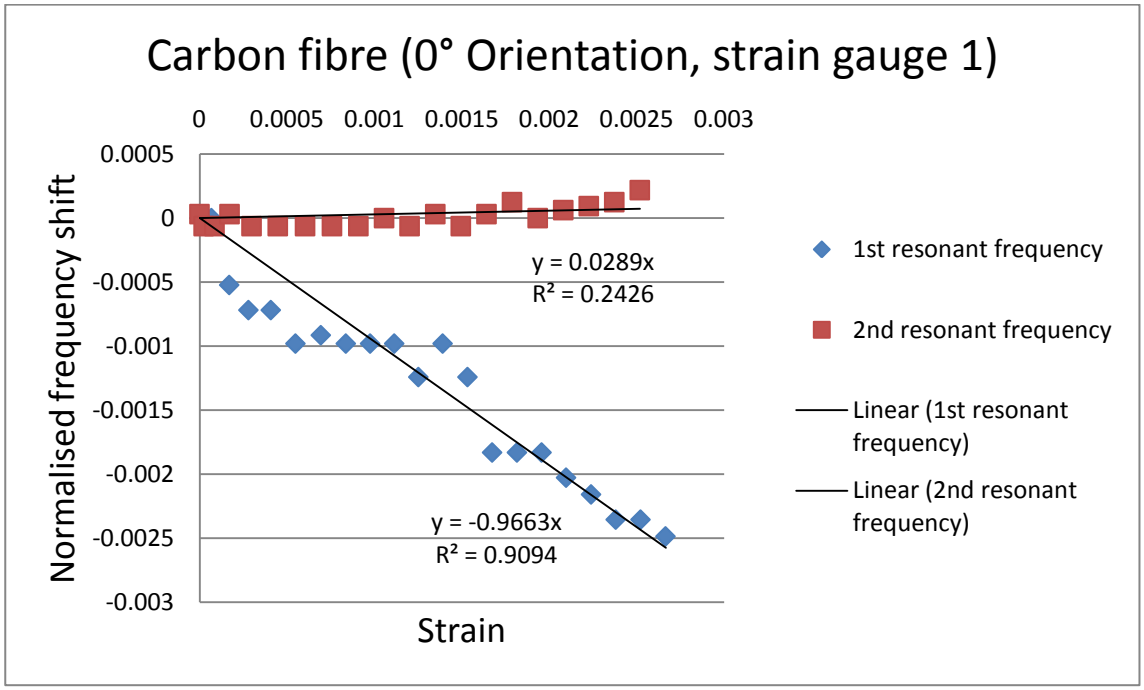

Figure 7.6 Strain and frequency shift relationship at 1st and 2nd resonant frequencies of the patch at 0° orientation (Circular microstrip patch antenna).

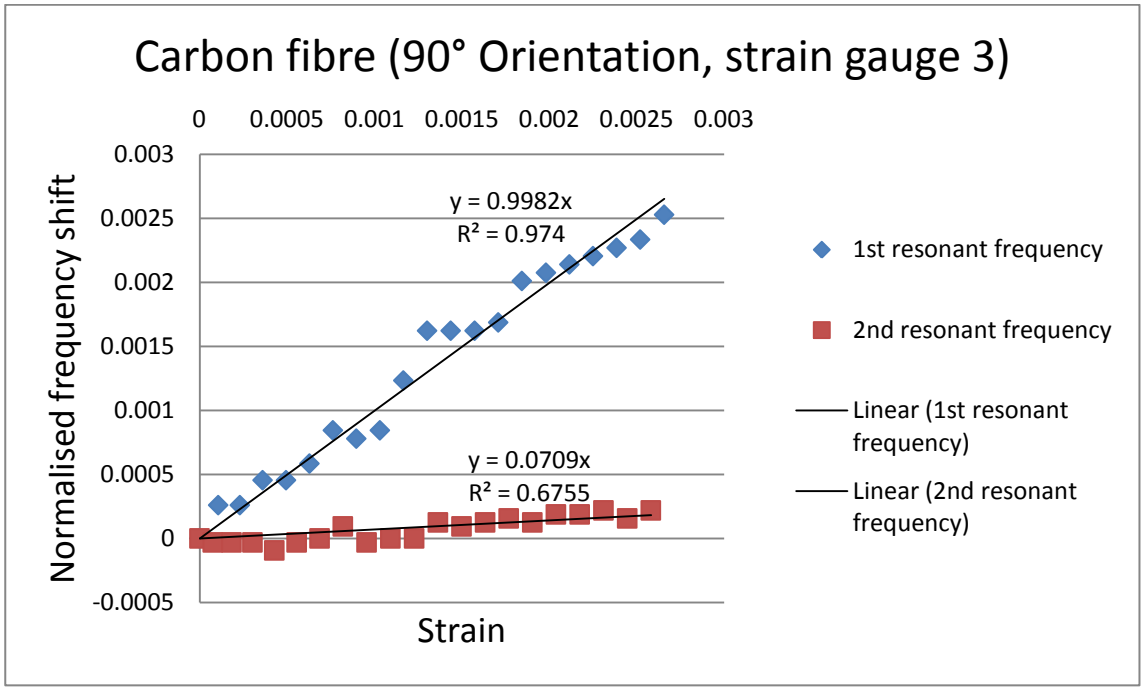

Figure 7.7 Strain and frequency shift relationship at 1st and 2nd resonant frequencies of the patch at 90° orientation (Circular microstrip patch antenna).

Experimental and FEA results for the aluminium plate both show a linear relationship between strain and frequency shift. Both experimental and FEA results confirm the analytical calculations. The experimental relationship between strain and frequency shift in comparison with FEA results and theoretical model (Equation 4.11) are shown in Figures 7.8 and 7.9, respectively. There is general agreement up to about 1500 μstrain between the theoretical, analytical and computational results.

The discrepancies between experimental and FEA results with theoretical model (and analytical calculations (Figure 4.2)) are due to the difference in loading conditions, i.e. three point bend test for experiments and FEA compared to pure tension for theoretical model (and analytical calculations). For the carbon fibre plate, the different locations of strain gauges ((1) and (2) for the 0^0 loading orientation and the strains gauges (3) and (4) in the 90^0 loading orientation) as shown in Figure 6.4, represent decreasing strain levels going from strain locations 1 to 2 and 3 to 4 in the 0^0 and 90^0 loading directions, respectively. This is lucidly shown as different gradients in Figures 7.10 and 7.11.

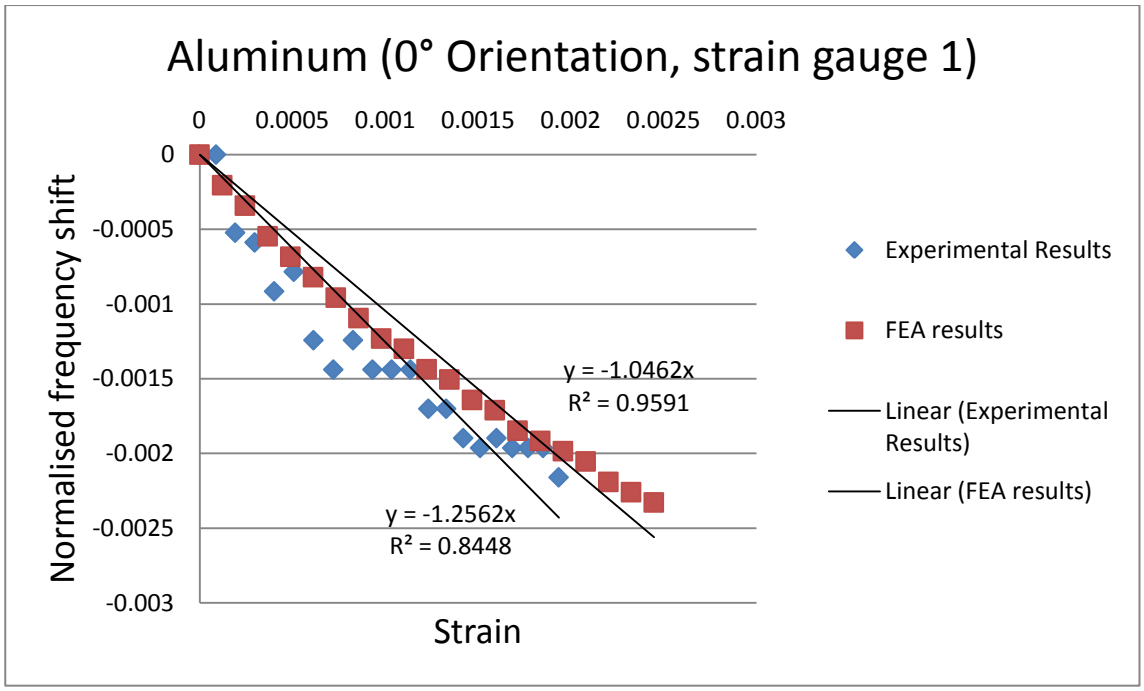

Figure 7.8 Comparison of measured and FEA results of strain and frequency shift (Circular microstrip patch antenna).

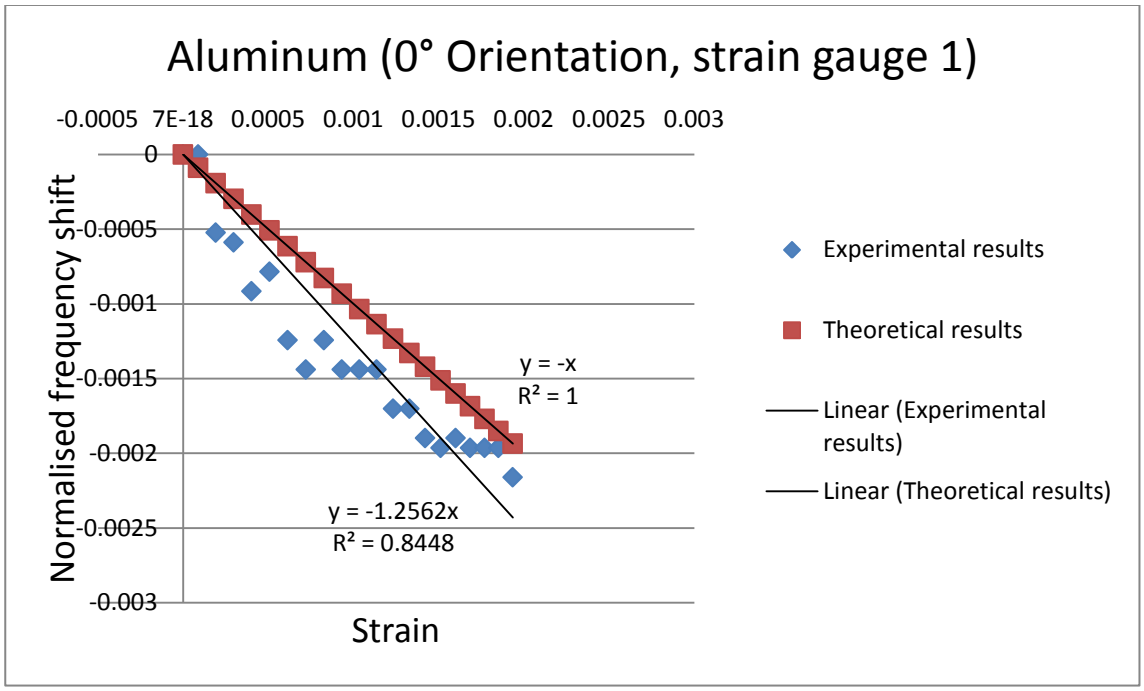

Figure 7.9 Comparison of measured and theoretical results of strain and frequency shift (Circular microstrip patch antenna).

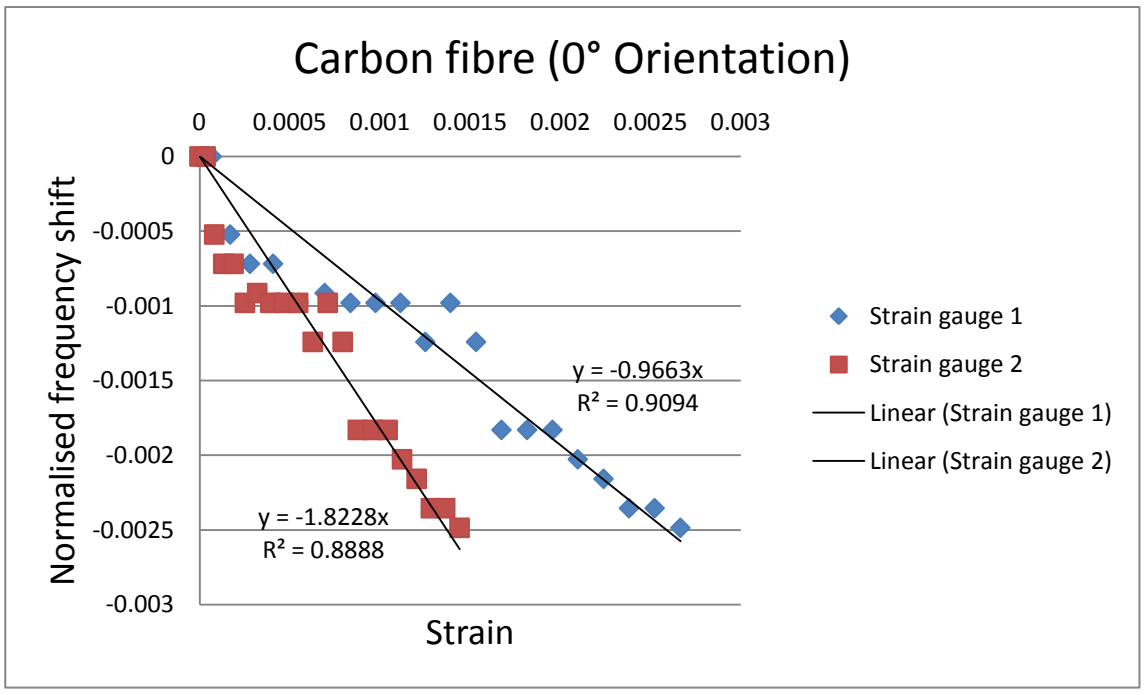

Figure 7.10 Test results of strain and frequency shift at 0° orientation for circular patch (Strain gauge 1 is 14 cm away from the edge of the plate, and strain gauge 2 is 7 cm away from the edge of the plate).

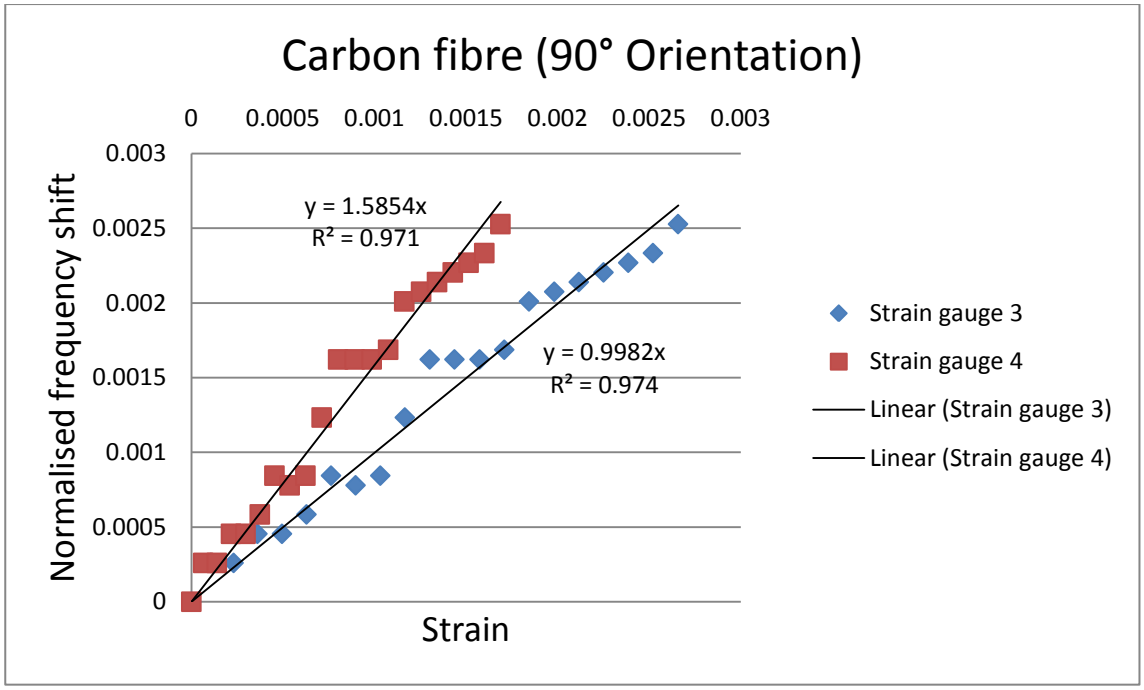

Figure 7.11 Test results of strain and frequency shift at 90° orientation for circular patch (Strain gauge 3 is 14 cm away from the edge of the plate, and strain gauge 4 is 7 cm away from the edge of the plate).

Table 7.1 shows the effect of test plate material on the amount of shift in the resonant frequency of the circular microstrip patch antenna. Based on these results, the circular microstrip patch antenna is suitable to measure strain in aluminium and carbon fibre; however, more investigations are required regarding its use for fibre glass material. The amount of shift in 0° and 90° orientations is 100 kHz which indicates that for the operating frequency of the antenna (1.5 GHz) the sensitivity of the antenna needs to be increased. In addition, this antenna sensor is not able to detect strain in 45° orientation which is an important disadvantage. However, the results provided in this section show that microstrip patch antennas are capable to detect strain. In order to overcome the shortcoming of this antenna sensor, new antennas are designed, simulated and tested which are described in the following sections.

Table 7.1 Comparison of the amount of shift in the resonant frequency of the circular microstrip patch antenna attached to test plates from different materials.

Material	Aluminium			Carbon fibre			Fibre glass		
Bending Angle	0	45	90	0	45	90	0	45	90
Frequency Shift (kHz)	−100	0	+100	−100	0	+100	−50	0	+50

7.3 Slotted Circular Microstrip Patch Antenna

The results derived from FEA and experiments for slotted circular microstrip patch antenna are shown in the following figures. Here, the data from three steps of bending (0 mm, 5 mm and 10 mm) are used in order to compare FEA results with experimental results. The orientation of the 3-point bend configuration is the relative angle between the upper part of the wooden jig and the slot in the circular patch; where, 0° and 90° happen when the jig is perpendicular and parallel to the slot, respectively (Figure 7.12).

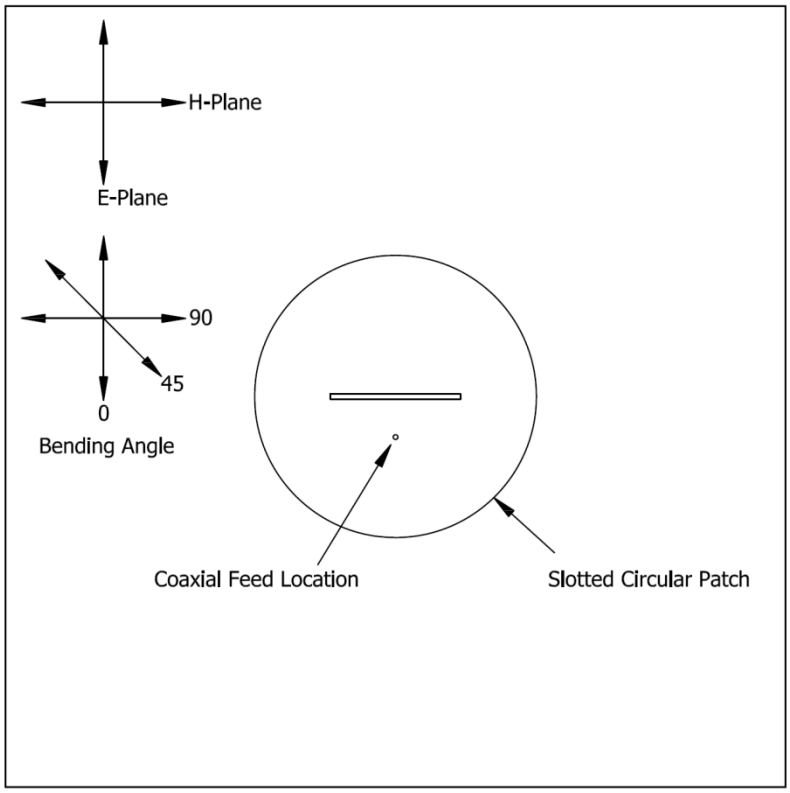

Figure 7.12 Bending directions; and E-plane and H-plane orientations for slotted circular microstrip patch antenna.

Figure 7.13 shows the shift in the resonant frequency of the slot at different steps of loading where the antenna is attached to the aluminium plate and is bent in the 90° orientation. The total amount of shift after 10 mm bend is about 6 MHz in 90° and 3 MHz in 0° which are 3 and 1.5 times the amount of shift in the resonant frequency of a circular patch without the slot.

The percentage of the frequency shift for the carbon fibre plate and the aluminium plate are illustrated in Figures 7.14 and 7.15, respectively; where the effect of bending orientation is compared for each panel. For the carbon fibre panel the amount of shift in both 0° and 90°

are the same up to 5 mm bend and two lines start to diverge from then. In the aluminium panel the slope of line related to 90° bend is higher which causes the two lines to be separated from the beginning. The reason for this difference is presumably because the slot frequency is known to be more sensitive to changes in its width rather than its length.

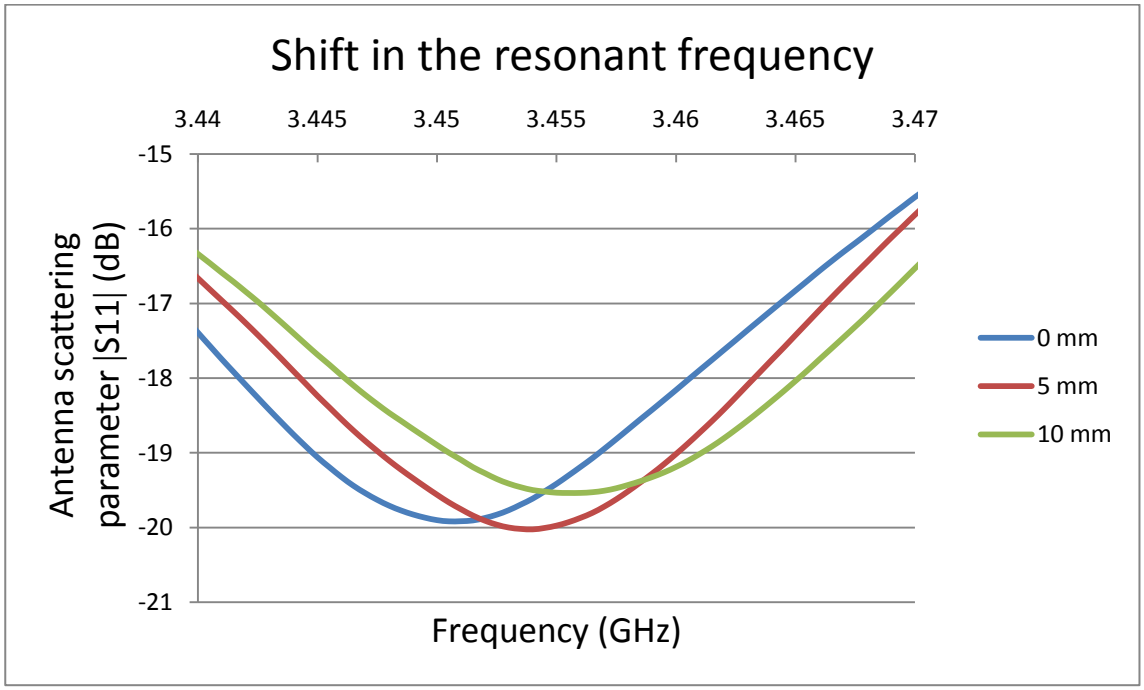

Figure 7.13 Shift in the resonant frequency of the slotted circular microstrip patch antenna sensor at 0° orientation (attached to the aluminium plate).

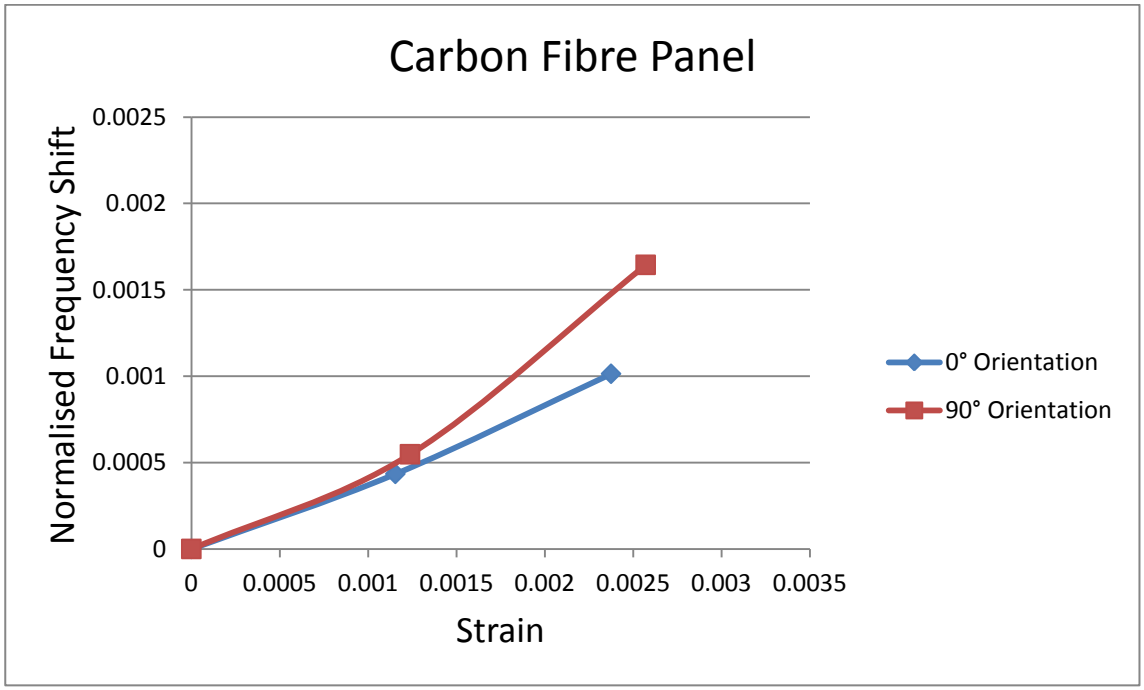

Figure 7.14 Experimental strain-frequency shift relationship for carbon fibre panel (Strain gauge 1 at 0° orientation and strain gauge 3 at 90° orientation).

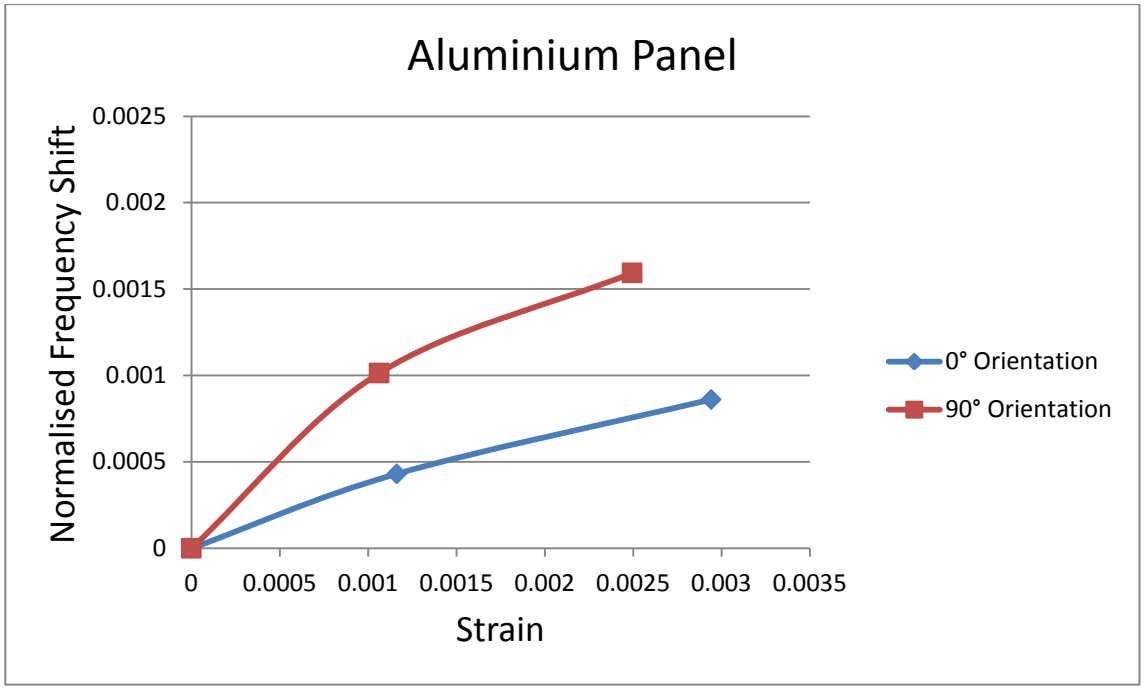

Figure 7.15 Experimental Strain-frequency shift relationship for aluminium panel (Strain gauge 1 at 0°orientation and strain gauge 3 at 90° orientation).

The comparison between the FEA results and experimental results are shown in Figures 7.16 and 7.17. The FEA model is based on the antenna sensor attached to the aluminium plate. The results from both materials are in good agreement with FEA results; whilst, the results from aluminium plate is closer to FEA results. The difference in the results of the carbon fibre plate can be accounted for given the micro-heterogeneity in the composite materials, which was not taken into account in the FEA model. The close comparison of the simulated and experimental results is essentially a validation of both techniques and particularly, the simulation technique used in this study. The consistent increase in the frequency shifts with strain from the simulated results (when compared with experimental results) might be accounted for by some of ideal conditions assumed with the simulations such as material dimension consistency and true material homogeneity.

When the plates are bent at the 0° orientation, the maximum strain is in the direction of strain gauges 1 and 2. Because strain gauge 1 is closer to the centre of the plate where a 2 cm hole is drilled in the plate it has the maximum strain. For the same reason when the bend is in 90° strain gauge 3 has the maximum strain. The comparison of results from different strain gauges (Figures 7.18 and 7.19) shows that the slope of the line in the graph is directly related to the location of strain gauges. Therefore, the slope of the line can be used to

measure strain in different locations of the plate, provided further experiments clarify their exact relationship.

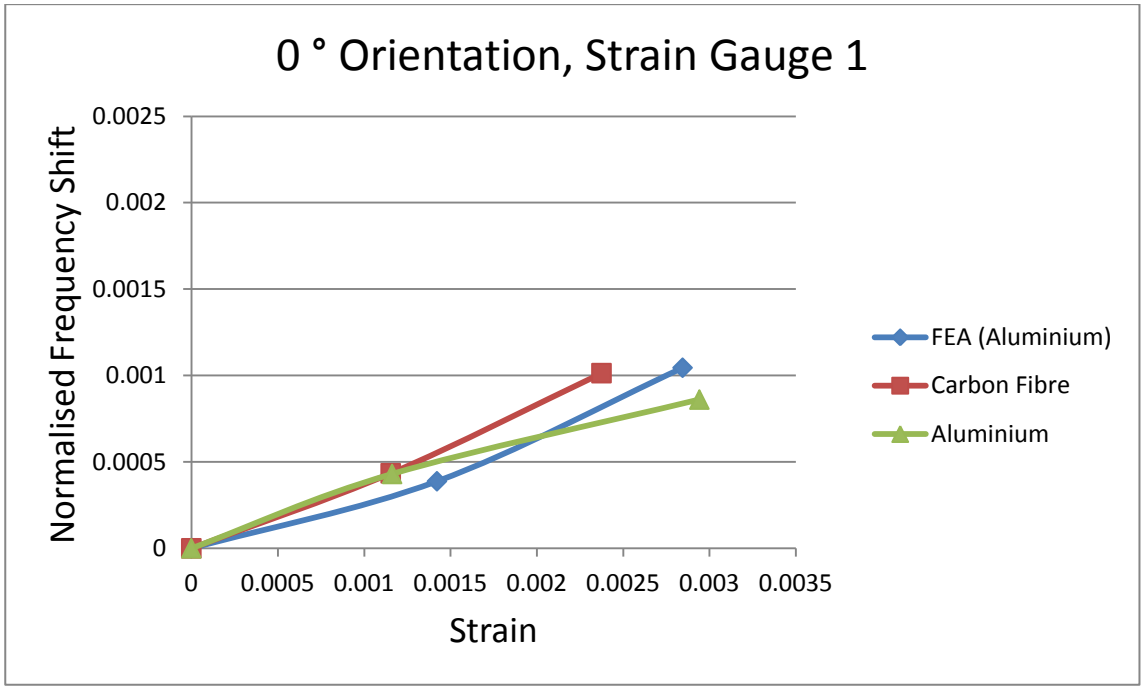

Figure 7.16 Comparison of FEA and experimental results in 0° orientation.

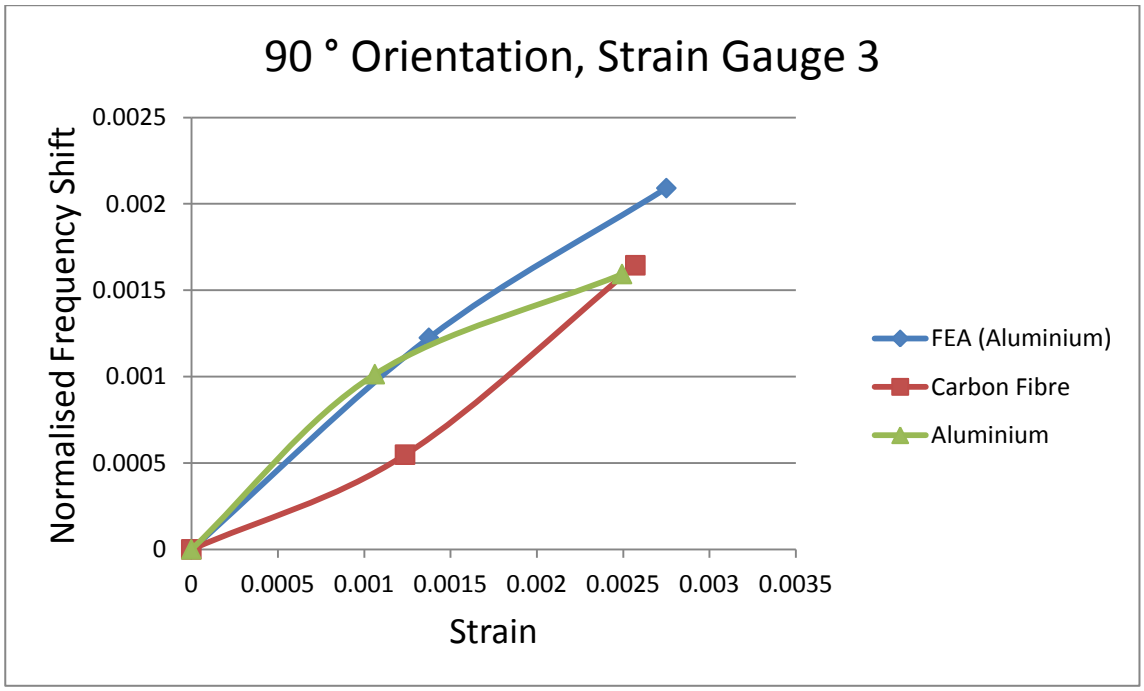

Figure 7.17 Comparison of FEA and experimental results in 90° orientation.

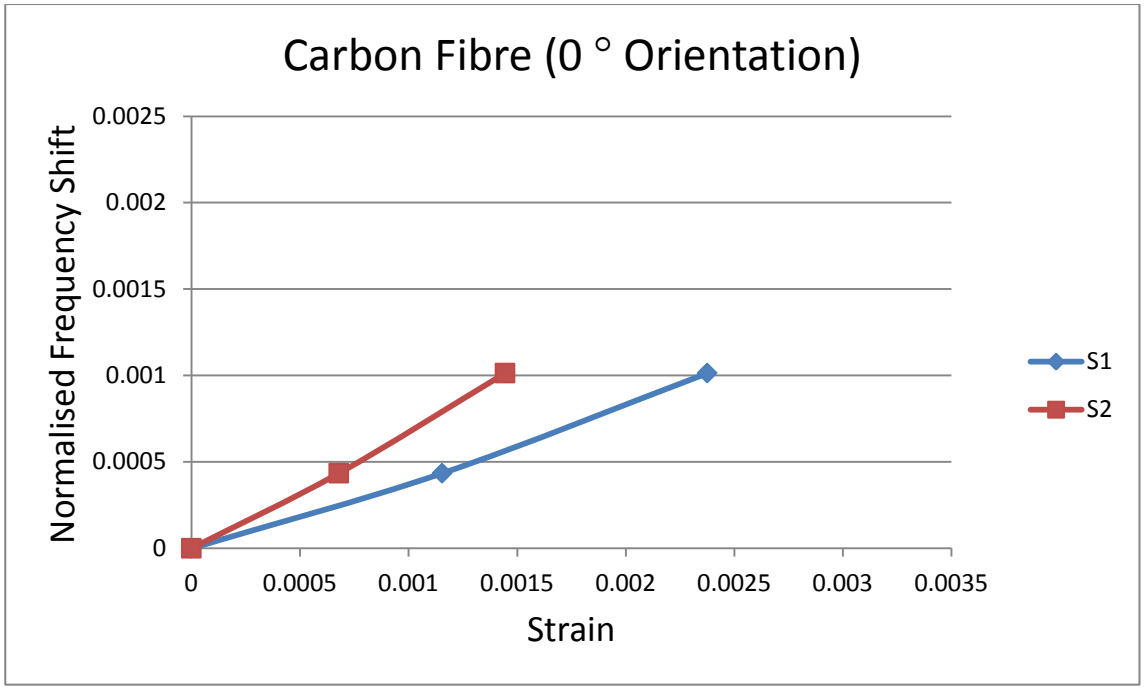

Figure 7.18 Effect of strain intensity in 0° orientation.

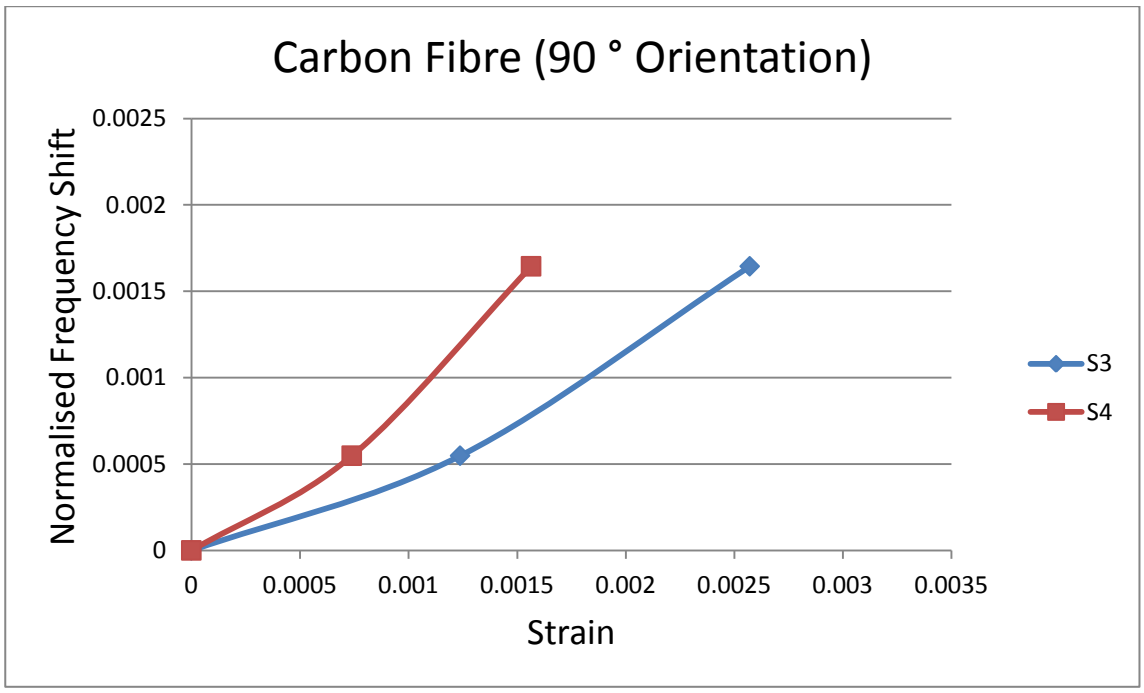

Figure 7.19 Effect of strain intensity in 90° orientation.

7.4 Meandered Circular Microstrip Patch Antenna

The shift in the resonant frequency of the meandered circular patch antenna after bending in the 45° orientation where the antenna is attached to the aluminium plate is shown in Figure 7.20. The amount of frequency shift after each step (0.5 mm) is 300 kHz. The amount of frequency shift is threefold increased compared to the circular microstrip patch antenna,

whilst its physical size is five times smaller. The bending orientations are shown in Figure 7.21.

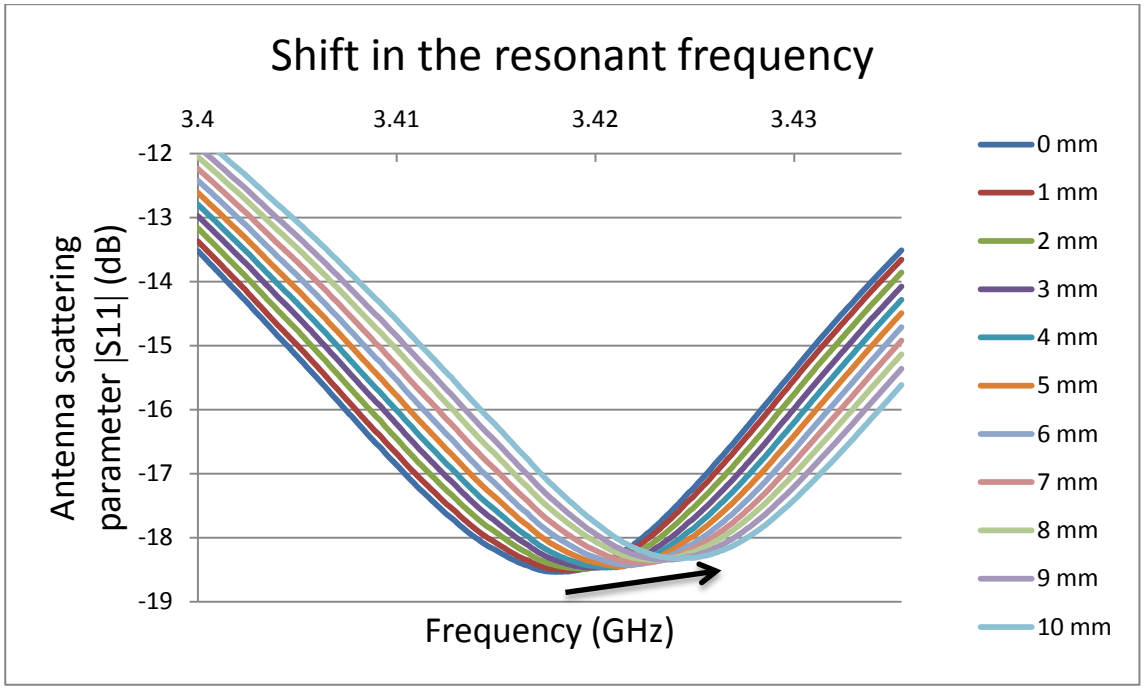

Figure 7.20 Shift in the resonant frequency of the meandered antenna sensor at 45° orientation (attached to the aluminium plate).

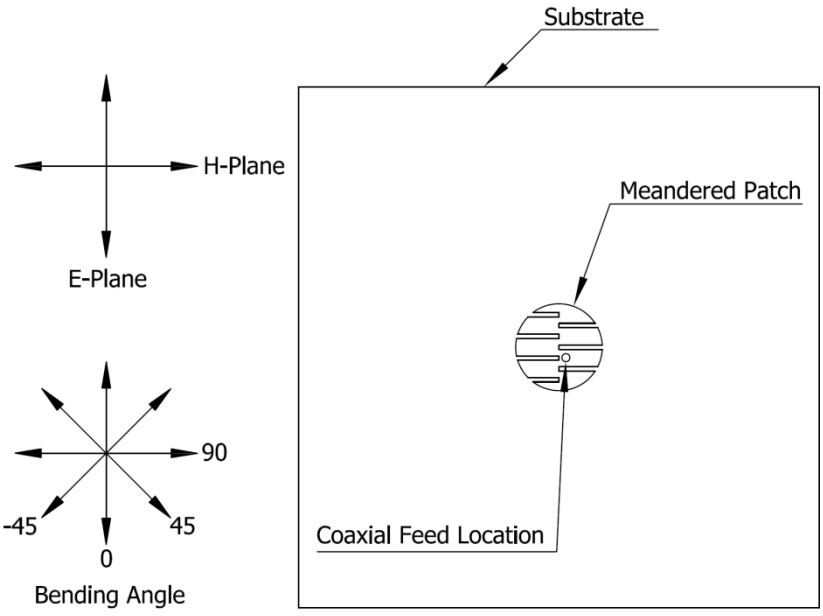

Figure 7.21 Bending directions; and E-plane and H-plane orientations for meandered circular microstrip patch antenna.

Figures 7.22, 7.23, and 7.24 illustrate the strain and frequency shift relationship for the meandered circular microstrip patch antenna in 0°, 90°, and 45° orientations, respectively. The comparison between FEA results and experimental results are in good agreement for all

three bending orientations, albeit, with increasing disparity with strain. The shift in the resonant frequency and therefore the relationship is more definitive than the simple circular patch antenna.

After bending the meandered patch in the 0° orientation, the patch frequency shifts 100 kHz toward lower frequencies. In addition, because of the resulting Poisson's ratio effect on the slots' width increase, a decrease in the resonant frequency results. However, length of the slots reduces which increases the resonant frequency and therefore the overall resonant frequency shifts 300 kHz toward higher frequencies. In 90° orientation, the resonant frequency of the patch increases by the amount of 100 kHz. This time, because of the Poisson's ratio the slots' length increases which reduces the patch frequency. However, because the decrease in the slots' width is bigger than the increase in the slots' length and therefore it has more effect on the frequency, the overall frequency shifts 300 kHz toward higher frequencies. In addition, unlike normal circular patch, at 45° orientation the resonant frequency shifts 300 kHz toward higher frequencies. This is because 45° orientation is a superposition of 0° and 90° orientations. As a result, the overall frequency shift is the same as two other orientations.

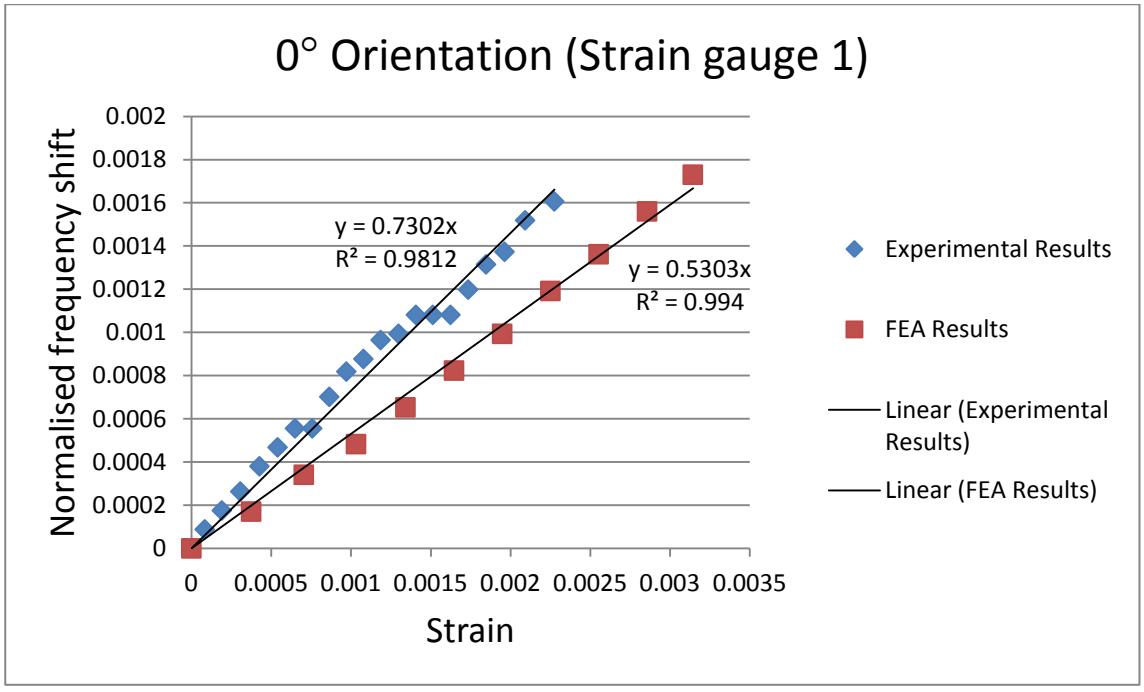

Figure 7.22 Comparison of measured and FEA results of strain and frequency shift relationship at 0° orientation for meandered patch.

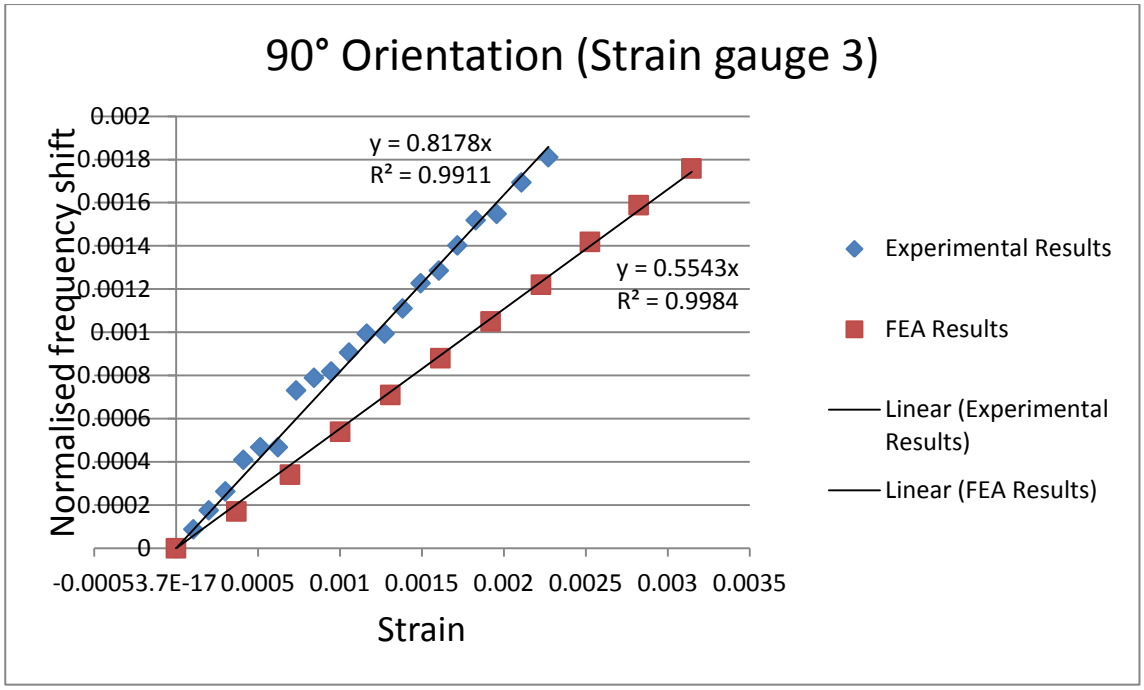

Figure 7.23 Comparison of measured and FEA results of strain and frequency shift relationship at 90° orientation for meandered patch.

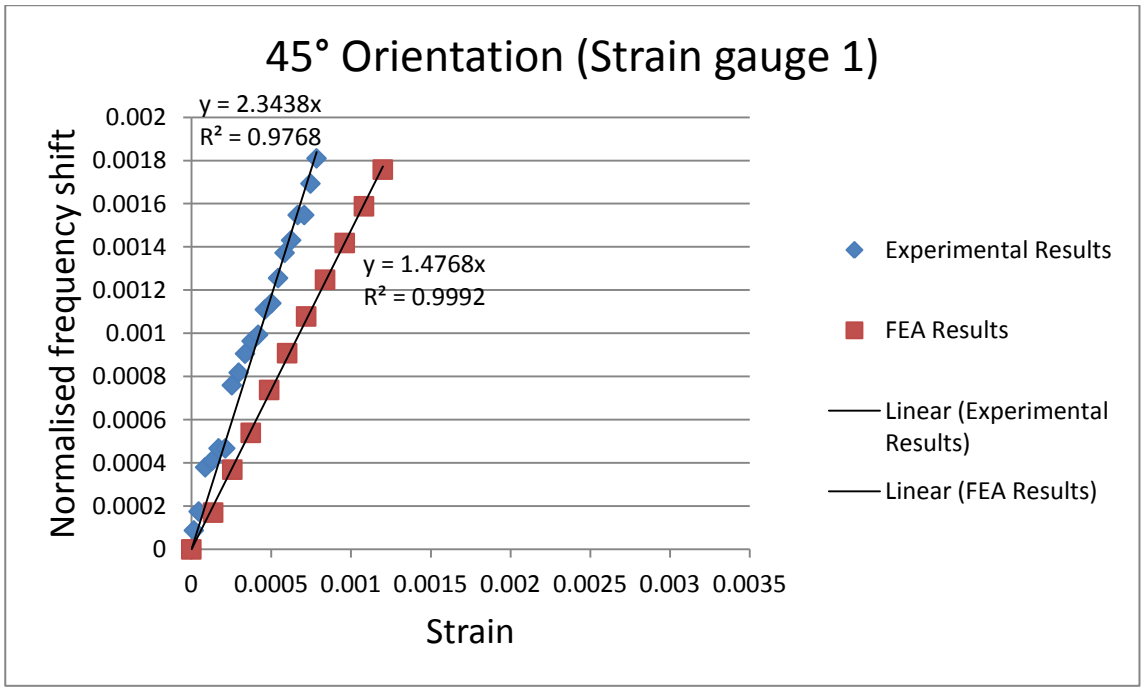

Figure 7.24 Comparison of measured and FEA results of strain and frequency shift relationship at 45° orientation for meandered patch.

The slope of the line in Figure 7.24 is higher because the strain is not the maximum in any of the four strain gauges in 45° orientation. However, Figure 7.25 shows the comparison of experimental results for all three directions which indicates the same performance for the meandered antenna in every direction. This directional strain measurement independence is

a significant advance on the strain measurement properties of the simple circular patch antenna.

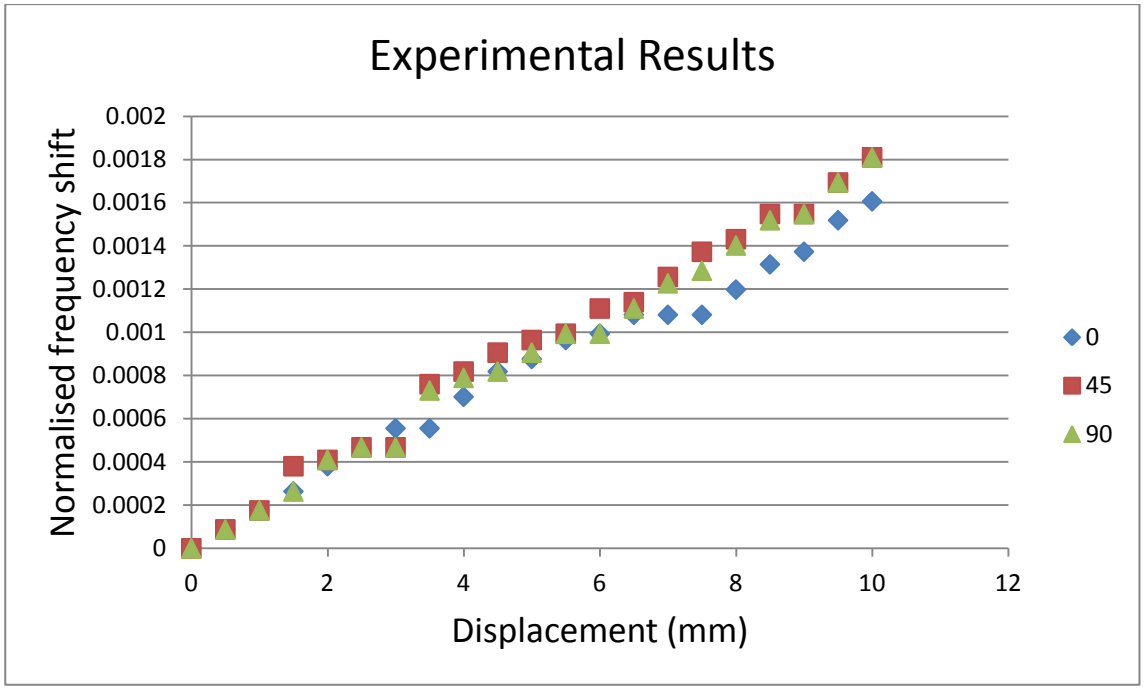

Figure 7.25 Comparison of experimental results of normalized frequency shift at different steps of bending at three different orientations for meandered patch.

Figure 7.26 compares the experimental results of both antennas attached to the aluminium plate in 90° orientation. This figure shows that the meandered patch has a more delineated response to the bending in the aluminium plate which results from its increased sensitivity. The normalised frequency shift of the circular patch at the maximum displacement is more because the operating frequencies of the circular and meandered antennas are 1.5 GHz and 3.5 GHz, respectively. However, the shift in the resonant frequency in each step of bending is 100 KHz and 300 kHz for the circular and meandered patch antennas, respectively.

In order to investigate the effect of drilled hole in the test plate on meandered antenna sensor performance, six antenna samples with same dimensions are attached to six octagon aluminium plates with different hole sizes (2.5 mm (sample 1) to 15 mm (sample 6) in 2.5 mm steps) and are tested under the same condition as other antennas. Figures 7.27 to 7.32 illustrate the strain and frequency shift relationship for the meandered circular microstrip patch antenna in -45°, 0°, 45°, and 90° orientations for samples 1 to 6, respectively; which indicate the same performance for the meandered antenna in every direction for all samples. Figures 7.33 to 7.36 show the comparison of strain-frequency shift relationship in different samples for each orientation. These figures indicate that the hole size does not have any

specific effect on the antenna sensor performance. The differences between different samples are because of manufacturing tolerances including the bonding between the antenna and the plate.

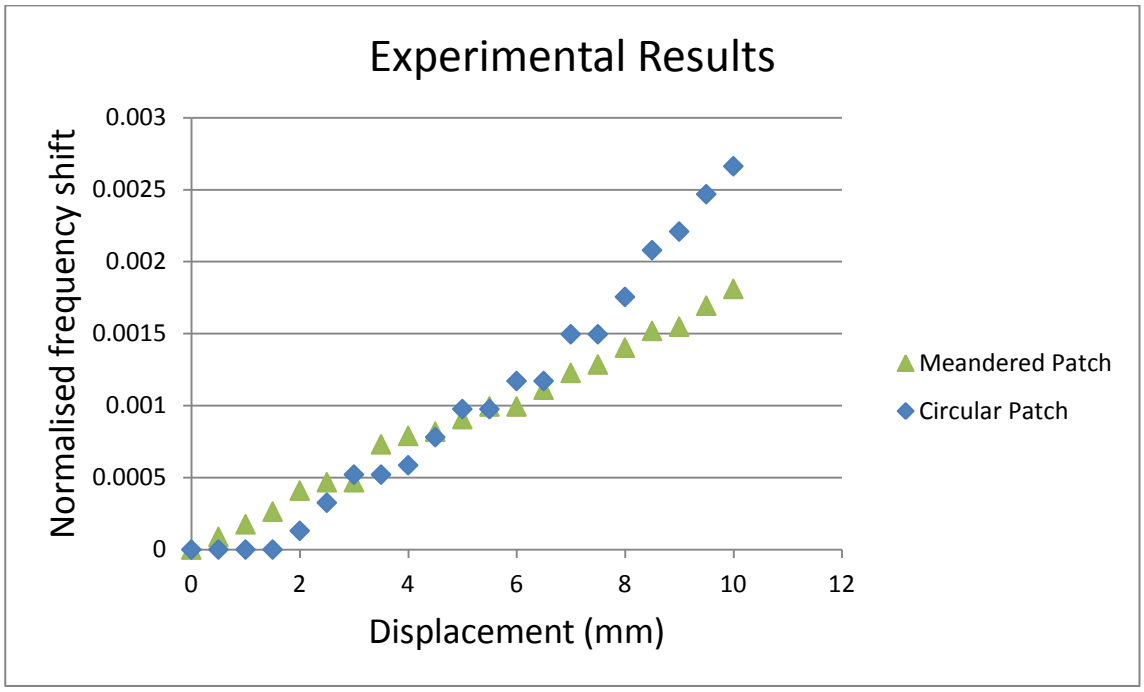

Figure 7.26 Comparison of experimental results of normalized frequency shift at different steps of bending at 90° orientation for circular and meandered patch.

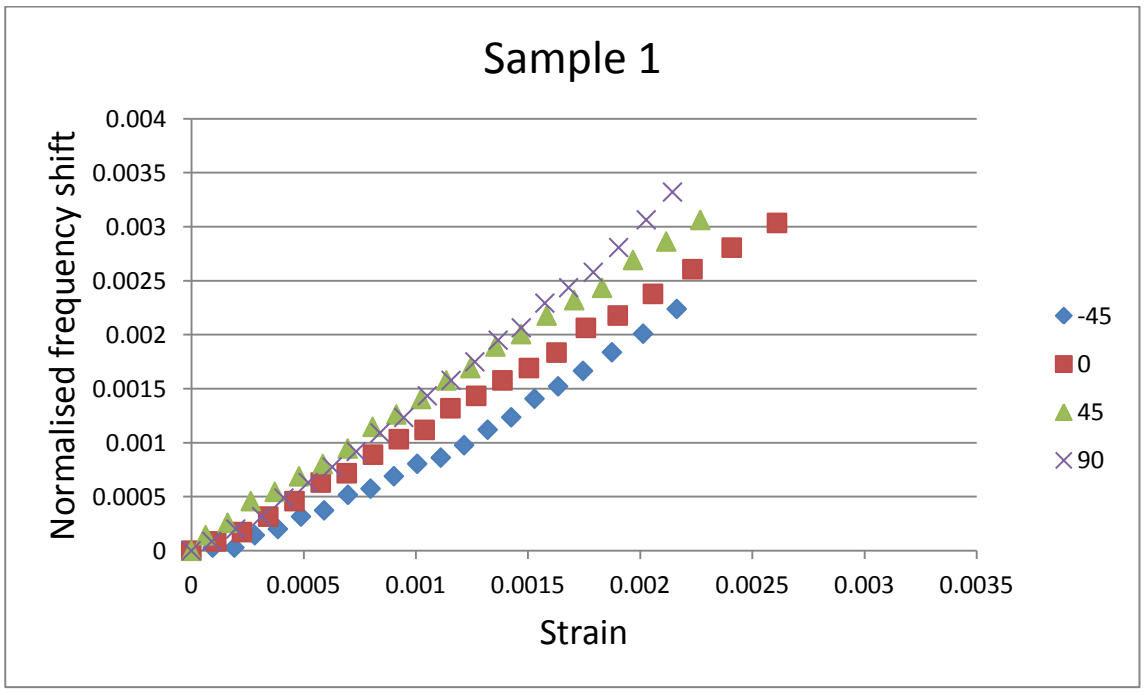

Figure 7.27 Comparison of measured results of normalized frequency shift at different steps of bending at four different orientations for meandered patch sample number 1 (hole diameter: 2.5 mm).

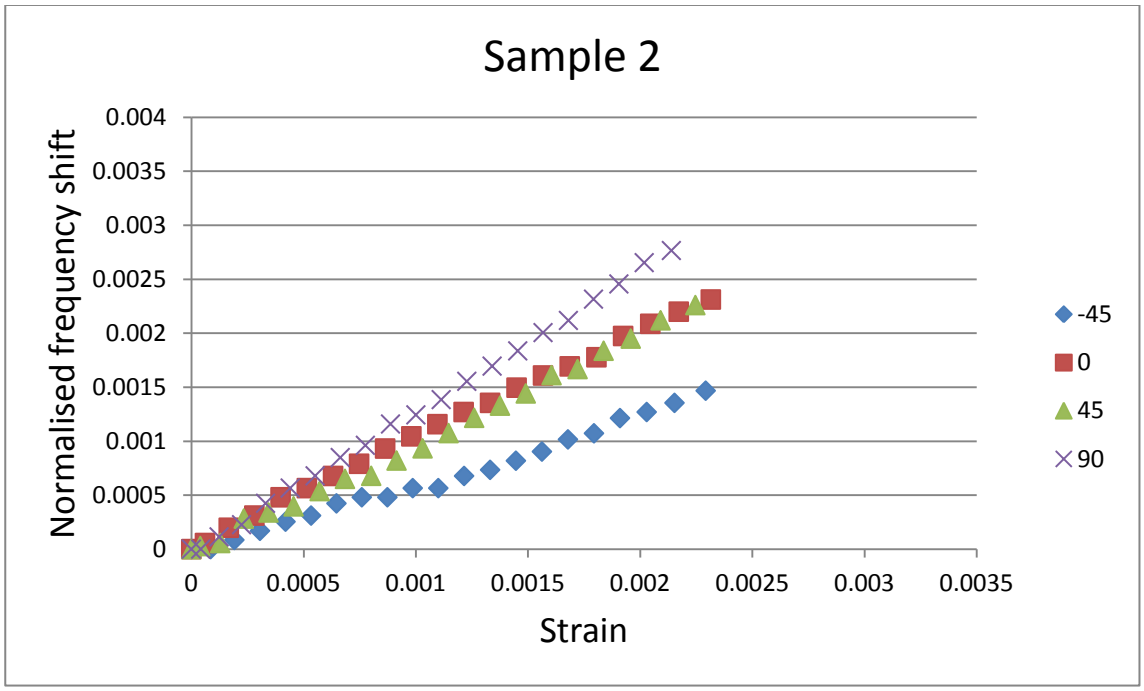

Figure 7.28 Comparison of measured results of normalized frequency shift at different steps of bending at four different orientations for meandered patch sample number 2 (hole diameter: 5 mm).

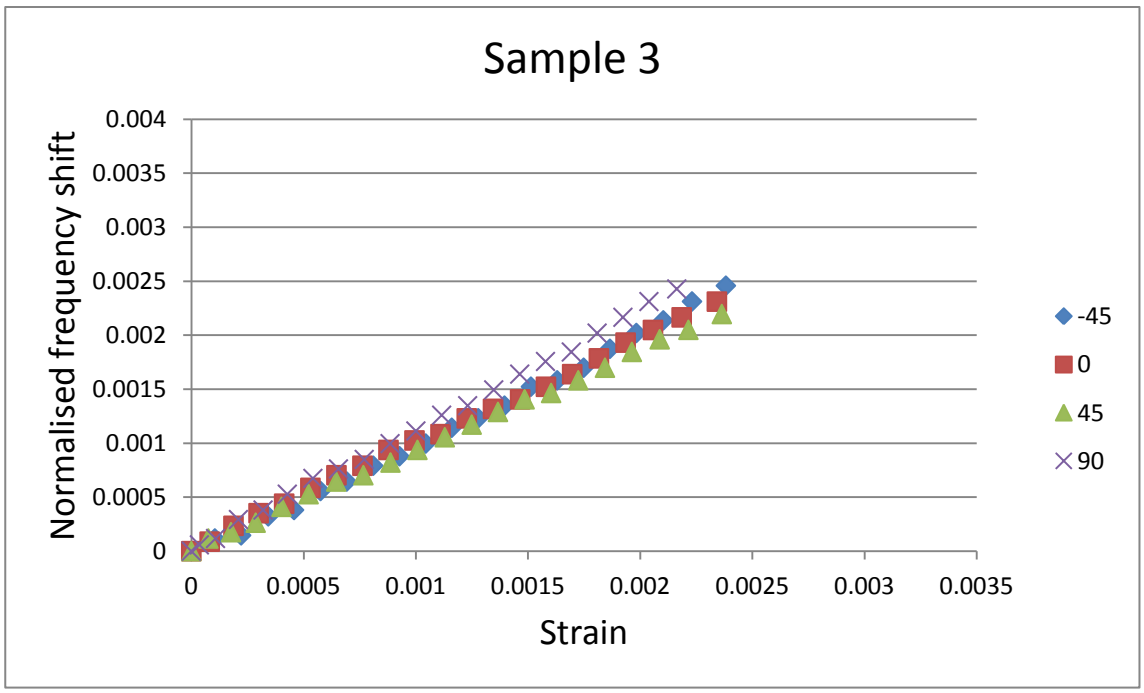

Figure 7.29 Comparison of measured results of normalized frequency shift at different steps of bending at four different orientations for meandered patch sample number 3 (hole diameter: 7.5 mm).

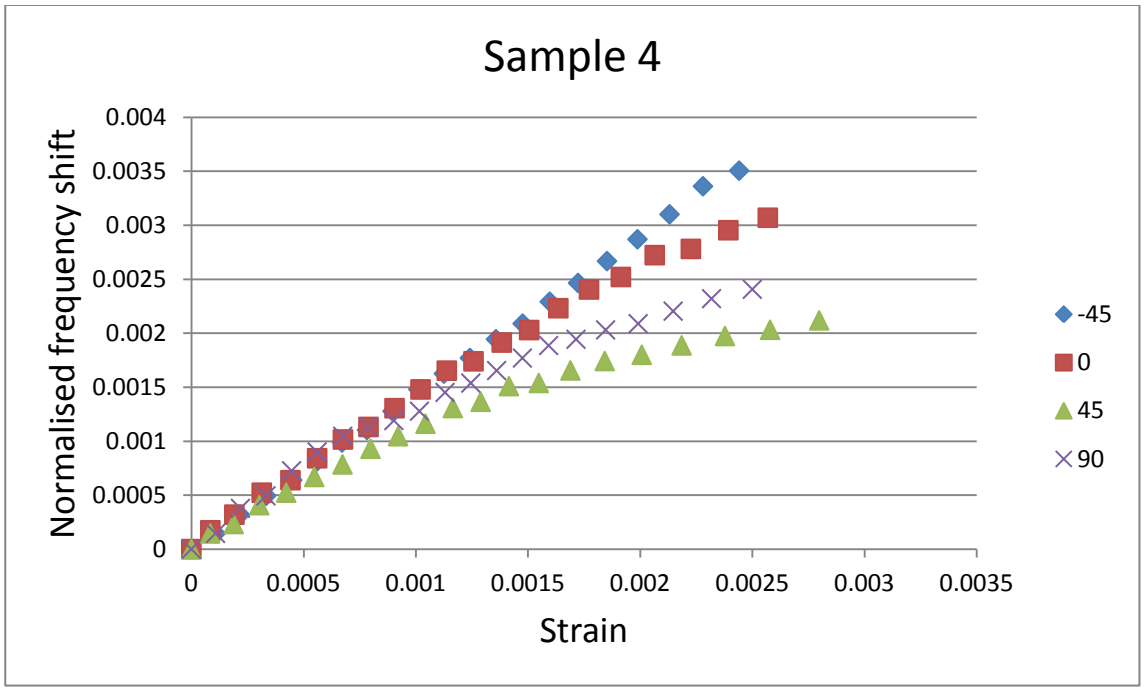

Figure 7.30 Comparison of measured results of normalized frequency shift at different steps of bending at four different orientations for meandered patch sample number 4 (hole diameter: 10 mm).

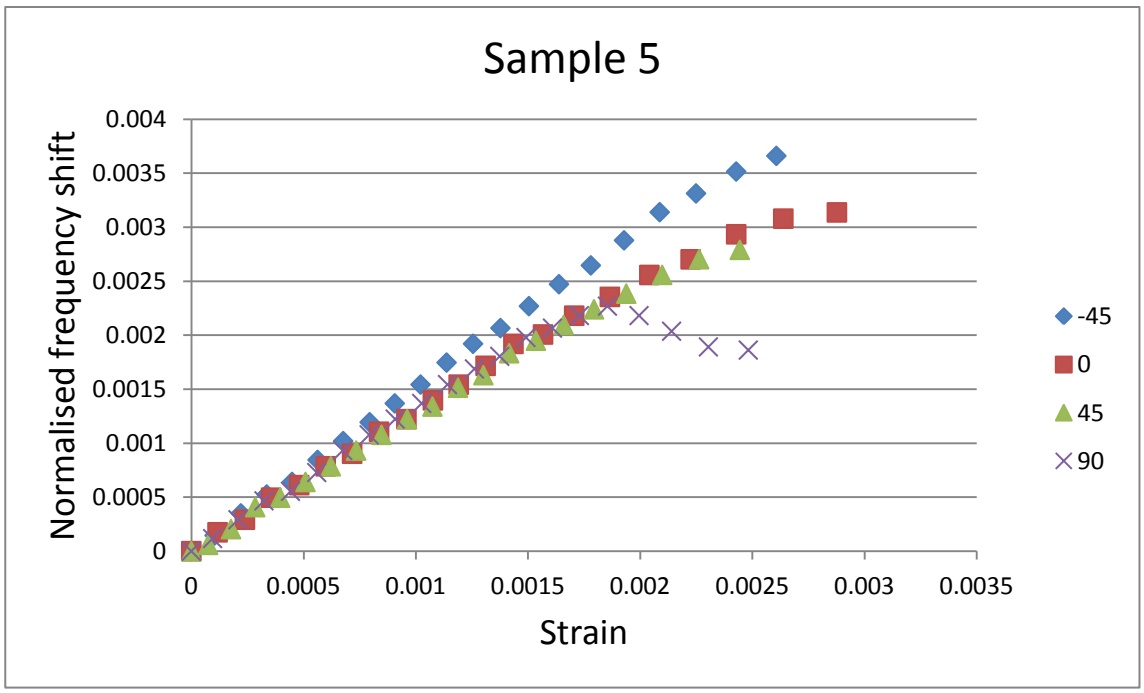

Figure 7.31 Comparison of measured results of normalized frequency shift at different steps of bending at four different orientations for meandered patch sample number 5 (hole diameter: 12.5 mm).

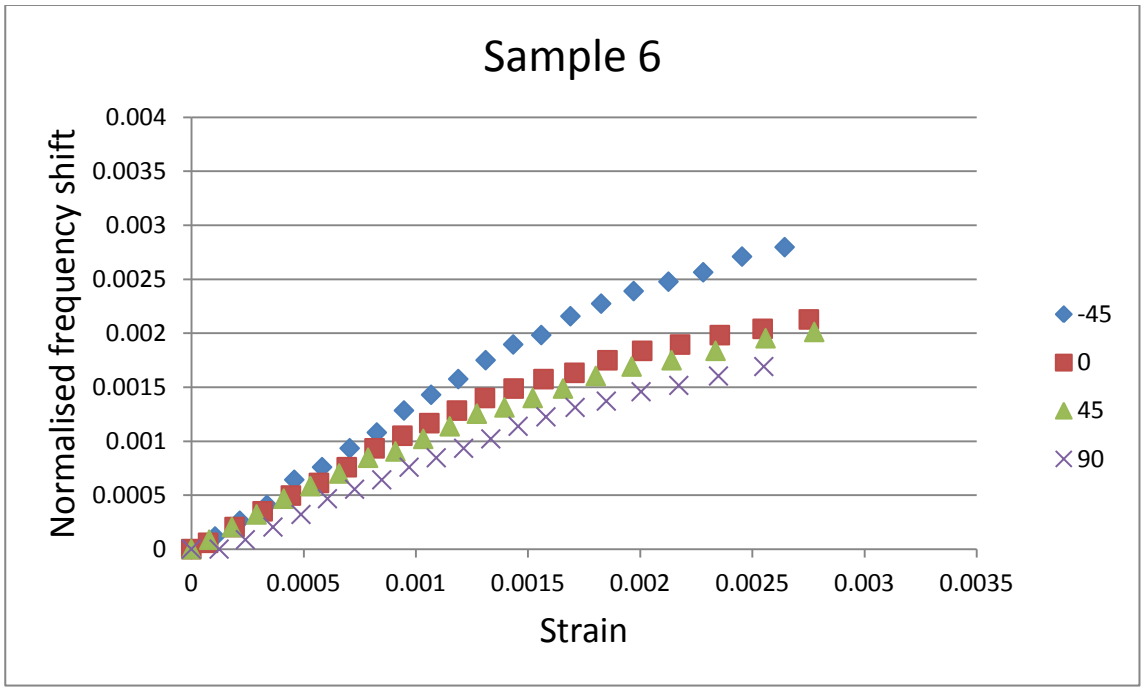

Figure 7.32 Comparison of measured results of normalized frequency shift at different steps of bending at four different orientations for meandered patch sample number 6 (hole diameter: 15 mm).

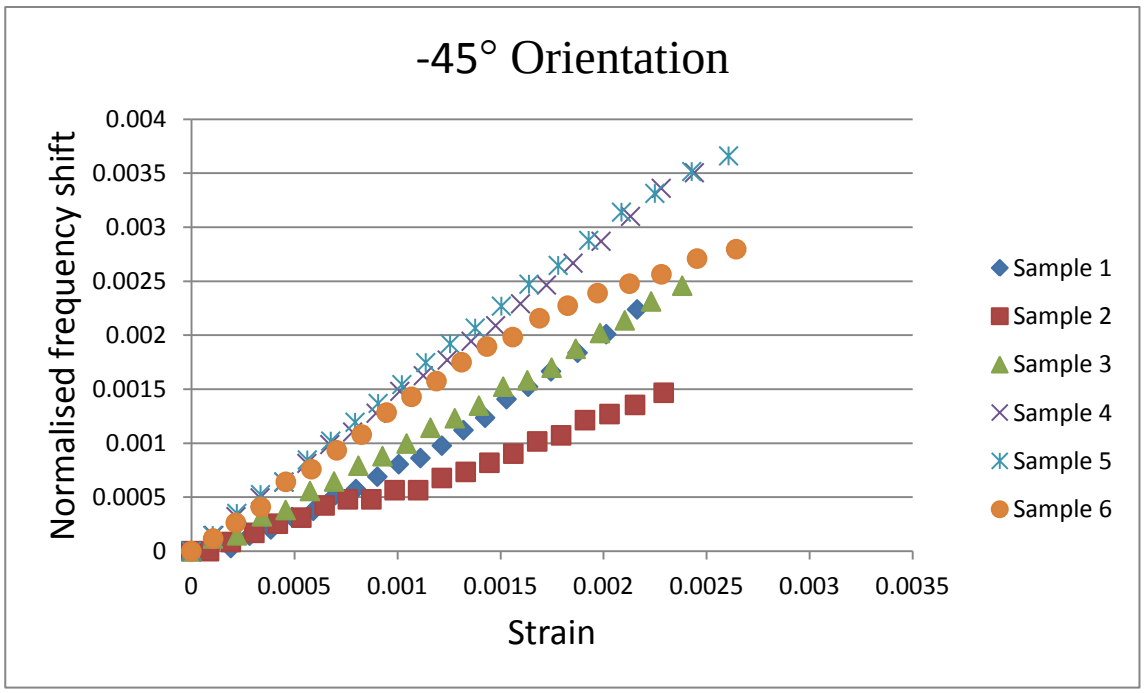

Figure 7.33 Comparison of measured results of normalized frequency shift at different steps of bending at -45° orientations for meandered patch samples number 1 to 6.

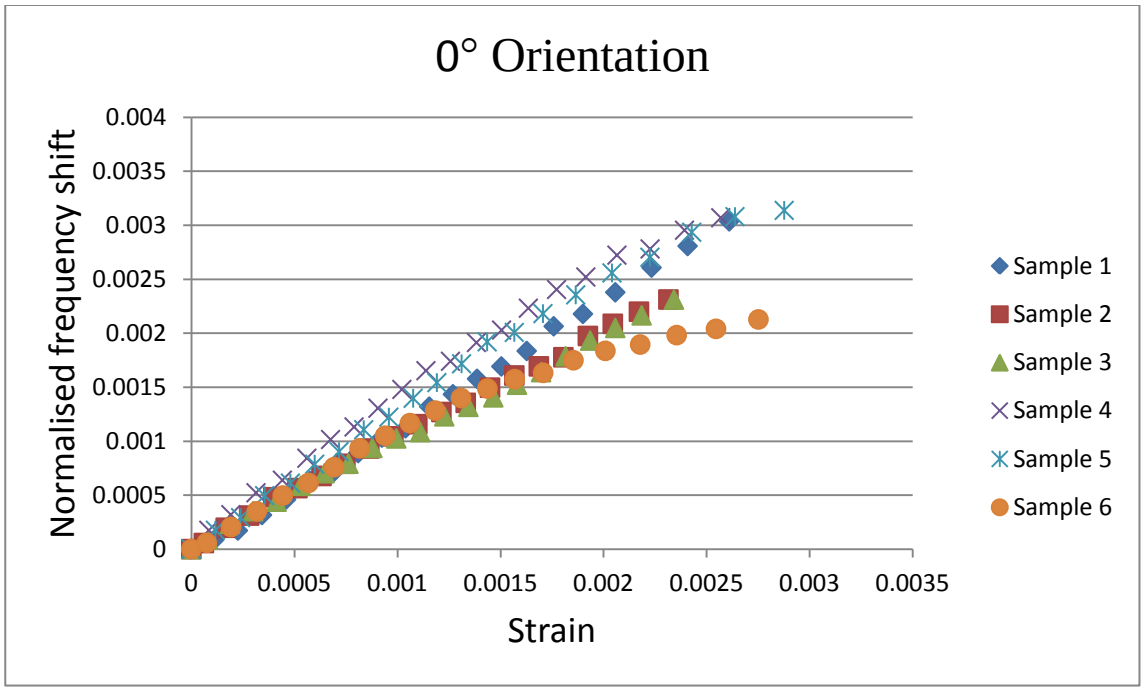

Figure 7.34 Comparison of measured results of normalized frequency shift at different steps of bending at 0° orientations for meandered patch samples number 1 to 6.

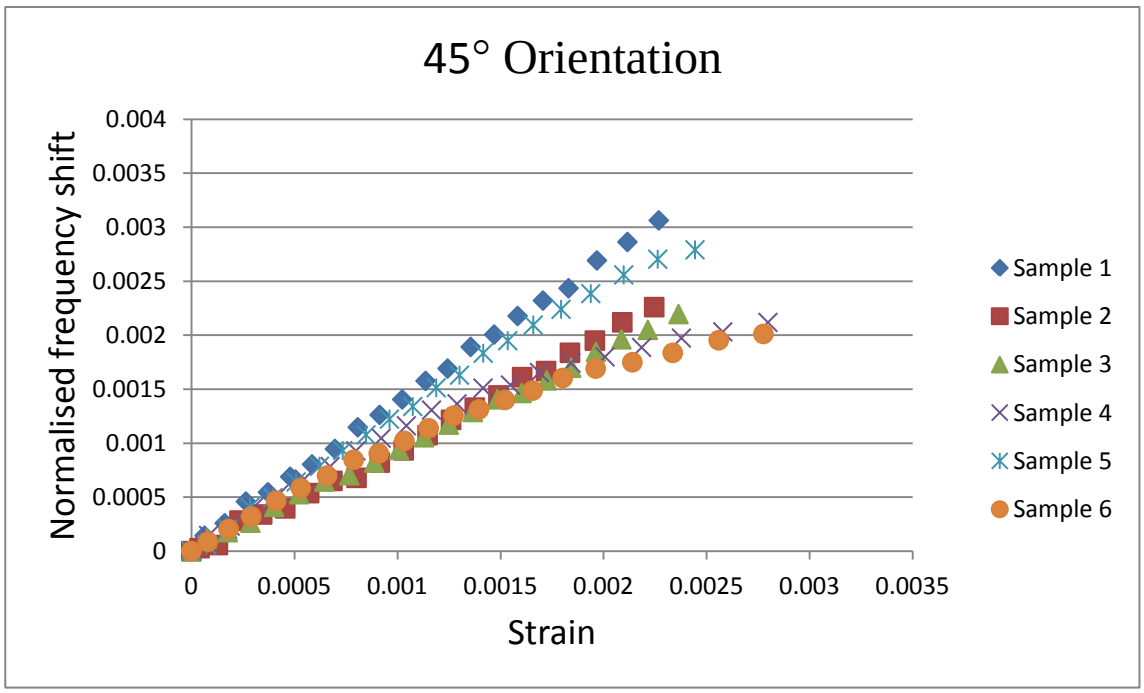

Figure 7.35 Comparison of measured results of normalized frequency shift at different steps of bending at 45° orientations for meandered patch samples number 1 to 6.

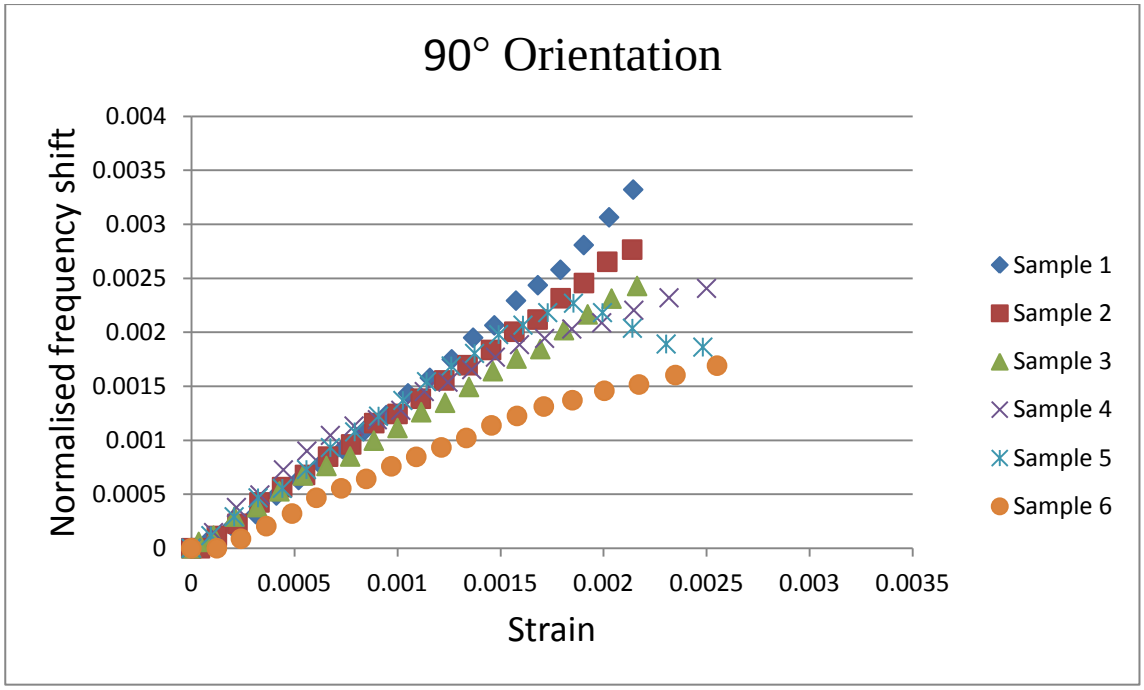

Figure 7.36 Comparison of measured results of normalized frequency shift at different steps of bending at 90° orientations for meandered patch samples number 1 to 6.

A meandered circular microstrip patch antenna is able to detect strain and possibly damage in the structure with more certainty because a similar strain results in a larger shift in the resonant frequency of the antenna. In addition, because of smaller size of the meandered antenna the measured strain is more localised.

7.5 Comparison of Different Antenna/Sensor Designs

Table 7.2 shows the comparison between three microstrip patch antennas which are investigated during this research. Circular microstrip patch antenna is able to detect strain only in two different directions and it is not sensitive enough. A slotted circular microstrip patch antenna made from same material with almost same physical size has increased sensitivity while its operating frequency is increased. Because the shift in resonant frequency in this antenna is positive in two perpendicular directions with different magnitude, this antenna could be further developed to detect magnitude and direction of strain simultaneously. This could be done by using a cross slotted circular microstrip patch antenna (Figure 7.37) and measuring the frequency of two slots.

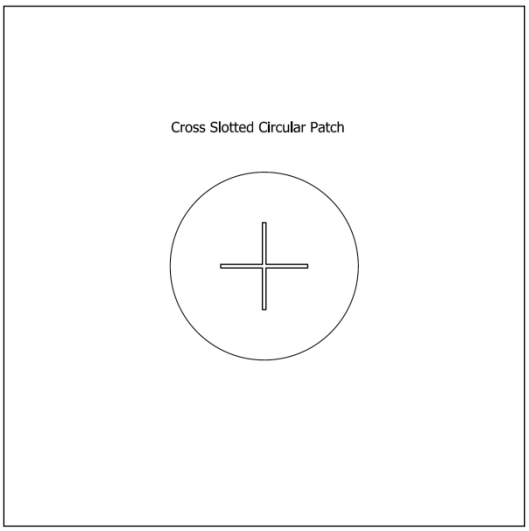

Figure 7.37 Cross slotted circular microstrip patch antenna.

Meandered circular microstrip patch antenna is a novel design which utilizes meandering technique to reduce the size of patch, and simultaneously, increase sensitivity of the antenna sensor. It is able to detect strain in any direction which is a great advantage compared to circular patch. The amount of shift in this antenna is threefold compared to circular patch and patch size is fivefold smaller. The thickness of the substrate is also smaller which results in more accurate strain measurement.

Table 7.2 Comparison between three microstrip patch antennas.

Antenna	**Circular patch**			**Slotted circular patch**			**Meandered circular patch**		
Frequency (GHz)	1.5			3.4			3.5		
Substrate size	150mm×150mm			150mm×150mm			60mm×60mm		
Patch radius	27.1mm			27.7mm			5mm		
Thickness	1.5mm			1.5mm			0.2mm		
Material	FR4			FR4			Modified FR4		
Bending Angle	0	45	90	0	45	90	0	45	90
Frequency Shift (kHz)	−100	0	+100	+200	NA	+300	+300	+300	+300

7.6 Conclusion

The results for three microstrip patch antennas which are the subject of this research are discussed in detail. The theoretical results from Chapter 4 are compared with FEA and experimental results for the circular microstrip patch antenna. In addition, the effect of different materials on strain measurement capability of this antenna is provided. Experimental results and FEA results for slotted circular microstrip patch antenna and meandered circular microstrip patch antenna are discussed in detail. The effect of load orientation on the three antenna sensors is discussed in detail. Finally, the comparison between these three antennas suggests that the meandered circular patch antenna is more suitable for localized strain measurement and can detect strain in every direction. However, the slotted circular patch with more modifications in the future could be used to detect strain magnitude and direction simultaneously.

CHAPTER 8

Wireless Strain Measurement

8.1 Introduction

In the previous chapters it is shown that microstrip patch antennas can be used for strain measurement. Finite element analysis and experimental tests show a linear relationship between strain and the resonant frequency of different microstrip patch antenna designs. Novel antenna sensor designs which increase the sensitivity of the antenna sensor and reduce its physical size show promising results.

In order to achieve the final aim of this research project which is to implement the wireless detection of strain, further studies were required to complement the work in previous chapters. This chapter includes the appropriate steps that have been taken toward achieving wireless strain measurement. Primary investigation of the feasibility of measuring the resonant frequency of circular microstrip patch antennas was the first step which is described here. By considering the effect of near field for horn antennas, the appropriate wireless reading technique was chosen which was followed by finite element analysis. The final step was the evaluation and demonstration of wireless strain measurements with experiments. These steps are described in detail in this chapter.

8.2 Wireless Reading of Circular Microstrip Patch Antenna Resonant Frequency

In order to investigate the feasibility of measuring the resonant frequency of circular microstrip patch antennas wirelessly, a primary experimental study was conducted. The aim of this study was to develop a technique to read the resonant frequency using horn antennas which are standard antennas for antenna measurements. The most difficult challenge toward this goal is the effect of the back plate material which the antenna sensor needs to be attached to. Most of aerospace structures are made from metals especially aluminium alloys

or most recently carbon fibre reinforced polymers (CFRP). The electrical conductivity of metals as well as CFRP introduces an obstacle toward wireless measurement. This is because conductive materials reflect the electromagnetic wave back to the source. In addition, the size of the back plate is large compared to the antenna sensor; hence, the reflected (backscattered) wave from the sensor is not distinguishable from the reflected wave of the back plate.

In order to overcome this problem, the configuration illustrated in Figure 8.1 is used to separate two mentioned segments of the reflected wave and read the resonant frequency of the antenna/sensor. In this configuration two horn antennas are placed with the relative angle of 90° to each other and the relative angle of 45° to the test plate. As a result of this configuration the backscattered wave from the back plate and the antenna will be separated. One horn antenna acts as a transmitter and the other one act as the receiver antenna while the resonant frequency of the patch antenna can be measured by measuring the transmission coefficient between these two horn antennas.

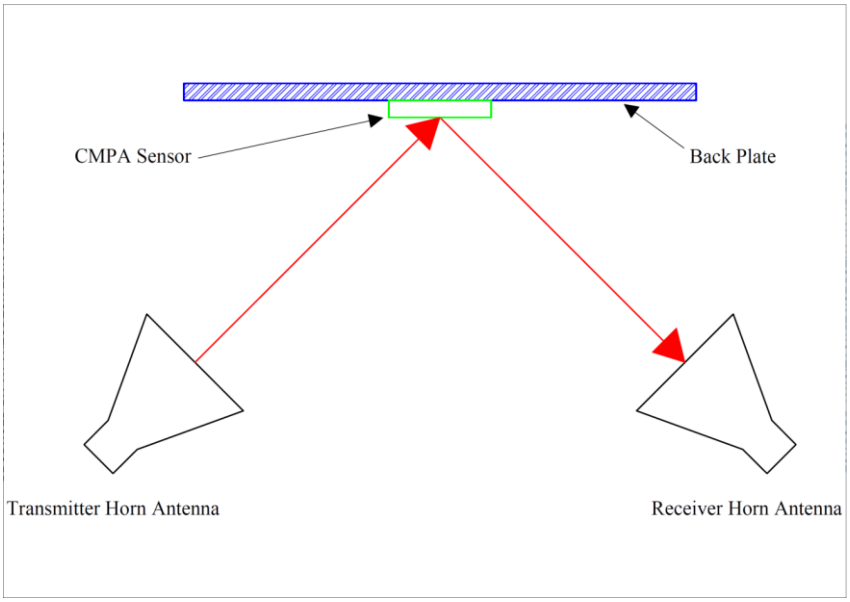

Figure 8.1 Two horn configuration for wireless measurement of CMPA resonant frequency.

If the horn antennas are with the relative angle of 180° and both look at the sensor and back plate with a 0° angle, then it is not possible to see the resonant frequency of the patch antenna by measuring the transmission coefficient of the horn antennas even when the back plate is not conductive. This matter has been investigated experimentally using a circular microstrip patch antenna. The final setup configuration for this test is shown in Figure 8.2.

The horn antennas used for this research are broadband horn antenna model DRH-118™ from Sunol Sciences™ (1-18 GHz, Transmit/Receive).

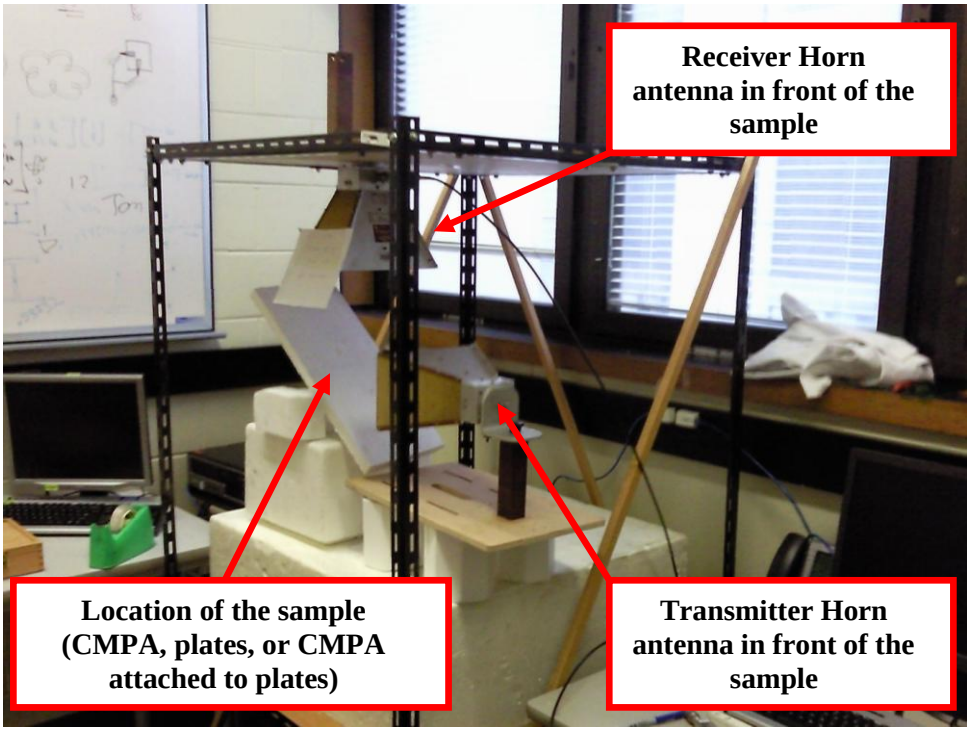

Figure 8.2 Final setup for wireless measurement using the two horn configuration.

The resonant frequency of circular microstrip patch antenna attached to three different plates made from aluminium, CFRP and fibre glass which is measured by connecting a coaxial cable to the back of the antenna is shown in Figure 8.3. These resonant frequencies are used as reference to see if the resonant frequency of CMPA can be located using the proposed technique.

Figure 8.4 shows the comparison of the transmission coefficient of horn antennas when the CMPA is placed in front of two horn antennas for two different configurations. First, back of the CMPA is faced toward transmitted signal which means a conductive plate is in front of the signal. Then, the circular patch is facing the transmitted signal. The comparison of these two configurations can indicate whether there is a difference between the backscatter signals for a conductive plate compared to a circular microstrip patch antenna.

The results show that when the circular patch is facing the transmitted signal there is a dip in the curve of transmission coefficient exactly at the resonant frequency of the patch antenna. This suggests that the resonant frequency of the patch antenna can be measured wirelessly by using two horn antennas. In order to investigate the effect of back plate material the

experiment was repeated for an aluminium plate, a CFRP plate and a fibre glass plate when there is no CMPA attached to them compared to when there is a CMPA attached to the plate. Similar results (Figures 8.5 to 8.7) are obtained from these experiments which show that using the proposed technique, regardless of the back plate material, the resonant frequency of the CMPA can be measured wirelessly.

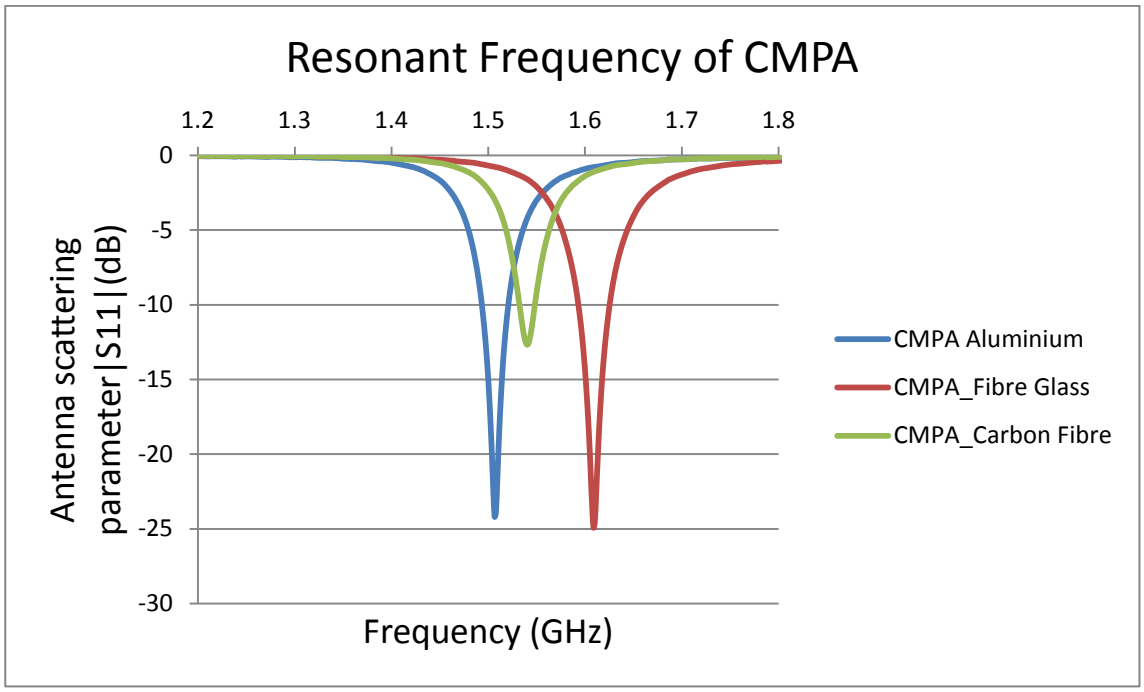

Figure 8.3 Resonant frequency of CMPA attached to three plates with different materials (measured by connecting a coaxial cable to the CMPA).

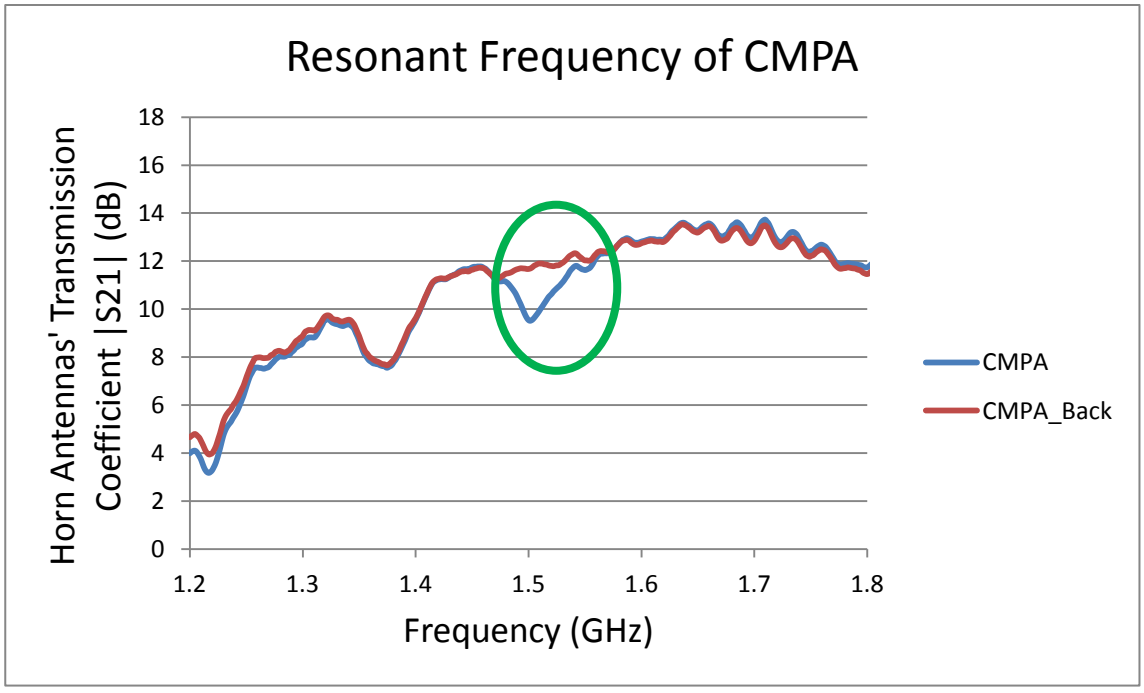

Figure 8.4 Transmision coeficeint of two horn antennas in front of CMPA/CMPA_back.

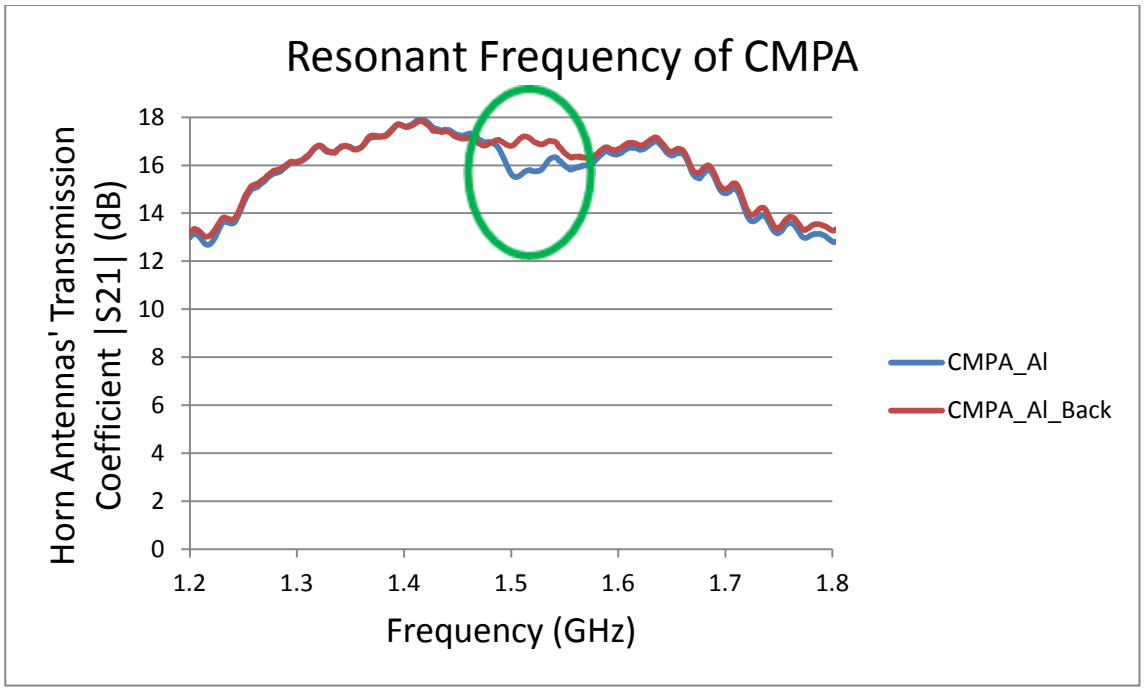

Figure 8.5 Transmision coeficeint of two horn antennas in front of CMPA/Aluminium plate.

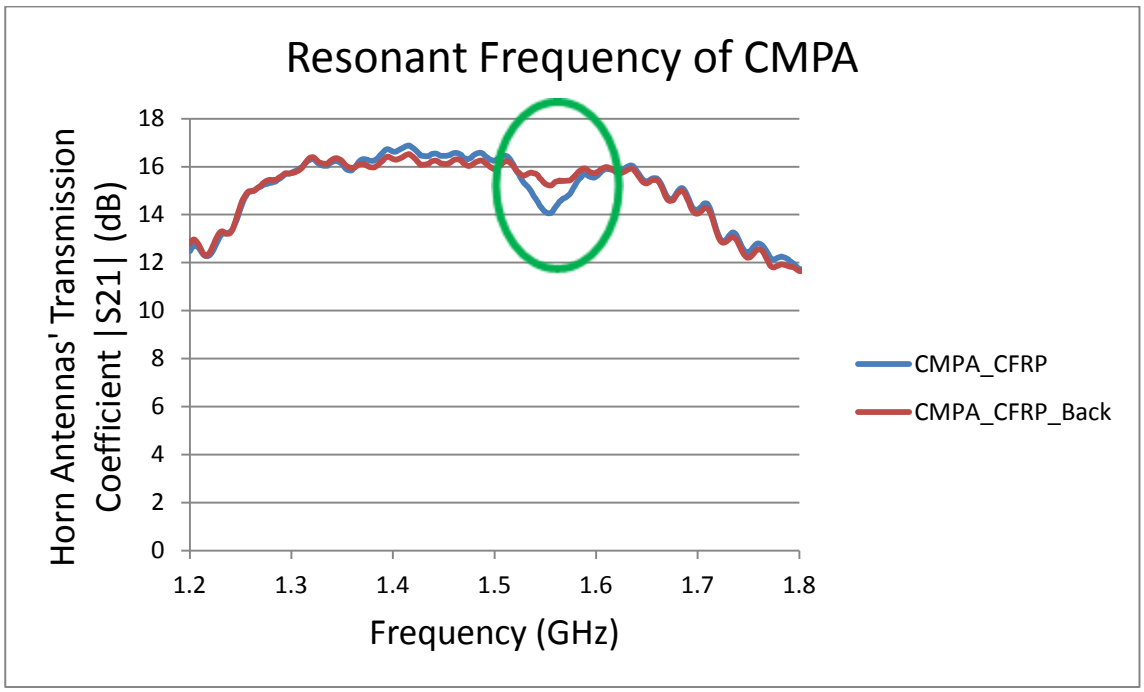

Figure 8.6 Transmision coeficeint of two horn antennas in front of CMPA/CFRP plate.

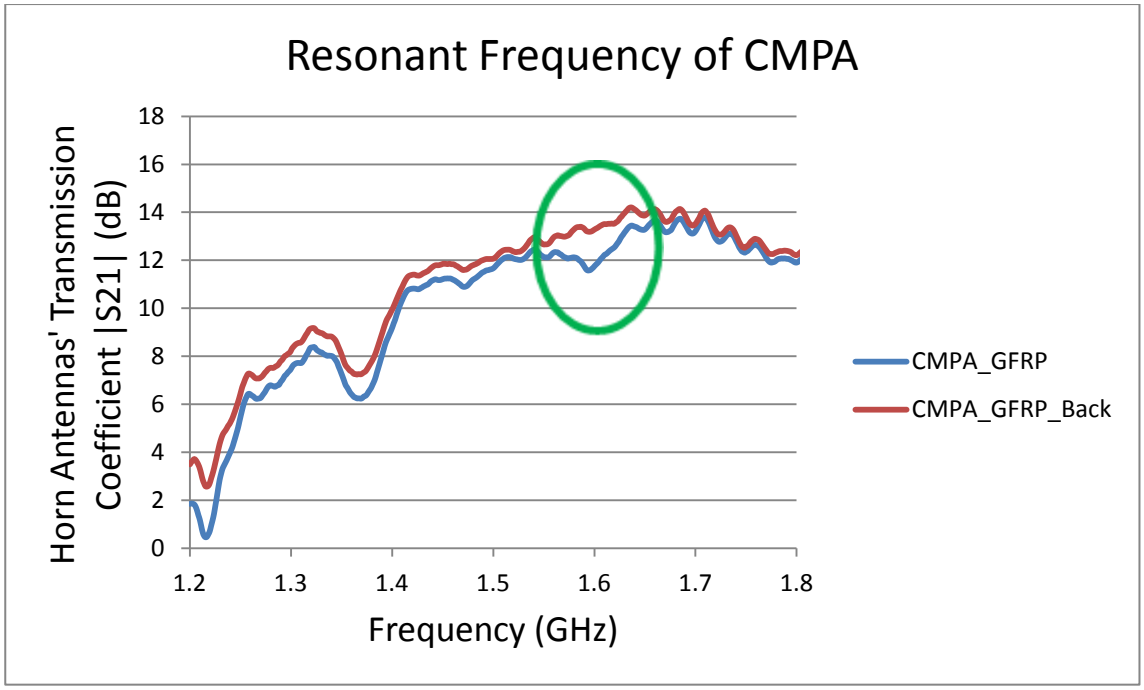

Figure 8.7 Transmision coeficeint of two horn antennas in front of CMPA/GFRP plate.

Based on the aforementioned results new set of experiments were conducted to investigate the feasibility of wireless strain measurement using the proposed technique. When strain was applied to the structure by stretching the back plates an overall shift in the transmission coefficient curve was observed. However, because the magnitude of the dip in the S21 curve is about 2 dB, it was not possible to measure the change in the minimum of the S21 curve at the location of resonant and measure the shift in the resonant frequency of the CMPA sensor. Therefore, it was decided to study the operational principles of horn antennas with regard to the radiated fields. The result of this study is presented in the following subsection.

8.3 Near Field and Far Field Conditions

The electromagnetic field in the surrounding space of an antenna can exist in three different forms. These forms depend on the distance of the measuring point from the antenna and therefore divide the space around the antenna into three regions (Figure 8.8); namely, Reactive Near-Field, Radiating Near-Field (Fresnel) and Far-Field (Fraunhofer) (Balanis, 2005).

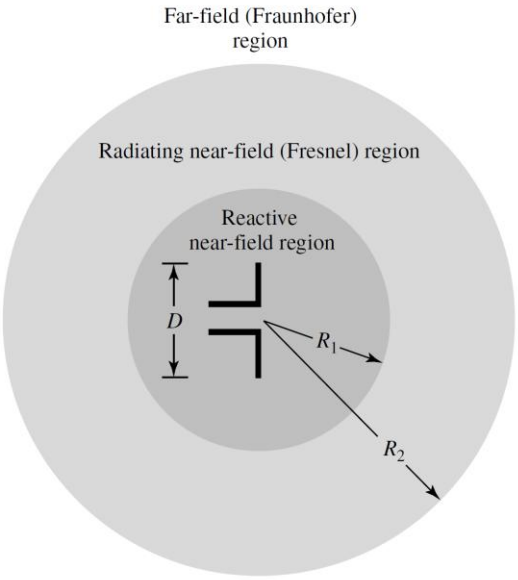

Figure 8.8 Three regions of electromagnetic field in the surrounding space of an antenna (Balanis, 2005).

Reactive near-field region is "that portion of the near-field region immediately surrounding the antenna wherein the reactive field predominates." The outer boundary of this region is at the distance $R_1 < 0.62\sqrt{\frac{D^3}{\lambda}}$ (Balanis, 2005), where

λ is the wavelength;

And

D is the largest dimension of the antenna.

Radiating near-field (Fresnel) region is "that region of the field of an antenna between the reactive near-field region and the far-field region wherein radiation fields predominate and wherein the angular field distribution is dependent upon the distance from the antenna." And Far-field (Fraunhofer) region is "that region of the field of an antenna where the angular field distribution is essentially independent of the distance from the antenna." The inner boundary of this region is at the distance $R_2 > \frac{2D^2}{\lambda}$ (Balanis, 2005).

Therefore, for the horn antenna used in this research with the maximum dimension of 24 cm the boundary between these regions at the frequency of 1.5 GHz can be defined as:

$R_1 = 16.3\,\text{cm}$ and $R_2 = 57.6\,\text{cm}$.

The amplitude pattern of an antenna changes from reactive near-field toward the far-field region of the antenna (Figure 8.9). As it is shown in Figure 8.9, in the reactive near-field region the pattern is nearly uniform with slight variations. However, by moving toward the far-field region the pattern starts to form lobes and become directional (Balanis, 2005). This phenomenon indicates that in near-field region especially in the reactive near-field region the magnitude of the antenna fields are uniform in different directions.

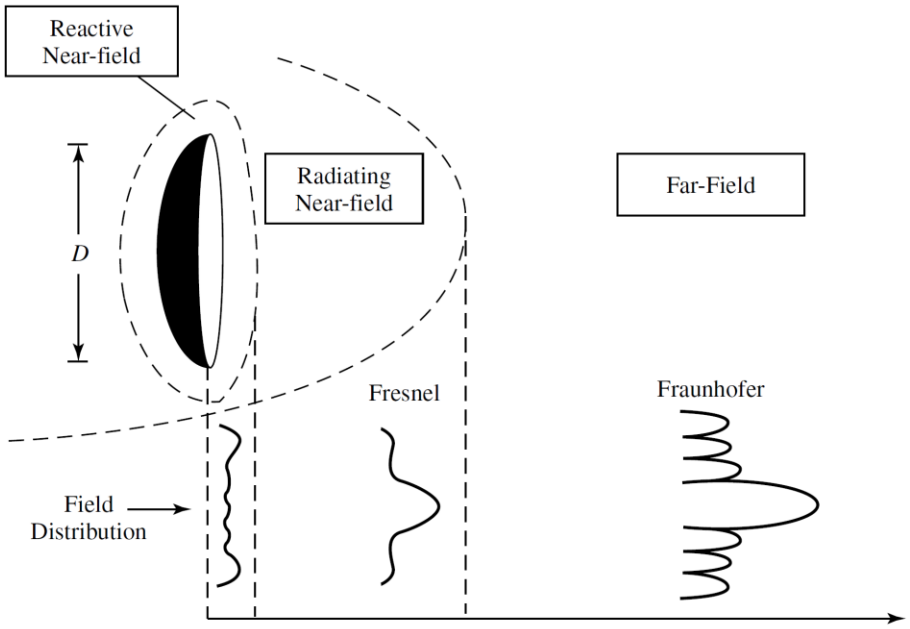

Figure 8.9 The amplitude pattern of an antenna in three different electromagnetic field regions (Balanis, 2005).

In an spherical coordinate system the electric field can be expressed as three different components including E_r, E_ϕ and E_θ. Therefore, the magnitude of the electric field can be calculated by the following equation (Balanis, 2005):

$$|E| = \sqrt{|E_r|^2 + |E_\phi|^2 + |E_\theta|^2} \qquad (8.1)$$

In the near-field region E_ϕ is zero and the dominant term is E_r; however, by moving toward the far-field region E_r starts to become smaller and finally disappear. As a result, in far-field region the term E_r becomes zero and the only element of the electric field is E_θ. This is because E_r is inversely proportional to square of the distance from the antenna (r^2) whereas the E_θ is inversely proportional to the distance from the antenna (r) (Balanis, 2005). This results in a larger magnitude of electric field in the near-field of the antenna.

It should be mentioned that in both near-field and far-field of the antenna the magnitude of electric field reduces by moving away from the source antenna. However, this variation has a larger gradient in the near-field. This phenomenon is illustrated below, in Figure 8.10. In this graph the variation in the magnitude of electric and magnetic field of an antenna are depicted compared to the normalised distance from the antenna. The distance is normalised using Beta which is the wave number and is dependent on the frequency of operation. Therefore, the results are independent from the operation frequency (Huang, 2008).

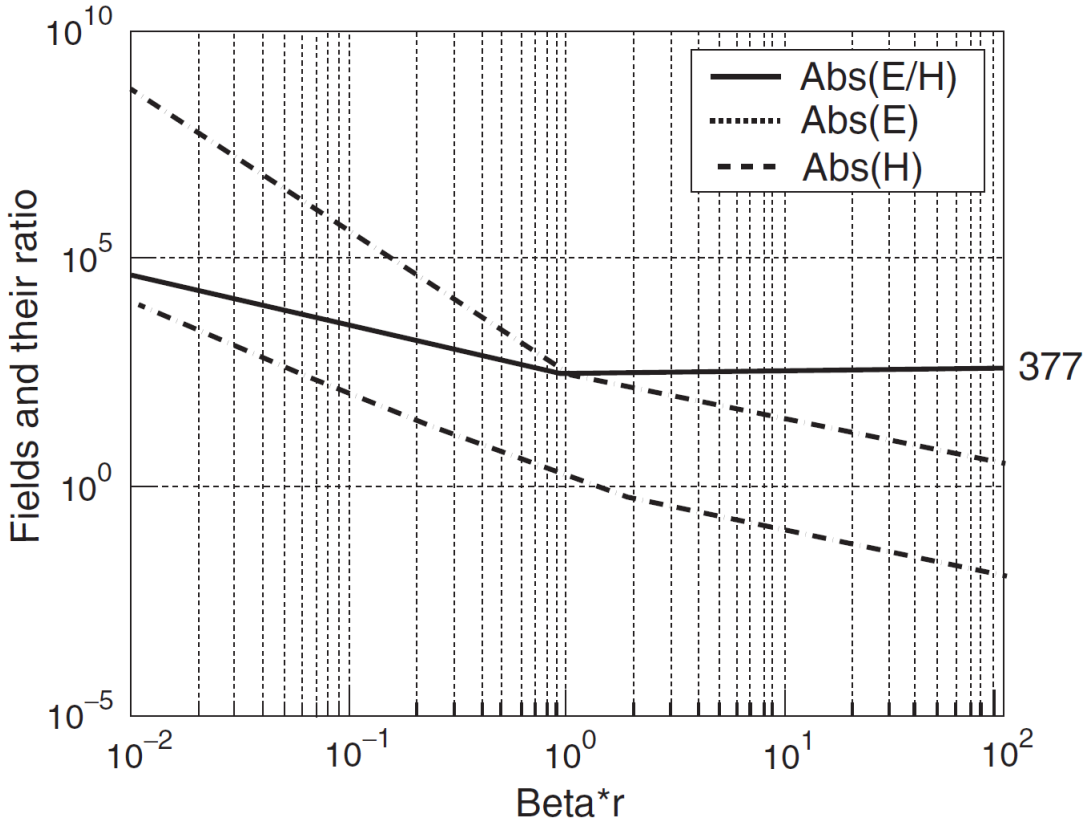

Figure 8.10 Variation in the magnitude of electric and magnetic field of an antenna against the normalised distance from the antenna (Huang, 2008).

Based on the above discussion, it was decided to measure the resonant frequency of the circular microstrip patch antenna in the near-field of the horn antenna. As a result of this change the effect of wave attenuation and the effect of noise in the environment will be minimised. In addition, because the measurements must be in close proximity of the horn antenna, only one horn antenna should be used as both the transmitter and the receiver antennas (using the backscattering technique). In order to investigate the effect of near-field a more detailed study using finite element analysis is required before progressing toward experimental measurements. This is explained in the following subsection.

8.4 Finite Element Analysis

In order to investigate the effect of horn antenna near-field region on wireless measurement of CMPA resonant frequency and subsequently the wireless strain measurement HFSS™ software was used. The available excitation sources in HFSS™ software and similar simulation packages that can be applied to the simulation environment are limited to standard ports including wave port, lumped port, plane wave and so on. These standard ports do not take the effect of horn antenna near field into account and the applied excitation is an ideal port which can be used for simulating antenna far-field.

Therefore, in order to simulate the near-field of the horn antenna, the full model of the horn antenna must be included in the simulation environment. As a result, the exact dimensions of the horn antenna are required to model the near-field accurately. The following subsections describe the modelling of the horn antenna and finite element analysis of the CMPA exited by the horn antenna.

8.4.1 Modelling of the Horn Antenna

In order to accurately model the horn antenna to be used in FEA by HFSS™ software, a combination of three different approaches were used. Some of the dimensions of the antenna were obtained from a paper by Kerr (1973) which is a technical paper provided to the author by the help of Sunol Sciences™. In addition some of the outer dimensions of the antenna were measured using a digital calliper. However, because the horn antenna includes many details which their exact dimensions are not provided in Kerr (1973) and it is not possible to accurately measure those dimensions another technique is required.

In order measure the horn antenna dimensions, an image processing software can be used to model the antenna in a 3D environment by taking several pictures from the antenna. Then this 3D model can be used for further measurement and accurate modelling of the horn antenna in HFSS™ software. Among the available image processing software in the market, Autodesk Project Photofly™ version 2.0.0.103 was chosen due to its accuracy, availability and user friendly environment.

3D modelling process using Autodesk Project Photofly™ include the following steps:

1. Downloading and installing Autodesk Photo Scene Editor™ Software from Autodesk™ website. This software was used to upload photos and further edit the 3D model.
2. More than 400 photos were taken from the horn antenna from different angles. The object which is required to be modelled (horn antenna in this project) needs to be fixed and do not move. The pictures must cover the object in 360 degree 3D environment. Also, some extra pictures are required for locations were more precision in required.
3. The pictures were uploaded to Autodesk™ server using the Autodesk Photo Scene Editor™ and the 3D mesh generated by the cloud computer was downloaded.
4. Further manual editing was required to insure the accuracy of the model.
5. The final accurate mesh was generated by the Autodesk™ server and used for final modelling of the horn antenna.

Figure 8.11 shows the Autodesk Photo Scene Editor™ environment including the horn antenna pictures and 3D model. The final model of the horn antenna in HFSS™ software is shown in Figures 8.12 to 8.14.

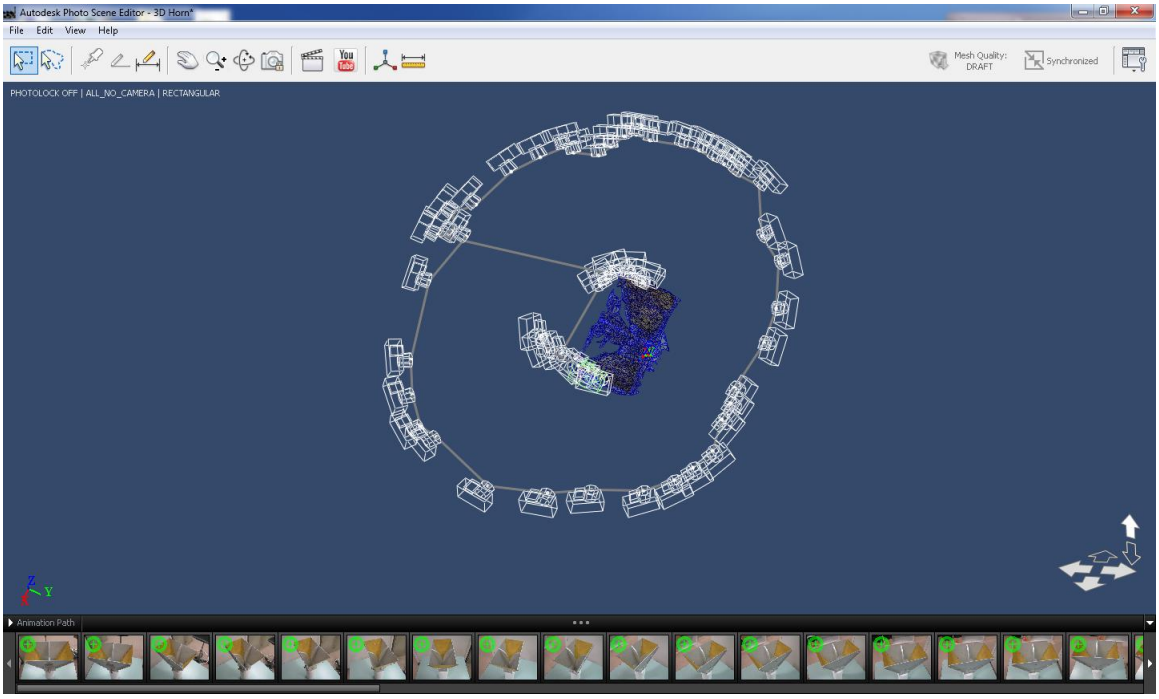

Figure 8.11 The Autodesk Photo Scene Editor™ environment.

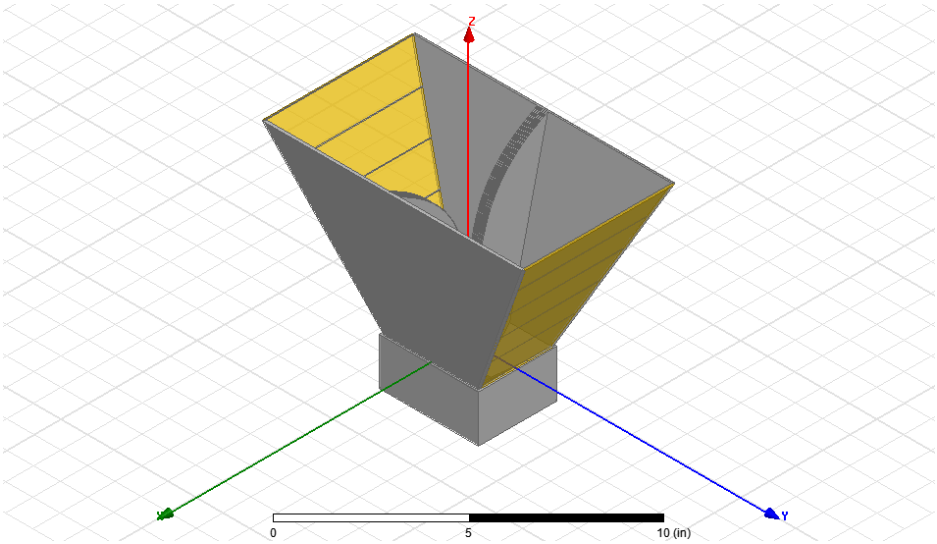

Figure 8.12 The final model of the horn antenna (View 1).

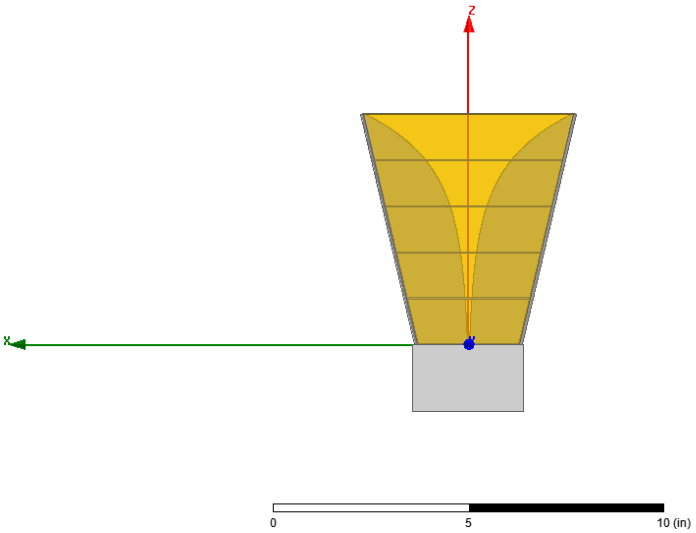

Figure 8.13 The final model of the horn antenna (View 2).

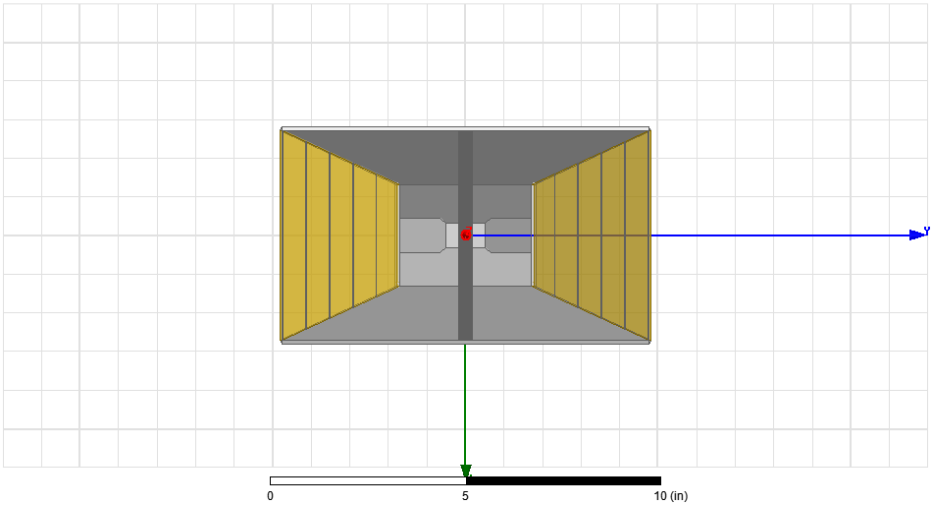

Figure 8.14 The final model of the horn antenna (View 3).

8.4.2 Patch Excitation and Strain Measurement

The 3D model of the horn antenna was created and simulated in the HFSS™ software and the results were compared to the manufacturer's information to insure the accuracy of the model. In modelling the horn antenna, PML layers were used as absorbing boundary condition and the antenna was fed using a 50 ohm wave port at the location of coaxial feed of the horn antenna.

The gain of the modelled horn antenna is shown in Figure 8.15 which shows the maximum of 9.3434 dB for the antenna when there is no object in front of it. Next, a 35 cm×35 cm aluminium plate was placed in front of the horn antenna with the distance of 1 cm from the aperture of the horn antenna. The size of the aluminium plate is according to test plates and the distance is chosen to make sure the plate is in the near field of the antenna. The gain of the horn antenna with the aluminium plate in front of it is shown in Figure 8.16. It is apparent that the maximum gain of the antenna is in the opposite direction compared to a standalone horn antenna. This is because most of the radiated electromagnetic wave is reflected by the conductive plate. The maximum gain in this case is 6.4953 dB which is 2.8481 dB lower than the previous gain. This reduction in gain is because of the scattering of the electromagnetic wave by the aluminium plate. In addition, some of the energy goes back into the horn antenna.

In the next step, a layer of FR4 substrate is added to the centre of the aluminium plate in front of the horn antenna. The dimensions of the substrate material are according to the CMPA sensors designed and fabricated in previous stages of the research (150 mm×150 mm×1.5 mm). Figure 8.17 shows the gain of the horn antenna in this configuration. While the radiation pattern of the antenna is not changed significantly, the maximum gain is reduced by the amount of 0.0549 dB to 6.4404 dB. This small reduction in gain is because of the loss in dielectric material and also the backscattering caused by the substrate geometry.

In the two steps describe above the assembly in front of the horn antenna is not a microstrip patch antenna. In order to make a circular microstrip patch antenna a layer of copper needs to be added on top of the substrate material to model the CMPA sensor. After adding the circular patch and conducting the simulation, the gain of the antenna was changed to 4.3457 dB. This is a 2.0947 dB reduction in the gain which is caused by the excitation of the patch

antenna by the radiated field of the horn antenna (Figure 8.18). Figure 8.19 shows the contour of electric field on the patch surface which is because of excitation by the horn antenna.

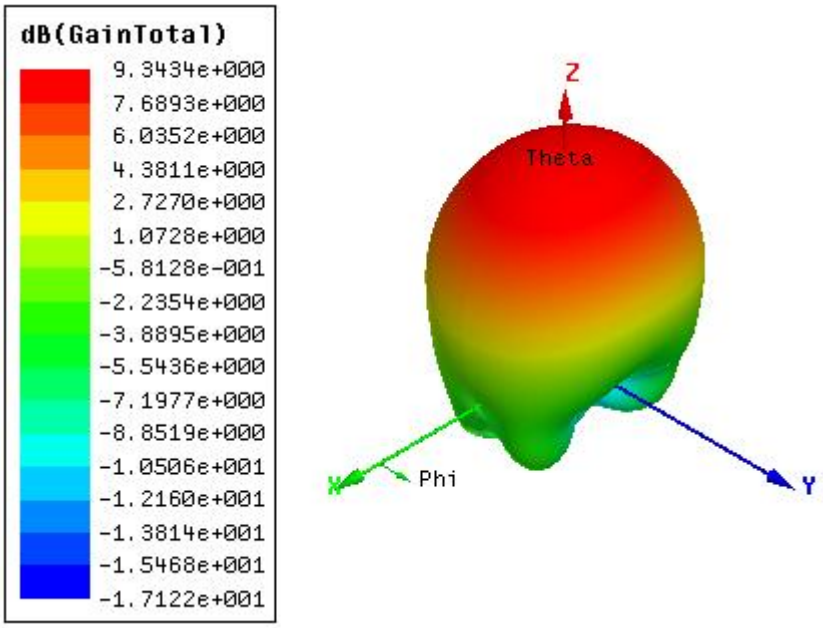

Figure 8.15 The gain of the horn antenna (faced toward free space).

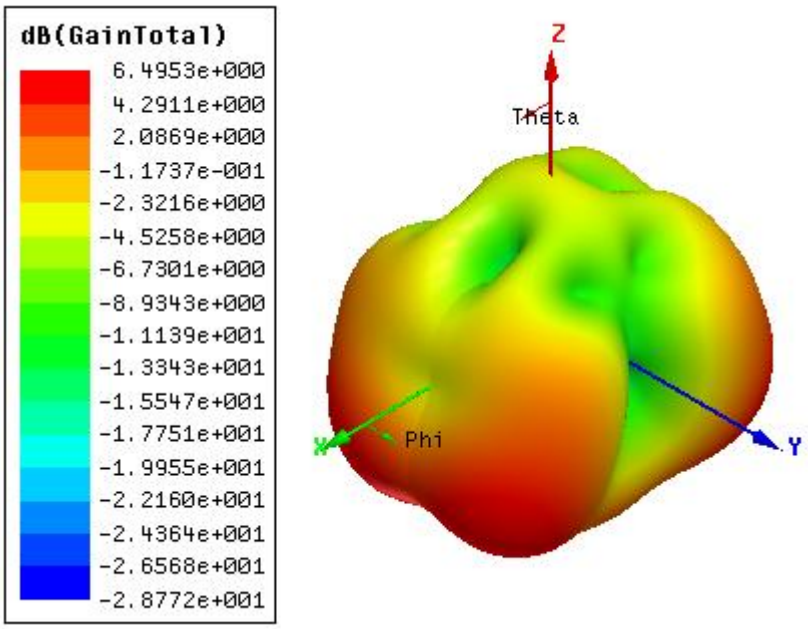

Figure 8.16 The gain of the horn antenna (faced toward an aluminium plate).

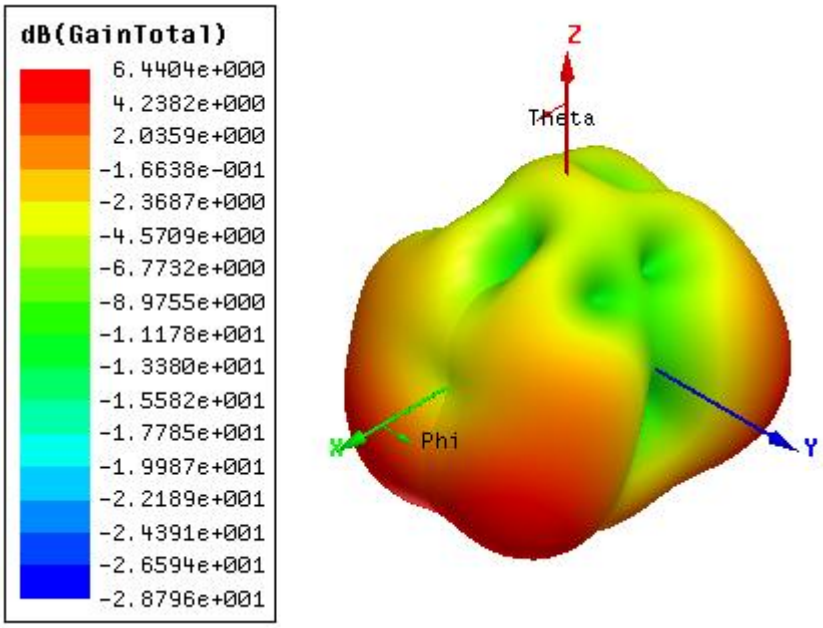

Figure 8.17 The gain of the horn antenna (faced toward an FR4 substrate attached to an aluminium plate).

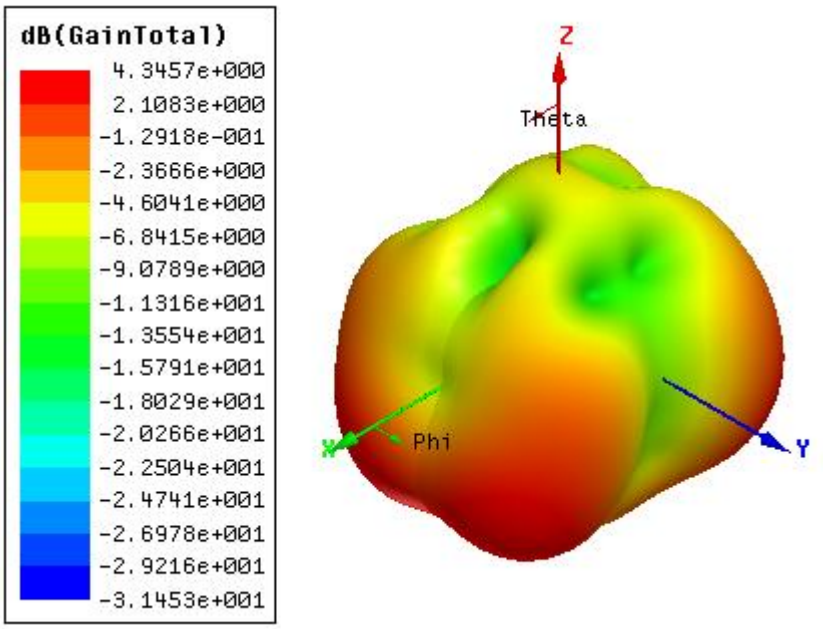

Figure 8.18 The gain of the horn antenna (faced toward a CMPA attached to an aluminium plate).

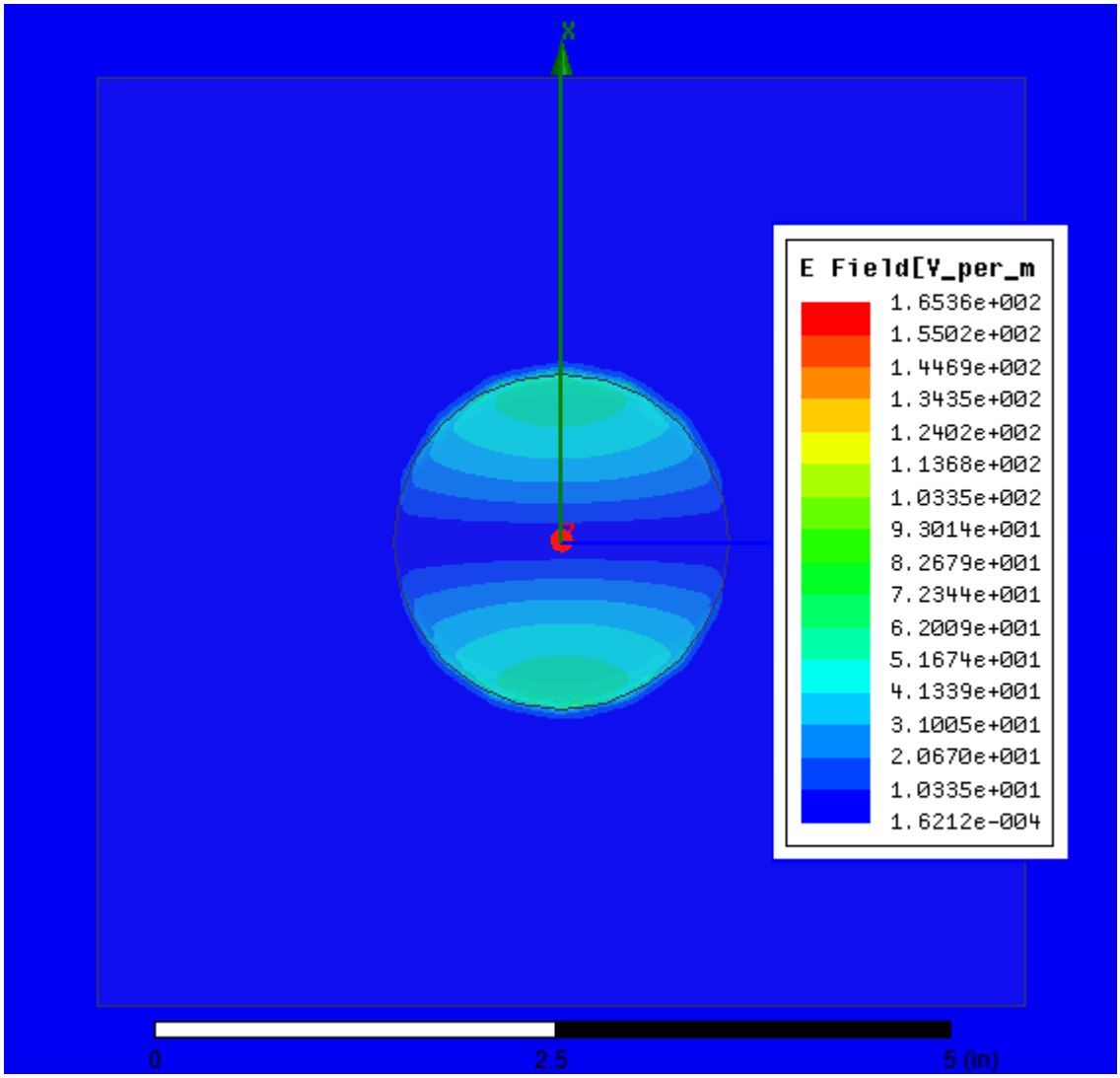

Figure 8.19 Contour of electric field on CMPA surface (excited by horn antenna).

These computational results show that CMPA can be exited using a single horn antenna when it is in the near-field of the horn antenna. Also, having a conductive material behind the CMPA does not affect the wireless excitation of the patch. Moreover, the radiating edges of the patch antenna (locations of maximum electric field at Figure 8.19) ,which in the case of coaxial fed CMPA is defined by the location of the coaxial cable, are defined by the direction of the electric field of the radiated wave. Therefore, because the horn antenna is a linearly polarised antenna (plane containing the electric field is in the plane containing the ridges of the horn antenna) the radiating edges of the CMPA can be changed by rotating the horn antenna (and as a result of that, rotating the E-plane). This phenomenon can be used to measure strain in different directions by adjusting the direction of the horn antenna relative to the CMPA.

Figure 8.20 shows the return loss (scattering parameter) of the horn antenna for four different scenarios discussed above at the frequency range of 1 to 2 GHz. This figure shows a reduction in the magnitude of S11 after adding the aluminium plate or aluminium plate with substrate material attached to it in front of the horn. There are also two dips at about 1.2 GHz and 1.4 GHz which are caused by the edge effect of the aluminium plate. By adding the circular patch on top of the substrate material another dip is introduced in the S11 curve at 1.54 GHz which is the resonant frequency of the patch antenna. This again shows that the CMPA is excited by the radiated electromagnetic field of the horn antenna.

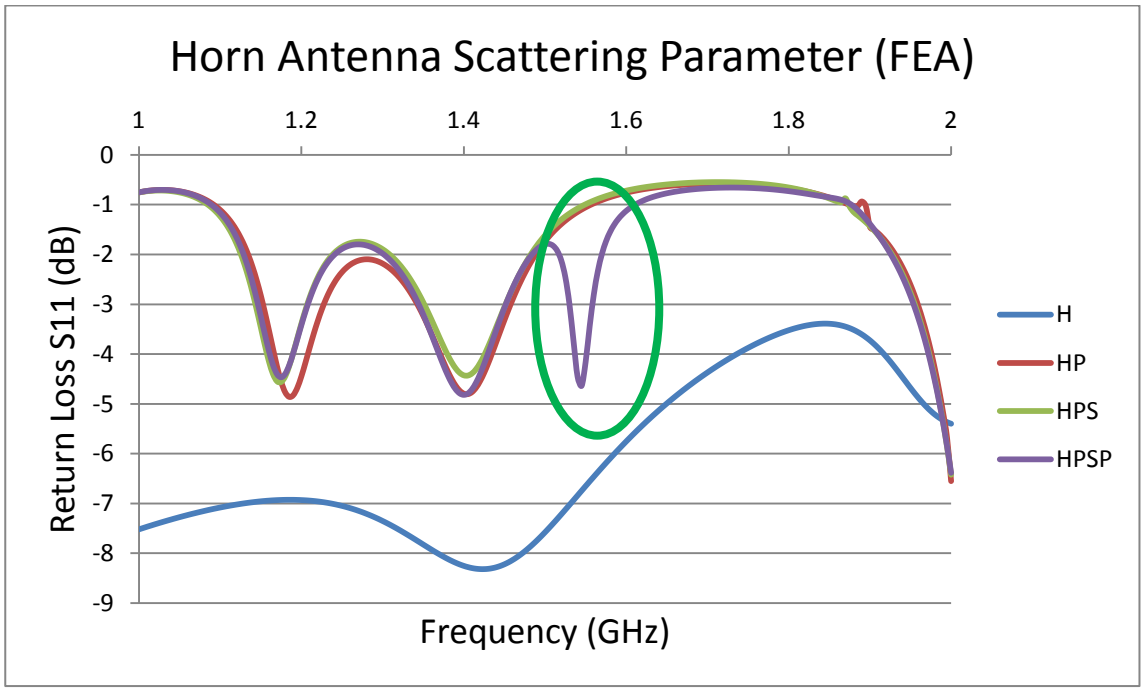

Figure 8.20 Return loss of the horn antenna for, H: Horn antenna facing free space; HP: Horn antenna facing aluminium plate; HPS: Horn antenna facing substrate attached to aluminium plate; and HPSP: Horn antenna facing CMPA attached to aluminium plate.

In order to investigate the feasibility of wireless strain measurement using this technique the patch antenna after applying strain must be modelled. In this case, because the computational domain is so large (due to the presence of the horn antenna) the technique used in Chapter 5 cannot be used. This technique requires a very fine mesh and with the available computational power, the simulation will be prohibitively long in terms of time taken. While the technique introduced in Chapter 5 is very accurate and can be used in the near future with more powerful computer, in this stage a simplified strain is applied to the CMPA. Hence, a strain of 1600 $\mu\varepsilon$ (Similar to the maximum strain that can be applied in experimental tests) were used to stretch on axis of the circular patch. In order to take the

effect of Poisson's ratio into account, the other axis of the circular patch was compressed by one third of the applied strain; resulting in an ellipse which is depicted in Figure 8.21.

The resultant ellipse patch was added to the top of the substrate instead of the circular patch and the same simulation was conducted to derive the S11 curve of the horn antenna. The comparison of the return loss for these two scenarios is illustrated in Figure 8.22 where the frequency range is 1.5 GHz to 1.6 GHz to only include the resonant frequency of the CMPA. This figure shows that the resonant frequency of the patch (measured wirelessly by the horn antenna) shifts toward lower frequencies. This behaviour is similar to the patch antenna fed by a coaxial cable which is explained in previous chapters. These results encouraged the author to further investigate the wireless strain measurement by experimental tests which are described in the following subsection.

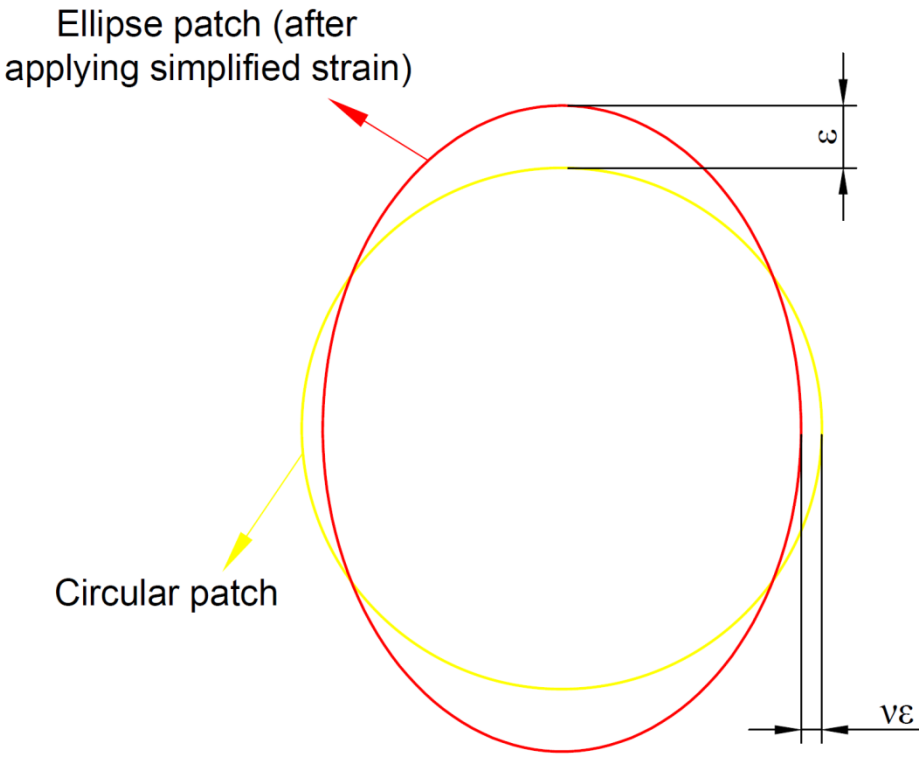

Figure 8.21 Simplified strain configuration used for FEA.

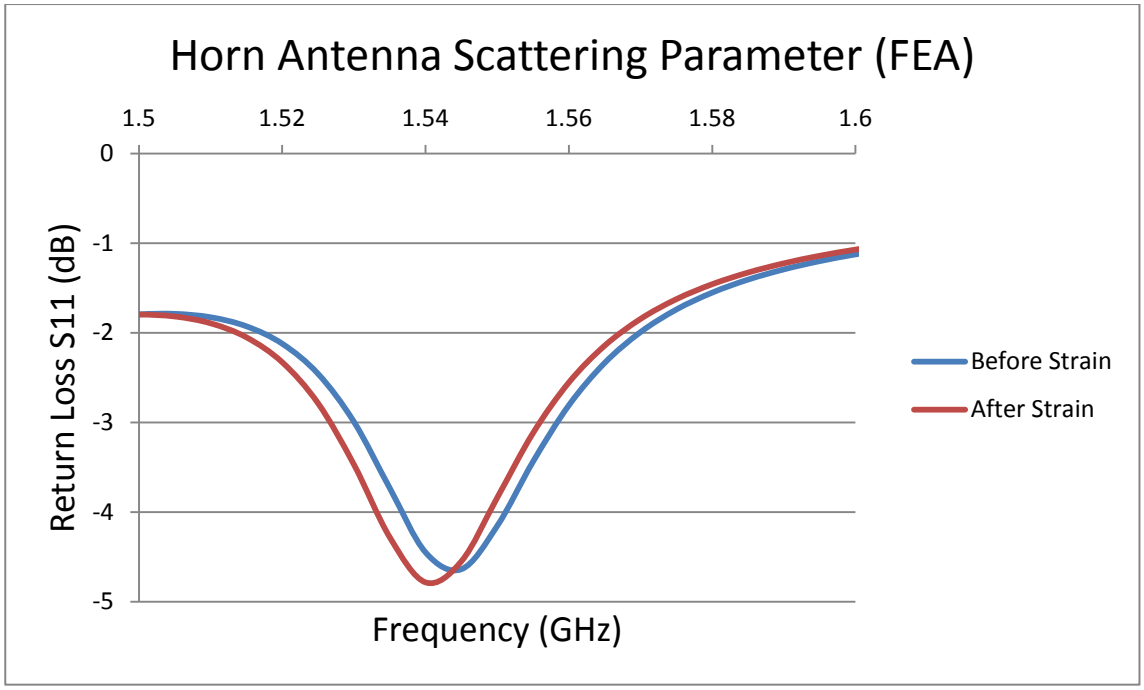

Figure 8.22 Shift in the resonant frequency of the CMPA after applying simplified strain (FEA).

8.5 Experimental Wireless Measurement of Strain

The last step toward wireless strain measurement is the experimental tests which can validate the FEA results described in the previous subsection. In this subsection, first the wireless test setup used for wireless strain measurement is described and then the results from experiments are presented and discussed in detail.

In the experimental tests the effect of different parameters including the effect of back plate material, the effect of interrogation distance between horn antenna and CMPA sensor, the effect of horn antenna orientation (relative to CMPA) and the effect of horn antenna location (offset from centre of CMPA) are investigated.

8.5.1 Wireless Test Setup

The test setup used for wireless strain measurement is similar to the test setup used for previous experimental tests. In this case, however, tensile force was applied to the back plate instead of using 3-point bend test. The reason for this change was to avoid the effect of wooden jig on wireless measurement of antenna resonant frequency. Figure 8.23 shows the final setup used for wireless strain measurement.

In order to apply strain to the back plate, a tensile force of 20 kN was applied to the assembly in 20 steps (1 kN in each step) using 100 kN INSTRON™ machine available at

RMIT University Material Testing Laboratory. Four strain gauges were attached to the back of each plate according to the descriptions in Chapter 6. Test plates and the dimensions of the CMPA are similar to those used in previous chapters. In each step of loading the return loss (S11) of the horn antenna as well as the strain from strain gauges were measured.

The experiment was repeated with three different materials for the back plate; namely, aluminium, CFRP and glass fibre reinforced polymer (GFRP). For the aluminium plate the interrogation distance between the CMPA sensor and the horn antenna were varied from 1 cm to 10 cm in 1cm steps. Figure 8.24 shows the relative distance between CMPA sensor attached to the aluminium plate and the horn antenna at interrogation distance of 10 cm. For each step the test was repeated for 0°, 45° and 90° orientation of the horn antenna relative to the direction of loading. Figure 8.25 shows the horn antenna in front of the CMAP sensor at relative angle of 45°. These three orientations were repeated for the CFRP and GFRP plates but only at interrogation distances of 1 cm, 5 cm and 10 cm. Figures 8.26 and 8.27 show the horn antenna in front of a CFRP and a GFRP plate at 0° and 90° orientations, respectively.

For the aluminium plate at the interrogation distance of 1 cm and horn antenna orientation of 0° the test was repeated in 5 cm and -5 cm offset of the location of horn antenna relative to the CMPA centre. Figures 8.28, 8.29 and 8.30 show the horn location at the offset distance of 0 cm, 5 cm and -5 cm, respectively.

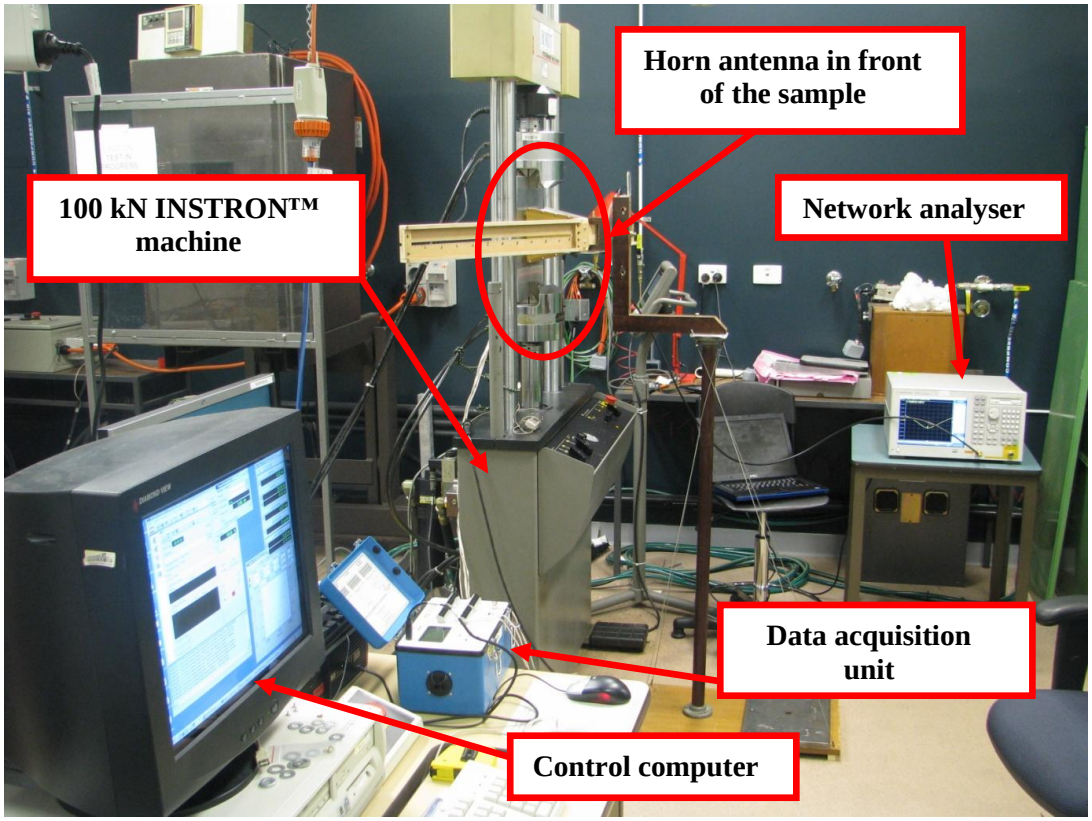

Figure 8.23 The final setup used for wireless strain measurement.

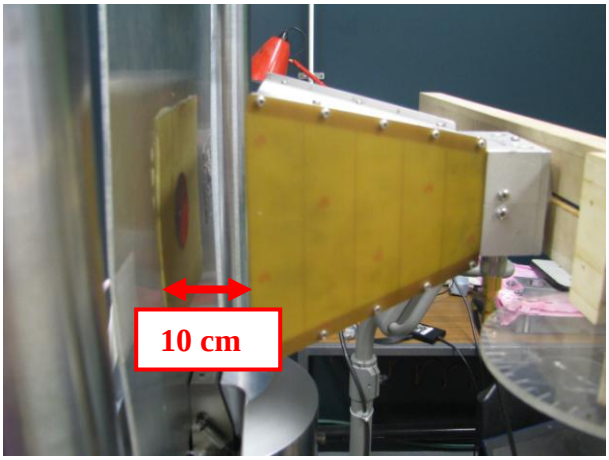

Figure 8.24 The interrogation distance between CMPA sensor and horn antenna (10 cm).

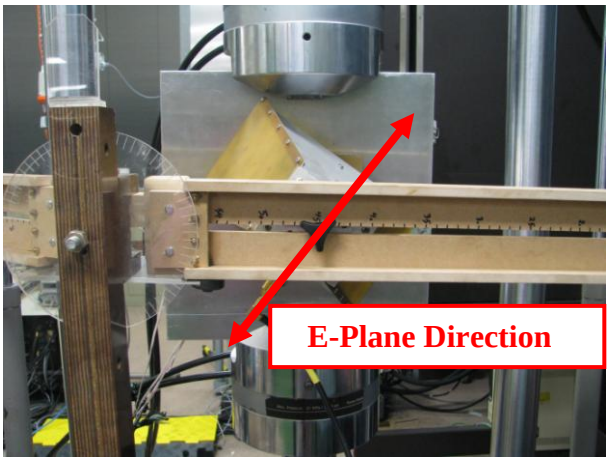

Figure 8.25 The horn antenna in front of the CMAP sensor at relative angle of 45°.

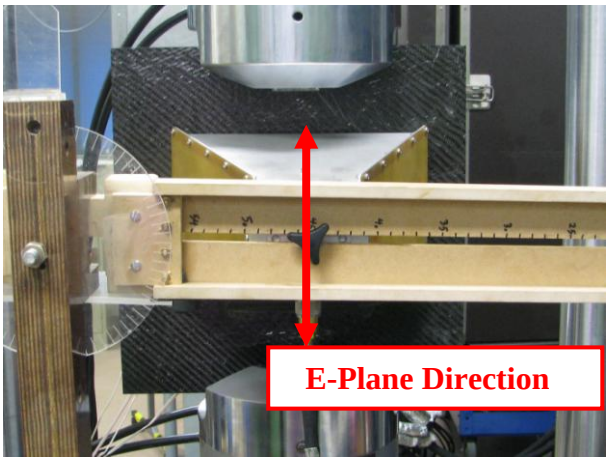

Figure 8.26 The horn antenna in front of a CFRP plate at 0° orientation.

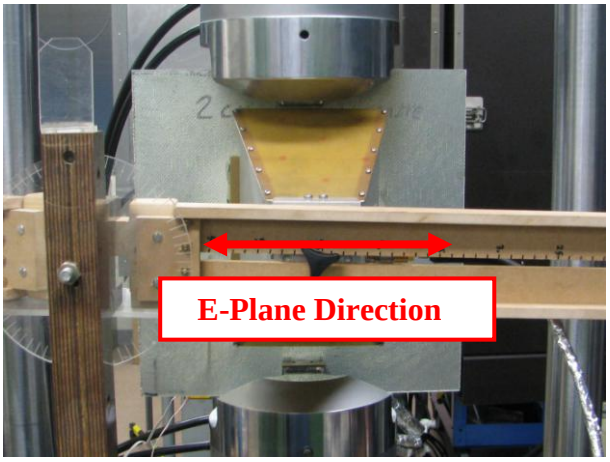

Figure 8.27 The horn antenna in front of a GFRP plate at 90° orientation.

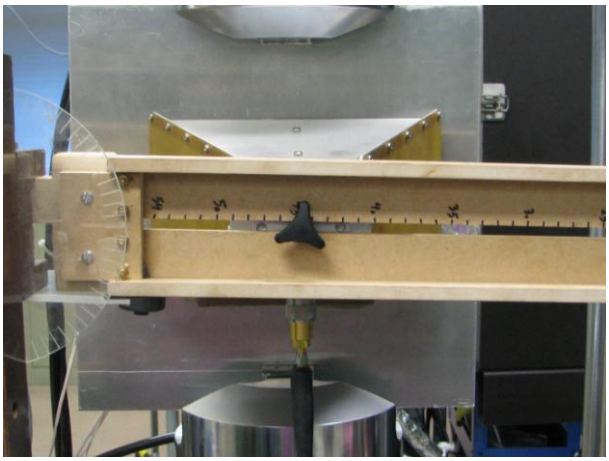

Figure 8.28 The horn location at the reference distance of 0 cm.

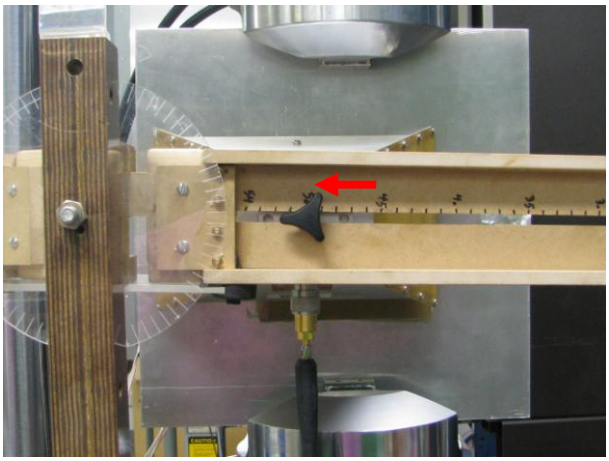

Figure 8.29 The horn location at the offset distance of 5 cm.

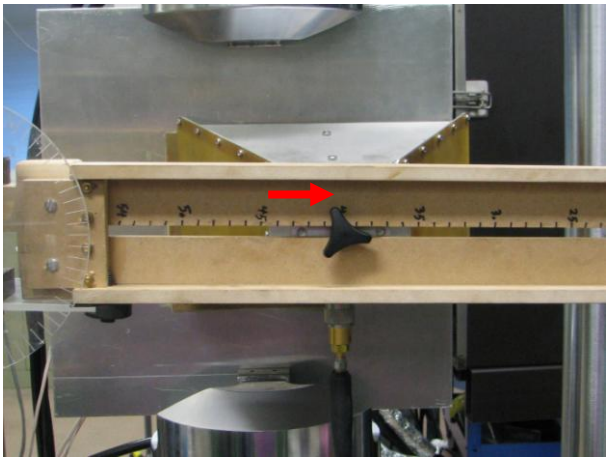

Figure 8.30 The horn location at the offset distance of -5 cm.

8.5.2 Strain Measurement and Effect of Important Parameters

The results derived from experimental wireless reading of the CMPA sensor as well as wireless measurement of strain are presented and explained here. The first study before measuring strain was to investigate the feasibility of wireless reading of the CMPA resonant frequency and exploring the effect of interrogation distance.

Figures 8.31, 8.32 and 8.33 illustrate the effect of interrogation distance on the return loss of the horn antenna at the resonant frequency of the CMPA attached to an aluminium plate at 0°, 45° and 90° orientations, respectively. These figures show the feasibility of locating the resonant frequency of the CMPA wirelessly using a single horn antenna. In addition, regardless of the horn antenna orientation the magnitude of S11 decreases by increasing the interrogation distance from 1 cm to 5 cm. However, at 6 cm the magnitude of the S11 increases and then continues to decrease with the similar manner from 6 cm to 10 cm. This may be related to the wavelength of the CMPA which is 20 cm. Therefore, after a quarter of a wavelength the same manner repeats. However, as it is discussed earlier in this chapter the magnitude of the electric field decreases by increasing the interrogation distance and therefore the S11 curve becomes smoother.

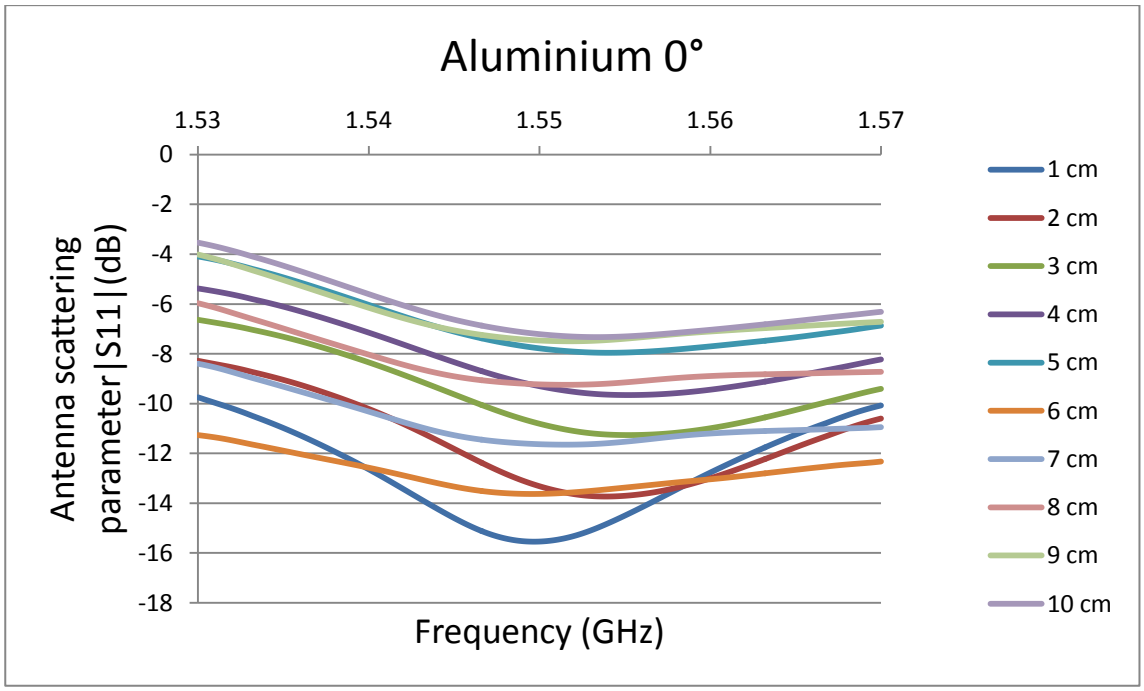

Figure 8.31 Effect of interrogation distance on the return loss of the horn antenna at the resonant frequency of the CMPA, attached to an aluminium plate at 0° orientation.

It was also observed that by increasing the interrogation distance the level of noise in S11 curve increases. This resulted in increasing the variations in the S11 curve and reducing the stability of the curve by increasing the distance. This instability in S11 curve makes the interrogation distance the most important parameter in wireless measurement of strain as by increasing the distance the variations in S11 can be bigger than the shift in the resonant frequency (which is caused by the applied strain).

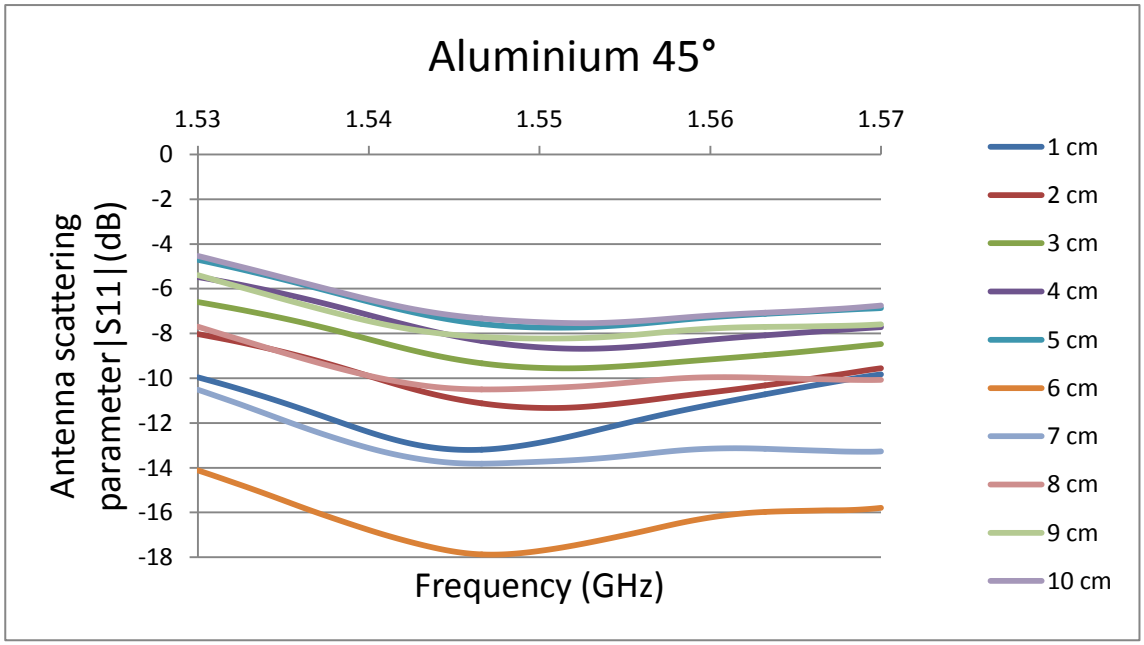

Figure 8.32 Effect of interrogation distance on the return loss of the horn antenna at the resonant frequency of the CMPA, attached to an aluminium plate at 45° orientation.

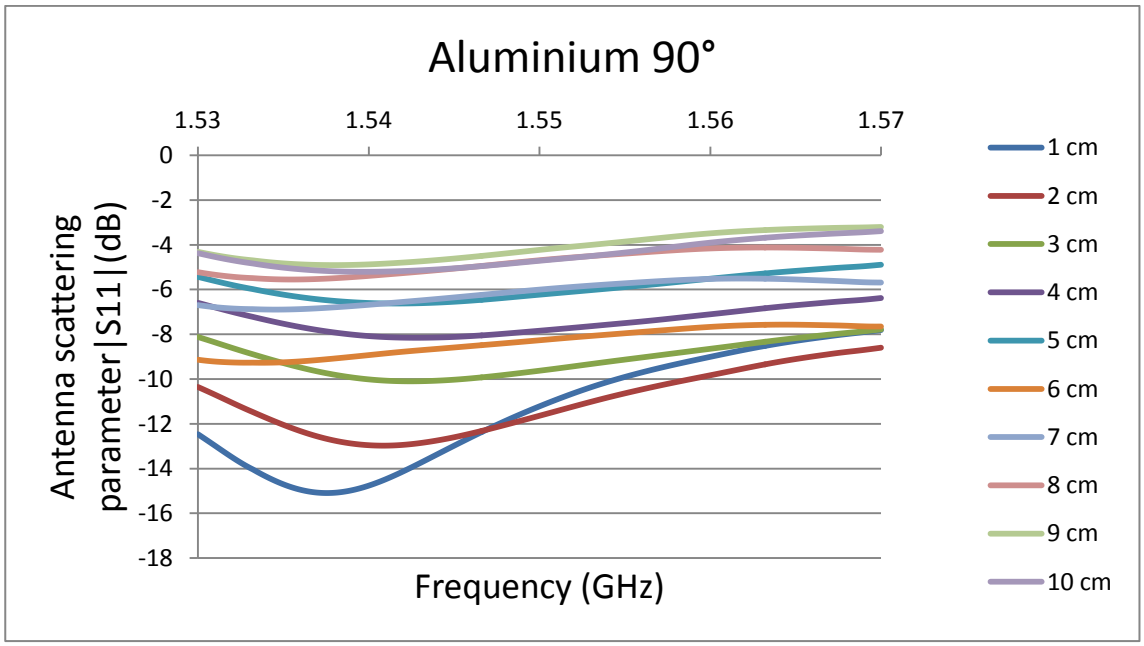

Figure 8.33 Effect of interrogation distance on the return loss of the horn antenna at the resonant frequency of the CMPA, attached to an aluminium plate at 90° orientation.

Figures 8.34, 8.35 and 8.36 show the effect of horn antenna orientation on the resonant frequency of the CMPA attached to an aluminium plate (S11 curve) for interrogation distances of 1 cm, 5 cm and 10 cm, respectively. From 0° orientation toward 90° degree orientation the resonant frequency of the CMPA has a shift toward lower frequencies. This is because of the reflection caused by the bend in the coaxial cable that connects the horn antenna to the network analyser. As the cable was bent more at 90° compared to 45°, the resultant change in the resonant frequency is larger.

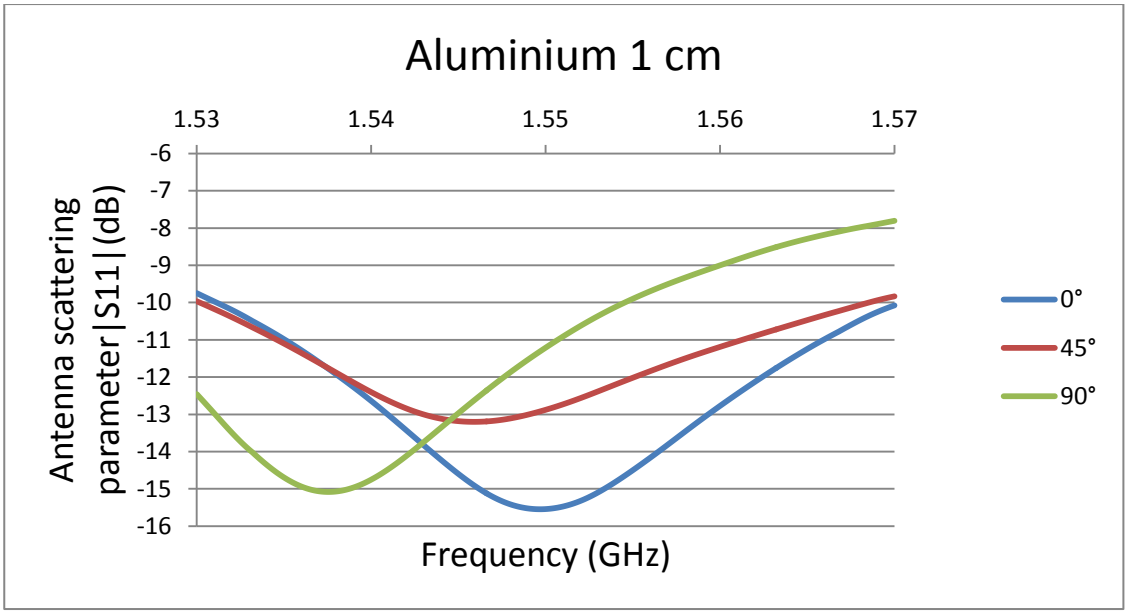

Figure 8.34 Effect of horn antenna orientation on the resonant frequency of the CMPA attached to an aluminium plate for the interrogation distance of 1 cm.

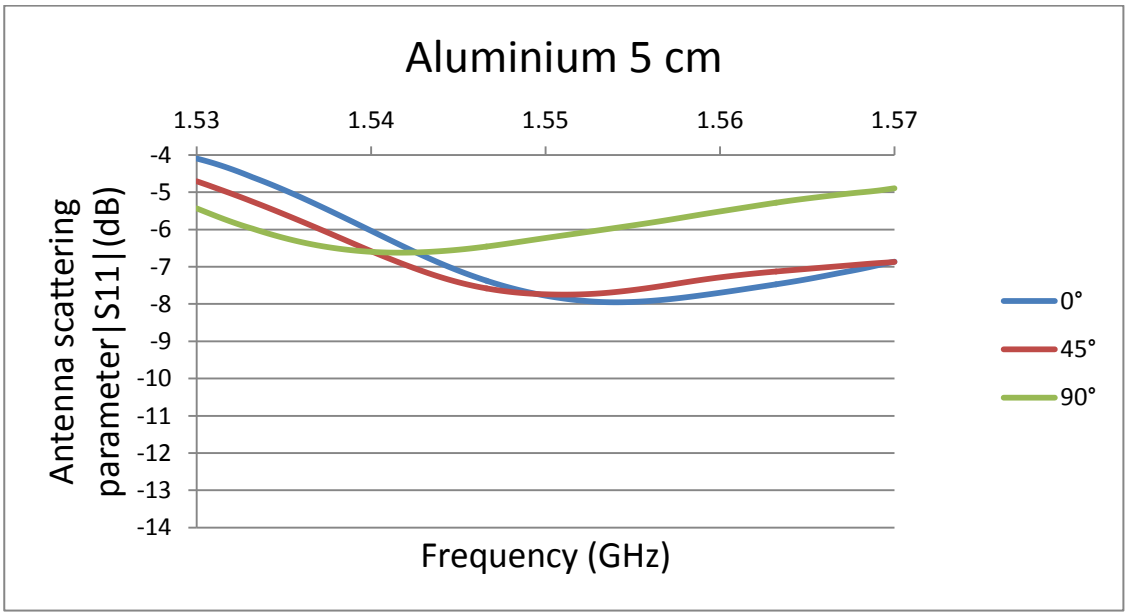

Figure 8.35 Effect of horn antenna orientation on the resonant frequency of the CMPA attached to an aluminium plate for the interrogation distance of 5 cm.

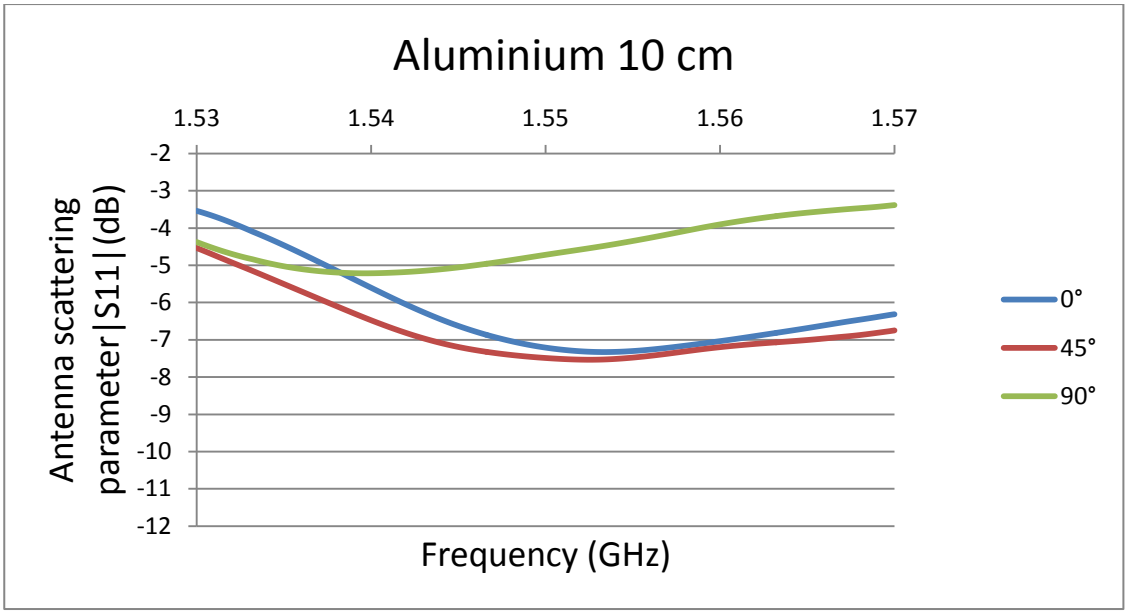

Figure 8.36 Effect of horn antenna orientation on the resonant frequency of the CMPA attached to an aluminium plate for the interrogation distance of 10 cm.

Figures 8.37, 8.38 and 8.39 show the shift in the resonant frequency of the CMPA attached to an aluminium plate (measured by horn antenna S11) for different steps of tensile load at the interrogation distance of 1 cm for 0°, 45° and 90° orientations, respectively. These figures demonstrate the feasibility of measuring strain wirelessly using a single horn antenna while the CMPA sensor is in the near-field of the horn antenna. The minimum point in the S11 curve for each step of applied strain can be located clearly and the shift in the resonant frequency can be measured.

Figure 8.37 shows that at 0° orientation the resonant frequency of the CMPA shifts toward lower frequencies. At 45° orientation (Figure 8.38) the resonant frequency of the CMPA shifts toward lower frequencies; however, the amount of shift is less than the amount of shift at 0° orientation. Figure 8.39 shows that the shift in the resonant frequency, while the horn antenna is rotated 90° relative to the loading direction, is toward higher frequencies. The amount of shift at 90° is about one third of the amount of shift at 0° orientation. This phenomenon indicates that the shift in the resonant frequency of the patch is related to the direction of the horn antenna or more precisely the direction of the E-plane of the horn antenna. This further confirm the results predicted by FEA which show the horn antenna can measure applied strain to the structure in any direction. These results establish the feasibility of wireless measurement of strain using CMPA sensors.

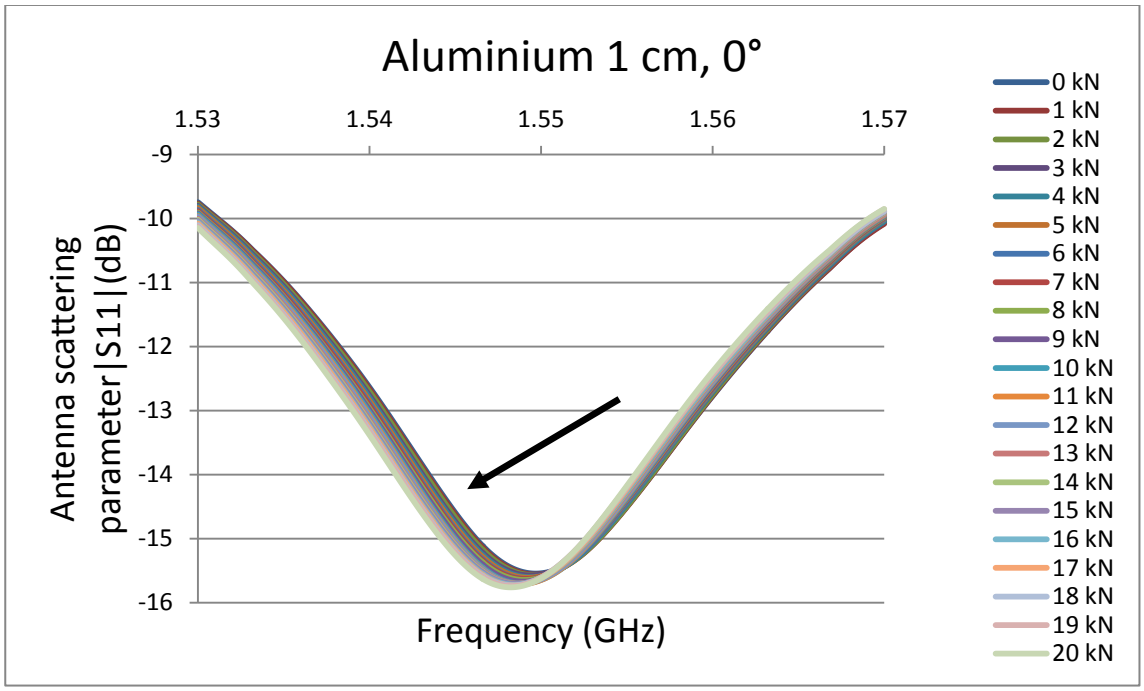

Figure 8.37 Shift in the resonant frequency of the CMPA attached to an aluminium plate at interrogation distance of 1 cm and 0° orientation.

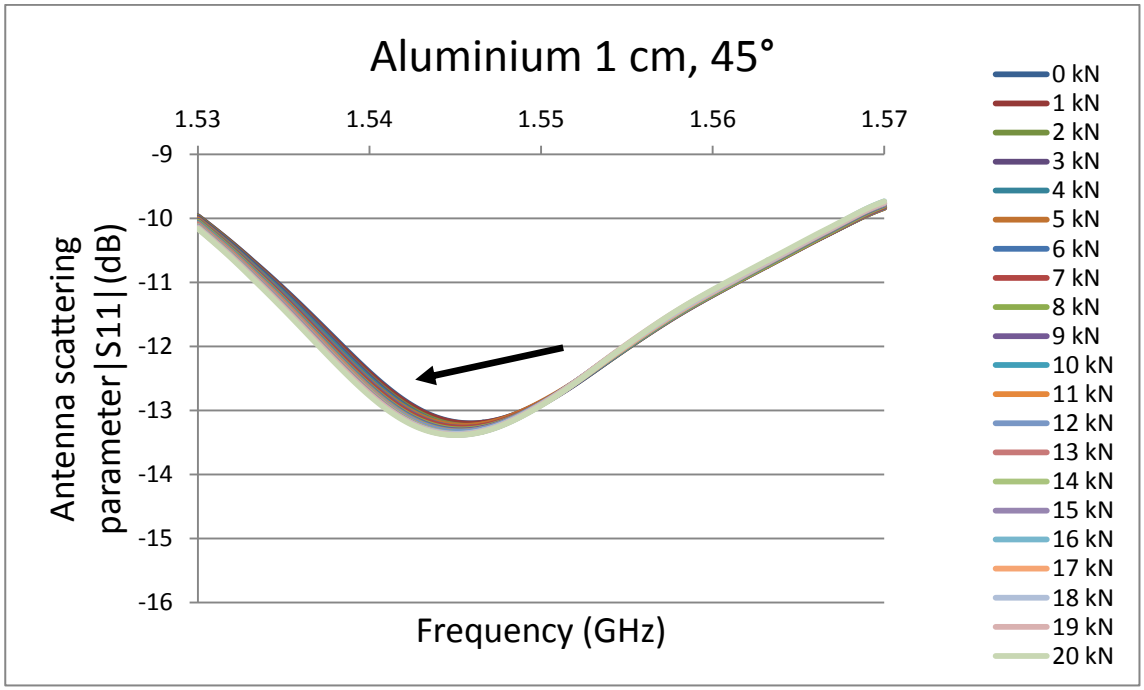

Figure 8.38 Shift in the resonant frequency of the CMPA attached to an aluminium plate at interrogation distance of 1 cm and 45° orientation.

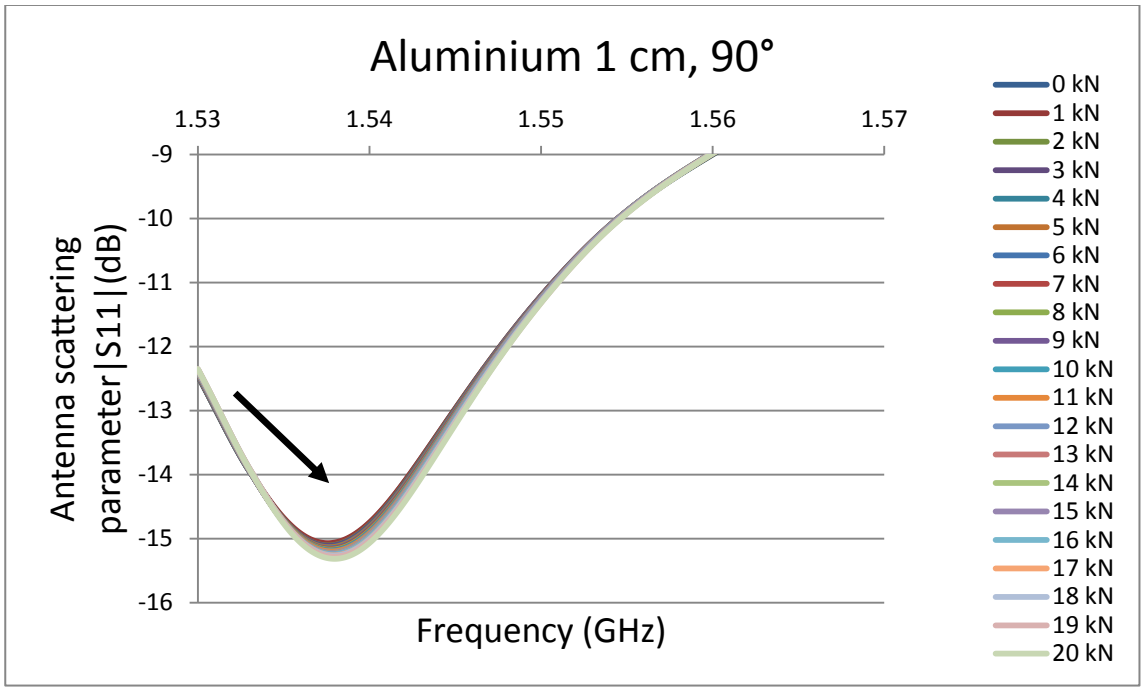

Figure 8.39 Shift in the resonant frequency of the CMPA attached to an aluminium plate at interrogation distance of 1 cm and 90° orientation.

Figures 8.40 to 8.49 illustrate the normalised shift in the resonant frequency of the CMPA attached to an aluminium plate against the applied strain for three different horn orientations at interrogation distances of 1 cm to 10 cm, respectively. Figure 8.40 shows that the relationship between strain and the shift in the resonant frequency of the CMPA is linear. It also indicates that the amount of shift in 90° orientation (slope of linear line) is about one third of the shift at 0° orientation which is because of the Poisson's ratio effect.

However, as it is obvious from these figures, by increasing the interrogation distance because of the increase in the noise level and changes in the magnitude of the horn antenna electric field the nonlinearity in the results increases. In addition, while the direction of shift in different orientations is still the same and as expected, the relative relationship between the slopes of linear lines for different orientations changes. This again indicates the importance of the interrogation distance on the wireless measurement of strain.

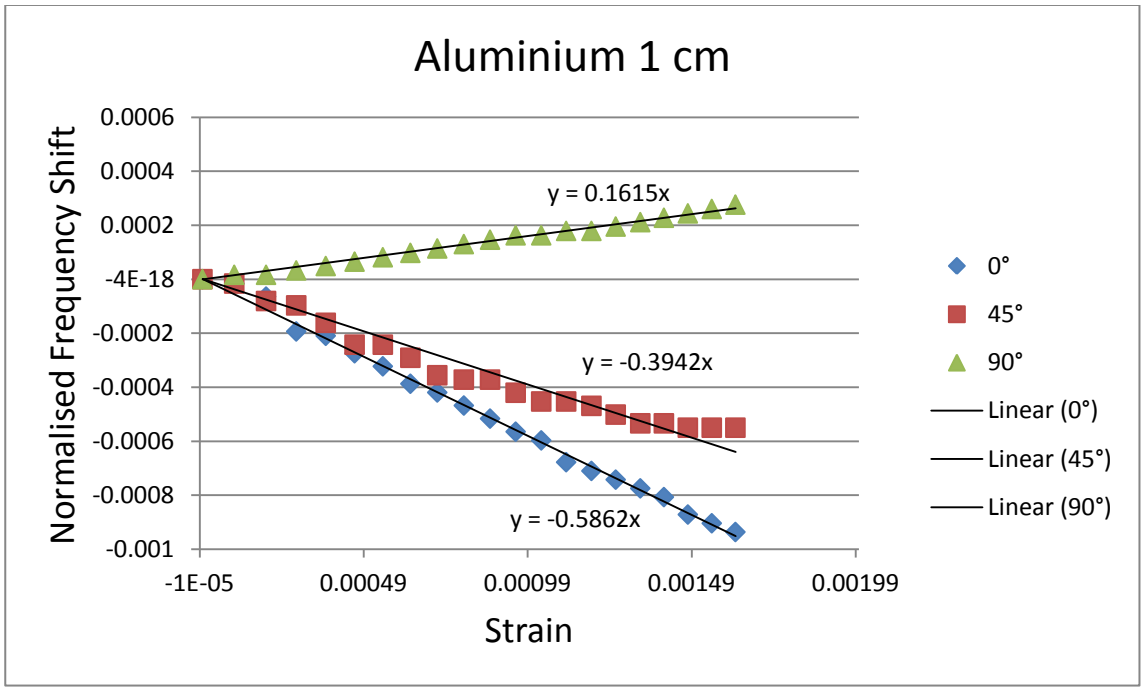

Figure 8.40 Normalised shift in the resonant frequency of the CMPA attached to an aluminium plate against the applied strain for three different horn orientations at interrogation distance of 1 cm.

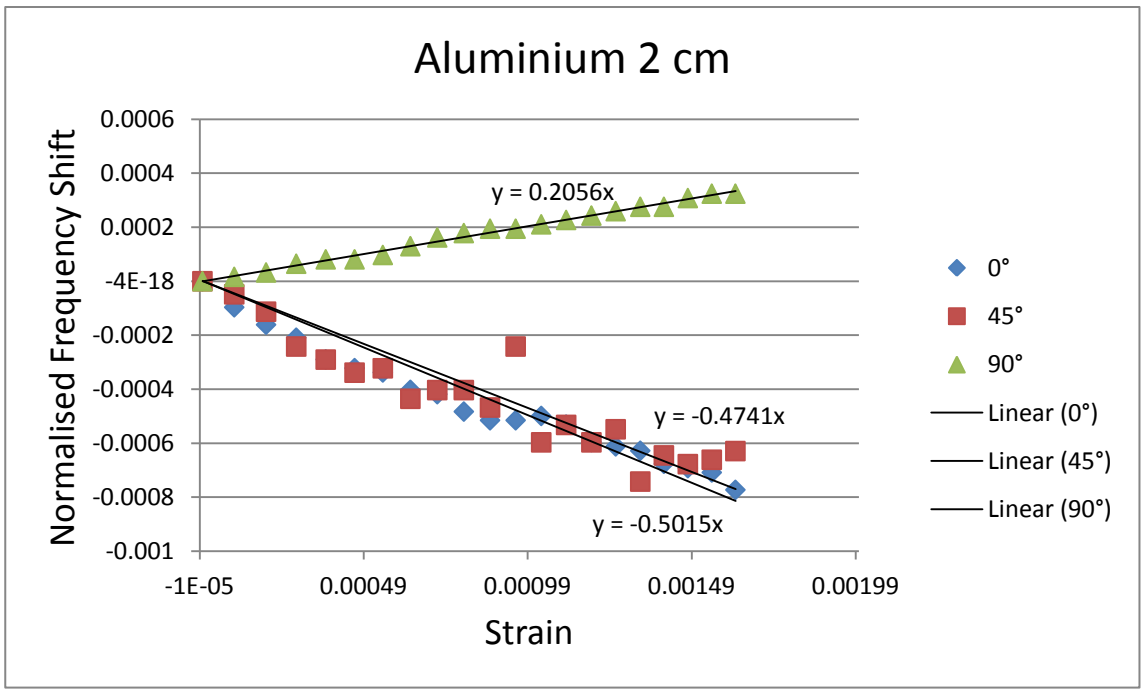

Figure 8.41 Normalised shift in the resonant frequency of the CMPA attached to an aluminium plate against the applied strain for three different horn orientations at interrogation distance of 2 cm.

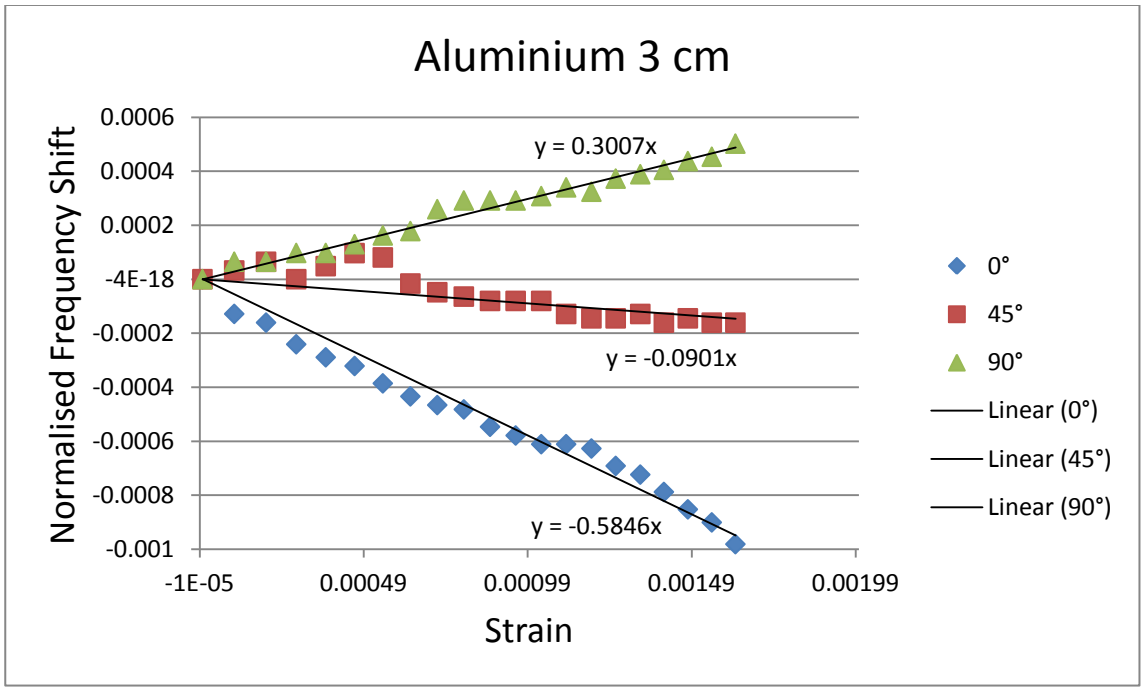

Figure 8.42 Normalised shift in the resonant frequency of the CMPA attached to an aluminium plate against the applied strain for three different horn orientations at interrogation distance of 3 cm.

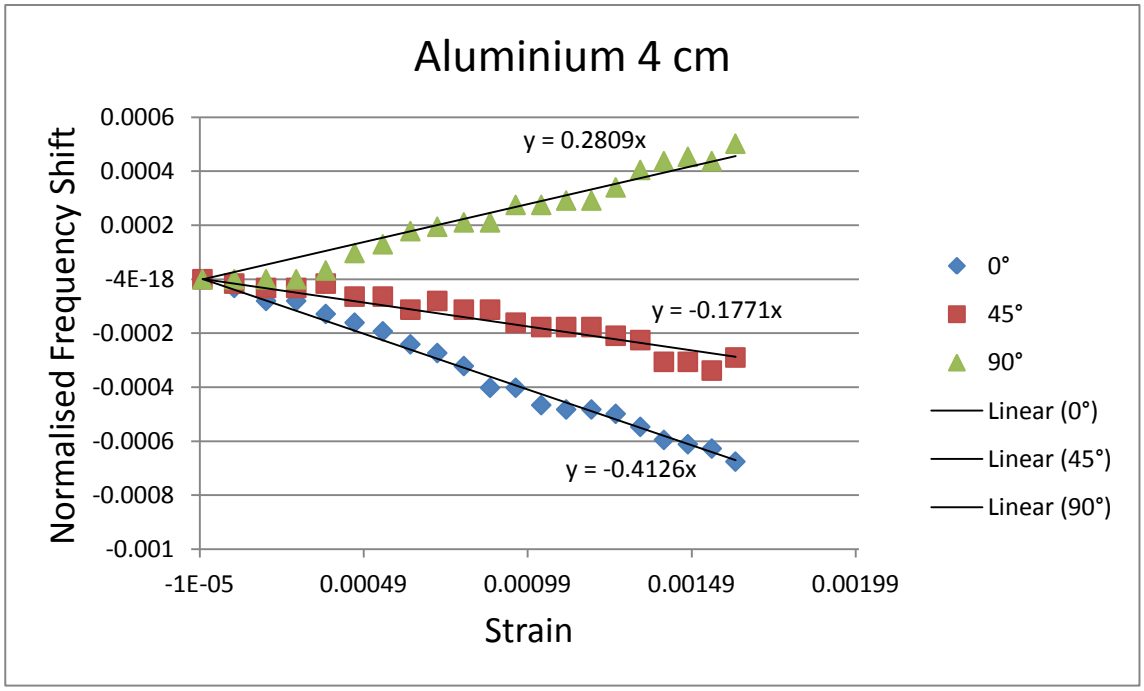

Figure 8.43 Normalised shift in the resonant frequency of the CMPA attached to an aluminium plate against the applied strain for three different horn orientations at interrogation distance of 4 cm.

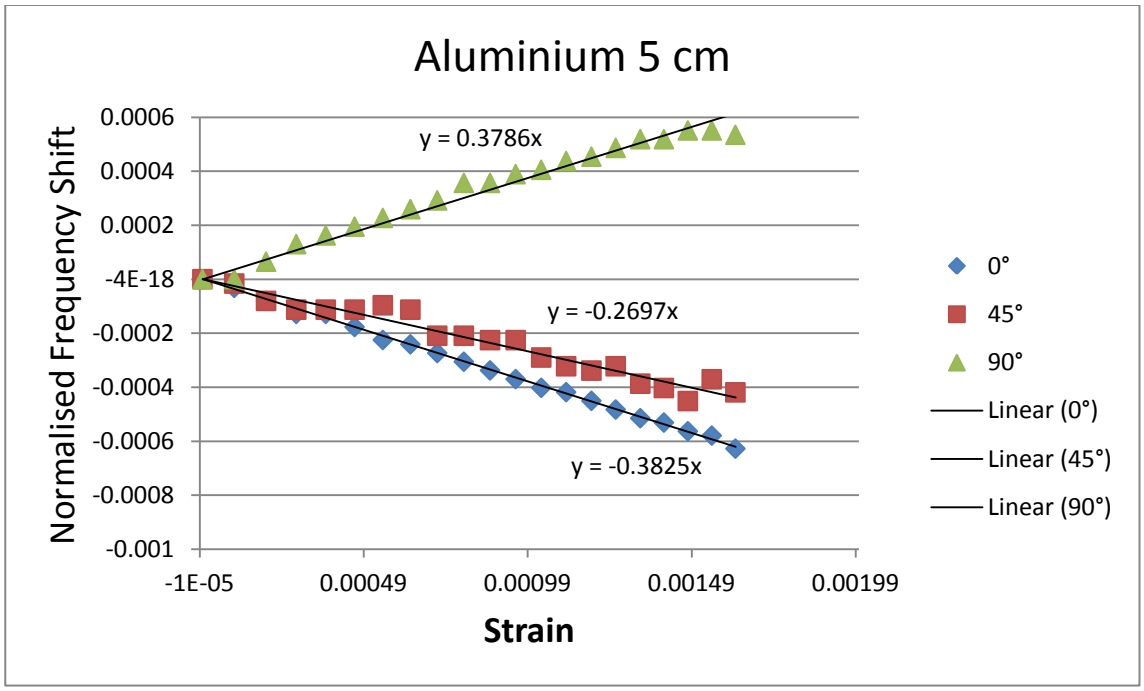

Figure 8.44 Normalised shift in the resonant frequency of the CMPA attached to an aluminium plate against the applied strain for three different horn orientations at interrogation distance of 5 cm.

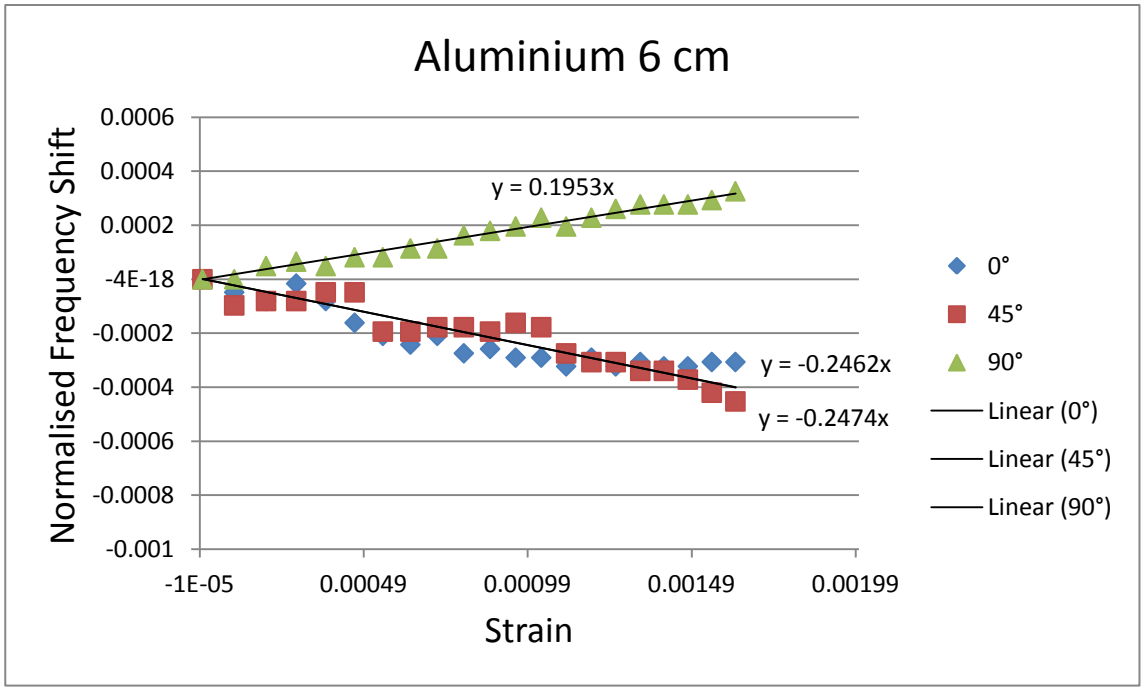

Figure 8.45 Normalised shift in the resonant frequency of the CMPA attached to an aluminium plate against the applied strain for three different horn orientations at interrogation distance of 6 cm.

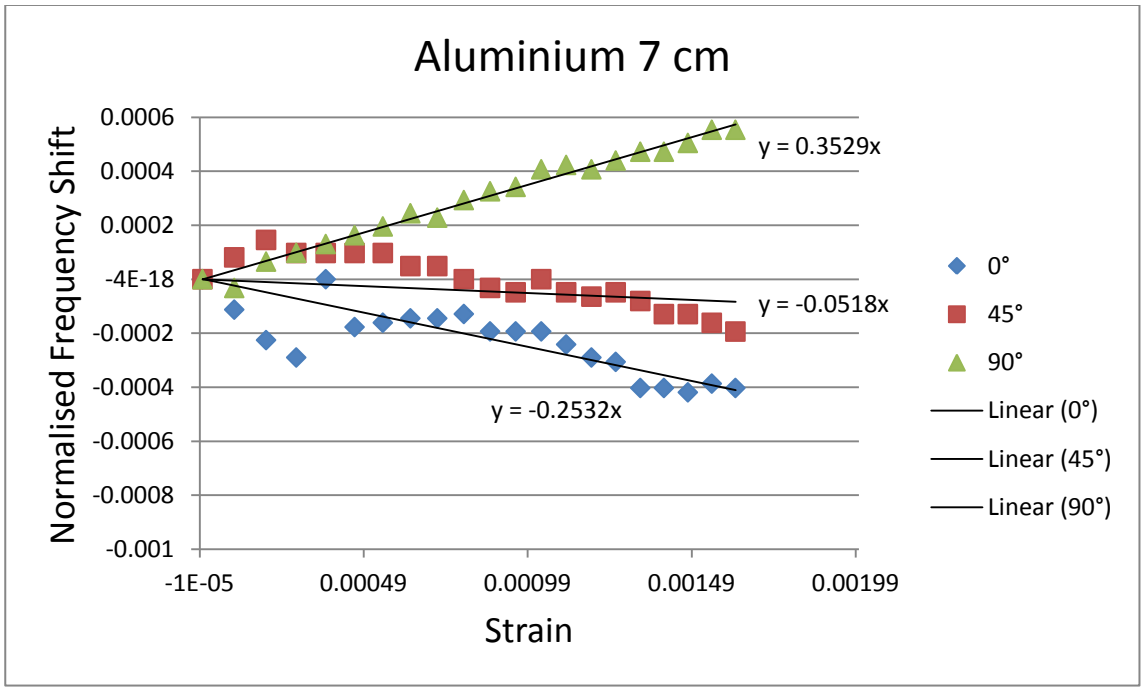

Figure 8.46 Normalised shift in the resonant frequency of the CMPA attached to an aluminium plate against the applied strain for three different horn orientations at interrogation distance of 7 cm.

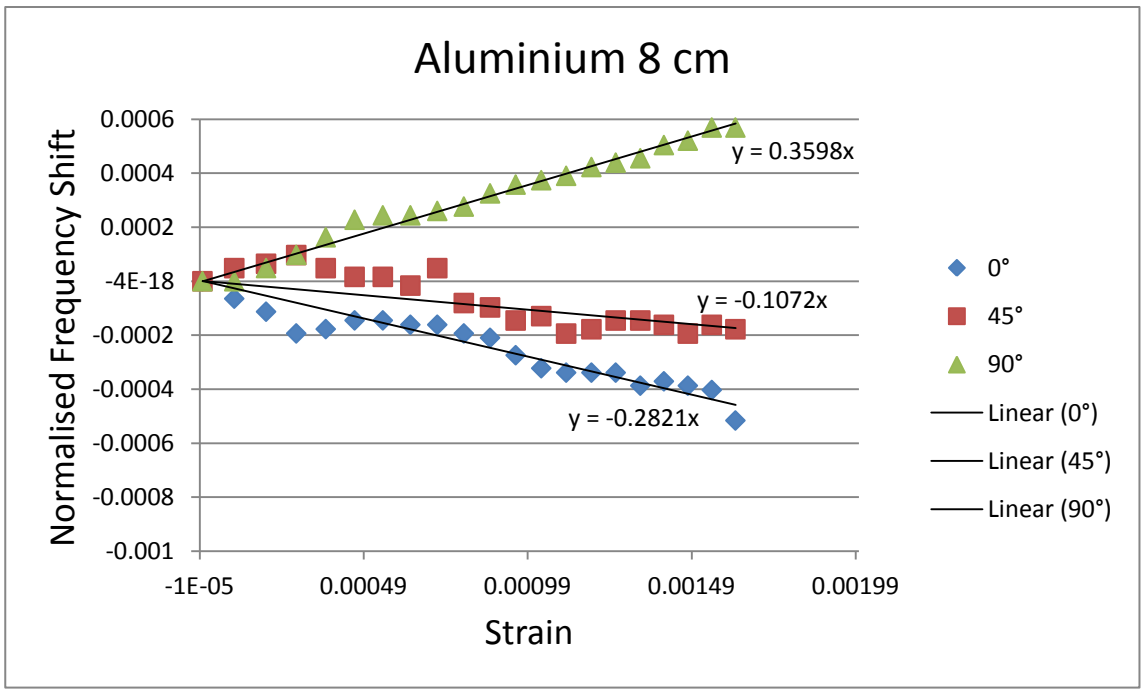

Figure 8.47 Normalised shift in the resonant frequency of the CMPA attached to an aluminium plate against the applied strain for three different horn orientations at interrogation distance of 8 cm.

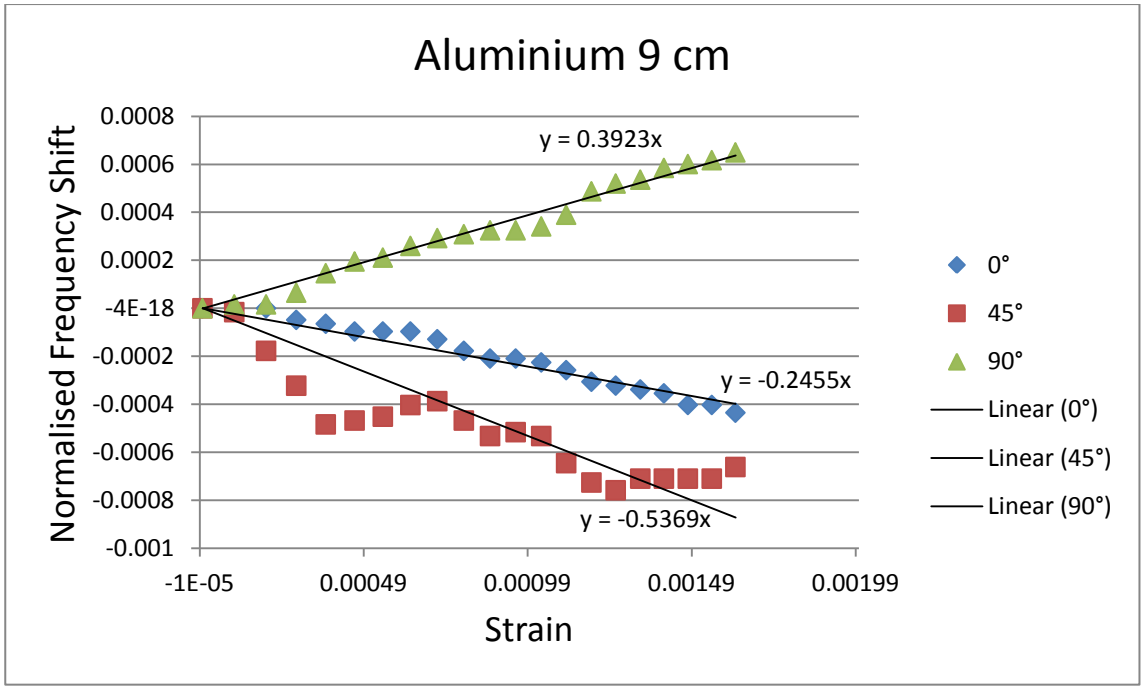

Figure 8.48 Normalised shift in the resonant frequency of the CMPA attached to an aluminium plate against the applied strain for three different horn orientations at interrogation distance of 9 cm.

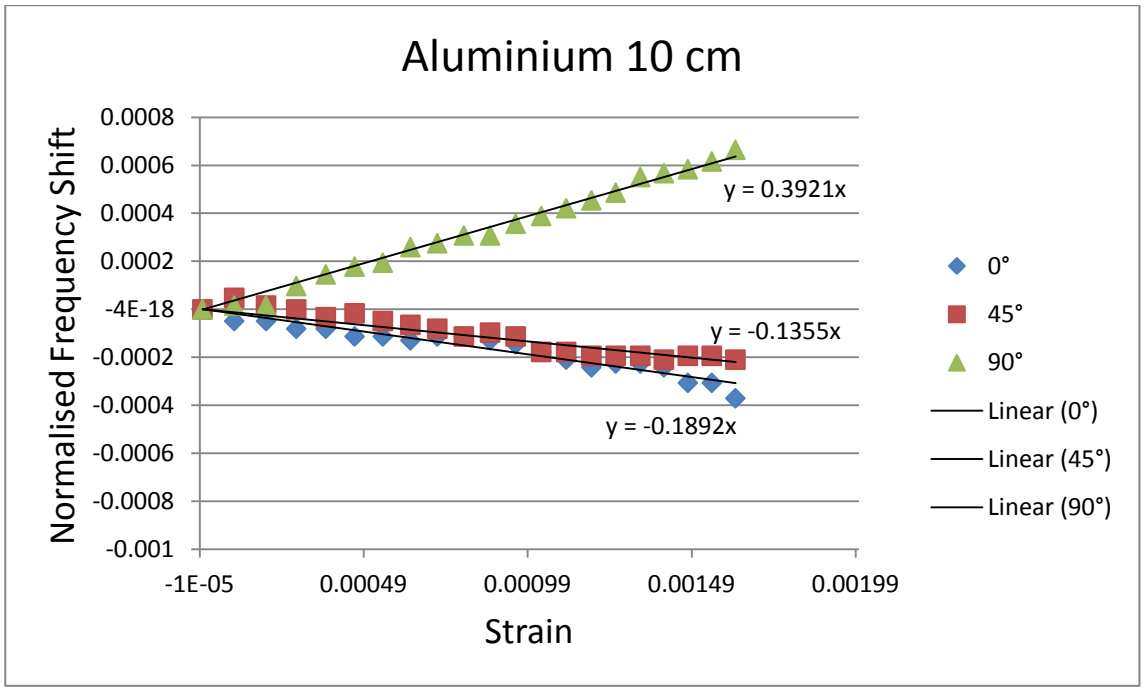

Figure 8.49 Normalised shift in the resonant frequency of the CMPA attached to an aluminium plate against the applied strain for three different horn orientations at interrogation distance of 10 cm.

Figures 8.50, 8.51 and 8.52 show the shift in the resonant frequency of the CMPA attached to a CFRP plate at the interrogation distance of 1 cm at different steps of loading for 0°, 45° and 90° orientations, respectively. These figures show the feasibility of wireless strain measurement while the back plate material is CFRP. Again, as it was expected, the resonant

frequency of the CMPA shift toward lower frequencies at 0° and 45° orientations with larger amount of shift for 0° orientation (Figures 8.50 and 8.51). Figure 8.52 indicates that in 90° orientation the resonant frequency shifts toward higher frequencies with a lower amount compared to 0° orientation.

The normalised shift in the resonant frequency against applied strain for the CMPA attached to the CFRP plate for three different horn antenna orientations are illustrated in Figures 8.53, 8.54 and 8.55 for interrogation distances of 1 cm, 5 cm and 10 cm, respectively. These figures establish the linearity of the relationship between normalised shift and the applied strain in wireless measurement for CFRP back plate. The direction of the shift relative to the horn orientation is similar to the aluminium plate and according to predictions. However, again, by increasing the interrogation distance the nonlinearity of the curves increases and the relative relationship between slopes of linear lines changes.

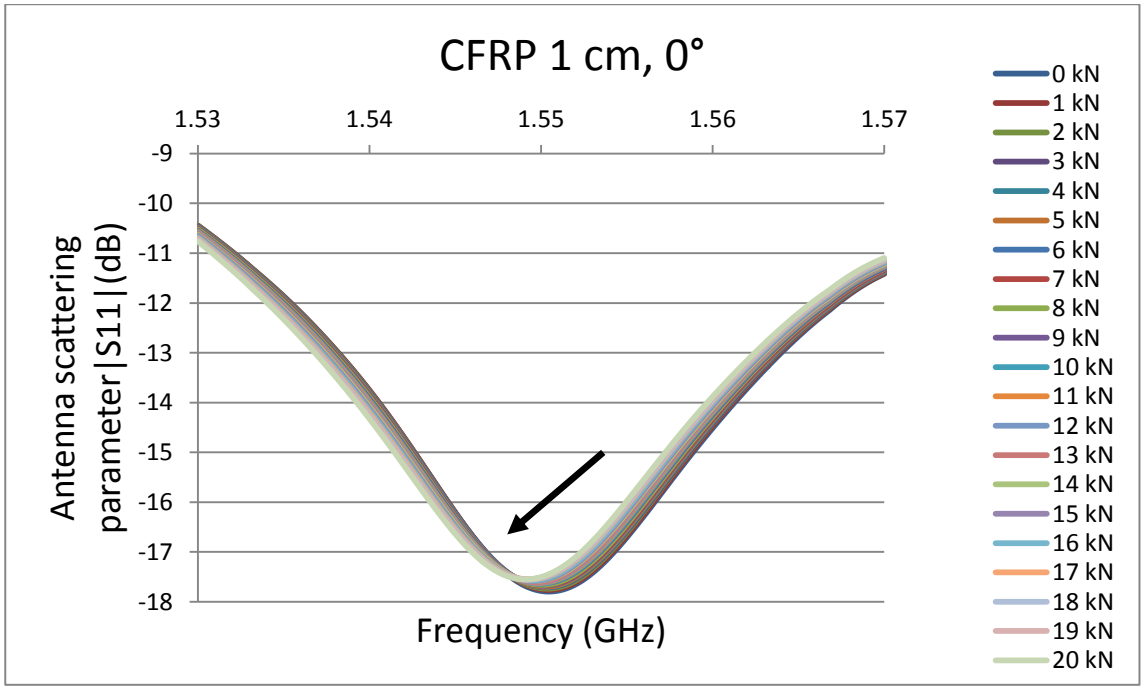

Figure 8.50 Shift in the resonant frequency of the CMPA attached to a CFRP plate at interrogation distance of 1 cm and 0° orientation.

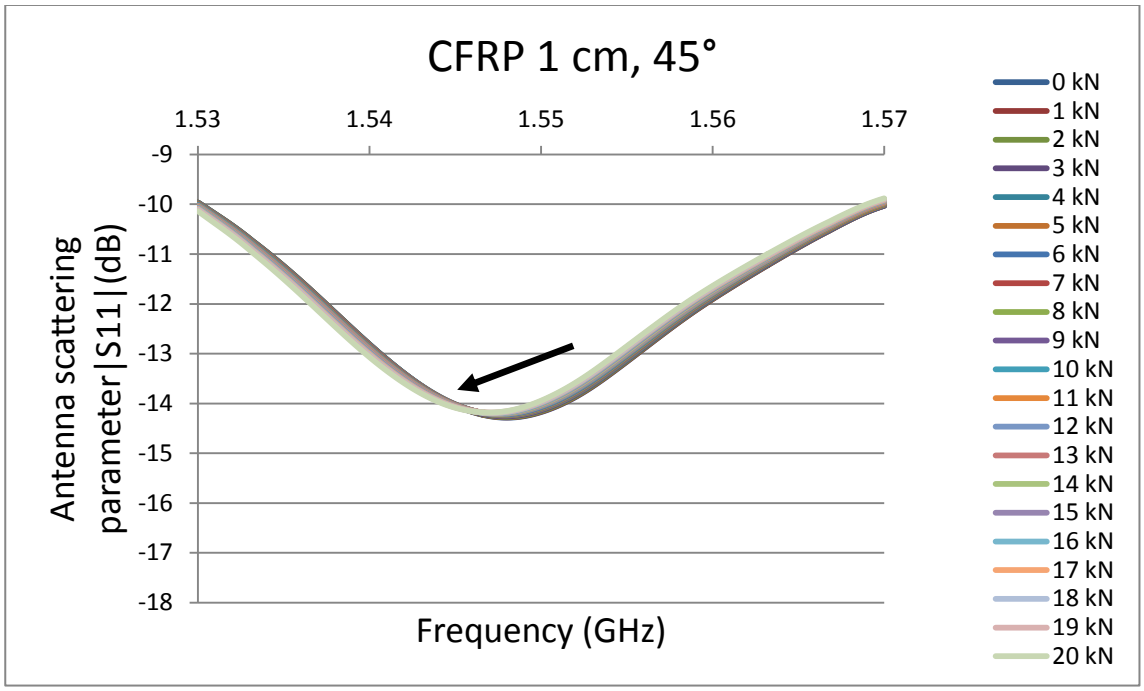

Figure 8.51 Shift in the resonant frequency of the CMPA attached to a CFRP plate at interrogation distance of 1 cm and 45° orientation.

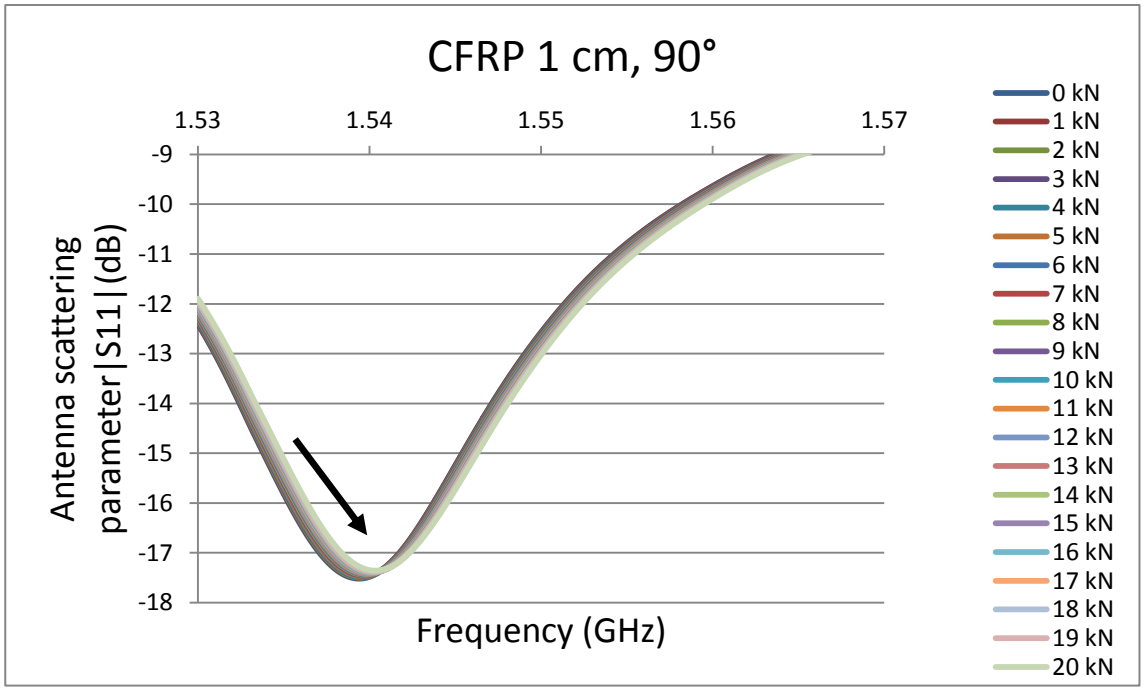

Figure 8.52 Shift in the resonant frequency of the CMPA attached to a CFRP plate at interrogation distance of 1 cm and 90° orientation.

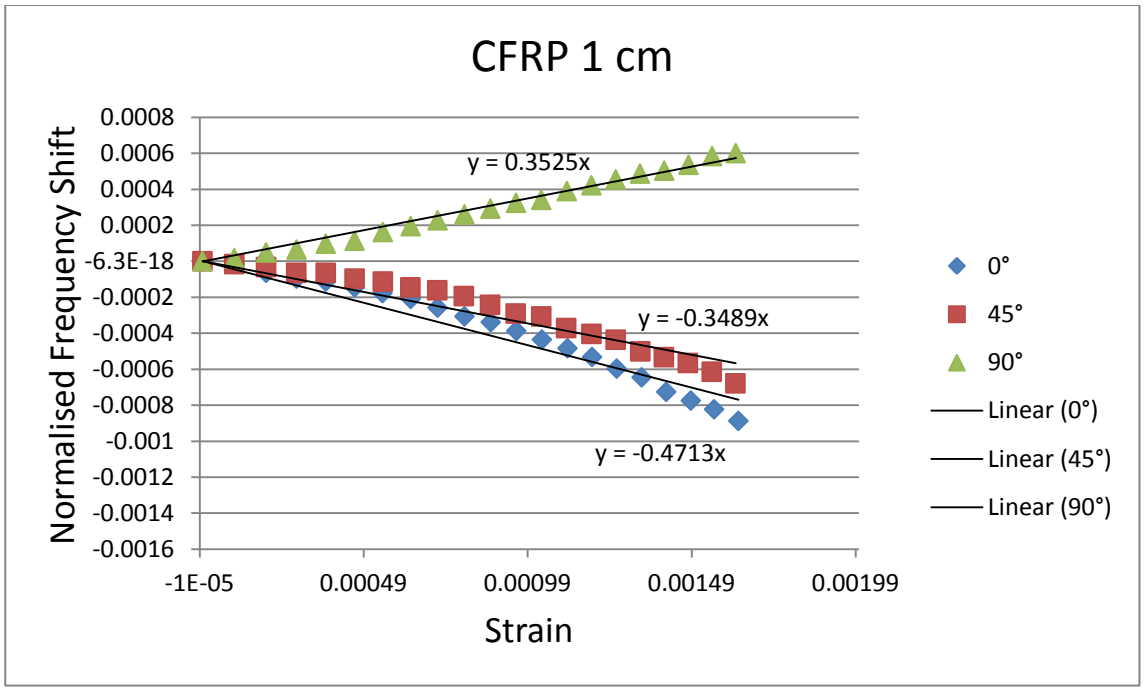

Figure 8.53 Normalised shift in the resonant frequency of the CMPA attached to a CFRP plate against the applied strain for three different horn orientations at interrogation distance of 1 cm.

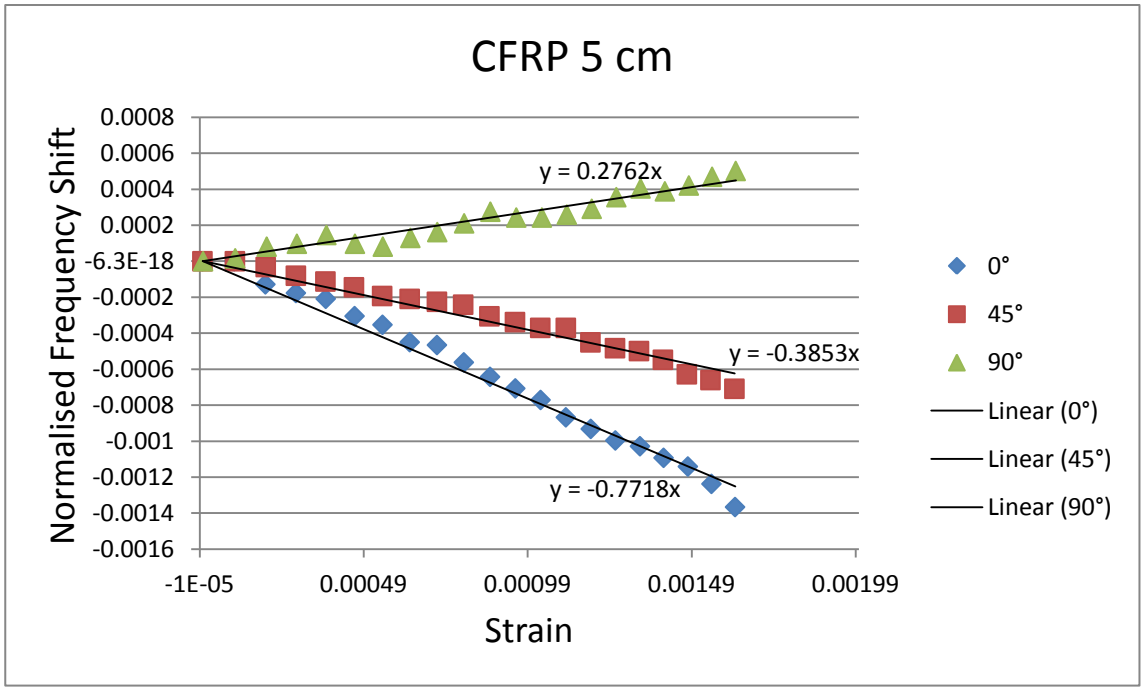

Figure 8.54 Normalised shift in the resonant frequency of the CMPA attached to a CFRP plate against the applied strain for three different horn orientations at interrogation distance of 5 cm.

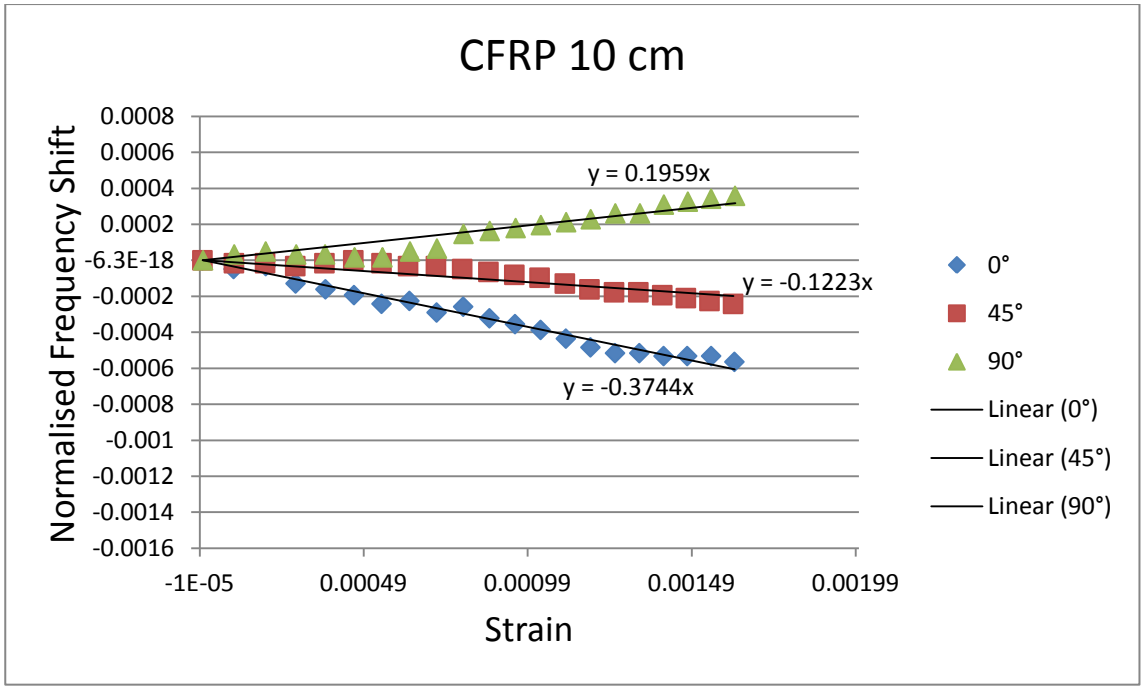

Figure 8.55 Normalised shift in the resonant frequency of the CMPA attached to a CFRP plate against the applied strain for three different horn orientations at interrogation distance of 10 cm.

Figures 8.56, 8.57 and 8.58 show the shift in the resonant frequency of the CMPA attached to a GFRP plate at the interrogation distance of 1 cm at different steps of loading for 0°, 45° and 90° orientations, respectively. These figures establish the feasibility of wireless strain measurement while the back plate material is a nonconductive material such as GFRP. Similar to the aluminium and CFRP plates, the resonant frequency of the CMPA shift toward lower frequencies at 0° and 45° orientations with larger amount of shift for 0° orientation (Figures 8.56 and 8.57). Figure 8.58 demonstrates that in 90° orientation the resonant frequency shifts toward higher frequencies with a lower amount compared to the shift at 0° orientation.

The normalised shift in the resonant frequency against applied strain for the CMPA attached to the GFRP plate for three different horn antenna orientations are illustrated in Figures 8.59, 8.60 and 8.61 for interrogation distances of 1 cm, 5 cm and 10 cm, respectively. These figures establish the overall linearity of the relationship between normalised shift and the applied strain in wireless measurement for GFRP back plate. The direction of the shift relative to the horn orientation is similar to the aluminium and CFRP plates. However, again, by increasing the interrogation distance the nonlinearity of the curves increases and the relative relationship between slopes of linear lines changes. In addition, in all interrogation distances, the level of noise for the resonant frequency of the CMPA attached

to the GFRP plate is much higher than the level of the noise for similar interrogation distances for aluminium and CFRP plates.

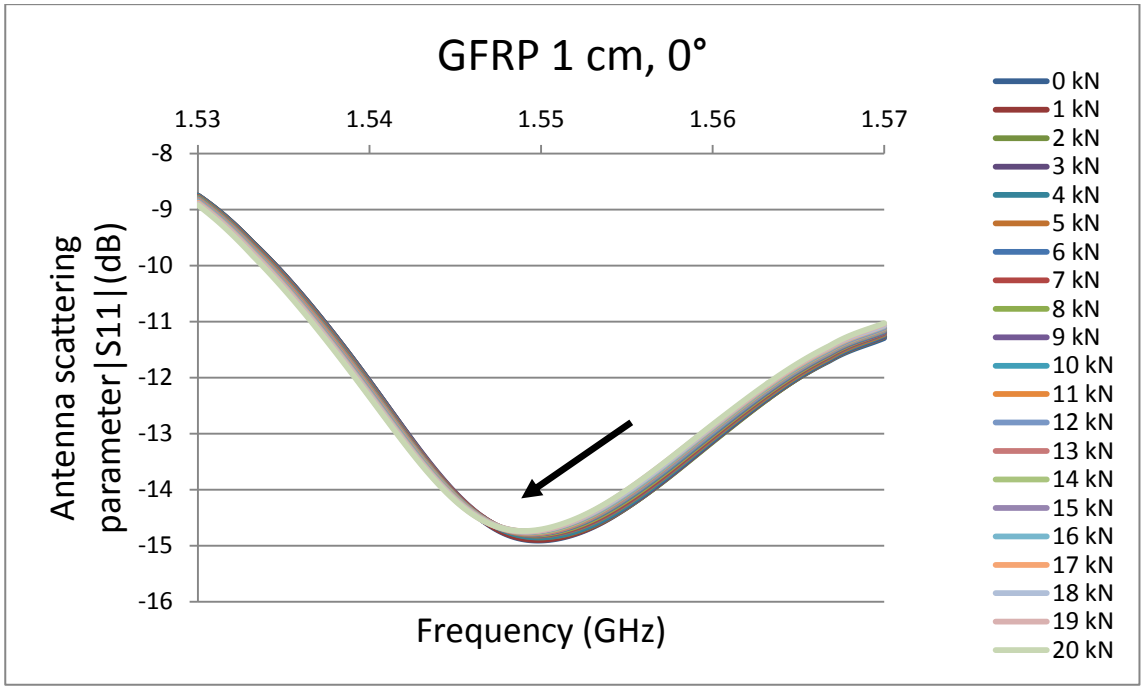

Figure 8.56 Shift in the resonant frequency of the CMPA attached to a GFRP plate at interrogation distance of 1 cm and 0° orientation.

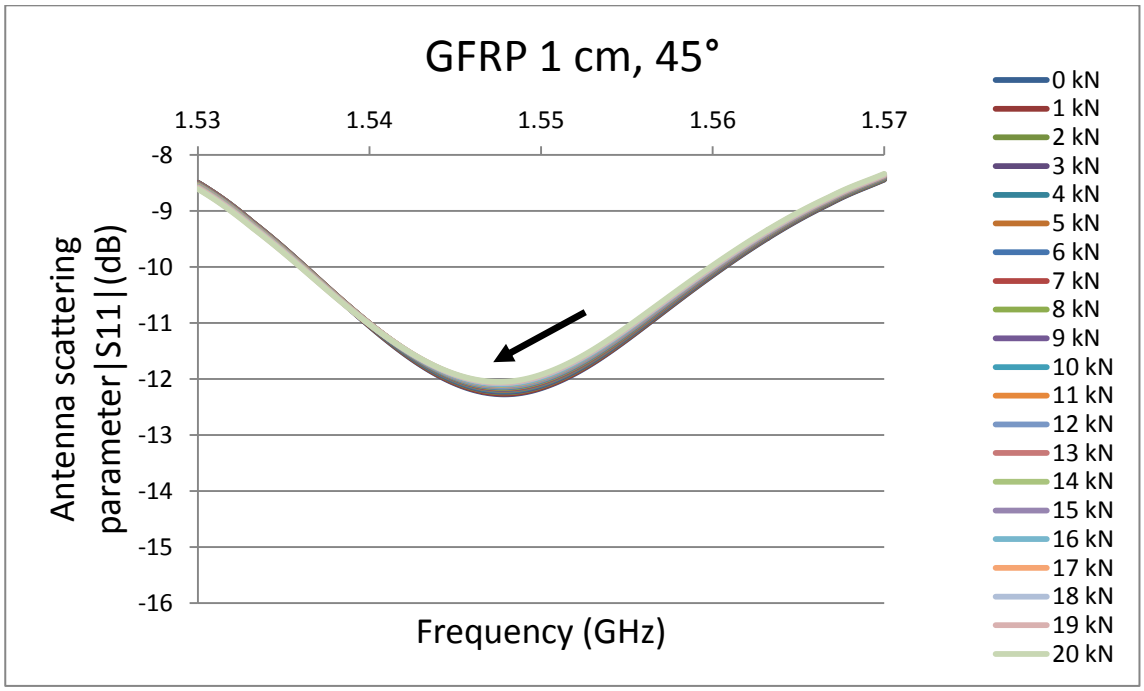

Figure 8.57 Shift in the resonant frequency of the CMPA attached to a GFRP plate at interrogation distance of 1 cm and 45° orientation.

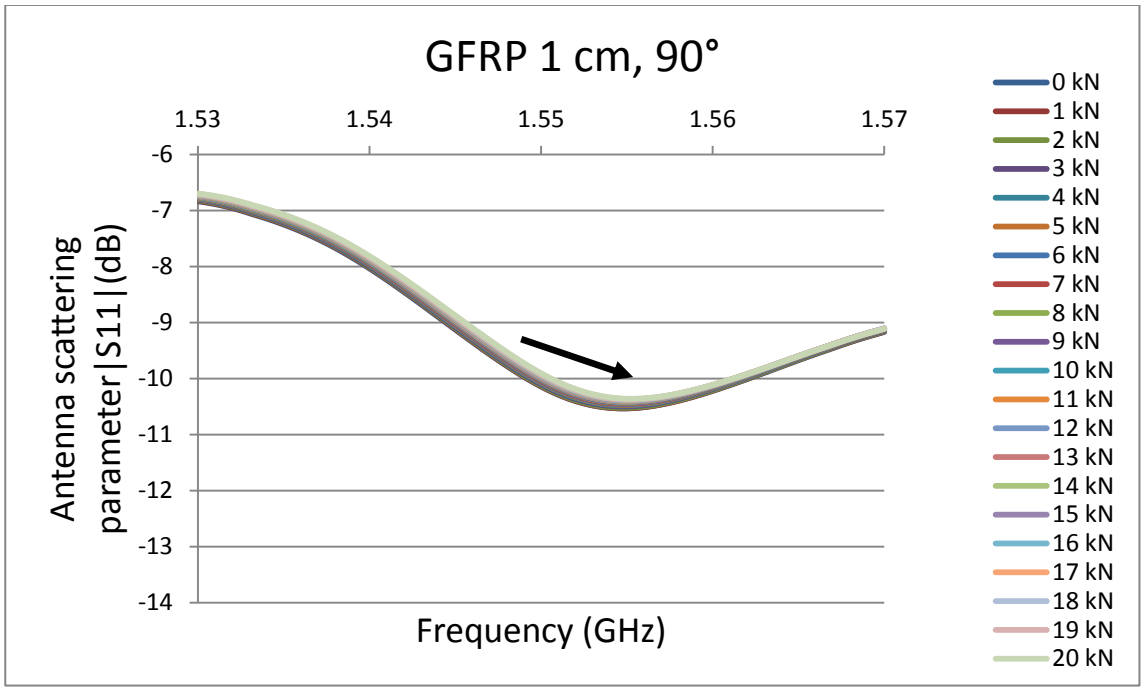

Figure 8.58 Shift in the resonant frequency of the CMPA attached to a GFRP plate at interrogation distance of 1 cm and 90° orientation.

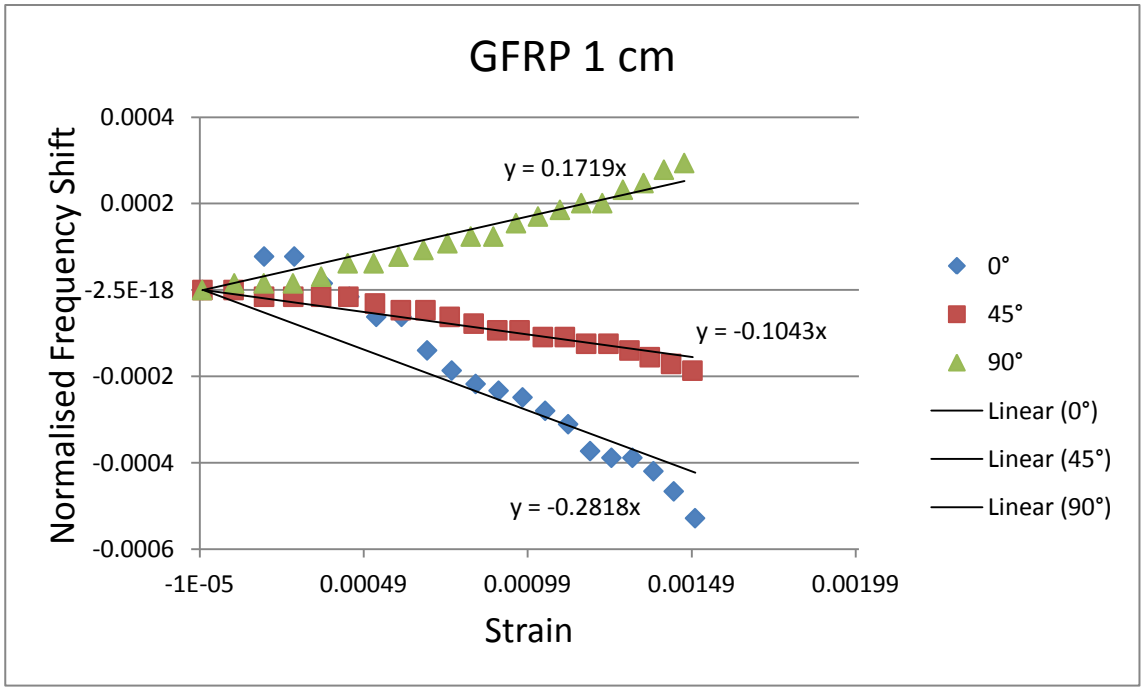

Figure 8.59 Normalised shift in the resonant frequency of the CMPA attached to a GFRP plate against the applied strain for three different horn orientations at interrogation distance of 1 cm.

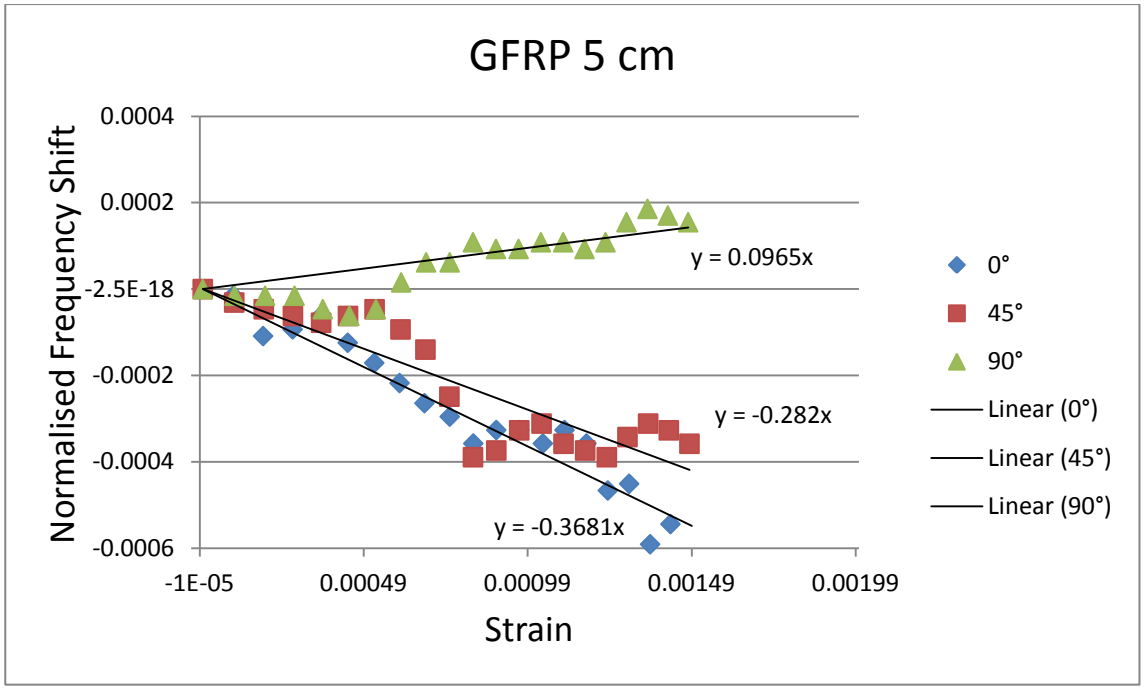

Figure 8.60 Normalised shift in the resonant frequency of the CMPA attached to a GFRP plate against the applied strain for three different horn orientations at interrogation distance of 5 cm.

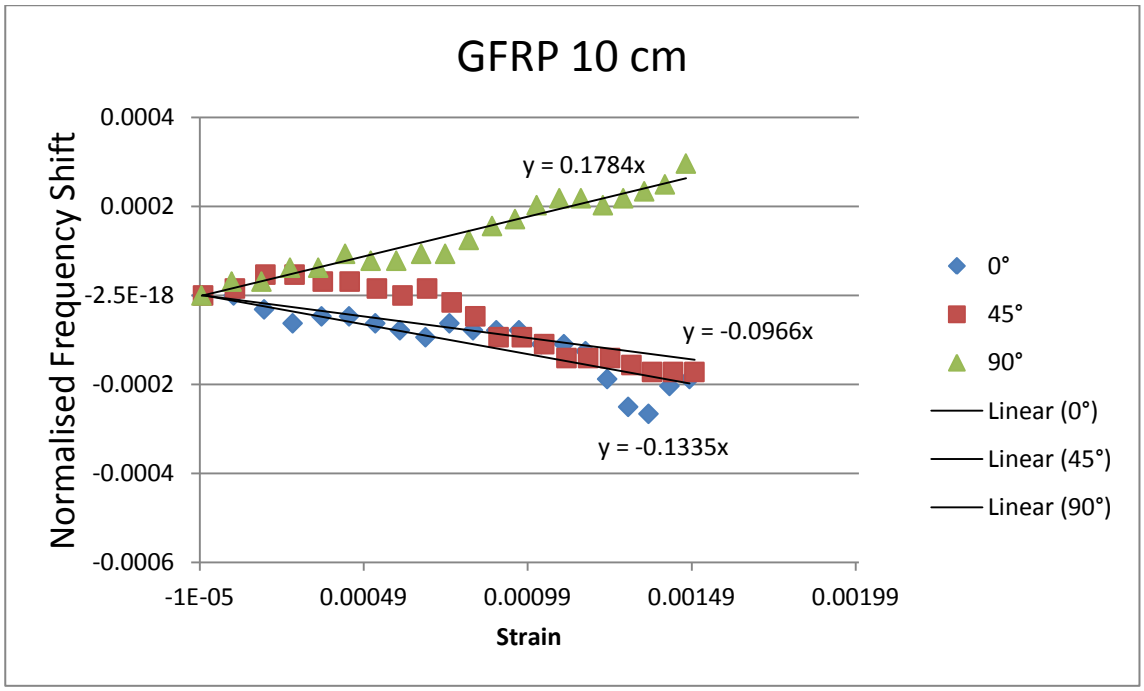

Figure 8.61 Normalised shift in the resonant frequency of the CMPA attached to a GFRP plate against the applied strain for three different horn orientations at interrogation distance of 10 cm.

Figures 8.62, 8.63 and 8.64 show the comparison of the relationship between applied strain and the normalised shift in the resonant frequency of the CMPA for different interrogation distances at 0°, 45° and 90° orientations, respectively. These figures show that by increasing the distance between the sensor and the horn antenna linearity of the relationship decreases

which is the result of increased noise level. The level of noise at 45° degree orientation is higher than the other two orientations at all distances. The level of noise depends on the environmental noise as well as the quality and configuration of the coaxial cable that connect the horn antenna to the network analyser. At 90° orientation, there is a slight increase in the amount of shift by moving the horn away from the CMPA. This is also a result of increased noise level which was observed during the experiments.

For better clarity, these results are repeated in Figures 8.65 to 8.67 only for 1 cm, 5 cm and 10 cm interrogation distances. The linear lines in these figures indicate that apart from the change in the amount of shift, the linearity of the relationship does not change significantly. Similar results for CFRP and GFRP plates are shown in Figures 8.68 to 8.70 and Figures 8.71 to 8.73, respectively. The results for the CFRP back plate is similar to the aluminium plate except for the 90° orientation case where the amount of shift in the resonant frequency of the CMPA decreases with the increase in the interrogation distance. For GFRP back plate, the results are similar to the results for CFRP back plate; however, there is a poor linearity in the plotted results. This nonlinearity is caused by the higher level of noise that was observed for GFRP back plate compared to the other two plates. This indicates that wireless measurement of strain is more reliable for conductive back plates compared to dielectric back plates for the same interrogation distance and test conditions.

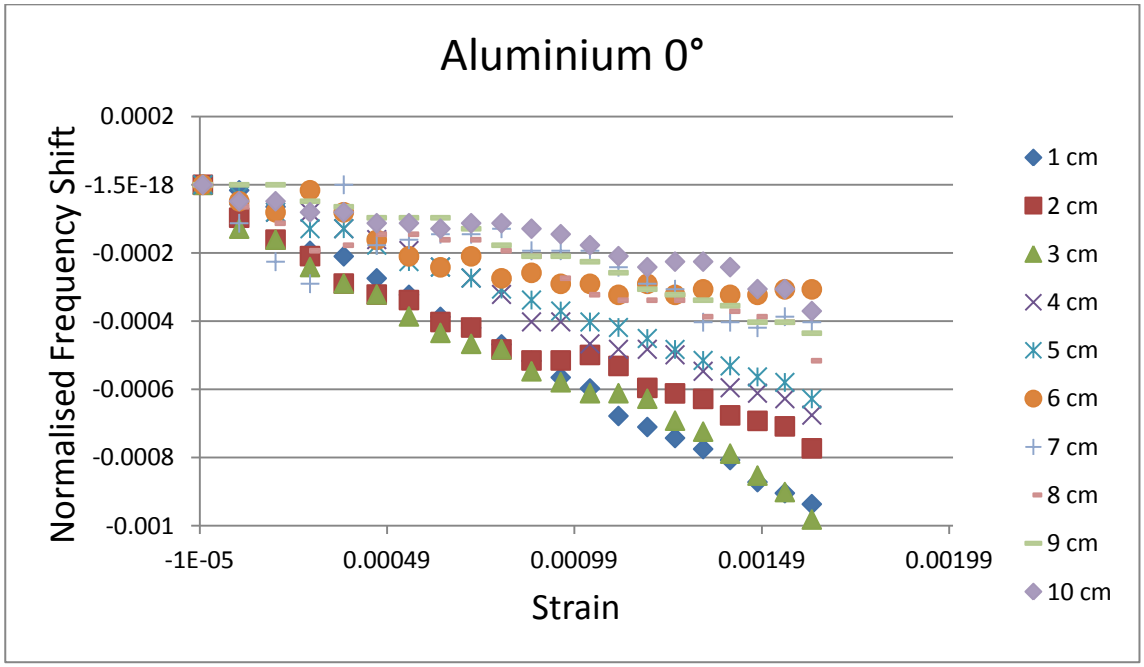

Figure 8.62 Comparison of the relationship between applied strain and the normalised shift in the resonant frequency of the CMPA for different interrogation distances at 0° orientation.

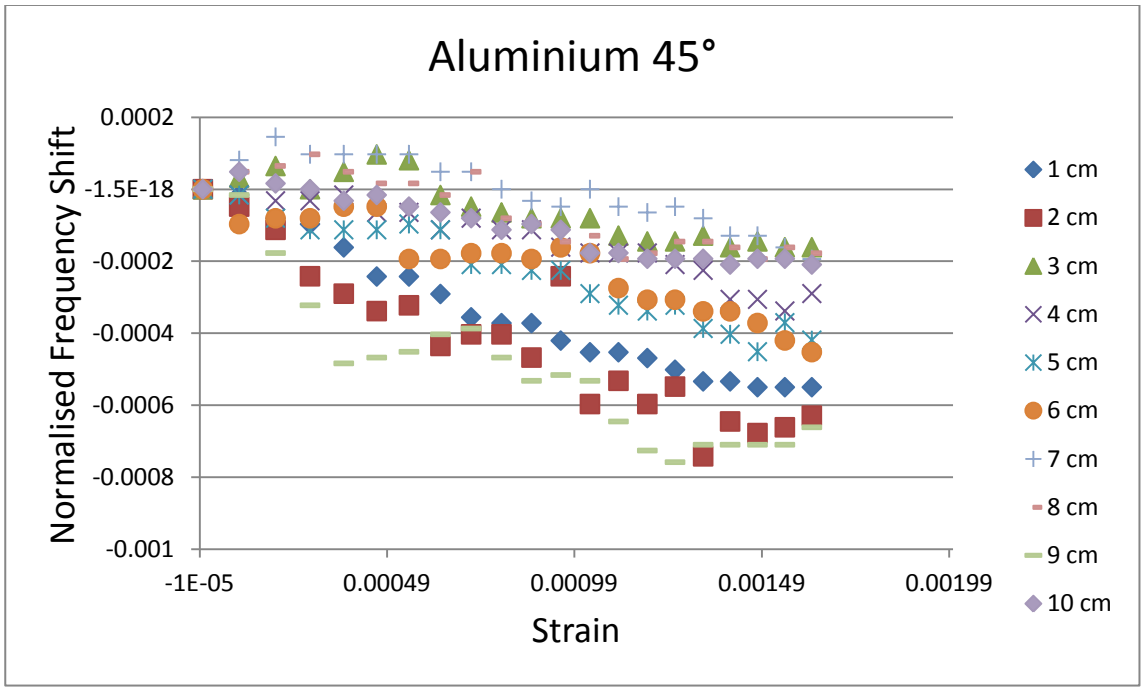

Figure 8.63 Comparison of the relationship between applied strain and the normalised shift in the resonant frequency of the CMPA for different interrogation distances at 45° orientation.

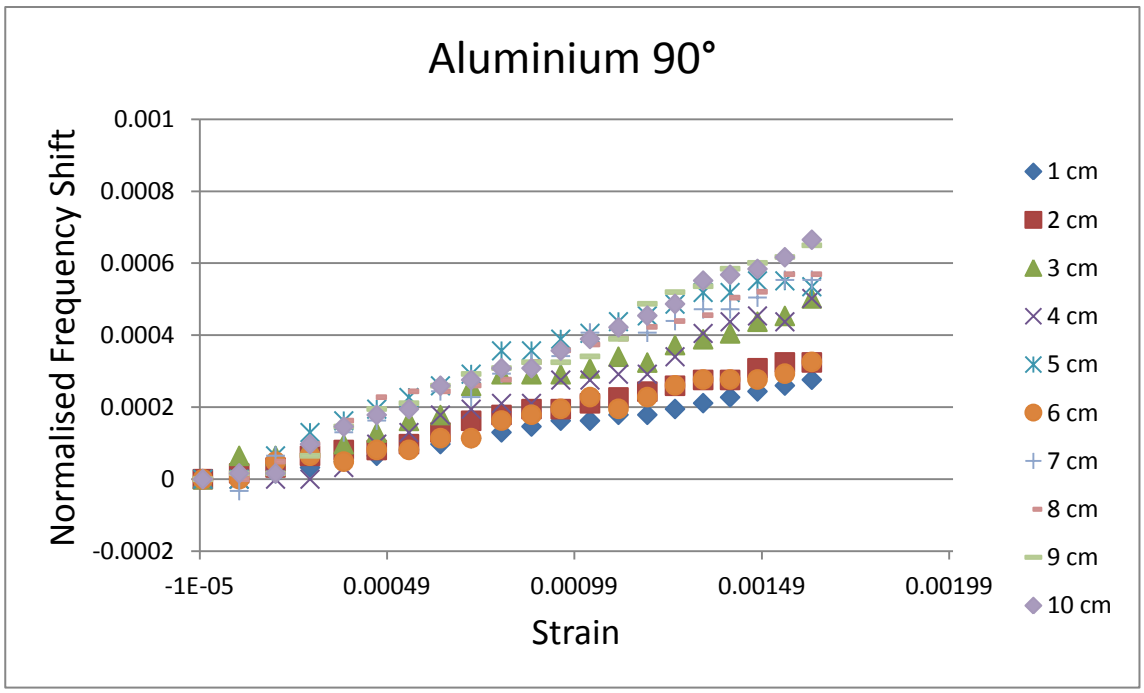

Figure 8.64 Comparison of the relationship between applied strain and the normalised shift in the resonant frequency of the CMPA for different interrogation distances at 90° orientation.

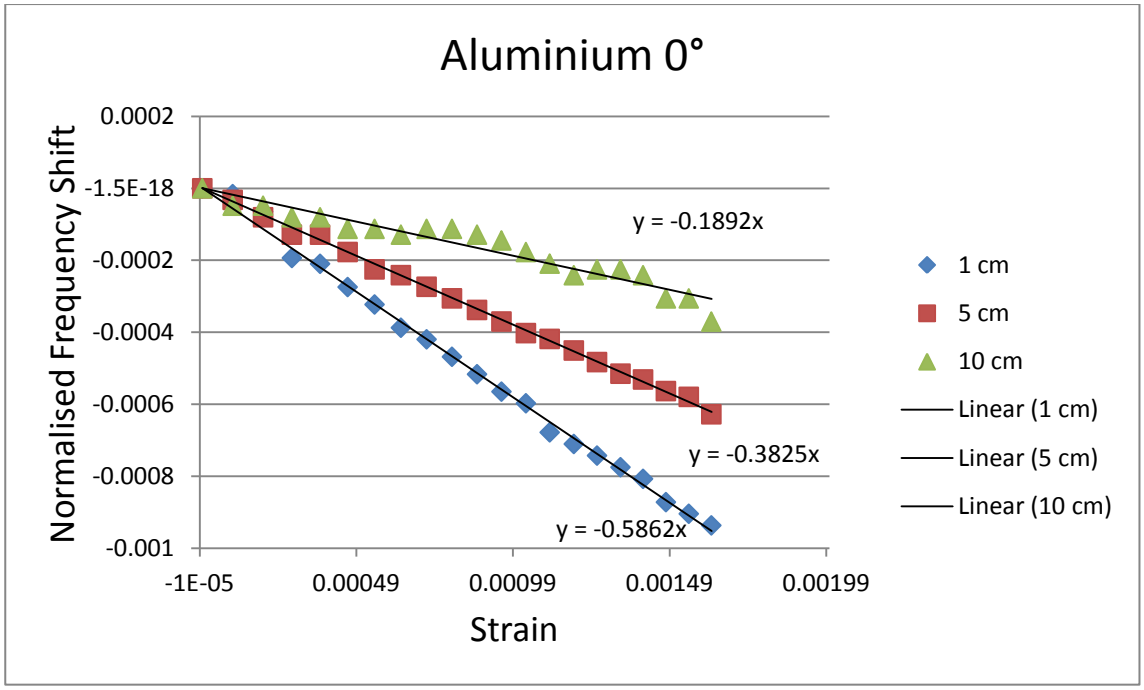

Figure 8.65 Comparison of the relationship between applied strain and the normalised shift in the resonant frequency of the CMPA attached to an aluminium plate for interrogation distances of 1 cm, 5 cm and 10 cm at 0° orientation.

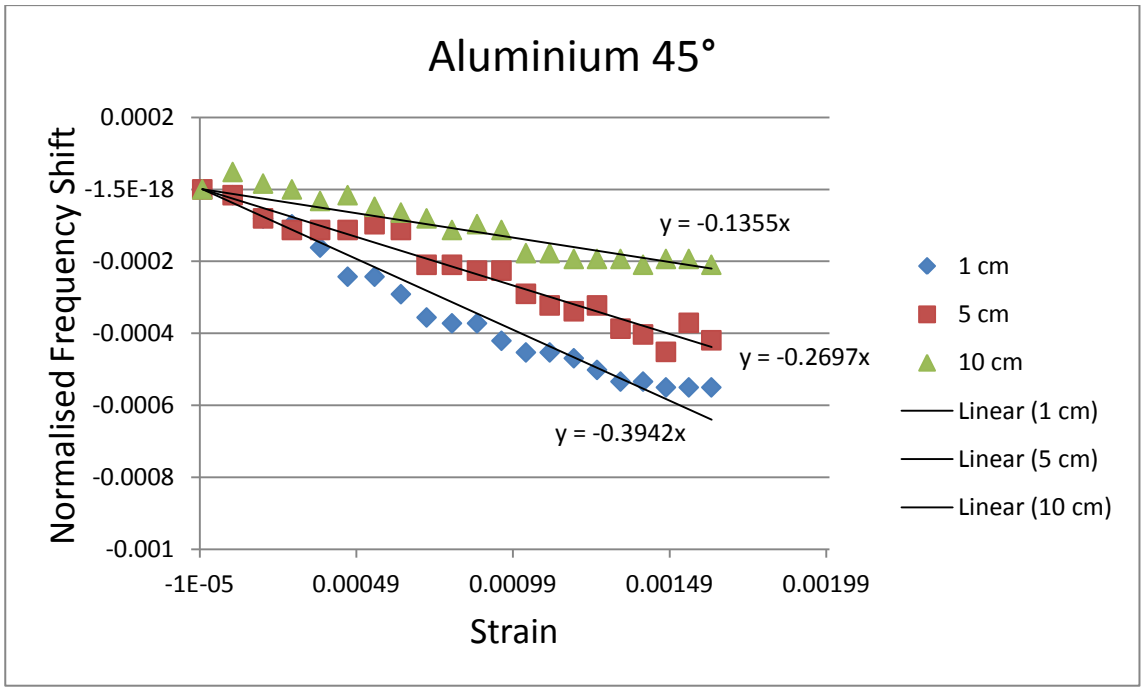

Figure 8.66 Comparison of the relationship between applied strain and the normalised shift in the resonant frequency of the CMPA attached to an aluminium plate for interrogation distances of 1 cm, 5 cm and 10 cm at 45° orientation.

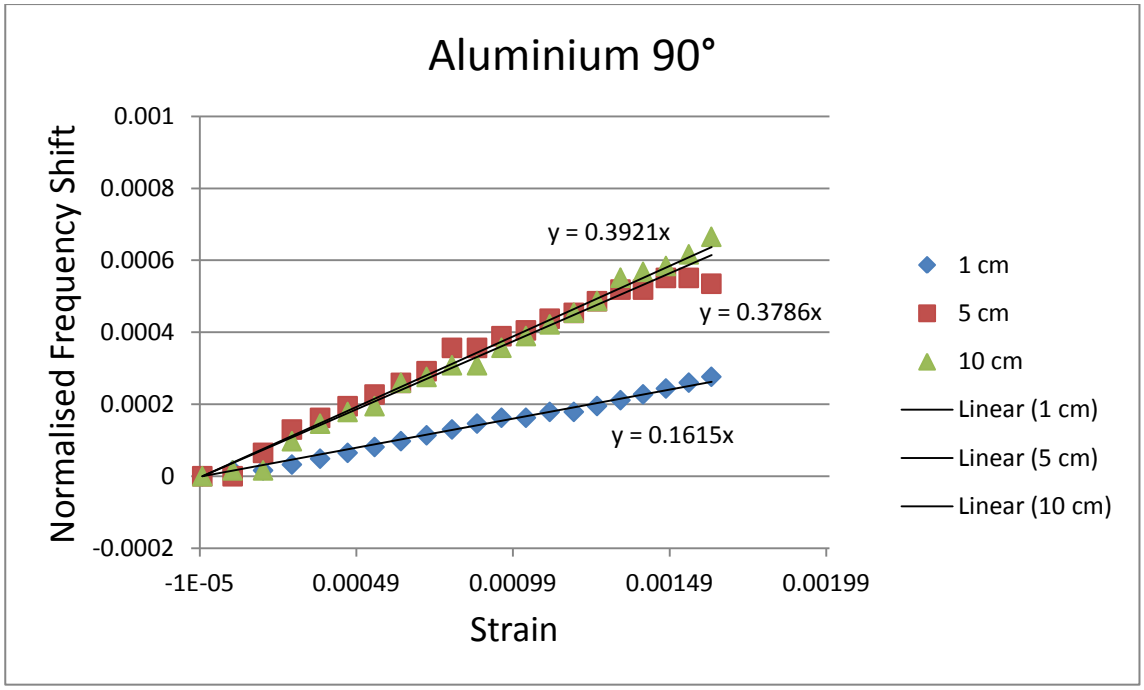

Figure 8.67 Comparison of the relationship between applied strain and the normalised shift in the resonant frequency of the CMPA attached to an aluminium plate for interrogation distances of 1 cm, 5 cm and 10 cm at 90° orientation.

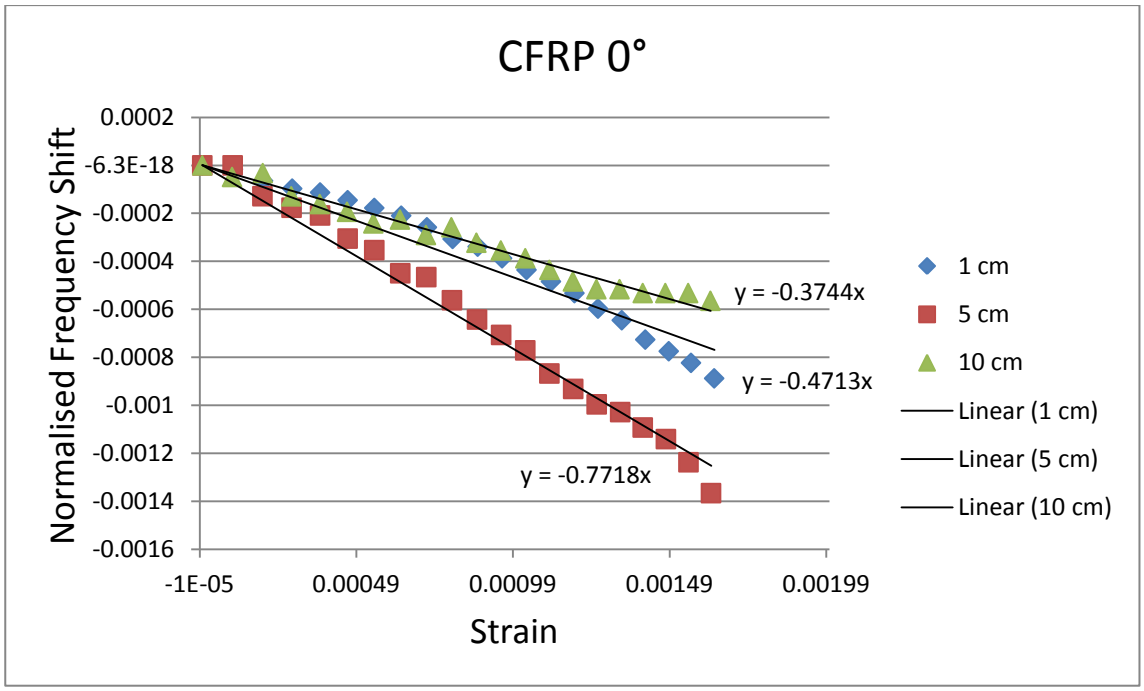

Figure 8.68 Comparison of the relationship between applied strain and the normalised shift in the resonant frequency of the CMPA attached to a CFRP plate for interrogation distances of 1 cm, 5 cm and 10 cm at 0° orientation.

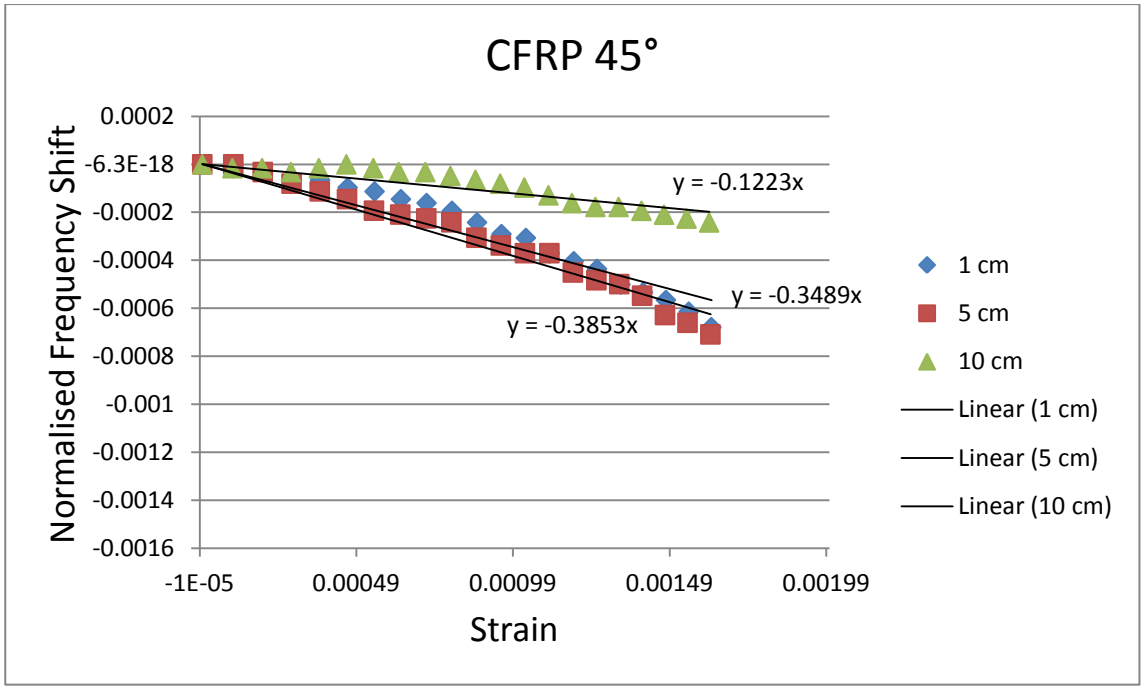

Figure 8.69 Comparison of the relationship between applied strain and the normalised shift in the resonant frequency of the CMPA attached to a CFRP plate for interrogation distances of 1 cm, 5 cm and 10 cm at 45° orientation.

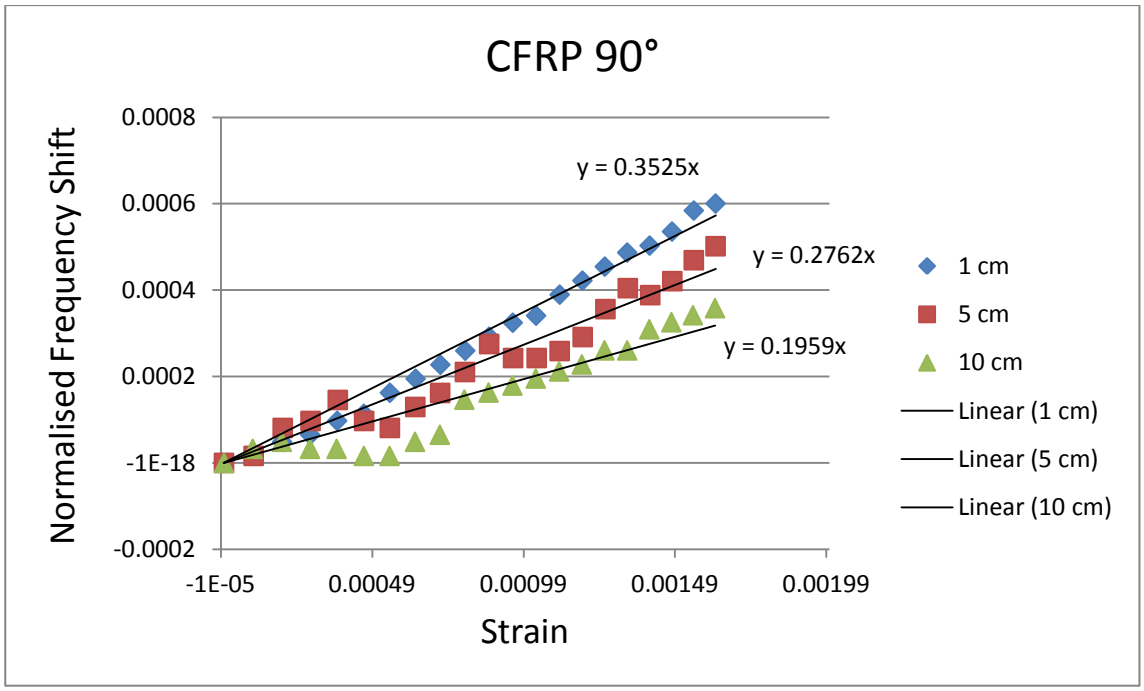

Figure 8.70 Comparison of the relationship between applied strain and the normalised shift in the resonant frequency of the CMPA attached to a CFRP plate for interrogation distances of 1 cm, 5 cm and 10 cm at 90° orientation.

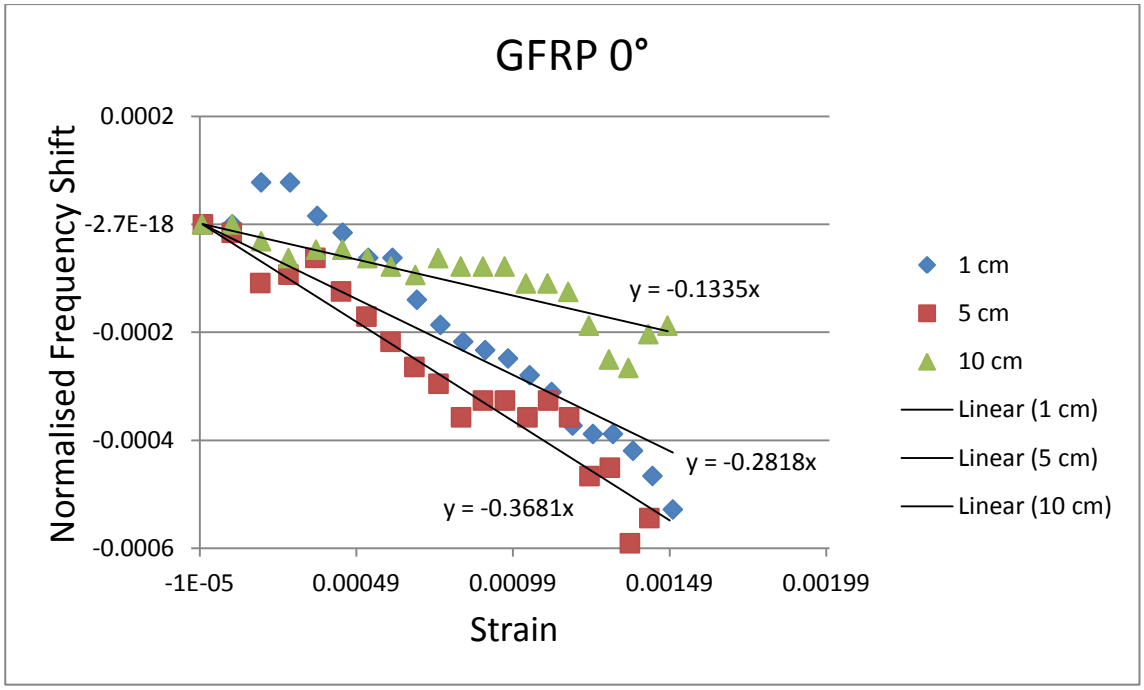

Figure 8.71 Comparison of the relationship between applied strain and the normalised shift in the resonant frequency of the CMPA attached to a GFRP plate for interrogation distances of 1 cm, 5 cm and 10 cm at 0° orientation.

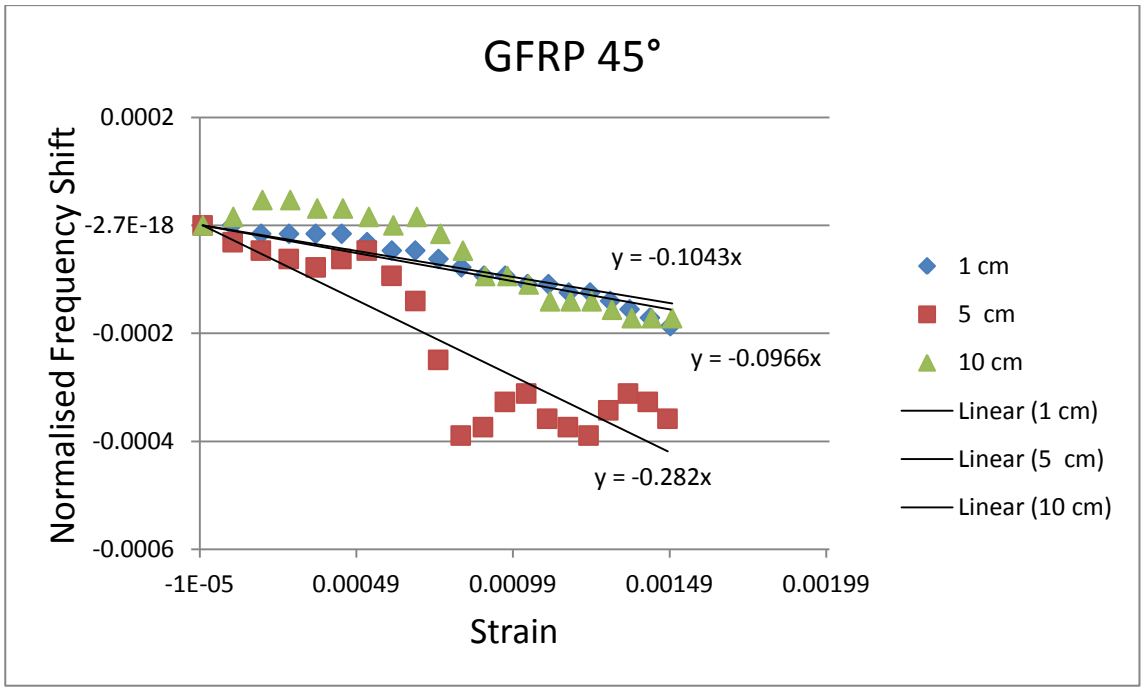

Figure 8.72 Comparison of the relationship between applied strain and the normalised shift in the resonant frequency of the CMPA attached to a GFRP plate for interrogation distances of 1 cm, 5 cm and 10 cm at 45° orientation.

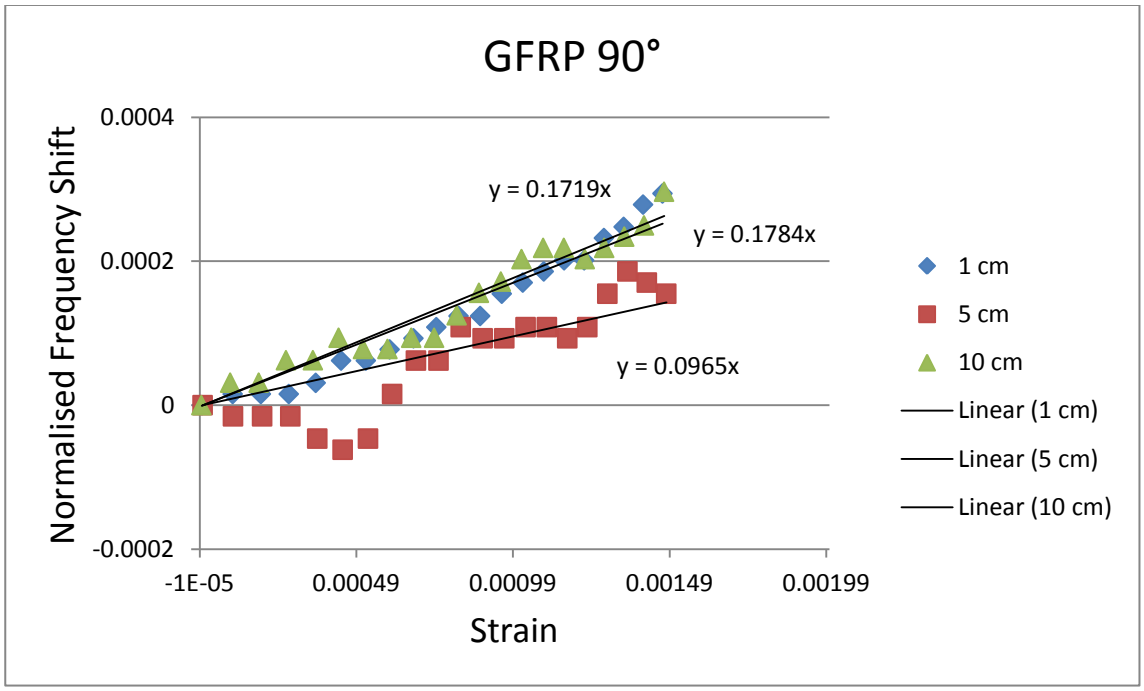

Figure 8.73 Comparison of the relationship between applied strain and the normalised shift in the resonant frequency of the CMPA attached to a GFRP plate for interrogation distances of 1 cm, 5 cm and 10 cm at 90° orientation.

Figure 8.74 shows the comparison of strain-normalised frequency shift relationship at interrogation distance of 1 cm and the 0° orientation for reference and offset locations of horn antenna. The test results for the reference location (centre of the horn antenna was in front of the CMPA centre) are repeated twice and compared to 5 cm and -5 cm offset for horn location. The comparison between the resonant frequencies of the CMPA for these different offset locations before applying the tensile load is presented in Figure 8.75. These figures indicate that apart from the change in the reference frequency of the CMPA (as a result of changing the location of the horn antenna), the relationship between strain and normalised frequency shift is same for all the cases. This demonstrates that the amount of shift in the resonant frequency is not sensitive to the offset distance.

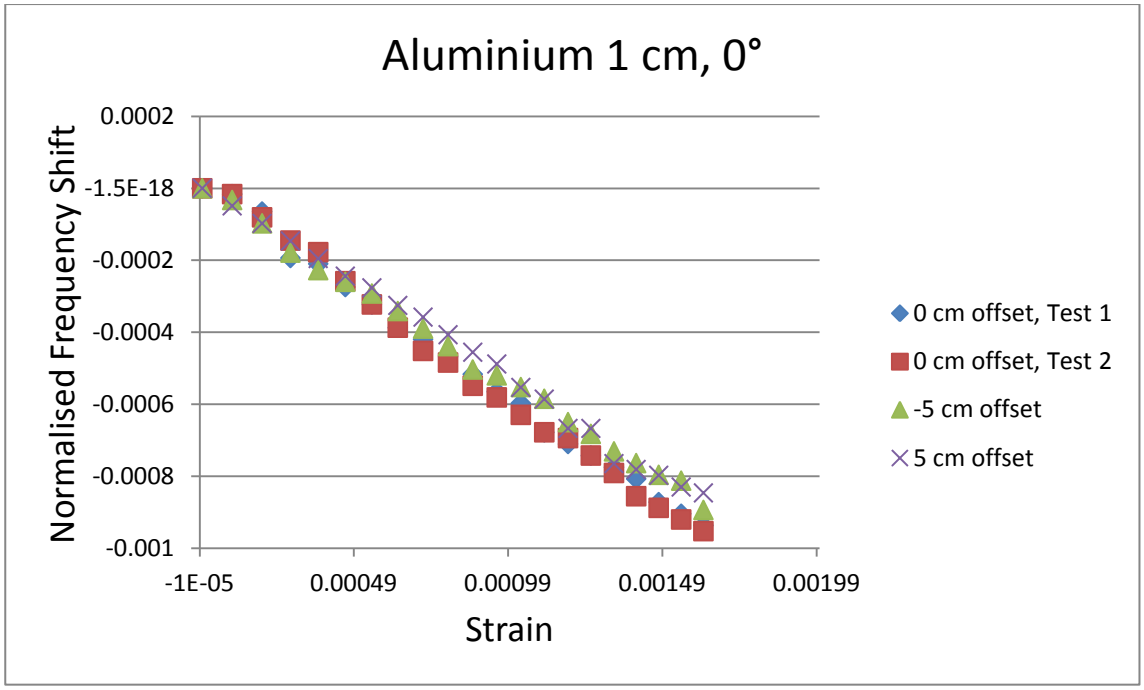

Figure 8.74 Comparison of strain-normalised frequency shift relationship at interrogation distance of 1 cm and 0° orientation for reference and offset locations of horn antenna.

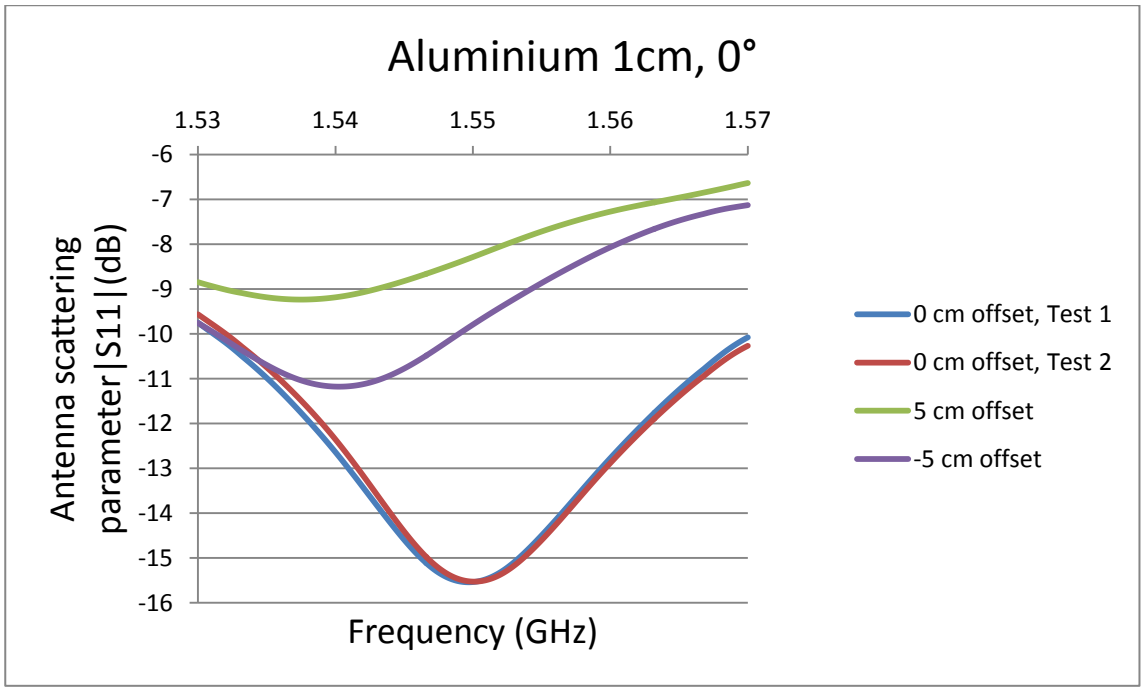

Figure 8.75 Comparison of resonant frequency of CMPA at interrogation distance of 1 cm and 0° orientation for reference and offset locations of horn antenna.

Figure 8.76 shows the comparison between the resonant frequencies of three different CMPA sensors attached to three back plates with different materials. The resonant frequency of the CMPA attached to the GFRP plate is about 600 MHz higher than other plates. This is the result of manufacturing tolerances and is not a result from the back plate

material effect. The dip in the resonant frequency of the CMPA attached to the CFRP plate is larger than the other two sensors.

Figures 8.77 to 8.85 show the comparison of the relationship between strain and the normalised shift for three different back plate materials at 1 cm, 5 cm and 10 cm interrogation distances and 0°, 45° and 90° orientations. The slope of the linear line for Aluminium plate shows a higher amount of shift except 1 cm 90°, 5 cm 0° and 10 cm 0° cases where the amount of shift is higher for the CFRP plate. The amount of shift for GFRP plate is less than the other two plates in all of the scenarios. It is very difficult to conclude a general trend based on the effect of back plate material on the relationship between strain and normalised shift. However, it is obvious that the linearity of this relationship is consistent for all of these materials. Also, it should be mentioned that the level of noise for GFRP plate was higher during the tests which resulted in discrepancy of the results for this material. Overall, wireless measurement of strain is feasible for all the materials used for these tests.

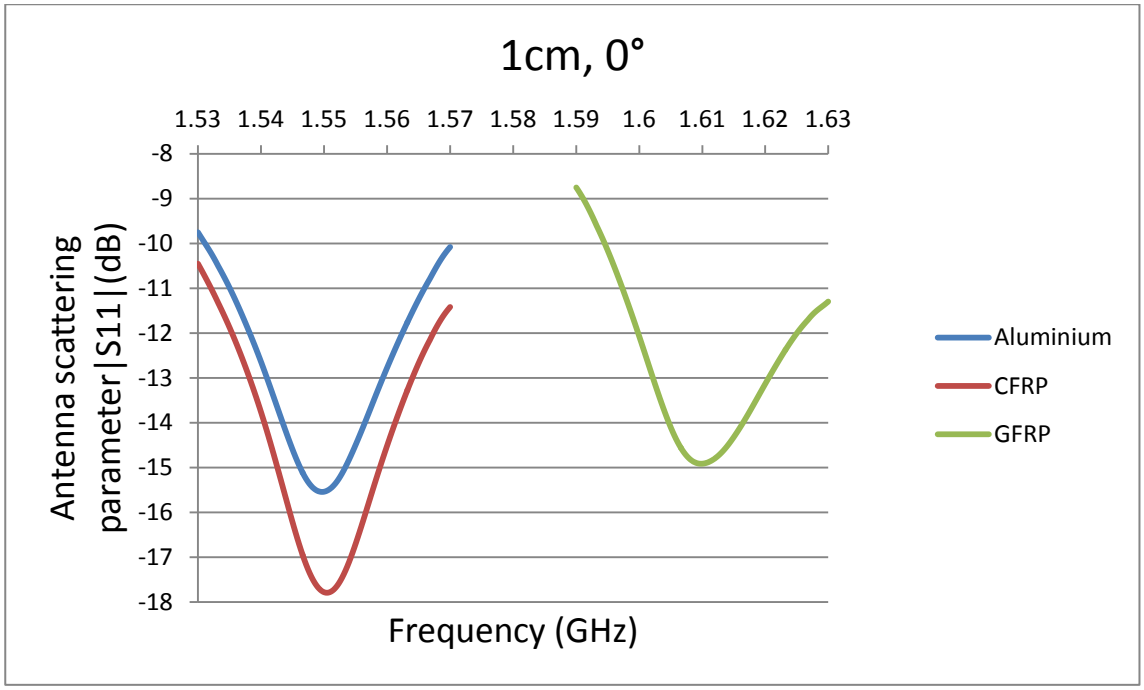

Figure 8.76 Comparison of resonant frequency of CMPA attached to three different plates at interrogation distance of 1 cm and 0° orientation.

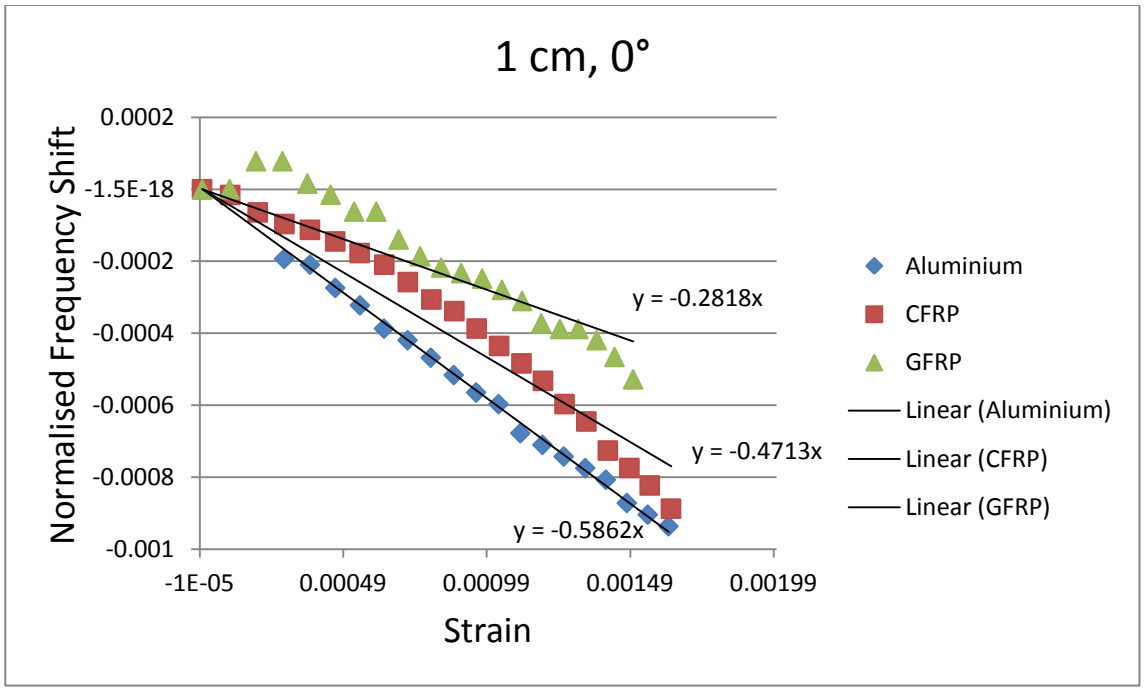

Figure 8.77 Comparison of strain-normalised frequency shift relationship at interrogation distance of 1 cm and 0° orientation for three different plates.

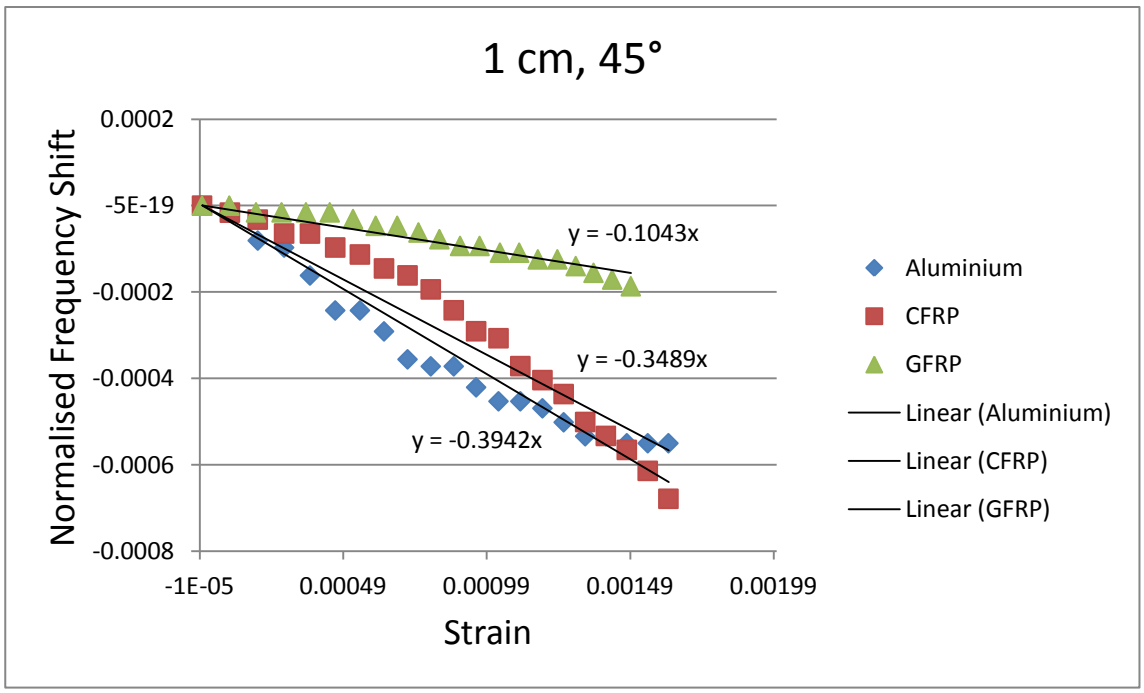

Figure 8.78 Comparison of strain-normalised frequency shift relationship at interrogation distance of 1 cm and 45° orientation for three different plates.

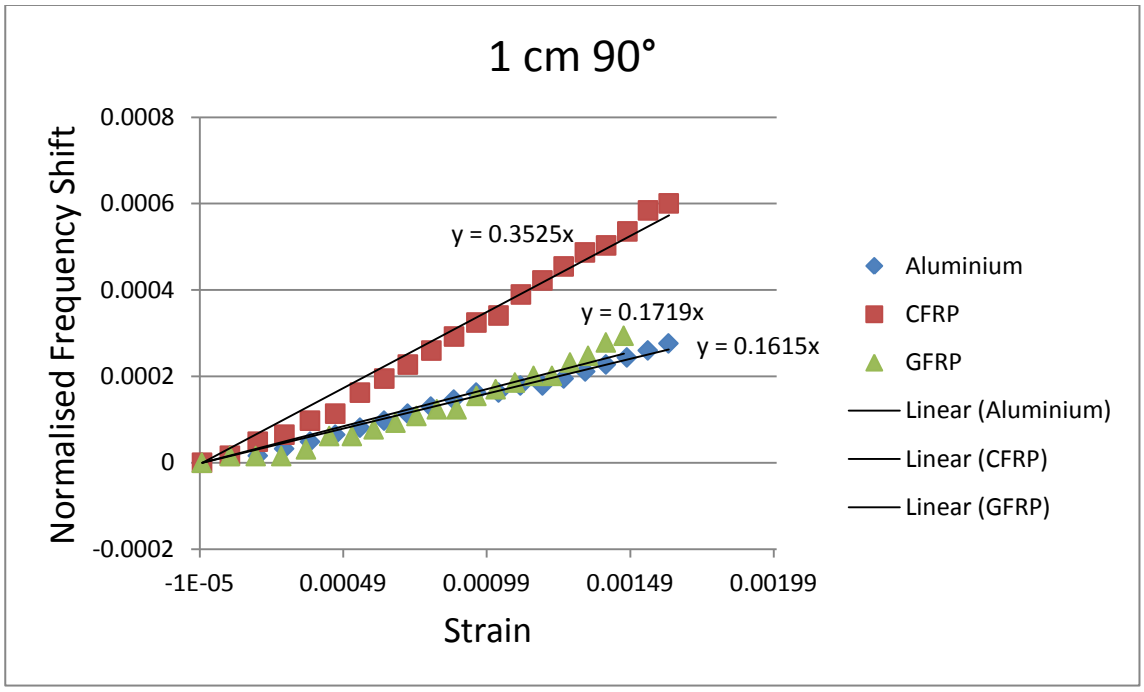

Figure 8.79 Comparison of strain-normalised frequency shift relationship at interrogation distance of 1 cm and 90° orientation for three different plates.

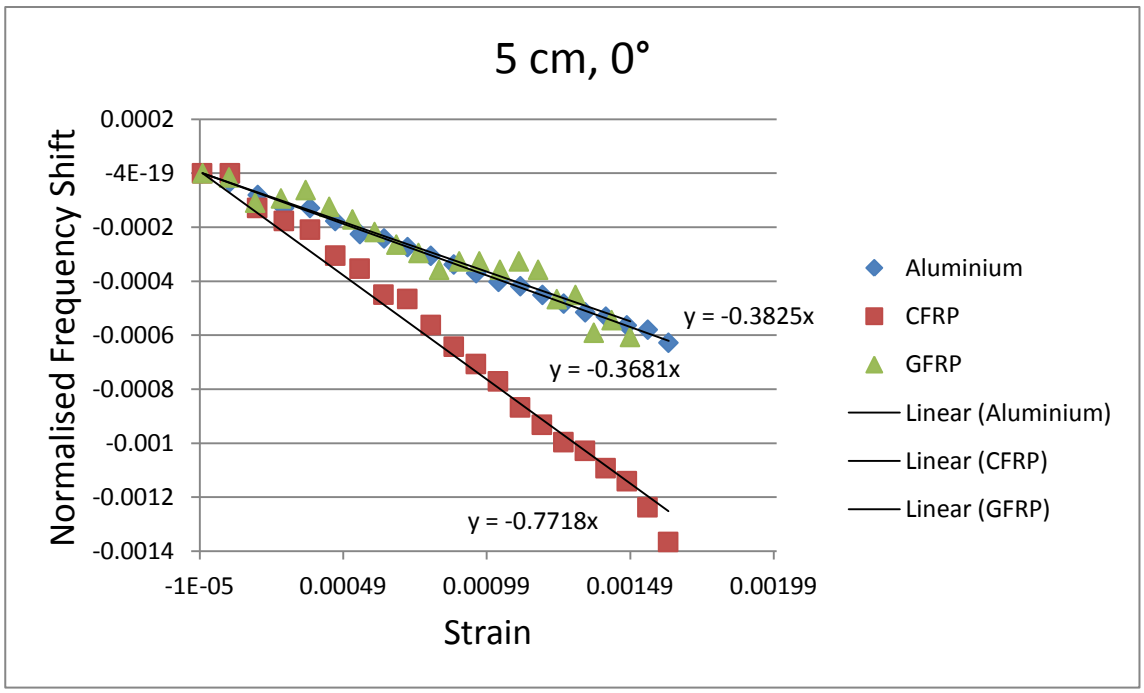

Figure 8.80 Comparison of strain-normalised frequency shift relationship at interrogation distance of 5 cm and 0° orientation for three different plates.

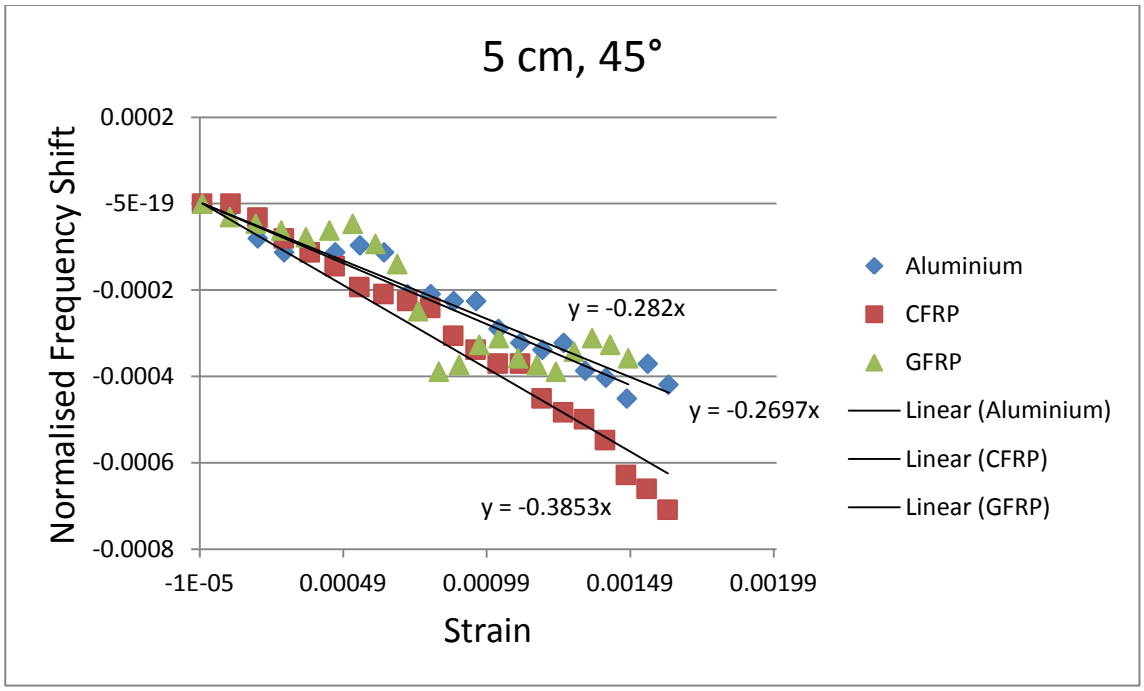

Figure 8.81 Comparison of strain-normalised frequency shift relationship at interrogation distance of 5 cm and 45° orientation for three different plates.

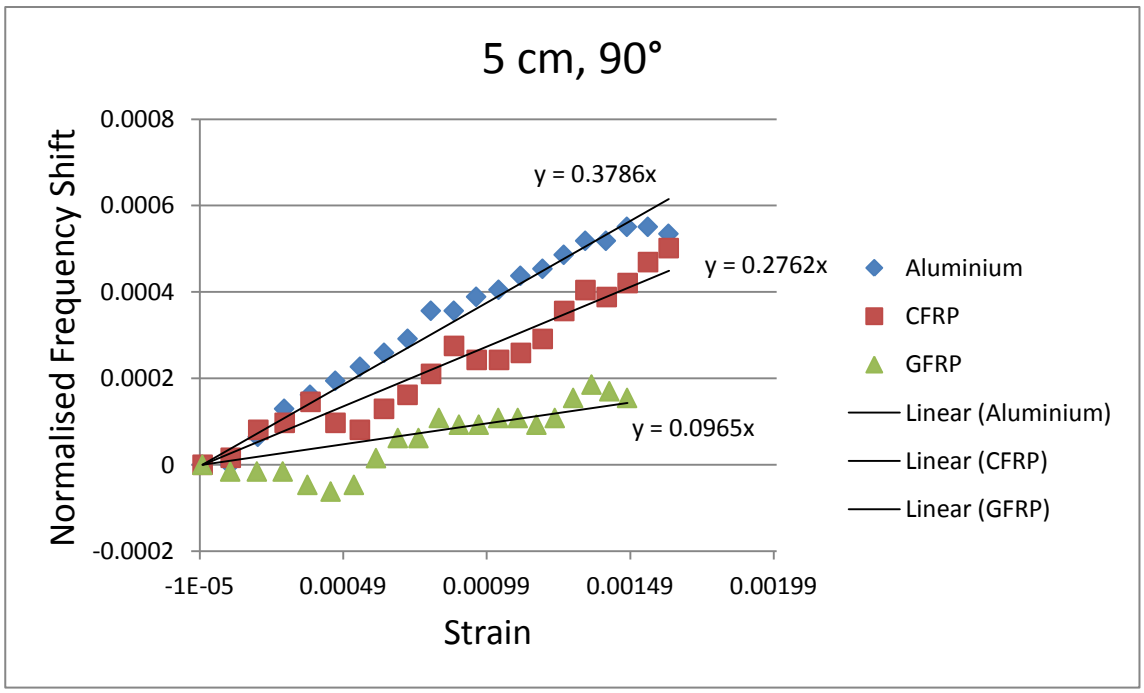

Figure 8.82 Comparison of strain-normalised frequency shift relationship at interrogation distance of 5 cm and 90° orientation for three different plates.

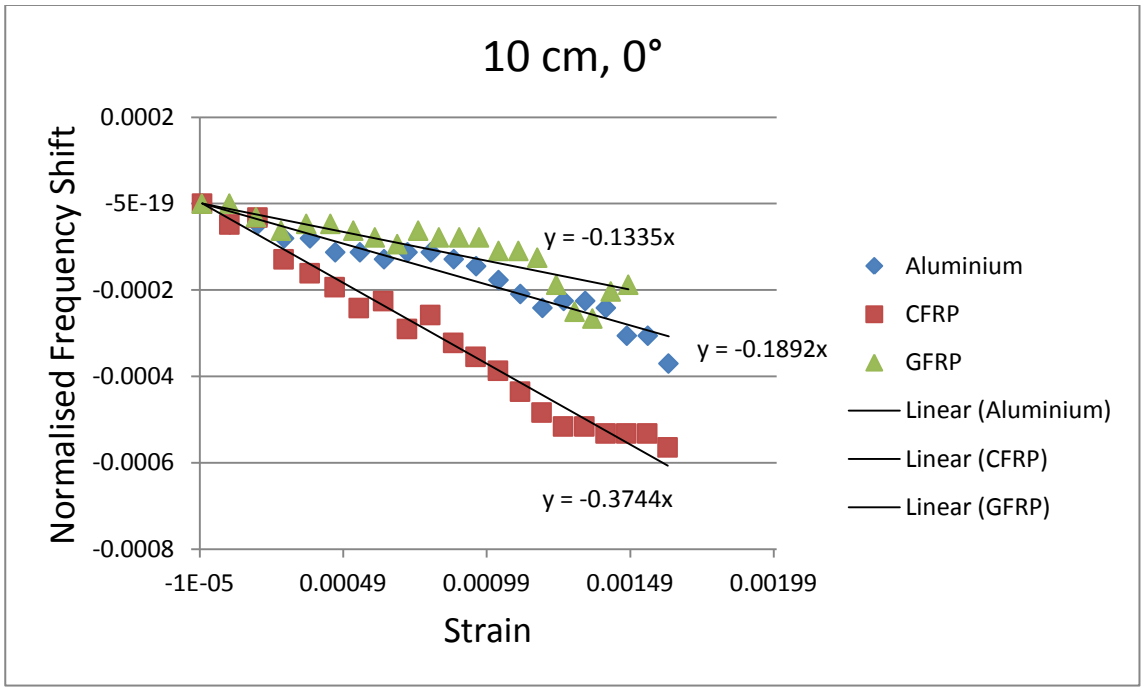

Figure 8.83 Comparison of strain-normalised frequency shift relationship at interrogation distance of 10 cm and 0° orientation for three different plates.

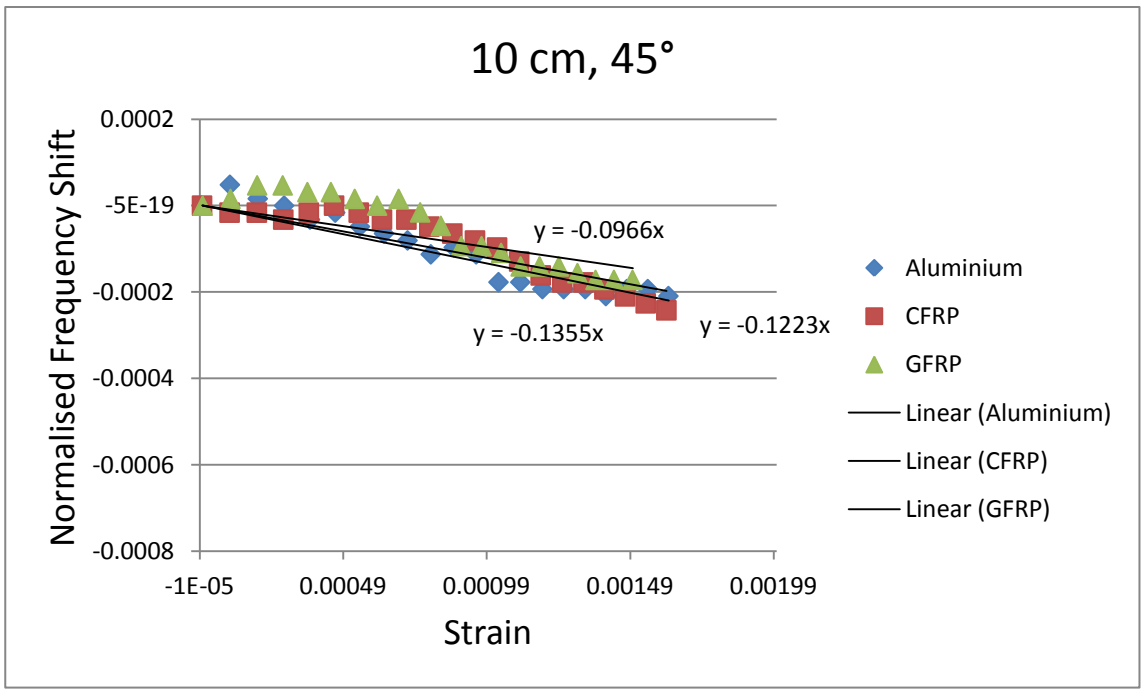

Figure 8.84 Comparison of strain-normalised frequency shift relationship at interrogation distance of 10 cm and 45° orientation for three different plates.

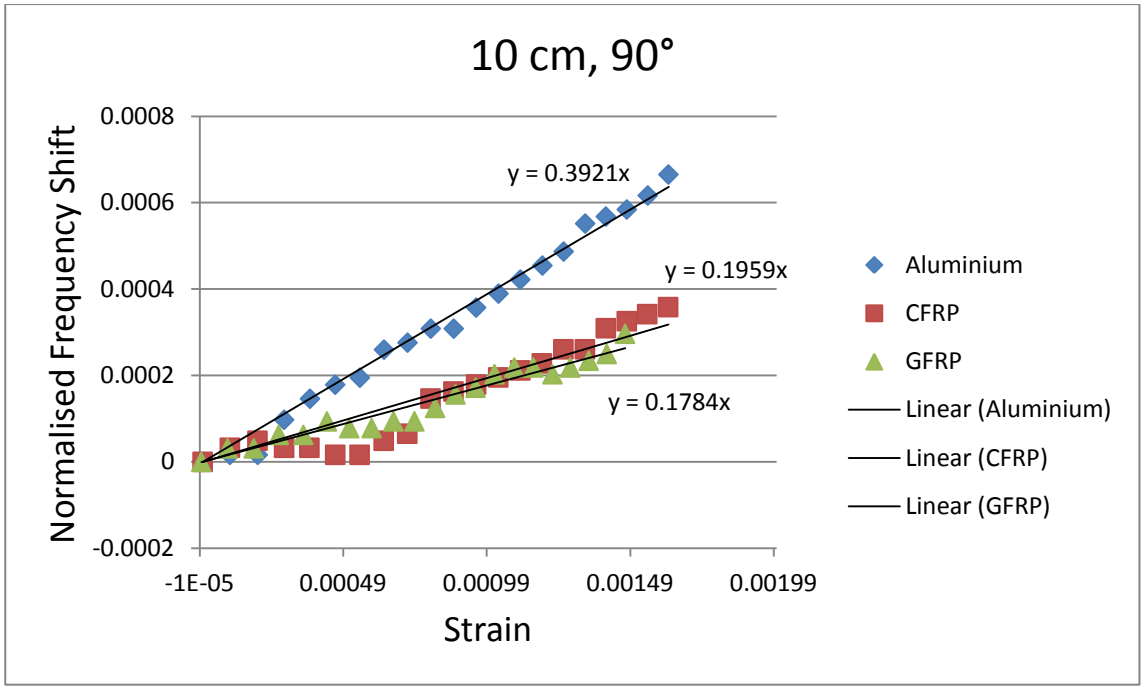

Figure 8.85 Comparison of strain-normalised frequency shift relationship at interrogation distance of 10 cm and 90° orientation for three different plates.

8.6 High Quality Factor Antennas

Based on the results shown in previous section, it is obvious that the magnitude of the maximum of the return loss curve for the horn antenna (a result of exciting the patch antenna/sensor) plays an important part in the amount of shift and therefore the sensitivity of the antenna. It also has a vital effect on the maximum distance between the horn antenna and the sensor. In addition, the bandwidth of the antenna (the width of the curve at the resonant frequency of the patch) has an important effect on the sensitivity of the sensor. Decreasing the bandwidth of the antenna/sensor and increasing its quality factor can improve the sensitivity of the antenna as well as increasing the wireless interrogation distance.

The fractional bandwidth of an antenna is inversely proportional to the quality factor of the antenna with the following relationship (Balanis, 2005):

$$\text{Fractional Bandwidth} = \frac{\Delta f}{f_0} = \frac{1}{Q_t} \qquad (8.2)$$

Where

Q_t is the total quality factor of the antenna.

A more precise relationship can be defined by accounting for the impedance matching of the antenna (Balanis, 2005). However, for the wireless excitation of the patch this is not the case.

The quality factor of an antenna can be defined as the representative of the antenna losses (Balanis, 2005). According to Balanis (2005) the total quality factor for a circular microstrip patch antenna can be calculated from the following equation:

$$\frac{1}{Q_t} = \frac{1}{Q_{rad}} + \frac{1}{Q_c} + \frac{1}{Q_d} + \frac{1}{Q_{sw}} \tag{8.3}$$

Where

Q_t is the total quality factor of the antenna;

Q_{rad} is the quality factor of the antenna due to radiation losses;

Q_c is the quality factor of the antenna due to conductive losses;

Q_d is the quality factor of the antenna due to dielectric losses;

And

Q_{sw} is the quality factor of the antenna due to surface waves.

For very thin substrates the losses due to surface waves are very small and can be neglected in calculation of the total quality factor (Balanis, 2005). This indicates that by reducing the thickness of the patch antenna, the quality factor due to surface waves can be improved, and as a result of that, the total quality factor of the antenna can be improved.

For very thin substrates ($h << \lambda_0$), the other three quality factors can be calculated using following equations (Balanis, 2005):

$$Q_c = h\sqrt{\pi f \mu \sigma} \tag{8.4}$$

$$Q_d = \frac{1}{\tan\delta} \tag{8.5}$$

$$Q_{rad} = \frac{2\omega\varepsilon_r}{hG_t/l} k_p \tag{8.6}$$

Where

h is the substrate thickness;

f is the resonant frequency of the antenna;

μ is the permeability of the substrate;

σ is the conductivity of the patch and ground plane;

$\tan\delta$ is the loss tangent of the substrate;

ω is the wave angular frequency;

ε_r is the substrate dielectric constant;

G_t/l is the total conductance per unit length of the radiating aperture;

And

k_p is a factor that depends on the geometry of the patch.

The quality factor due to dielectric losses can be improved by using low loss materials for substrate. Also, conductive losses can be reduced by increasing the conductivity of the patch and ground plane as well as increasing the substrate thickness. These result in improving the quality factor due to conductive losses. However, according to Balanis (2005), for very thin substrates the dominant factor is the radiation quality factor. This part of total quality factor is proportional to the substrate dielectric constant and inverse of the substrate thickness. Therefore, by using substrate materials with high dielectric constant and low thickness the radiation quality factor and subsequently the total quality factor of the patch antenna can be improved. Hence, it is recommended to use such materials for better designs in the future that can result in improved sensitivity and increased interrogation distance of wireless microstrip patch antenna sensors. This will form the basis for further work in this field.

8.7 Conclusion

In this chapter, the feasibility of wireless strain measurement has been investigated using finite element analysis and experimental tests. It has been shown that the resonant frequency of a CMPA can be measured wirelessly using two different techniques. One of the proposed techniques, based on the near-field effect of horn antennas, was shown to measure strain wirelessly.

The results show that strain can not only be measured wirelessly but also, the strain in different directions can be detected by rotating the horn antenna in the desired direction. This phenomenon was established for measuring strain on three different materials, namely

aluminium, CFRP and GFRP. In addition, the effect of the interrogation distance and horn offset location has been investigated and the results were explained.

Based on the results provided, the most important factor affecting the wireless strain measurement is the interrogation distance between the CMPA sensor and the reader antenna (horn antenna). By increasing the interrogation distance the effect of noise on the measurement increases which reduces the accuracy of the measurement. In order to overcome this problem in the future, the sensitivity of the CMPA must be improved and as a result of that the amount of shift must be higher than the variation on S11 curve. While investigating different design configurations is a possible option, increasing the quality factor of the CMPA or using high quality factor resonators is recommended.

CHAPTER 9

Conclusion

9.1 Overview

The main aim of this research was to investigate the feasibility of measuring strain using microstrip patch antennas. The key objective of this research was to study different antenna sensor configurations in order to investigate the sensitivity and directionality of the antenna strain sensors. The following sub-sections explain the main findings from this work.

9.2 Theory of Strain-Frequency Shift Relationship

The relationship between applied strain on a circular microstrip patch antenna and the resultant shift in its resonant frequency is derived (Chapter 4, Section 2.1.1). The formulation derived shows that a linear relationship exists between strain and frequency shift. This initial study enhanced the theory of strain measurement using electromagnetic resonators including microstrip patch antennas.

In order to evaluate the proposed theory, circular microstrip patch resonant frequency formulation is used for the analytical study of the aforementioned relationship. The results obtained from MATLAB™ codes confirms that there is a linear relationship between antenna frequency shift and change in physical dimensions of the circular patch resulted from applied strain (Chapter 4, Section 2.1.1).

To further develop this theory for other potential electromagnetic resonators, a comprehensive study was conducted (Chapter 4). It is shown that, the other configurations (including rectangular microstrip patch antenna, dielectric resonators and split ring resonators) which are described in Chapter 4 can also be utilised to measure strain (same as circular microstrip patch antenna).

9.3 Computational (FEA) Models

To further evaluate this linear relationship, a simulation by ANSYS™ software was conducted (Chapter 5, Section 3). The connection between structural analysis and electromagnetic analysis was achieved using ANSYS APDL™ and FORTRAN™. The simulation was based on a 3-point bend test of the circular microstrip patch antenna attached to an aluminium plate. The results obtained from FEA confirm the proposed theory and the feasibility of measuring strain using circular microstrip patch antennas.

The STEMCOF data processing protocol was developed (Chapter 5, Section 5). This successfully combined two different commercial FEA packages (ANSYS Workbench™ and HFSS™). The main rationale for developing this data processing protocol was designing new antenna configurations to overcome circular microstrip patch antenna shortcomings. This protocol of FEA can be used to further investigate on antenna sensitivity to strain and also for developing damage detection techniques in the future.

9.4 Experimental Validation

Final evaluation approach for all the proposed antenna sensors was the experimental tests. All three antennas, which already were studied using FEA, were tested under a 3-point bend test condition (Chapters 6 & 7). The experimental results proved the concept of strain measurement using circular microstrip patch antenna, and the improvement introduced by novel antenna sensor designs (Chapter 7).

9.5 Circular Microstrip Patch Antenna

The feasibility of measuring strain using a circular microstrip patch antenna has been shown using theoretical studies (Chapter 4, Section 2.1.1), experimental results (Chapters 6 & 7), and finite element analysis (Chapter 5, Section3 and Chapter 7, Section 2). The relationship between the shift of the resonant frequency of a circular microstrip patch antenna and the strain applied to the antenna is discussed for three different material types (carbon fibre composite, fibre glass composite and aluminium) (Chapter 6 & Chapter 7, Section 2). There is general agreement up to about 1500 μstrain between the analytical, computational and experimental results.

The results indicate that the resonant frequency of the antenna shifts by applying strain, if the antenna is attached to carbon fibre or aluminium plate. In addition, the effect of bending angle on the strain-frequency shift relationship was studied (Chapter 7, Section 2). The amount of shift in 0° and 90° load orientations is almost the same but it is in different directions for a circular microstrip patch antenna. There is virtually no shift if the plate is bent at 45° which is a shortcoming for this type of antenna.

9.6 Novel Antenna/Sensor Configurations

The new slotted circular microstrip patch antenna strain sensor proposed in this study is 3 times more sensitive than the circular microstrip patch antenna (Chapter 7, Section 3). The effect of the slot in the patch makes strain measurement easier while the working frequency of the slot is more than double the frequency of the simple patch. The sensitivity of the antenna sensor depends on the relative direction of strain and slot length (or width). This could be used for detecting strain in different directions by using a cross slotted circular microstrip patch antenna. Both finite element analysis and experimental results are in good agreement and show that the slotted patch is able to detect strain in aluminium and carbon fibre composites (Chapter 7, Section 3).

By applying a meandering technique and consequently developing a meandered circular microstrip patch sensor (Chapter 5, Section 4.2), a more definitive frequency shift is obtained (Chapter 7, Section 4). The resultant antenna sensor is threefold more sensitive than a simple circular patch, while its physical dimension is fivefold smaller (Chapter 7, Section 4). This antenna sensor is capable of detecting more localised strain with even greater accuracy. In addition, this new sensor has demonstrated its omni-directional strain sensing ability (Chapter 7, Section 4). This is a significant improvement to the circular patch antenna.

Both FEA and measured results showed reasonable agreement which confirm the feasibility of using a meandered circular patch antenna to detect strain. Experimental results show that the size of the hole in aluminium plate does not have any specific effect on overall performance of the antenna including the omni-directional feature (Chapter 7, Section 4).

9.7 Wireless Strain Measurement

In order to excite the CMPA wirelessly and measure its resonant frequency, two different techniques have been proposed in this study (Chapter 8). These techniques are based on using horn antennas to excite the CMPA and read its resonant frequency using back scattering techniques. Further studies regarding the effect of horn antennas' near-field and far-field regions (Chapter 8, Section 3) resulted in choosing one of the aforementioned techniques for wireless strain measurement.

Finite element studies using accurate modelling of horn antenna and considering the effect of horn antennas' near-field region demonstrates the feasibility of wireless strain measurement (Chapter 8, Section 4). This proposed technique was further evaluated by experimental tests (Chapter 8, Section 5) which demonstrated wireless strain measurement using CMPA sensors and horn antennas. This technique establishes the wireless strain measurement in any desired direction only by rotating the horn antenna toward that direction.

Further studies on the effect of different parameters show that CMPAs can be used for wireless strain measurement in different conductive and dielectric materials such as aluminium, carbon fibre reinforced polymers and glass fibre reinforced polymers (Chapter 8, Section 5). The most important factor in the reliability of wireless measurements is the interrogation distance between the sensor and the reader antenna which may be further improved by using high quality factor resonators (Chapter 8, Section 6).

This antenna sensor could be further developed for wireless SHM applications. A wireless sensor eliminates the use of wires in SHM applications and therefore decreases the complexity and weight of the sensory unit. This also increases the reliability of the SHM system because wires inherently increase the potential disconnection points in a wired sensory network. The antenna sensor also has an advantage over available wireless sensors by obviating the need for a battery.

A miniature microstrip patch antenna may be able to detect strain and possibly damage in the structure with more accuracy because a small strain may result in a larger shift in the resonant frequency of the antenna. From the results obtained in this research, it appears that an array of antennas or other resonator elements has the potential to detect damage wirelessly for in-situ health monitoring. As a result, the weight, cost, and overall complexity

of the SHM system could be decreased. This enables the deployment of more sensors on critical structures without the concomitant increase in complexity and unreliability of the system.

9.8 Future Work

The results from this study open new areas of research which require profound multidisciplinary inputs. Some of the ideas that could be developed further in the future include:

1. Optimisation techniques could be used to achieve more sensitive antenna sensors with physically smaller sizes to be able to detect localised strain and damage in the structure.

2. Several different electromagnetic resonators including the ones analytically studied in Chapter 4 of this thesis can be studied further using FEA techniques developed in this work as well as experimental tests to investigate their performance as strain sensors.

3. Multi-directional strain measurement using cross slotted circular microstrip patch antenna proposed in this research is another area of development which will have important advantages over current strain sensors.

4. The relationship between different types of damage and specific antenna types should be investigated in the future. The challenge in this field is the determination of the smallest damage zone (relative to the size of the structure) that is detectable using this technique.

5. Finally, the interrogation distance (which is the most important factor in wireless measurements) between the CMPA sensor and the reader (Horn Antenna) should be improved for future wireless strain measurements. This can be achieved by investigating the use of high quality factor resonators or by increasing the quality factor of current CMPA sensors (using substrate materials with high dielectric constant and low thickness). This may also increase the sensitivity of the antenna sensor.

Appendix A - MATLAB™ Codes

A.1 MATLAB™ Code to Compute Circular Microstrip Patch Antenna Strain-Frequency Shift Relationship

```
clear % Clear workspace
c = 3e8; % Speed of light in vacuum
per = input('Substrate Permitivity='); % Substrate dielectric constant
a = input('Patch radius(cm)=').*1e-2; % Patch radius befor strain
h = input('Substrate thickness(mm)=').*1e-3; % Substrate thickness
s = input('Strain(%)='); % Strain
pr = input('Substrate poisson ratio='); % Substrate poisson ratio
ae = a.*sqrt(1+((2.*h)./(pi.*a.*per)).*(log((pi.*a)./(2.*h))+1.7726)); % Effective radius
befor strain
fr = (1.8412.*c)./(2.*pi.*ae.*sqrt(per)); % Frequency before strain
% After strain
hs = h.*(1-pr.*s); % Substrate thickness after strain
as = a.*(1+s); % Patch radius after strain
aes = as.*sqrt(1+((2.*hs)./(pi.*as.*per)).*(log((pi.*as)./(2.*hs))+1.7726)); % Effective
radius after strain
frs = (1.8412.*c)./(2.*pi.*aes.*sqrt(per)); % Frequency after strain
dfr = frs-fr; % Frequency shift
frsh = dfr./frs; % Frequency shift percentage
plot(s,frsh); % Plot the results
```

A.2 MATLAB™ Code to Compute Rectangular Microstrip Patch Antenna Strain-Frequency Shift Relationship

```
clear % Clear workspace
c = 3e8; % Speed of light in vacuum
per = input('Substrate Permitivity='); % Substrate dielectric constant
l = input('Patch length(cm)=').*1e-2; % Patch length befor strain
w = input('Patch width(cm)=').*1e-2; % Patch width befor strain
```

```
h = input('Substrate thickness(mm)=').*1e-3; % Substrate thickness
s = input('Strain(%)='); % Strain
pr = input('Substrate poisson ratio='); % Substrate poisson ratio
eper = ((per+1)./2)+(((per-1)./2).*((1+12.*(h./w)).^-0.5)); % Effective permittivity befor strain
dl = (0.412.*h).*(((eper+0.3).*((w/h)+0.264))./((eper-0.258).*((w./h)+0.8))); % To calculate effective length befor strain
le = l+(2.*dl); % Effective length befor strain
fr = c./(2.*le.*sqrt(eper)); % Frequency before strain
 % After strain in the direction of antenna length
hs = h.*(1-pr.*s); % Substrate thickness after strain
ls = l.*(1+s); % Patch length after strain
ws = w.*(1-pr.*s); % Patch width after strain
epers = ((per+1)./2)+(((per-1)./2).*((1+12.*(hs./ws)).^-0.5)); % Effective permittivity after strain
dls = (0.412.*hs).*(((epers+0.3).*((ws/hs)+0.264))./((epers-0.258).*((ws./hs)+0.8))); % To calculate effective length after strain
les = ls+(2.*dls); % Effective length after strain
frsl = c./(2.*les.*sqrt(epers)); % Frequency after strain
dfrl = frsl-fr; % Frequency shift
frshl = dfrl./frsl; % Frequency shift percentage
 % After strain in the direction of antenna width
hs = h.*(1-pr.*s); % Substrate thickness after strain
ls = l.*(1-pr.*s); % Patch length after strain
ws = w.*(1+s); % Patch width after strain
epers = ((per+1)./2)+(((per-1)./2).*((1+12.*(hs./ws)).^-0.5)); % Effective permittivity after strain
dls = (0.412.*hs).*(((epers+0.3).*((ws/hs)+0.264))./((epers-0.258).*((ws./hs)+0.8))); % To calculate effective length after strain
les = ls+(2.*dls); % Effective length after strain
frsw = c./(2.*les.*sqrt(epers)); % Frequency after strain
dfrw = frsw-fr; % Frequency shift
frshw = dfrw./frsw; % Frequency shift percentage
plot(s,frshl,s,frshw); % Plot the results
```

A.3 MATLAB™ Code to Compute Hemispherical Dielectric Resonator Antenna Strain-Frequency Shift Relationship

```
clear % Clear workspace
per = input('Permitivity='); % Dielectric constant
a = input('H-DRA radius(cm)='); % H-DRA radius befor strain
s = input('Strain(%)='); % Strain
pr = input('H-DRA poisson ratio='); % H-DRA poisson ratio
kaM1 = 2.8316.*(per.^-0.47829); % For TE111 mode
kaM2 = 4.47226.*(per.^-0.505); % For TM101 mode
frM1 = (4.7713.*kaM1)./a; % Frequency before strain for TE111 mode
frM2 = (4.7713.*kaM2)./a; % Frequency before strain for TM101 mode
 % After strain
as = a.*(1+s); % H-DRA radius after strain
frM1s = (4.7713.*kaM1)./as; % Frequency after strain for TE111 mode
frM2s = (4.7713.*kaM2)./as; % Frequency after strain for TM101 mode
dfrM1 = frM1s-frM1; % Frequency shift for TE111 mode
frshM1 = dfrM1./frM1s; % Frequency shift percentage for TE111 mode
dfrM2 = frM2s-frM2; % Frequency shift for TM101 mode
frshM2 = dfrM2./frM2s; % Frequency shift percentage for TM101 mode
plot(s,frshM1,s,frshM2); % Plot the results
```

A.4 MATLAB™ Code to Compute Cylindrical Dielectric Resonator Antenna Strain-Frequency Shift Relationship

```
clear % Clear workspace
per = input('Permitivity='); % Dielectric constant
a = input('C-DRA radius(cm)='); % C-DRA radius befor strain
h = input('C-DRA thickness(cm)='); % C-DRA thickness before strain
s = input('Strain(%)='); % Strain
pr = input('C-DRA poisson ratio='); % C-DRA poisson ratio
kaM1 = (2.327./sqrt(per+1)).*(1+0.2123.*(a./h)-0.00898.*((a./h).^2)); % For TE01 mode
kaM2 = (sqrt((3.83).^2+((pi.*a)./(2.*h)).^2))./(sqrt(per+2)); % For TM01 mode
kaM3 = (6.324./sqrt(per+2)).*(0.27+0.36.*(a./(2.*h))+0.02.*((a./(2.*h)).^2)); % For HE11
mode
```

```
frM1 = (4.7713.*kaM1)./a; % Frequency before strain for TE01 mode
frM2 = (4.7713.*kaM2)./a; % Frequency before strain for TM01 mode
frM3 = (4.7713.*kaM3)./a; % Frequency before strain for HE11 mode
 % After strain
as = a.*(1+s); % C-DRA radius after strain
hs = h.*(1-pr.*s); % C-DRA thickness after strain
kaM1s = (2.327./sqrt(per+1)).*(1+0.2123.*(as./hs)-0.00898.*((as./hs).^2)); % For TE01
mode
kaM2s = (sqrt((3.83).^2+((pi.*as)./(2.*hs)).^2))./(sqrt(per+2)); % For TM01 mode
kaM3s = (6.324./sqrt(per+2)).*(0.27+0.36.*(as./(2.*hs))+0.02.*((as./(2.*hs)).^2)); % For
HE11 mode
frM1s = (4.7713.*kaM1s)./as; % Frequency after strain for TE01 mode
frM2s = (4.7713.*kaM2s)./as; % Frequency after strain for TM01 mode
frM3s = (4.7713.*kaM3s)./as; % Frequency before strain for HE11 mode
dfrM1 = frM1s-frM1; % Frequency shift for TE01 mode
frshM1 = dfrM1./frM1s; % Frequency shift percentage for TE01 mode
dfrM2 = frM2s-frM2; % Frequency shift for TM01 mode
frshM2 = dfrM2./frM2s; % Frequency shift percentage for TM01 mode
dfrM3 = frM3s-frM3; % Frequency shift for HE11 mode
frshM3 = dfrM3./frM3s; % Frequency shift percentage for HE11 mode
plot(s,frshM1,s,frshM2,s,frshM3); % Plot the results
```

A.5 MATLAB™ Code to Compute Rectangular Dielectric Resonator Antenna Strain-Frequency Shift Relationship

```
clear % Clear workspace
per = input('Permitivity='); % Dielectric constant
w = input('R-DRA width(cm)='); % R-DRA width befor strain
h = input('R-DRA thickness(cm)='); % R-DRA thickness before strain
d = input('R-DRA depth(cm)='); % R-DRA depth befor strain
s = input('Strain(%)='); % Strain
pr = input('R-DRA poisson ratio='); % R-DRA poisson ratio
a0 = 2.57-0.8.*(d./(2.*h))+0.42.*((d./(2.*h)).^2)-0.05.*((d./(2.*h)).^3); % To calculate
normalised frequency
```

```
a1 = 2.71.*((d./(2.*h)).^-0.282); % To calculate normalised frequency
a2 = 0.16; % To calculate normalised frequency
F = a0+a1.*(w./(2.*h))+a2.*((w./(2.*h)).^2); % Normalised frequency
fr = (15.*F)./(w.*pi.*sqrt(per)); % Frequency before strain
% After strain in the direction of antenna width
ws = w.*(1+s); % R-DRA width after strain
hs = h.*(1-pr.*s); % R-DRA thickness after strain
ds = d.*(1-pr.*s); % R-DRA depth after strain
a0s = 2.57-0.8.*(ds./(2.*hs))+0.42.*((ds./(2.*hs)).^2)-0.05.*((ds./(2.*hs)).^3); % To
calculate normalised frequency after strain
a1s = 2.71.*((ds./(2.*hs)).^-0.282); % To calculate normalised frequency after strain
a2s = 0.16; % To calculate normalised frequency after strain
Fs = a0s+a1s.*(ws./(2.*hs))+a2s.*((ws./(2.*hs)).^2); % Normalised frequency after strain
frsw = (15.*Fs)./(ws.*pi.*sqrt(per)); % Frequency after strain
dfrw = frsw-fr; % Frequency shift
frshw = dfrw./frsw; % Frequency shift
 % After strain in the direction of antenna depth
ws = w.*(1-pr.*s); % R-DRA width after strain
hs = h.*(1-pr.*s); % R-DRA thickness after strain
ds = d.*(1+s); % R-DRA depth after strain
a0s = 2.57-0.8.*(ds./(2.*hs))+0.42.*((ds./(2.*hs)).^2)-0.05.*((ds./(2.*hs)).^3); % To
calculate normalised frequency after strain
a1s = 2.71.*((ds./(2.*hs)).^-0.282); % To calculate normalised frequency after strain
a2s = 0.16; % To calculate normalised frequency after strain
Fs = a0s+a1s.*(ws./(2.*hs))+a2s.*((ws./(2.*hs)).^2); % Normalised frequency after strain
frsd = (15.*Fs)./(ws.*pi.*sqrt(per)); % Frequency after strain
dfrd = frsd-fr; % Frequency shift
frshd = dfrd./frsd; % Frequency shift percentage
plot(s,frshw,s,frshd); % Plot the results
```

A.6 MATLAB™ Code to Compute EC-SRR Strain-Frequency Shift Relationship

```
clear % Clear workspace
s = [0 .0005 .001 .0015 .002 .0025 .003]; % Strain
```

```
pr = 1.2e-1; % Substrate poisson ratio
t = 4.9e-4; % Substrate thickness
d = 1.7e-4; % Separation
r = 2.54e-3; % EC-SRR Radius
c = 1.9e-4; % Width of the strips
mu0 = 4.*pi.*1e-7; % Permeability of free space
ep0 = 8.85419.*1e-12; % Permittivity of free space
ep = 2.43.*ep0; % Substrate permittivity
a = r-(c./2);
b = r+(c./2);
LF = @(k) ((1./k.^2).*(b.*(stvh0(k.*b).*besselj(1,(k.*b))-stvh1(k.*b).*besselj(0,(k.*b)))-
a.*(stvh0(k.*a).*besselj(1,(k.*a))-stvh1(k.*a).*besselj(0,(k.*a)))).^2); % To calculate
Inductance
L = [(mu0.*pi.^3)./(4.*c.^2)].*quadl(LF,1e-6,4500); % Inductance
aa = d./2;
bb = (d./2)+c;
kk = aa./bb;
kk1 = sinh((pi.*aa)./(2.*t))./sinh((pi.*bb)./(2.*t));
kp = sqrt(1-kk.^2);
kp1 = sqrt(1-kk1.^2);
if (kk>=0 & kk<=0.7)
   Fkk = (1./pi).*[log(2.*((1+sqrt(kp))./(1-sqrt(kp))))];
   Fkk1 = (1./pi).*[log(2.*((1+sqrt(kp1))./(1-sqrt(kp1))))];
elseif (kk>=0.7 & kk<=1)
   Fkk = pi.*[log(2.*((1+sqrt(kk))./(1-sqrt(kk))))].^-1;
   Fkk1 = pi.*[log(2.*((1+sqrt(kk1))./(1-sqrt(kk1))))].^-1;
end
epe = 1+(((ep-ep0)./(2.*ep0)).*(Fkk./Fkk1));
Cpul = ep0.*epe.*Fkk; % To calculate capacitance
C = pi.*r.*Cpul; % Capacitance
fr = (1./(2.*pi)).*sqrt(2./(L.*C)); % Resonant frequency
 % After Strain
 ts = t.*(1-pr.*s); % Substrate thickness after strain
ds = d.*(1+s); % Separation after strain
```

```
rs = r.*(1+s); % EC-SRR radius after strain
cs = c.*(1+s); % Width of the strips after strain
as = rs-(cs./2);
bs = rs+(cs./2);
for m = 1:length(s)
   LFs = @(k) ((1./k.^2).*(bs(1,m).*(stvh0(k.*bs(1,m)).*besselj(1,(k.*bs(1,m)))-
stvh1(k.*bs(1,m)).*besselj(0,(k.*bs(1,m))))-
as(1,m).*(stvh0(k.*as(1,m)).*besselj(1,(k.*as(1,m)))-
stvh1(k.*as(1,m)).*besselj(0,(k.*as(1,m))))).^2); % To calculate Inductance after strain
   Ls(1,m) = [(mu0.*pi.^3)./(4.*cs(1,m).^2)].*quadl(LFs,1e-6,4500); % Inductance after
strain
end
aas = ds./2;
bbs = (ds./2)+cs;
kks = aas./bbs;
kk1s = sinh((pi.*aas)./(2.*ts))./sinh((pi.*bbs)./(2.*ts));
kps = sqrt(1-kks.^2);
kp1s = sqrt(1-kk1s.^2);
if (kks>=0 & kks<=0.7)
  Fkks = (1./pi).*[log(2.*((1+sqrt(kps))./(1-sqrt(kps))))];
  Fkk1s = (1./pi).*[log(2.*((1+sqrt(kp1s))./(1-sqrt(kp1s))))];
elseif (kks>=0.7 & kks<=1)
  Fkks = pi.*[log(2.*((1+sqrt(kks))./(1-sqrt(kks))))].^-1;
  Fkk1s = pi.*[log(2.*((1+sqrt(kk1s))./(1-sqrt(kk1s))))].^-1;
end
epes = 1+(((ep-ep0)./(2.*ep0)).*(Fkks./Fkk1s));
Cpuls = ep0.*epe.*Fkks; % To calculate capacitance
Cs = pi.*rs.*Cpuls; % Capacitance after strain
frs = (1./(2.*pi)).*sqrt(2./(Ls.*Cs)); % Resonant frequency after strain
dfr = frs-fr; % Frequency shift
frsh = dfr./frs; % Frequency shift percentage
plot(s,frsh); % Plot the results
```

A.7 MATLAB™ Code to Design Rectangular Microstrip Patch Antenna According to Huang and Boyle (2008) and Balanis (2005)

```
clear % Clear workspace
c = 3e8; % Speed of light in vacuum
per = input('Substrate Permitivity='); % Substrate dielectric constant
fr = input('Resonant Frequency(GHz)=').*1e9; % Resonant frequency
h = input('Substrate thickness(mm)=').*1e-3; % Substrate thickness
w = (c./(2.*fr)).*(2./(per+1)).^0.5; % Patch width for an efficient radiator
eper = ((per+1)./2)+(((per-1)./2).*((1+(12.*(h./w))).^-0.5)); % Effective permitivity
dl = 0.412.*h.*(((eper+0.3).*((w./h)+0.264))./((eper-0.258).*((w./h)+0.8))); % Difference of patch length and its effective length
l = (c./(2.*fr.*eper.^0.5))-(2.*dl); % Patch length
landa0 = c./fr; % Wave length in vacuum
k0 = 2.*pi./landa0; % Phase constant for free space
x = k0.*w; % To calculate G1
I1 = -2+cos(x)+(x.*sinint(x))+(sin(x)./x); % To calculate G1
G1 = I1./(120.*(pi.^2)); % The conductance
for m = 1:length(fr)
   G12F = @(y)
((sin((k0(1,m).*w(1,m)./2).*cos(y))./cos(y)).^2).*besselj(0,k0(1,m).*l(1,m).*sin(y)).*(sin(y)
.^3); % To calculate G12
   G12(1,m) = quadl(G12F,0,pi)./(120.*pi.^2); % The mutual conductance
end
Rin = 1./(2.*(G1+G12)); % Input impedance at the leading radiating edge of the patch
y0 = (l./pi).*acos(sqrt(50./Rin)); % Inset feed point distance
dlmwrite('Results12.txt',[fr./1e9;w.*1e3;l.*1e3;y0.*1e3],'\t'); % Print the results in a file
```

A.8 MATLAB™ Code to Design Rectangular Microstrip Patch Antenna According to Volakis (2007)

```
clear %Clear workspace
c = 3e8; %Speed of light in vacuum
per = input('Substrate Permitivity='); %Substrate dielectric constant
fr = input('Resonant Frequency(GHz)=').*1e9; %Resonant frequency
```

```
h = input('Substrate thickness(mm)=').*1e-3; %Substrate thickness
w = (c./(2.*fr)).*(2./(per+1)).^0.5; % Patch width for an efficient radiator
eper = ((per+1)./2)+(((per-1)./2).*((1+(10.*(h./w))).^-0.5)); %Effective permitivity
dl = 0.412.*h.*(((eper+0.3).*((w./h)+0.264))./((eper-0.258).*((w./h)+0.8))); % Difference of patch length and its effective length
l = (c./(2.*fr.*per.^0.5))-(2.*dl); %Patch length
landa0 = c./fr; % Wave length in vacuum
k0 = 2.*pi./landa0; % Phase constant for free space
x = k0.*w; % To calculate G1
I1 = -2+cos(x)+(x.*sinint(x))+(sin(x)./x); % To calculate G1
G1 = I1./(120.*(pi.^2)); % The conductance
for m = 1:length(fr)
   G12F = @(y)
((sin((k0(1,m).*w(1,m)./2).*cos(y))./cos(y)).^2).*besselj(0,k0(1,m).*l(1,m).*sin(y)).*(sin(y)
.^3); % To calculate G12
   G12(1,m) = quadl(G12F,0,pi)./(120.*pi.^2); % The mutual conductance
end
Rin = 1./(2.*(G1+G12)); % Input impedance at the leading radiating edge of the patch
y0 = (l./pi).*acos(sqrt(50./Rin)); % Inset feed point distance
dlmwrite('Results3.txt',[fr./1e9;w.*1e3;l.*1e3;y0.*1e3],'\t'); % Print the results in a file
```

A.9 MATLAB™ Code to Design Rectangular Microstrip Patch Antenna According to Garg et al. (2000)

```
clear %Clear workspace
c = 3e8; %Speed of light in vacuum
per = input('Substrate Permitivity='); %Substrate dielectric constant
fr = input('Resonant Frequency(GHz)=').*1e9; %Resonant frequency
h = input('Substrate thickness(mm)=').*1e-3; %Substrate thickness
w = (c./(2.*fr)).*(2./(per+1)).^0.5; % Patch width for an efficient radiator
eper = ((per+1)./2)+(((per-1)./2).*((1+(12.*(h./w))).^-0.5)); %Effective permitivity
dl = 0.412.*h.*(((eper+0.3).*((w./h)+0.264))./((eper-0.258).*((w./h)+0.813))); % Difference of patch length and its effective length
l = (c./(2.*fr.*eper.^0.5))-(2.*dl); %Patch length
```

```
landa0 = c./fr; % Wave length in vacuum
k0 = 2.*pi./landa0; % Phase constant for free space
x = k0.*w; % To calculate G1
I1 = -2+cos(x)+(x.*sinint(x))+(sin(x)./x); % To calculate G1
G1 = I1./(120.*(pi.^2)); % The conductance
for m = 1:length(fr)
   G12F = @(y)
((sin((k0(1,m).*w(1,m)./2).*cos(y))./cos(y)).^2).*besselj(0,k0(1,m).*l(1,m).*sin(y)).*(sin(y)
.^3); % To calculate G12
   G12(1,m) = quadl(G12F,0,pi)./(120.*pi.^2); % The mutual conductance
end
Rin = 1./(2.*(G1+G12)); % Input impedance at the leading radiating edge of the patch
y0 = (l./pi).*acos(sqrt(50./Rin)); % Inset feed point distance
dlmwrite('Results4.txt',[fr./1e9;w.*1e3;l.*1e3;y0.*1e3],'\t'); % Print the results in a file
```

A.10 MATLAB™ Code to Design Circular Microstrip Patch Antenna According to Balanis (2005) and Volakis (2007)

```
% Antenna Dimensions
clear % Clear workspace
c = 3e8; % Speed of light in vacuum
per = input('Substrate Permitivity='); % Substrate dielectric constant
fr = input('Resonant Frequency(GHz)=').*1e9; % Resonant frequency
h = input('Substrate thickness(mm)=').*1e-3; % Substrate thickness
con = input('Conductivity(S/m)='); % Conductivity of the patch and ground plane
lt = input('Loss tangent of substrate='); % Loss tangent of substrate
ae = (1.8412.*c)./(2.*pi.*fr.*sqrt(per)); % Effective radius
a = ae./sqrt(1+((2.*h)./(pi.*ae.*per)).*(log((pi.*ae)./(2.*h))+1.7726)); % Actual radius
aa = ae;
n = ones(1,length(fr)); % Number of iterations
for i = 1:length(fr)
  while abs(aa(1,i)-a(1,i)) > 1e-6
     aa(1,i) = a(1,i);
```

```
    a(1,i) = ae(1,i)./sqrt(1+((2.*h)./(pi.*aa(1,i).*per)).*(log((pi.*aa(1,i))./(2.*h))+1.7726));
% Actual radius
    n(1,i)=n(1,i)+1; % Number of iterations
  end
end
% Probe Feed Location
 mu0 = 4.*pi.*1e-7; % Permeability of free space
landa0 = c./fr; % Wave length in vacuum
k0 = 2.*pi./landa0; % Phase constant for free space
k = k0.*sqrt(per); % Wave phase constant
m = 1; % Tmnp (T110) mode
Em0 = 1;
Gc = ((Em0.*pi.*(pi.*mu0.*fr).^(-3./2))./(4.*h.^2.*sqrt(con))).*(((k.*ae).^2)-m.^2); %
Ohmic conduction loss conductance
Gd = ((Em0.*lt)./(4.*mu0.*h.*fr)).*(((k.*ae).^2)-m.^2); % Dielectric loss conductance
for p = 1:length(fr)
   GradF = @(y) ((besselj(0,k0(1,p).*ae(1,p).*sin(y))-
besselj(2,k0(1,p).*ae(1,p).*sin(y))).^2+((cos(y)).^2).*(besselj(0,k0(1,p).*ae(1,p).*sin(y))+b
esselj(2,k0(1,p).*ae(1,p).*sin(y))).^2).*sin(y); % To calculate Grad
   Grad(1,p) = (((k0(1,p).*ae(1,p)).^2)./480).*quadl(GradF,0,pi./2); % Radiation loss
conductance
end
Gt = Grad+Gc+Gd; % Total conductance
Rin = 1./Gt; % Input impedance at the leading radiating edge of the patch
for t = 1:length(fr)
   k11RfF = @(x) besselj(1,x)-sqrt(50./Rin(1,t)).*besselj(1,1.8412); % To calculate k11Rf
   k11Rf(1,t) = fzero(k11RfF,[0 1.8412]); % Feed point distance from centre of the patch
multiply k11
end
k11 = 1.8412./a; % k11
Rf = k11Rf./k11; % Feed point distance from centre of the patch
dlmwrite('CResults1.txt',[fr./1e9;a.*1e3;Rf.*1e3],'\t'); % Print the results in a file
```

A.11 MATLAB™ Code to Design Circular Microstrip Patch Antenna According to Garg et al. (2000)

```
% Antenna Dimensions
clear % Clear workspace
c = 3e8; % Speed of light in vacuum
per = input('Substrate Permitivity='); % Substrate dielectric constant
fr = input('Resonant Frequency(GHz)=').*1e9; % Resonant frequency
h = input('Substrate thickness(mm)=').*1e-3; % Substrate thickness
con = input('Conductivity(S/m)='); % Conductivity of the patch and ground plane
lt = input('Loss tangent of substrate='); % Loss tangent of substrate
ae = (1.84118.*c)./(2.*pi.*fr.*sqrt(per)); % Effective radius
a =
ae./sqrt(1+((2.*h)./(pi.*ae.*per)).*(log(ae./(2.*h))+(1.41.*per+1.77)+(h./ae).*(0.268.*per+1.
65))); % Actual radius
aa = ae;
n = ones(1,length(fr)); % Number of iterations
for i = 1:length(fr)
   while abs(aa(1,i)-a(1,i)) > 1e-6
      aa(1,i) = a(1,i);
      a(1,i) =
ae(1,i)./sqrt(1+((2.*h)./(pi.*aa(1,i).*per)).*(log(aa(1,i)./(2.*h))+(1.41.*per+1.77)+(h./aa(1,i))
.*(0.268.*per+1.65))); % Actual radius
      n(1,i)=n(1,i)+1; % Number of iterations
   end
end
% Probe Feed Location
 mu0 = 4.*pi.*1e-7; % Permeability of free space
landa0 = c./fr; % Wave length in vacuum
k0 = 2.*pi./landa0; % Phase constant for free space
k = k0.*sqrt(per); % Wave phase constant
m = 1; % Tmnp (T110) mode
Em0 = 1;
```

```
Gc = ((Em0.*pi.*(pi.*mu0.*fr).^(-3./2))./(4.*h.^2.*sqrt(con))).*(((k.*ae).^2)-m.^2); % Ohmic conduction loss conductance
Gd = ((Em0.*lt)./(4.*mu0.*h.*fr)).*(((k.*ae).^2)-m.^2); % Dielectric loss conductance
for p = 1:length(fr)
   GradF = @(y) ((besselj(0,k0(1,p).*ae(1,p).*sin(y))-besselj(2,k0(1,p).*ae(1,p).*sin(y))).^2+((cos(y)).^2).*(besselj(0,k0(1,p).*ae(1,p).*sin(y))+besselj(2,k0(1,p).*ae(1,p).*sin(y))).^2).*sin(y); % To calculate Grad
   Grad(1,p) = (((k0(1,p).*ae(1,p)).^2)./480).*quadl(GradF,0,pi./2); % Radiation loss conductance
end
Gt = Grad+Gc+Gd; % Total conductance
Rin = 1./Gt; % Input impedance at the leading radiating edge of the patch
for t = 1:length(fr)
   k11RfF = @(x) besselj(1,x)-sqrt(50./Rin(1,t)).*besselj(1,1.84118); % To calculate k11Rf
   k11Rf(1,t) = fzero(k11RfF,[0 1.84118]); % Feed point distance from centre of the patch multiply k11
end
k11 = 1.84118./a; % k11
Rf = k11Rf./k11; % Feed point distance from centre of the patch
dlmwrite('CResults2.txt',[fr./1e9;a.*1e3;Rf.*1e3],'\t'); % Print the results in a file
```

A.12 MATLAB™ Code to Design EC-SRR

```
clear % Clear workspace
t = 4.9e-4; % Substrate thickness
d = 1.7e-4; % Separation
r = 2.54e-3; % EC-SRR Radius
c = 1.9e-4; % Width of the strips
mu0 = 4.*pi.*1e-7; % Permeability of free space
ep0 = 8.85419.*1e-12; % Permittivity of free space
ep = 2.43.*ep0; % Substrate permittivity
a = r-(c./2);
b = r+(c./2);
```

```
LF = @(k) ((1./k.^2).*(b.*(stvh0(k.*b).*besselj(1,(k.*b))-stvh1(k.*b).*besselj(0,(k.*b)))-
a.*(stvh0(k.*a).*besselj(1,(k.*a))-stvh1(k.*a).*besselj(0,(k.*a))))).^2); % To calculate
Inductance
L = [(mu0.*pi.^3)./(4.*c.^2)].*quadl(LF,1e-6,4500); % Inductance
aa = d./2;
bb = (d./2)+c;
kk = aa./bb;
kk1 = sinh((pi.*aa)./(2.*t))./sinh((pi.*bb)./(2.*t));
kp = sqrt(1-kk.^2);
kp1 = sqrt(1-kk1.^2);
if (kk>=0 & kk<=0.7)
   Fkk = (1./pi).*[log(2.*((1+sqrt(kp))./(1-sqrt(kp))))];
   Fkk1 = (1./pi).*[log(2.*((1+sqrt(kp1))./(1-sqrt(kp1))))];
elseif (kk>=0.7 & kk<=1)
   Fkk = pi.*[log(2.*((1+sqrt(kk))./(1-sqrt(kk))))].^-1;
   Fkk1 = pi.*[log(2.*((1+sqrt(kk1))./(1-sqrt(kk1))))].^-1;
end
epe = 1+(((ep-ep0)./(2.*ep0)).*(Fkk./Fkk1));
Cpul = ep0.*epe.*Fkk; % To calculate capacitance
C = pi.*r.*Cpul; % Capacitance
fr = (1./(2.*pi)).*sqrt(2./(L.*C)); % Resonant frequency
```

A.13 MATLAB™ Code to Design 50ohms Microstrip Line & Quarter-wavelength Transformer

```
clear % Clear workspace
c = 3e8; % Speed of light in vacuum
per = input('Substrate Permittivity='); % Substrate dielectric constant
fr = input('Resonant Frequency(GHz)=').*1e9; % Resonant frequency
h = input('Substrate thickness(mm)=').*1e-3; % Substrate thickness
ZL = input('Patch Edge Impedance(ohms)='); % Characteristic impedance of the microstrip
patch antenna at the edge
landa0 = c./fr; % Wave length in free space
eper = (per+1)./2; % First order approximation of effective permittivity
```

```
w = h; % First order approximation of 50ohms microstrip line width
w0 = 0;
n = 0; % Number of iterations
while abs(w-w0) > 1e-6
   w0 = w;
   if (w./h) > 1
      w = h.*([(120.*pi)./(50.*(eper.^0.5))]-1.393-0.667.*log((w./h)+1.444)); % Width of
50ohms microstrip line
   else
      d = 4.*h.*exp((50.*(eper.^0.5))./60);
      f = @(x) x.^2-d.*x+(32.*h.^2);
      w = fzero(f,h); % Width of 50ohms microstrip line
   end
   eper = [(per+1)./2]+[((per-1)./2).*(1+12.*h./w).^-0.5]; %effective permittivity
   n = n+1; % Number of iterations
end
landa = landa0./(eper.^0.5); % Wave length in substrate
l = landa./4; % Length of a quarter-wavelength transformer
ZT = (50.*ZL).^0.5; % Characteristic impedance of the quarter-wavelength transformer
eper = (per+1)./2; % First order approximation of effective permittivity
wT = w; % First order approximation of the quarter-wavelength transformer width
w0 = 0;
m = 0; % Number of iterations
while abs(wT-w0) > 1e-6
   w0 = wT;
   if (wT./h) > 1
      wT = h.*([(120.*pi)./(ZT.*(eper.^0.5))]-1.393-0.667.*log((wT./h)+1.444)); % Width of
the quarter-wavelength transformer
   else
      d = 4.*h.*exp((ZT.*(eper.^0.5))./60);
      f = @(x) x.^2-d.*x+(32.*h.^2);
      wT = fzero(f,w); % Width of the quarter-wavelength transformer
   end
   eper = [(per+1)./2]+[((per-1)./2).*(1+12.*h./wT).^-0.5]; %effective permittivity
```

```
    m = m+1; % Number of iterations
end
dlmwrite('Wm_Lt.txt',[fr./1e9;w.*1e3;l.*1e3;wT.*1e3],'\t'); % Print the results in a file
```

A.14 MATLAB™ Function to Compute Struve function H0(x) for use in A.6 and A.12 (Barrowes, 2004)


```
function [sh0]=stvh0(x);
pi=3.141592653589793d0;
s=1.0d0;
r=1.0d0;
if(x <= 20.0d0);
a0=2.0.*x./pi;
for  k=1:60;
r=-r.*x./(2.0d0.*k+1.0d0).*x./(2.0d0.*k+1.0d0);
s=s+r;
if(abs(r)< abs(s).*1.0d-12)break; end;
end;
sh0=a0.*s;
else;
km=fix(.5.*(x+1.0));
if(x >= 50.0)km=25; end;
for  k=1:km;
```

```
r=-r.*((2.0d0.*k-1.0d0)./x).^2;
s=s+r;
if(abs(r)< abs(s).*1.0d-12)break; end;
end;
t=4.0d0./x;
t2=t.*t;
p0=((((-.37043d-5.*t2+.173565d-4).*t2-.487613d-4).*t2+.17343d-3).*t2-.1753062d-
2).*t2+.3989422793d0;
q0=t.*(((((.32312d-5.*t2-.142078d-4).*t2+.342468d-4).*t2-.869791d-4).*t2+.4564324d-
3).*t2-.0124669441d0);
ta0=x-.25d0.*pi;
by0=2.0d0./sqrt(x).*(p0.*sin(ta0)+q0.*cos(ta0));
sh0=2.0d0./(pi.*x).*s+by0;
end;
return;
end
```

A.15 MATLAB™ Function to Compute Struve function H1(x) for use in A.6 and A.12 (Barrowes, 2004)


```
function [sh1]=stvh1(x);
pi=3.141592653589793d0;
r=1.0d0;
```

```
if(x <= 20.0d0);
s=0.0d0;
a0=-2.0d0./pi;
for  k=1:60;
r=-r.*x.*x./(4.0d0.*k.*k-1.0d0);
s=s+r;
if(abs(r)< abs(s).*1.0d-12)break; end;
end;
sh1=a0.*s;
else;
s=1.0d0;
km=fix(.5.*x);
if(x > 50.d0)km=25; end;
for  k=1:km;
r=-r.*(4.0d0.*k.*k-1.0d0)./(x.*x);
s=s+r;
if(abs(r)< abs(s).*1.0d-12)break; end;
end;
t=4.0d0./x;
t2=t.*t;
p1=((((.42414d-5.*t2-.20092d-4).*t2+.580759d-4).*t2-.223203d-3).*t2+.29218256d-
2).*t2+.3989422819d0;
q1=t.*(((((-.36594d-5.*t2+.1622d-4).*t2-.398708d-4).*t2+.1064741d-3).*t2-.63904d-
3).*t2+.0374008364d0);
ta1=x-.75d0.*pi;
by1=2.0d0./sqrt(x).*(p1.*sin(ta1)+q1.*cos(ta1));
sh1=2.0./pi.*(1.0d0+s./(x.*x))+by1;
end;
return;
end
```

A.16 MATLAB™ Code to Combine VNA *.CSV Files

```
% All the data files must be placed in a directory named 'rawdata' in the work directory of MATLAB™
% *.CSV files must be named with the format 'aa bb cc d'; where, aa is the number of sample, bb is the number of load orientation, cc is the number of load step and d is the number of trace
clear all % Clear workspace
maxnumberofsamples=input('maximum number of samples:'); % Maximum number of samples (*.CSV files)
numberofangles=input('number of angles:'); % Number of load orientations
numberofsteps=input('number of steps(excluding zero):'); % Number of load steps
numberoftraces=input('number of traces:'); % Number of traces (files) saved by VNA for each step of load
numberofpoints=input('number of points:'); % Number of VNA data points for frequency sweep
data=[];
data0=[];
data1=[];
for i=1:numberoftraces
   for j=1:maxnumberofsamples
      for k=1:numberofangles
         filename=['rawdata\' '0' int2str(j) ' 0' int2str(k) ' 00' ' ' int2str(i) '.csv'];
         fid=fopen(filename,'r');
         if fid>=3
            data0=textscan(fid,'%f%*f%*f',numberofpoints,'delimiter',',','headerlines',3);
            fclose(fid);
         end
         data=[data data0];
         data0=[];
         for l=0:numberofsteps
            if l<=9
               filename=['rawdata\' '0' int2str(j) ' 0' int2str(k) ' 0' int2str(l) ' ' int2str(i) '.csv'];
            else
```

```
            filename=['rawdata\' '0' int2str(j) ' 0' int2str(k) ' ' int2str(l) ' ' int2str(i) '.csv'];
        end
        fid=fopen(filename,'r');
        if fid>=3
            data1=textscan(fid,'%*f%f%f',numberofpoints,'delimiter',',','headerlines',3);
            fclose(fid);
        end
        data=[data data1];
        data1=[];
      end
    end
  end
end
data=cell2mat(data);
dlmwrite('Results.csv',data,'precision','%+12.11E','newline','pc'); % Save the combined
results in a file
```

Appendix B - ANSYS™ Codes

B.1 ANSYS APDL™ Code for Coupled-Field Structural/High Frequency Electromagnetic Analysis of Circular Microstrip Patch Antenna

```
! Set preferences for structural analysis
/NOPR
/PMETH,OFF,0
KEYW,PR_SET,1
KEYW,PR_STRUC,1
KEYW,PR_THERM,0
KEYW,PR_FLUID,0
KEYW,PR_ELMAG,0
KEYW,MAGNOD,0
KEYW,MAGEDG,0
KEYW,MAGHFE,0
KEYW,MAGELC,0
KEYW,PR_MULTI,0
KEYW,PR_CFD,0
/GO

! Enter Pre-Processor and define parameters
/PREP7                          ! Enter Pre-Processor
IMMED,0                         ! Not to show changes immediately in GUI
Lenght=0.2                      ! Length of Substrate plus PML (m)
Width=0.2                       ! Width of substrate plus PML (m)
Lenght_Al=0.351                 ! Length of aluminium plate (m)
Width_Al=0.351                  ! Width of aluminium plate (m)
Pml=0.0251                      ! PML thickness from edge of substrate (m)
Thick=0.0015                    ! Thickness of substrate (m)
Thick_Al=0.003                  ! Thickness of aluminium plate (m)
PRadius=0.0271                  ! Radius of patch (m)
```

```
HRadius=0.01                ! Radius of hole (m)
FeedL=0.0078                ! Distance from centre of patch to feed location (m)
CRadius_In=0.00046          ! Coaxial probe inner radius (m)
CRadius_Out=0.00205         ! Coaxial probe outer radius (m)
Force=0                     ! Applied load (N)
Displacement=0.015          ! Applied Displacement (m)
FLenght=0.25                ! Length of area under applied load (m)
Fwidth=0.005                ! Width of area under applied load (m)
LDiv_2D1=20                 ! Number of line divisions for substrate plus PML
LDiv_2D2=30                 ! Number of line divisions for substrate only
LDiv_2D3=60                 ! Number of line divisions for patch
LDiv_2D4=15                 ! Number of line divisions for coax outer radius
LDiv_2D5=15                 ! Number of line divisions for coax inner radius
LDiv_2D6=4                  ! Number of line divisions for PML only
LDiv_2D7=10                 ! Number of line divisions for L/2-Pml-PR
LDiv_2D8=30                 ! Number of line divisions for PR-(HR-FL)
LDiv_2D9=10                 ! Number of line divisions for HR-CR_Out
LDiv_2D10=10                ! Number of line divisions for PR-FL-HR
LDiv_2D11=15                ! Number of line divisions for CR_Out-CR_In
LDiv_2D12=15                ! Number of line divisions for CR_In
LDiv_2D13=18                ! Number of line divisions for aluminium plate
LDiv_2D14=60                ! Number of line divisions for hole
LDiv_2D15=4                 ! Number of line divisions for alu-sub
LDiv_3D_1=1                 ! Number of line divisions for substrate thickness
LDiv_3D_2=1                 ! Number of line divisions for aluminium thickness
PRatio=0.12                 ! Poisson ratio of substrate
EModule=1.7e10              ! Elastic modulus of substrate (GPa)
PRatio_Al=0.35              ! Poisson ratio of aluminium plate
EModule_Al=7e10             ! Elastic modulus of aluminium plate (GPa)
LossT=0.01                  ! Loss tangent of the substrate
Epsr=4.5                    ! Relative permittivity of the substrate
Scale=1000                  ! Scale factor
Freq_B=1.4e9                ! Start frequency of sweep (GHz)
Freq_E=1.6e9                ! End frequency of sweep (GHz)
```

```
Freq_Inc=1e5                    ! Frequency sweep increment (GHz)

! Define elements and material properties
ET,1,SOLID186                   ! Element type 1 (Substrate and Aluminium Plate)
ET,2,SOLID186                   ! Element type 2 (Air)
ET,3,SOLID186                   ! Element type 3 (PML)
ET,4,MESH200,7                  ! Element type 4 (2D Mesh)
MP,EX,1,EModule                 ! Material 1 (Substrate) elastic modulus
MP,PRXY,1,PRatio                ! Material 1 (Substrate) Poisson ratio
MP,EX,2,EModule                 ! Material 2 (Air) elastic modulus
MP,PRXY,2,PRatio                ! Material 2 (Air) Poisson ratio
MP,EX,3,EModule                 ! Material 3 (PML) elastic modulus
MP,PRXY,3,PRatio                ! Material 3 (PML) Poisson ratio
MP,EX,4,EModule_Al              ! Material 4 (Aluminium) elastic modulus
MP,PRXY,4,PRatio_Al             ! Material 4 (Aluminium) Poisson ratio

! Build 2D model
RECTNG,0,Width_Al/2,-Lenght_Al/2,Lenght_Al/2
RECTNG,0,Width/2,-Lenght/2,Lenght/2
ASBA,1,2,,DELETE,KEEP
RECTNG,0,-Pml+Width/2,Pml-Lenght/2,-Pml+Lenght/2
ASBA,2,1,,DELETE,KEEP
CYL4,0,0,PRadius,-90,,90
ASBA,1,2,,DELETE,KEEP
CYL4,0,-FeedL,HRadius,-90,,90
ASBA,2,1,,DELETE,KEEP
CYL4,0,-FeedL,CRadius_Out,-90,,90
ASBA,1,2,,DELETE,KEEP
CYL4,0,-FeedL,CRadius_In,-90,,90
ASBA,2,1,,DELETE,KEEP
ALLSEL,ALL
AGLUE,ALL

! Define number of divisions for each line in 2D mesh
```

```
LSEL,S,LENGHT,,Width/2
LESIZE,ALL,,,LDiv_2D1/2,,,,,0
LSEL,S,LENGHT,,Lenght
LESIZE,ALL,,,LDiv_2D1,,,,,0
LSEL,S,LENGHT,,(Width-2*Pml)/2
LESIZE,ALL,,,LDiv_2D2/2,,,,,0
LSEL,S,LENGHT,,Lenght-2*Pml
LESIZE,ALL,,,LDiv_2D2,,,,,0
LSEL,S,RADIUS,,PRadius
LESIZE,ALL,,,LDiv_2D3,,,,,0
LSEL,S,RADIUS,,CRadius_Out
LESIZE,ALL,,,LDiv_2D4,,,,,0
LSEL,S,RADIUS,,CRadius_In
LESIZE,ALL,,,LDiv_2D5,,,,,0
LSEL,S,LENGHT,,pml
LESIZE,ALL,,,LDiv_2D6,,,,,0
LSEL,S,LENGHT,,Lenght/2-Pml-PRadius
LESIZE,ALL,,,LDiv_2D7,,,,,0
LSEL,S,LENGHT,,PRadius-(HRadius-FeedL)
LESIZE,ALL,,,LDiv_2D8,,,,,0
LSEL,S,LENGHT,,HRadius-CRadius_Out
LESIZE,ALL,,,LDiv_2D9,,,,,0
LSEL,S,LENGHT,,PRadius-FeedL-HRadius
LESIZE,ALL,,,LDiv_2D10,,,,,0
LSEL,S,LENGHT,,CRadius_Out-CRadius_In
LESIZE,ALL,,,LDiv_2D11,,,,,0
LSEL,S,LENGHT,,CRadius_In
LESIZE,ALL,,,LDiv_2D12,,,,,0
LSEL,S,LENGHT,,Width_Al/2
LESIZE,ALL,,,LDiv_2D13/2,,,,,0
LSEL,S,LENGHT,,Lenght_Al
LESIZE,ALL,,,LDiv_2D13,,,,,0
LSEL,S,RADIUS,,HRadius
LESIZE,ALL,,,LDiv_2D14,,,,,0
```

```
LSEL,S,LENGHT,,(Lenght_Al-Lenght)/2
LESIZE,ALL,,,LDiv_2D15,,,,,0

! Mesh 2D model
ALLSEL,ALL
ASEL,U,AREA,,3
TYPE,4
MSHAPE,0,2D
MSHKEY,0
AMESH,ALL
NUMSTR,NODE,1.5e5
ASEL,S,AREA,,3
TYPE,4
MSHAPE,0,2D
MSHKEY,0
AMESH,ALL
ALLSEL,ALL

! Mesh 3D model for structural analysis
TYPE,1
MAT,1
EXTOPT,ACLEAR,1
EXTOPT,ESIZE,LDiv_3D_1
ASEL,S,LOC,Z,0
ASEL,U,,,3
VEXT,ALL,,,,,Thick
MAT,4
EXTOPT,ACLEAR,1
EXTOPT,ESIZE,LDiv_3D_2
ASEL,S,LOC,Z,0
ASEL,U,,,1
ASEL,U,,,7
ASEL,U,,,8
VEXT,ALL,,,,,-Thick_Al
```

ALLSEL,ALL

! Write substrate and aluminium plate elements and nodes, delete all, read only substrate nodes and elements

ESEL,S,MAT,,1

EWRITE,TELEMENTS1,ELEM

NSLE,S,ALL

NWRITE,TNODES1,NODE

ESEL,INVE

NSEL,INVE

EWRITE,TELEMENTS2,ELEM

NWRITE,TNODES2,NODE

ALLSEL,ALL

VCLEAR,ALL

VDELE,ALL

NREAD,TNODES1,NODE

EREAD,TELEMENTS1,ELEM

NUMCMP,ALL

CM,N_Antenna,NODE

CM,E_Antenna,ELEM

! Count substrate elements and nodes

*GET, NodeNum, NODE, 0, COUNT

*GET, ElemNum, ELEM, 0, COUNT

! Generate air and PML elements, write elements and delete their nodes and elements

EGEN,3,NodeNum,ALL,,,1,1,,,,,,Thick

*GET,NodeNum2,NODE,0,COUNT

ALLSEL,ALL

ESEL,S,MAT,,1

EGEN,2,NodeNum2,ALL,,,2,,,,,,,-Thick

NUMCMP,NODE

ESEL,R,MAT,,3

NSLE,S,ALL

```
NSEL,R,LOC,X,0,(Width/2-Pml)-1e-8
NSEL,R,LOC,Y,(-Lenght/2+Pml)+1e-8,(Lenght/2-Pml)-1e-8
ESLN,S,1
*GET,E_Del_1,ELEM,0,COUNT
*DIM,E_Del_2,ARRAY,E_Del_1,1,1
*GET,E_Del_2(1),ELEM,0,NUM,MIN
*DO,ll,2,E_Del_1
        *GET,E_Del_2(ll),ELEM,E_Del_2(ll-1),NXTH
*ENDDO
CM,E_Del,ELEM
ALLSEL,ALL
*GET,NodeNum3,NODE,0,COUNT
NodeNum4=NodeNum3-NodeNum2
ALLSEL,ALL
EWRITE, ELEMENTS, ELEM
ALLSEL,ALL
NSEL,S,LOC,X,Width/2-Pml,Width/2
NSEL,A,LOC,Y,Lenght/2-Pml,Lenght/2
NSEL,A,LOC,Y,-Lenght/2+Pml,-Lenght/2
ESLN,S,1
*GET,E_Pml_1,ELEM,0,COUNT
*DIM,E_Pml_2,ARRAY,E_Pml_1,1,1
*GET,E_Pml_2(1),ELEM,0,NUM,MIN
*DO,ll,2,E_Pml_1
        *GET,E_Pml_2(ll),ELEM,E_Pml_2(ll-1),NXTH
*ENDDO
CM,E_Pml,ELEM
ALLSEL,ALL
EDELE, ElemNum+1, 4*ElemNum, 1
NDELE, NodeNum+1, 4*NodeNum, 1

! Read aluminium plate nodes and elements
NREAD,TNODES2.NODE
EREAD,TELEMENTS2,ELEM
```

```
NUMCMP,ALL
ALLSEL,ALL

! Save components in parameters
CMSEL,S,N_Antenna
NSEL,R,LOC,X,Width/2
*GET,N_X_PW_1,NODE,0,COUNT
*DIM,N_X_PW_2,ARRAY,N_X_PW_1,1,1
*GET,N_X_PW_2(1),NODE,0,NUM,MIN
*DO,ll,2,N_X_PW_1
        *GET,N_X_PW_2(ll),NODE,N_X_PW_2(ll-1),NXTH
*ENDDO
CM,N_X_PW,NODE

CMSEL,S,N_Antenna
NSEL,R,LOC,Y,-Lenght/2
*GET,N_Y_ML_1,NODE,0,COUNT
*DIM,N_Y_ML_2,ARRAY,N_Y_ML_1,1,1
*GET,N_Y_ML_2(1),NODE,0,NUM,MIN
*DO,ll,2,N_Y_ML_1
        *GET,N_Y_ML_2(ll),NODE,N_Y_ML_2(ll-1),NXTH
*ENDDO
CM,N_Y_ML,NODE

CMSEL,S,N_Antenna
NSEL,R,LOC,Y,Lenght/2
*GET,N_Y_PL_1,NODE,0,COUNT
*DIM,N_Y_PL_2,ARRAY,N_Y_PL_1,1,1
*GET,N_Y_PL_2(1),NODE,0,NUM,MIN
*DO,ll,2,N_Y_PL_1
        *GET,N_Y_PL_2(ll),NODE,N_Y_PL_2(ll-1),NXTH
*ENDDO
CM,N_Y_PL,NODE
```

```
CMSEL,S,N_Antenna
NSEL,R,LOC,Z,0
*GET,N_Z_0_1,NODE,0,COUNT
*DIM,N_Z_0_2,ARRAY,N_Z_0_1,1,1
*GET,N_Z_0_2(1),NODE,0,NUM,MIN
*DO,ll,2,N_Z_0_1
        *GET,N_Z_0_2(ll),NODE,N_Z_0_2(ll-1),NXTH
*ENDDO
CM,N_Z_0,NODE

CMSEL,S,N_Antenna
NSEL,R,LOC,Z,Thick
*GET,N_Z_PT_1,NODE,0,COUNT
*DIM,N_Z_PT_2,ARRAY,N_Z_PT_1,1,1
*GET,N_Z_PT_2(1),NODE,0,NUM,MIN
*DO,ll,2,N_Z_PT_1
        *GET,N_Z_PT_2(ll),NODE,N_Z_PT_2(ll-1),NXTH
*ENDDO
CM,N_Z_PT,NODE

CMSEL,S,N_Antenna
NSEL,R,LOC,Z,Thick
CSYS,1
NSEL,R,LOC,X,0,PRadius
CSYS,0
*GET,N_Patch_1,NODE,0,COUNT
*DIM,N_Patch_2,ARRAY,N_Patch_1,1,1
*GET,N_Patch_2(1),NODE,0,NUM,MIN
*DO,ll,2,N_Patch_1
        *GET,N_Patch_2(ll),NODE,N_Patch_2(ll-1),NXTH
*ENDDO
CM,N_Patch,NODE

CMSEL,S,N_Antenna
```

```
LOCAL,11,1,0,-FeedL,0
CSYS,11
NSEL,R,LOC,X,0,CRadius_In
CSYS,0
*GET,N_COAX_In_1,NODE,0,COUNT
*DIM,N_COAX_In_2,ARRAY,N_COAX_In_1,1,1
*GET,N_COAX_In_2(1),NODE,0,NUM,MIN
*DO,ll,2,N_COAX_In_1
        *GET,N_COAX_In_2(ll),NODE,N_COAX_In_2(ll-1),NXTH
*ENDDO
CM,N_COAX_In,NODE

CMSEL,S,N_Antenna
NSEL,R,LOC,Z,0
CSYS,11
NSEL,R,LOC,X,CRadius_In+1e-13,CRadius_Out
CSYS,0
*GET,N_COAX_Out_1,NODE,0,COUNT
*DIM,N_COAX_Out_2,ARRAY,N_COAX_Out_1,1,1
*GET,N_COAX_Out_2(1),NODE,0,NUM,MIN
*DO,ll,2,N_COAX_Out_1
        *GET,N_COAX_Out_2(ll),NODE,N_COAX_Out_2(ll-1),NXTH
*ENDDO
CM,N_COAX_Out,NODE
ALLSEL,ALL

! Define structural model constrains (Force, displacement, symmetry)
NSEL,S,LOC,Z,-Thick_Al
NSEL,R,LOC,X,0.12,0.13
D,ALL,UX,0,,,,UY,UZ
CMSEL,s,N_Z_PT
NSEL,R,LOC,X,0,FWidth/2
NSEL,R,LOC,Y,-FLenght/2,FLenght/2
F,ALL,FZ,Force
```

```
CMSEL,s,N_Z_PT
NSEL,R,LOC,X,0
NSEL,R,LOC,Y,-FLenght/2,FLenght/2
D,ALL,UZ,Displacement
NSEL,S,LOC,X,0
DSYM,SYMM,X,0
ALLSEL,ALL

! Define required array parameters and their dimensions
*DIM, Nod, ARRAY, NodeNum, 3, 1
*DIM, Disp, ARRAY, NodeNum, 3, 1
*DIM, NNod, ARRAY, NodeNum, 3, 1
*DIM, NNod2, ARRAY, NodeNum, 3, 1
*DIM, NNod3, ARRAY, NodeNum, 3, 1
*DIM, NNod4, ARRAY, NodeNum4, 3, 1

! Save the location of nodes before deformation in an array parameter (for substrate)
*VGET,Nod(1,1),NODE,1,LOC,X    ! Save the X component
*VGET,Nod(1,2),NODE,1,LOC,Y    ! Save the Y component
*VGET,Nod(1,3),NODE,1,LOC,Z    ! Save the Z component

! Enter Solution Processor, solve the structural model
/SOLU                          ! Enter Solution Processor
SOLVE                          ! Solve the structural model

! Enter General Post-Processor
/POST1                         ! Enter General Post-Processor

! Save the displacement of nodes after deformation in an array parameter (for
substrate)
*VGET,Disp(1,1),NODE,1,U,X     ! Save the X component
*VGET,Disp(1,2),NODE,1,U,Y     ! Save the Y component
*VGET,Disp(1,3),NODE,1,U,Z     ! Save the Z component
```

```
! Generate new location of nodes after deformation (for substrate)
*Do, j, 1, 3
    *Do, i, 1, NodeNum
        NNod(i,j)=Nod(i,j)+Disp(i,j)
    *ENDDO
*ENDDO

! Write the deformed shape (New node locations) in a file with a formatted sequence (for substrate)
*CFOPEN, NODES, NODE
*VWRITE, SEQU, NNod(1,1,1), NNod(1,2,1), NNod(1,3,1)
(F8.0,3G20.13)

! Get the number of nodes on bottom of the substrate and sort their numbers in an array parameter
CMSEL,S,N_Antenna
NSEL,R,LOC,Z,0
*GET,PNodeNum,NODE,0,COUNT
*DIM,PNN,ARRAY,PNodeNum,7,1
*GET,PNN(1,1),NODE,0,NUM,MIN
*DO,i,2,PNodeNum
    *GET,PNN(i,1),NODE,PNN(i-1,1),NXTH
*ENDDO

! Save the location and displacement of nodes on bottom of the substrate in an array parameter, generate PML under the substrate
*DO, j, 1, PNodeNum
    CMSEL, s, N_Antenna
    *GET, PNN(j,2), NODE, PNN(j,1), LOC, X
    *GET, PNN(j,3), NODE, PNN(j,1), LOC, Y
    *GET, PNN(j,4), NODE, PNN(j,1), LOC, Z
    *GET, PNN(j,5), NODE, PNN(j,1), U, X
    *GET, PNN(j,6), NODE, PNN(j,1), U, Y
    *GET, PNN(j,7), NODE, PNN(j,1), U, Z
```

```
        NSEL, R, LOC, X, PNN(j,2)-1e-13, PNN(j,2)+1e-13
        NSEL, R, LOC, Y, PNN(j,3)-1e-13, PNN(j,3)+1e-13
        *GET, PNodeNum2, NODE, 0, COUNT
        *DIM, PNN2, ARRAY, PNodeNum2, 1, 1
        *GET, PNN2(1), NODE, 0, NUM, MIN
        *DO, k, 2, PNodeNum2
                *GET, PNN2(k), NODE, PNN2(k-1), NXTH
        *ENDDO
        *DO,mm,1,PNodeNum2-1
                *DO,nn,mm+1,PNodeNum2
                        *GET,ZMin1,NODE,PNN2(mm),LOC,Z
                        *GET,ZMin2,NODE,PNN2(nn),LOC,Z
                        *IF,ZMin2,LT,ZMin1,Then
                                PNN2TEMP=PNN2(mm)
                                PNN2(mm)=PNN2(nn)
                                PNN2(nn)=PNN2TEMP
                        *ENDIF
                *ENDDO
        *ENDDO
        *DO, kk, 1, PNodeNum2
                NNod4(PNN2(kk),1)=PNN(j,2)+PNN(j,5)
                NNod4(PNN2(kk),2)=PNN(j,3)+PNN(j,6)
                NNod4(PNN2(kk),3)=Nod(PNN2(kk),3)-Thick+(PNN(j,7)/(PNodeNum2-
                1))*(kk-1)
        *ENDDO
        *DEL, PNN2
*ENDDO
```

! Get the number of nodes on top of the substrate and sort their numbers in an array parameter

```
CMSEL, s, N_Z_PT
*GET, SNodeNum, NODE, 0, COUNT
*DIM, SNN, ARRAY, SNodeNum, 7, 1
*GET, SNN(1,1), NODE, 0, NUM, MIN
```

```
*DO, i, 2, SNodeNum
        *GET, SNN(i,1), NODE, SNN(i-1,1), NXTH
*ENDDO

! Find the maximum displacement
MaxDis=0
*DO,ii,1,SNodeNum
        *GET,Dis,NODE,SNN(ii,1),U,Z
        *IF,Dis,ABGT,MaxDis,Then
                MaxDis=Dis
        *ENDIF
*ENDDO

! Save the location and displacement of nodes on top of the substrate in an array parameter, generate PML & Air on top of the substrate
*DO, j, 1, SNodeNum
        CMSEL, s, N_Antenna
        *GET, SNN(j,2), NODE, SNN(j,1), LOC, X
        *GET, SNN(j,3), NODE, SNN(j,1), LOC, Y
        *GET, SNN(j,4), NODE, SNN(j,1), LOC, Z
        *GET, SNN(j,5), NODE, SNN(j,1), U, X
        *GET, SNN(j,6), NODE, SNN(j,1), U, Y
        *GET, SNN(j,7), NODE, SNN(j,1), U, Z
        NSEL, R, LOC, X, SNN(j,2)-1e-13, SNN(j,2)+1e-13
        NSEL, R, LOC, Y, SNN(j,3)-1e-13, SNN(j,3)+1e-13
        *GET, SNodeNum2, NODE, 0, COUNT
        *DIM, SNN2, ARRAY, SNodeNum2, 1, 1
        *GET, SNN2(1), NODE, 0, NUM, MIN
        *DO, k, 2, SNodeNum2
                *GET, SNN2(k), NODE, SNN2(k-1), NXTH
        *ENDDO
        *DO,mm,1,SNodeNum2-1
                *DO,nn,mm+1,SNodeNum2
                        *GET,ZMin1,NODE,SNN2(mm),LOC,Z
```

```
                    *GET,ZMin2,NODE,SNN2(nn),LOC,Z
                    *IF,ZMin2,LT,ZMin1,Then
                        SNN2TEMP=SNN2(mm)
                        SNN2(mm)=SNN2(nn)
                        SNN2(nn)=SNN2TEMP
                    *ENDIF
                *ENDDO
            *ENDDO
            *DO, kk, 1, SNodeNum2
                NNod2(SNN2(kk),1)=SNN(j,2)+SNN(j,5)
                NNod2(SNN2(kk),2)=SNN(j,3)+SNN(j,6)
                NNod2(SNN2(kk),3)=Nod(SNN2(kk),3)+Thick+SNN(j,7)+((MaxDis-
                SNN(j,7))/(SNodeNum2-1))*(kk-1)
                NNod3(SNN2(kk),1)=SNN(j,2)+SNN(j,5)
                NNod3(SNN2(kk),2)=SNN(j,3)+SNN(j,6)
                NNod3(SNN2(kk),3)=Nod(SNN2(kk),3)+(2*Thick)+MaxDis+(3*(kk-
                1)*(Thick/(SNodeNum2-1)))
            *ENDDO
            *DEL, SNN2
*ENDDO
```

! Write the deformed shape (New node locations) in a file with a formatted sequence (for Air & PML)

```
*CFOPEN, NODES2, NODE
*VWRITE, SEQU, NNod2(1,1,1), NNod2(1,2,1), NNod2(1,3,1)
(F8.0,3G20.13)

*CFOPEN, NODES3, NODE
*VWRITE, SEQU, NNod3(1,1,1), NNod3(1,2,1), NNod3(1,3,1)
(F8.0,3G20.13)

*CFOPEN, NODES4, NODE
*VWRITE, SEQU, NNod4(1,1,1), NNod4(1,2,1), NNod4(1,3,1)
(F8.0,3G20.13)
```

```
! Run the FORTRAN code
/SYS,B.exe

! Save all parameters in a file
PARSAV, ALL, PARAMETE, PARM

! Get the strain data and save them in a file
SET,LAST                    ! Read the last data set from the results file

PATH,S1,2,30,20             ! Define path number 1 for first strain gauge
PPATH,1,,0.035,0,0.0015     ! First point to define path number 1
PPATH,2,,0.035,0,-0.003     ! Second point to define path number 1

PDEF,EX,EPTO,X,AVG          ! Get the X component of total mechanical strain
PDEF,EY,EPTO,Y,AVG          ! Get the Y component of total mechanical strain
PDEF,EZ,EPTO,Z,AVG          ! Get the Z component of total mechanical strain
PDEF,EXY,EPTO,XY,AVG        ! Get the XY component of total mechanical strain
PDEF,EYZ,EPTO,YZ,AVG        ! Get the YZ component of total mechanical strain
PDEF,EXZ,EPTO,XZ,AVG        ! Get the XZ component of total mechanical strain
PDEF,E1,EPTO,1,AVG          ! Get the first principal total strain
PDEF,E2,EPTO,2,AVG          ! Get the second principal total strain
PDEF,E3,EPTO,3,AVG          ! Get the third principal total strain
PDEF,INT,EPTO,INT,AVG       ! Get the total strain intensity
PDEF,EQV,EPTO,EQV,AVG       ! Get the total equivalent strain

PATH,S2,2,30,20             ! Define path number 2 for second strain gauge
PPATH,1,,0.125,0,0          ! First point to define path number 2
PPATH,2,,0.125,0,-0.003     ! Second point to define path number 2

PDEF,EX,EPTO,X,AVG          ! Get the X component of total mechanical strain
PDEF,EY,EPTO,Y,AVG          ! Get the Y component of total mechanical strain
PDEF,EZ,EPTO,Z,AVG          ! Get the Z component of total mechanical strain
PDEF,EXY,EPTO,XY,AVG        ! Get the XY component of total mechanical strain
```

```
PDEF,EYZ,EPTO,YZ,AVG        ! Get the YZ component of total mechanical strain
PDEF,EXZ,EPTO,XZ,AVG        ! Get the XZ component of total mechanical strain
PDEF,E1,EPTO,1,AVG          ! Get the first principal total strain
PDEF,E2,EPTO,2,AVG          ! Get the second principal total strain
PDEF,E3,EPTO,3,AVG          ! Get the third principal total strain
PDEF,INT,EPTO,INT,AVG       ! Get the total strain intensity
PDEF,EQV,EPTO,EQV,AVG       ! Get the total equivalent strain

PASAVE,ALL,STRAINS,PATH     ! Save strain data in a file

! Exit the processor, clear the database & start a new analysis
FINISH                      ! Exit the processor
/CLEAR,START                ! Clear the database & start a new analysis

! Set preferences for high frequency electromagnetic analysis
/NOPR
/PMETH,OFF,1
KEYW,PR_SET,1
KEYW,PR_STRUC,0
KEYW,PR_THERM,0
KEYW,PR_FLUID,0
KEYW,PR_ELMAG,1
KEYW,MAGNOD,0
KEYW,MAGEDG,0
KEYW,MAGHFE,1
KEYW,MAGELC,0
KEYW,PR_MULTI,0
KEYW,PR_CFD,0
/GO

! Enter Pre-Processor, read parameters file
/PREP7                      ! Enter Pre-Processor
PARRES,,PARAMETE,PARM       ! Read Parameters file
```

```
! Define elements and material properties
ET,1,HF120,,,,0                 ! Element type 1 (Substrate)
ET,2,HF120,,,,0                 ! Element type 2 (Air)
ET,3,HF120,,,,1                 ! Element type 3 (PML)
MP,MURX,1,1                     ! Material 1 (Substrate) relative permeability
MP,PERX,1,Epsr                  ! Material 1 (Substrate) relative permittivity
MP,LSST,1,LossT                 ! Material 1 (Substrate) loss tangent
MP,MURX,2,1                     ! Material 2 (Air) relative permeability
MP,PERX,2,1                     ! Material 2 (Air) relative permittivity
MP,MURX,3,1                     ! Material 3 (PML) relative permeability
MP,PERX,3,1                     ! Material 3 (PML) relative permittivity

! Read nodes and elements into the database
NREAD,NNODES,NODE
NREAD,NNODES2,NODE
NREAD,NNODES3,NODE
NREAD,NNODES4,NODE
EREAD,ELEMENTS,ELEM

! Scale the model
NSCALE,0,ALL, , ,Scale,Scale,Scale

! Read previously defined components
NSEL,NONE
*Do,lll,1,N_X_PW_1
        NSEL,A,NODE,,N_X_PW_2(lll)
*ENDDO
CM,N_X_PW,NODE

NSEL,NONE
*Do,lll,1,N_Y_ML_1
        NSEL,A,NODE,,N_Y_ML_2(lll)
*ENDDO
CM,N_Y_ML,NODE
```

```
NSEL,NONE
*Do,lll,1,N_Y_PL_1
        NSEL,A,NODE,,N_Y_PL_2(lll)
*ENDDO
CM,N_Y_PL,NODE

NSEL,NONE
*Do,lll,1,N_Z_0_1
        NSEL,A,NODE,,N_Z_0_2(lll)
*ENDDO
CM,N_Z_0,NODE

NSEL,NONE
*Do,lll,1,N_Z_PT_1
        NSEL,A,NODE,,N_Z_PT_2(lll)
*ENDDO
CM,N_Z_PT,NODE

NSEL,NONE
*Do,lll,1,N_Patch_1
        NSEL,A,NODE,,N_Patch_2(lll)
*ENDDO
CM,N_Patch,NODE

NSEL,NONE
*Do,lll,1,N_COAX_In_1
        NSEL,A,NODE,,N_COAX_In_2(lll)
*ENDDO
CM,N_COAX_In,NODE

NSEL,NONE
*Do,lll,1,N_COAX_Out_1
        NSEL,A,NODE,,N_COAX_Out_2(lll)
```

```
*ENDDO
CM,N_COAX_Out,NODE

ESEL,NONE
*Do,lll,1,E_Pml_1
        ESEL,A,ELEM,,E_Pml_2(lll)
*ENDDO
CM,E_Pml,ELEM

ESEL,NONE
*Do,lll,1,E_Del_1
        ESEL,A,ELEM,,E_Del_2(lll)
*ENDDO
CM,E_Del,ELEM

! Delete redundant elements
CMSEL,S,E_Del
EDELE,ALL

! Merge nodes, elements and key-points numbers
ALLSEL,ALL
NUMMRG,NODE
NUMMRG,ELEM
NUMMRG,KP

! Re-scale the model
NSCALE,0,ALL, , ,1/Scale,1/Scale,1/Scale

! Modify the PML elements type
ALLSEL,ALL
CMSEL,S,E_Pml
EMODIF,ALL,TYPE,3

! Define high frequency electromagnetic model constrains (PEC condition)
```

```
ALLSEL,ALL
NSEL,S,EXT
CMSEL,A,N_Patch
CMSEL,A,N_COAX_In
CMSEL,U,N_COAX_Out
NSEL,U,LOC,X,0
D,ALL,AX,0
ALLSEL,ALL

! Define the port
LOCAL,12,0,0,-FeedL,0
CMSEL,S,N_COAX_Out
SF,ALL,PORT,1
HFPORT,1,COAX,12,TEM,EXT,CRadius_In,CRadius_Out,,,1,0
ALLSEL,ALL
CSYS,0

! Enter Solution Processor, solve the high frequency electromagnetic model
/SOLU                                   ! Enter Solution Processor
SPSWP,Freq_B,Freq_E,Freq_Inc,1,,0,1     ! Perform a frequency sweep

! Exit the processor
FINISH                                  ! Exit the processor
```

B.2 ANSYS APDL™ Code for Preparing the Deformed Mesh of Slotted/Meandered Circular Microstrip Patch Antenna for ANSYS Finite Element Modeler™ (This code is a modified version of a code from ANSYS™ Tutorials (ANSYS, 2010))

```
! Enter General Post-Processor and read the last data set
/POST1                          ! Enter General Post-Processor
SET,LAST                        ! Read the last data set from the results file

! Enter Pre-Processor  and read component definition from original model
/PREP7                          ! Enter Pre-Processor
/INPUT,FILE,CMP,'D:\ANSYS files\WB_CMPA_files\dp0\SYS\MECH\'

! Update node coordinates
SHPP,OFF
UPCOORD,1

! Dummy Surf154 elements for mesh groups
ET,10000,SURF154

! Delete aluminium plate elements and only keep substrate elements
CMSEL,S,SUBSTRATE
ESEL,INVE
NSLE,S,ALL
EDELE,ALL
NDELE,ALL
ALLSEL

! Take node components to overlay surf element
*GET,numcomp,COMP,0,NCOMP
*DO,i,1,numcomp
        *GET,actcomp,COMP,i,NAME
        *IF,STRSUB(actcomp,1,5),EQ,'ORIGF',THEN
                CMSEL,S,actcomp
                ESEL,U,TYPE,,10000
                TYPE,10000
```

```
            ESURF
            ESEL,R,TYPE,,10000
            suf=STRSUB(actcomp,6,STRLENG(actcomp))
            grname='ORIG_e%suf%'
            ! Create group from surface elements
            CM,grname,ELEM
            ALLSEL
        *ENDIF
*ENDDO

! Delete node groups
*GET,numcomp,COMP,0,NCOMP
*DO,i,1,numcomp
        *GET,actcomp,COMP,i,NAME
        *IF,STRSUB(actcomp,1,5),EQ,'ORIGF',THEN
            CMDELE,actcomp
        *ENDIF
*ENDDO

! Write *.cdb File
CDWRITE
```

Appendix C - FORTRAN™ Code

```
! Start program, define preferences, define parameters type
PROGRAM Node_Numbers
IMPLICIT NONE
INTEGER, PARAMETER:: k = 8
REAL(kind=k) :: a1, b, c, d
INTEGER :: stat, a2, NodeNum

! Open required files
OPEN (unit=10, file="NODES.NODE", status="old", action="read")
OPEN (unit=12, file="NODES2.NODE", status="old", action="read")
OPEN (unit=14, file="NODES3.NODE", status="old", action="read")
OPEN (unit=16, file="NODES4.NODE", status="old", action="read")
OPEN (unit=11, file="NNODES.NODE", status="new", action="write")
OPEN (unit=13, file="NNODES2.NODE", status="new", action="write")
OPEN (unit=15, file="NNODES3.NODE", status="new", action="write")
OPEN (unit=17, file="NNODES4.NODE", status="new", action="write")

! Change the format of previously saved data
DO
        READ (unit=10, fmt="(F8.0,3G20.13)", iostat=stat), a1, b, c, d
        IF (stat < 0) EXIT
        a2 = a1
        NodeNum = a2
        WRITE (unit=11, fmt="(I8,3G20.13)"), a2, b, c, d
END DO

DO
        READ (unit=12, fmt="(F8.0,3G20.13)", iostat=stat), a1, b, c, d
        IF (stat < 0) exit
        a2 = a1 + NodeNum
```

```
        WRITE (unit=13, fmt="(I8,3G20.13)"), a2, b, c, d
END DO

DO
        READ (unit=14, fmt="(F8.0,3G20.13)", iostat=stat), a1, b, c, d
        IF (stat < 0) exit
        a2 = a1 + (2*NodeNum)
        WRITE (unit=15, fmt="(I8,3G20.13)"), a2, b, c, d
END DO

DO
        READ (unit=16, fmt="(F8.0,3G20.13)", iostat=stat), a1, b, c, d
        IF (stat < 0) exit
        a2 = a1 + (3*NodeNum)
        WRITE (unit=17, fmt="(I8,3G20.13)"), a2, b, c, d
END DO

! Close files
CLOSE (unit=10)
CLOSE (unit=11)
CLOSE (unit=12)
CLOSE (unit=13)
CLOSE (unit=14)
CLOSE (unit=15)
CLOSE (unit=16)
CLOSE (unit=17)

! End program
END PROGRAM Node_Numbers
```

Appendix D – ANSYS Workbench™ Instructions for Simulation of Slotted/Meandered Circular Microstrip Patch Antenna

The instructions provided in this Appendix are linked to section 5.5 (STEMCOF data processing protocol (ANSYS Workbench™-HFSS™)) in Chapter 5. These instructions are required to obtain accurate results in simulation of deformed shape of meandered circular microstrip patch antenna in ANSYS Workbench™. The same procedure is used for the slotted circular microstrip patch antenna. The numbers provided here are from the simulation files of the meandered circular microstrip patch antenna deformed in 0° orientation. The amount of displacement in the centre of antenna sensor is 10 mm. The version of ANSYS™ software used here is 12.1. It is presumed that the reader has basic knowledge of working with ANSYS Workbench™. In some parts of this instruction ANSYS (2010) is used as the reference.

1. Start ANSYS Workbench™ Software and save the project with the desirable name.
2. Drag a **Static Structural**, a **Mechanical APDL** and a **Finite Element Modeler** system from the **Toolbox** menu into **Project Schematic** window. Rename the first two to *3-Point Bend* and *Deformed Geometry*, respectively. Then connect the **Solution** box of *3-Point Bend* to **Analysis** in *Deformed Geometry* by dragging one into another. Also, connect **Analysis** in *Deformed Geometry* to **Model** in *Finite Element Modeler*.
3. Right click on the **Analysis** in *Deformed Geometry* and select **Add Input File** from the menu then select **Browse** and in the new opened window select the text file which contains the code provided in Appendix B.
4. Create the geometry of the antenna, aluminium plate and wooden jig in **ANSYS Design Modeler™** or import the geometry from a CAD file into the **Geometry** box of *3-Point Bend*. The geometry must have 5 solid parts, one for antenna, one for aluminium plate and one for each part of wooden jig.
5. In the **ANSYS Design Modeler™**, after creating the geometry (or importing the geometry), the **Share Topology** option must be activated. Then create a name

selection for each face of the antenna and name them as "*origf1, origf2 ...*". Also create one name selection for antenna solid, one for aluminium plate solid and one for wooden jig solids. Close **ANSYS Design Modeler™**.

6. Open **ANSYS Mechanical™** by double clicking on **Model** box, or **Setup** box or **Solution** box of *3-Point Bend*.
7. In the **Model** section, define the material for each solid part by selecting that part and changing the **Assignment** in **Definition** section of **Details** menu. The material properties must already be defined in **Engineering Data** box of *3-Point Bend*.
8. Define one **Coordinate System** at the location of each strain gauge.
9. The software automatically detects the contact between different parts. The contact type for all the contacts is "**Rough"** except the contact between the antenna and aluminium plate which is "**Bonded"**.
10. Define a **Sizing** mesh control for the patch, coaxial and pin faces and set the **Element Size** to *0.5 mm*.
11. In the **Static Structural** section, define one **Displacement** constraint for the outer face of the top part of wooden jig and set it to *-10 mm* for Z direction. Then define one **Displacement** constraint for the outer face of the two bottom parts of wooden jig and set it to *0 mm* for Z direction.
12. Add the "*CMWRITE,file,cmp*" command into the **Static Structural** section.
13. Define four **Strain Probes** for strain gauges by using the **Coordinate Systems** defined in 8.
14. Close **ANSYS Mechanical™**.
15. Click on the **Update Project** on the **Toolbar** of **ANSYS Workbench™** and wait for the software to solve the analysis.
16. When the simulation is finished, open **Finite Element Modeler™** by double clicking on **Model** box of *Finite Element Modeler*. The antenna mesh is processed by **Mechanical APDL™** in *Deformed Geometry* and is imported into the **Finite Element Modeler™**.
17. In **Finite Element Modeler™**, click on **Geometry Synthesis** and then select **Initial Geometry** form the **Tooolbar**. The software will process the imported mesh and create new surface parts.
18. Select **Initial Geometry** and then click on **Convert to Parasolid** from **Toolbar**. The software converts the model to Parasolid surface parts.

19. Select **Parasolid Geometry** then click on **Add a Sew Tool** form the **Toolbar**. In the **Details** window click on **Geometry** then right click in the **Graphics** window and click on **Select All** then click on **Apply**. Then click on **Generate the Parasolid Geometry** for the **Toolbar**. The software creates a solid part.
20. Save the created model as a Parasolid file by clicking on **Export to a Parasolid File** from the **Toolbar**. This file can be used for analysis in HFSS™ which is described in Appendix E.

Appendix E - HFSS™ Instructions for Simulation of Deformed Shape of Slotted/Meandered Circular Microstrip Patch Antenna

The instructions provided in this Appendix are linked to section 5.5 (STEMCOF data processing protocol (ANSYS Workbench™-HFSS™)) in Chapter 5 and must be followed after the instructions provided in Appendix D. These instructions are required to obtain accurate results in simulation of deformed shape of meandered circular microstrip patch antenna in HFSS™. The same procedure is used for the slotted circular microstrip patch antenna. The numbers provided here are from the simulation files of the meandered circular microstrip patch antenna deformed in 0° orientation. The amount of displacement in the centre of antenna sensor is 10 mm. The version of HFSS™ software used here is 12.1.2.

1. Start HFSS™ Software and save the project with the desirable name.
2. Click on the **Project** menu and select **Insert HFSS Design**.
3. To setup the solution type, click on the **HFSS** menu and select **Solution Type**. In the new opened window select **Driven Terminal** and click on **Ok**.
4. To import the deformed shape of the antenna click on the **Modeler** menu and select **Import**. In the new opened window (**Import File** window) select **Parasolid Files (*.x_t;*.x_b)** in the **Files of Type** drop down menu and then select the Parasolid file created in ANSYS Finite Element Modeler™ and click on **Open**.
5. Double-click on the imported object under the **Solids** in **Model** tree and change its name to *Substrate*.
6. Right-click on the *Substrate* under the **Solids** in **Model** tree and select **Assign Material**. In the new opened window select the appropriate material from the list of available materials or create your own material then click on **Ok**.
7. To create the air box around the antenna click on the **Draw** menu and select **Box** from the list. Then in the **Modeler** window click on three non-planar points to create the box. Double-click on the *Box1* under the **Solids** in **Model** tree and change its name to *Air_Box*.

8. Double click on the **CreateBox** under *Air_Box* in **Model** tree and in the new opened window change the **Position** to *-60, -60, -40* and change the **XSize**, **YSize** and **ZSize** to *120*, *120* and *60*, respectively. This is to insure that the distance between the antenna and *Air_Box* edges are 30 mm (moderately more than $\lambda/4$ for 3.5 GHz). The start position for the Z direction depends on the amount of bending and must be between -30 mm and -40 mm for displacements between 0 mm and 10 mm.
9. To subtract the *Substrate* from *Air_Box*, under the **Solids** in **Model** tree select *Air_Box* and then select *Substrate* by holding down the Ctrl key on the keyboard. Then click on **Subtract** from the **Toolbar**. In the new opened window check the **Clone tool objects before operation** option and then click on **Ok**.
10. Under the **Solids** in **Model** tree right-click on the *Air_Box* and select **View** then select **Hide In Active View**.
11. To create the *Probe* rotate the view to see the bottom side of the *Substrate* by holding down the Ctrl and Alt keys and mouse left button at the same time and dragging the mouse. Then press F key on the keyboard to only select surfaces. Now, select the pin surface and then click on the **Modeler** menu then select **Surface** then select **Sweep Faces Along Normal**. In the new opened window set the **Length of Sweep** to *-0.2* mm and click on **Ok**.
12. Right-click on the object created Under the **Solids** in **Model** tree and change its name to *Probe*. Change the material of *Probe* to *PEC* with the same procedure described in 6.
13. Do the same procedure as 11 to create the *Coax_Pin* (use 0.5 mm for the **Length of Sweep**) and use the same procedure as 12 to change its name to *Coax_Pin* and its material to *PEC*.
14. Similar to 11 create the *Coax* (use 0.5 mm for the **Length of Sweep**), rename it to *Coax* and change its material to *vacuum*.
15. In order to complete the *Coax* and *Coax_Pin* two auxiliary boxes must be created using the same procedure as 7. For *Box1* and *Box2* the **Position** must be set to *-5, -5, -11* and the **XSize**, **YSize** and **ZSize** to *10, 10* and *0.95*, respectively. The start position for the Z direction depends on the amount of bending and must be between -1 mm and -11 mm for displacements between 0 mm and 10 mm to make sure the thickness of *Coax* is almost 0.05 mm.

16. Using the same procedure as 9, subtract *Box1* from *Coax*, and *Box2* from *Coax_Pin* (this time do not check the **Clone tool objects before operation** option). This procedure is required to have a planar face on the *Coax* and *Coax_Pin* necessary for applying the excitation.
17. Select the meandered patch surface then click on the **Modeler** menu then select **Surface** then select **Create Object From Face**. Double-click on the created object under the **Sheets** (**Unassigned**) in the **Model** tree and rename it to *Patch*. Using the same procedure, create *Ground_Plane*, Coax_Out and *Port* by selecting the bottom face of the *Substrate*, outer face of *Coax* and bottom face of *Coax*, respectively.
18. Select *Ground_Plane* under the **Sheets** (**Unassigned**) in the **Model** tree and then click on the **HFSS** menu and select **Boundaries** then select **Assign** then select **Perfect E**. In the new opened window change the name to *Ground_Plane* and then click on **Ok**. Make sure the **Infinite Ground Plane** option is not checked. Do the same procedure for *Patch* and *Coax_Out*.
19. Select *Port* under the **Sheets** (**Unassigned**) in the **Model** tree and then click on the **HFSS** menu and select **Excitations** then select **Assign** then select **Lumped Port**. In the new opened window change the **Port Name** to *P1* and select *Coax_Out* as the reference conductor and click on **Ok**.
20. In order to set the initial meshing options, in the **Project Manager** window right-click on **Mesh Operations** then select **Initial Mesh Settings**. In the new opened window under the **Surface Approximation** tab set **Maximum Surface Deviation**, **Maximum Surface Normal Deviation** and **Maximum Aspect Ratio** to *0.01* mm, *5* deg and *1*, respectively. Also, check the **Apply curvilinear elements** option. Then under the **Meshing Method** tab select **Ansoft TAU Mesh** and set it to **Strict** then click on **Ok**.
21. Under the **Solids** in **Model** tree right-click on the *Substrate* and select **Assign Mesh Operation** then select **On Selection** then select **Length Based**. In the new opened window change the name to *Substrate* and check **Restrict Length of Elements** option and set **Maximum Length of Elements** to *5* mm and click on **Ok**. Do the same procedure for *Patch* and set **Maximum Length of Elements** to *0.5* mm.
22. Under the **Solids** in **Model** tree right-click on the *Air_Box* and select **View** then **Show In Active View**.
23. Select all outer faces of the *Air_Box* and then click on the **HFSS** menu and select **Boundaries** then select **PML Setup Wizard**. In the new opened window set the **Uniform Layer Thickness** to *50* mm and make sure **Create joining corner and**

edge objects and **Radiation Only** options are selected then click on **Next** to create the PML layers. In the new opened window make sure the **PML Objects Accept Free Radiation** option is selected and the **Minimum Frequency** is set to *1* GHz. Also, set the **Minimum Radiation Distance** to *100* mm and click on **Next**. In the next window click on **Finish**.

24. In order to set the analysis setup options, in the **Project Manager** window right-click on **Analysis** then select **Add Solution Setup**. In the new opened window under the **General** tab set the **Solution Frequency**, **Maximum Number of Passes** and **Maximum Delta S** to *3.5* GHz, *30* and *0.01*, respectively. Under the **Options** tab set **Minimum Converged Passes** to *2* and select **Mixed Order** as the **Order of Basis Functions** then click on **Ok**.
25. In order to set the frequency sweeps, in the **Project Manager** window right-click on **Setup1** then select **Add Frequency Sweep**. In the new opened window set **Sweep Type** to **Fast** then in the **Frequency Setup** section set **Type** to **LinearCount**. Also, set **Start**, **Stop** and **Count** to *3* GHz, *4* GHz and *401*, respectively. Then click on **Ok**.
26. Depending on the results for each step of bending, another frequency sweep must be created with the **Discrete Sweep Type**. Number of points for this sweep depends on the desirable resolution.
27. In Order to generate the results, in the **Project Manager** window right-click on **Results** then select **Create Terminal Solution Data Report** then select **Rectangular Plot**. In the new opened window default options are already set for S_{11} extraction. Click on **New Report**.
28. To solve the analysis, in the **Project Manager** window right-click on **Analysis** then select **Analyze All**.

References

ANSYS 2010, *ANSYS™ Tutorials*, ANSYS Inc., viewed 10 March 2010, < https://www1.ansys.com/customer/default.asp >

ANSYS 2011a, *About ANSYS™ Inc*, ANSYS Inc., viewed 15 April 2011, < http://www.ansys.com/About+ANSYS >

ANSYS 2011b, *HFSS™*, ANSYS Inc., viewed 15 April 2011, < http://www.ansoft.com/products/hf/hfss/ >

ANSYS 2011c, *HFSS™ product overview*, ANSYS Inc., viewed 15 April 2011, < http://www.ansoft.com/products/hf/hfss/overview.cfm >

ANSYS® Academic Research 2010a, Release 12.1, *Help System*, Mechanical APDL// ANSYS Parametric Design Language Guide // 1. Introducing APDL, ANSYS, Inc.

ANSYS® Academic Research 2010b, Release 12.1, *Help System*, Workbench// User's Guide // Overview, ANSYS, Inc.

ANSYS® Academic Research 2010c, Release 12.1, *Help System*, Mechanical APDL// High-Frequency Electromagnetic Analysis Guide, ANSYS, Inc.

ANSYS® Academic Research 2010d, Release 12.1, *Help System*, Mechanical APDL // Element Reference // I. Element Library // SOLID186, ANSYS, Inc.

ANSYS® Academic Research 2010e, Release 12.1, *Help System*, Mechanical APDL // Element Reference // I. Element Library // HF120, ANSYS, Inc.

Auweraer, H.V. and Peeters, B. 2003, 'International research projects on structural health monitoring: an overview', *Structural Health Monitoring*, vol.2, no.4, pp.341-358.

Baena, D.J., Marques, R., Medina, F. and Martel, J. 2004, 'Artificial magnetic metamaterial design by using spiral resonators', *Phys. Rev. B*, vol.69.

Balanis, C.A. 2005, *Antenna theory analysis and design*, 3rd edn, US: John Wiley & Sons Ltd.

Barrowes, B. 2004, *Computation of Special Functions*, MathWorks™, viewed 5 September 2009, <http://www.mathworks.com/matlabcentral/fileexchange/6218-computation-of-special-functions>

Bernhard, J.T., Hietpas, K., George, E., Kuchima, D. and Reis, H. 2003, 'An interdisciplinary effort to develop a wireless embedded sensor system to monitor and assess corrosion in the tendons of prestressed concrete girders', in: *IEEE Tropical Conference on Wireless Communication Technology*, Urbana, USA, Oct, 2003, pp.241-243.

BOEING 2011a, *787 dreamliner design highlights*, The Boeing Company, viewed 12 April 2011, <http://www.newairplane.com/787/design_highlights/>

BOEING 2011b, *About the 787 family*, The Boeing Company, viewed 12 April 2011, <http://www.boeing.com/commercial/787family/background.html>

Boufrioua, A. and Benghalia, A. 2006, 'Effects of the resistive patch and the uniaxial anisotropic substrate on the resonant frequency and the scattering radar cross section of a rectangular microstrip antenna', *Aerospace Science and Technology*, vol.10, no.3, pp.217–221.

Buttler, J.C., Vigliotti, A.J., Verdi, F.W. and Walsh S.M. 2002, 'Wireless, passive, resonant-circuit, inductively coupled, inductive strain sensor', *Sensors and Actuators A: Physical*, vol.102, no.1-2, pp.61-66.

Carmo, J.P., Mendes, P.M., Couto, C. and Correia, J.H. 2006, '5.7 GHz on-chip antenna/RF CMOS transceiver for wireless sensor networks', *Sensors and Actuators A: Physical*, vol.132, no.1, pp.47–51.

Chacon, R., Guzman, F., Mirambell, E., Real, E. and Onate, E. 2009, 'Wireless sensor networks for strain monitoring during steel bridges launching', *Structural Health Monitoring*, vol.8, no.3, pp.195–205.

Chaimanonart, N. and Young, D.J. 2006, 'Remote RF powering system for wireless MEMS strain sensors', *IEEE Sensors Journal*, vol.6, no.2, pp.484-489.

Chang, P.C., Flatau, A. and Liu, S.C. 2003, 'Review paper: health monitoring of civil infrastructure', *Structural Health Monitoring*, vol.2, no.3, pp.257–267.

Cheng, S., Ojefors, E. and Hallbjorner, P., Ogden, S., Margell, J., Hjort, K. And Rydberg, A. 2007, 'Body surface backed flexible antennas for 17 GHz wireless body area networks sensor applications', in: *Proceedings of the 10th European Conference on Wireless Technology*, Munich, Germany, Oct, 2007, pp.55-58.

Choi, H., Choi, S. and Cha, H. 2008, 'Structural health monitoring system based on strain gauge enabled wireless sensor nodes', in: *5th International Conference on Networked Sensing Systems (INSS2008)*, Jun, 2008, vol.2, no.4, pp.211–214.

Chuang, J., Thomson, D.J. and Bridges, G.E. 2005, 'Embeddable wireless strain sensor based on resonant RF cavities', *Review of Scientific Instruments*, vol.76, no.9.

Conway, G.A., Scanlon, W.G., Orlenius, C. and Walker, C. 2008, 'In situ measurement of UHF wearable antenna radiation efficiency using a reverberation chamber', *IEEE Antennas and Wireless Propagation Letters*, vol.7, pp.271–274.

Deshmukh, S., Mohammad, I., Tentzeris, M., Wu, T. and Huang, H. 2009, 'Crack detection and monitoring using passive wireless sensor', in: *Proceedings of the ASME 2009 conference on smart materials, adaptive structures and intelligent systems (SMASIS2009)*, Oxnard, USA, Sep, 2009, pp.511-516.

Fallah-Rad, M. and Shafai, L. 2008, 'Gain enhancement in embedded microstrip antennas', *Microwave and Optical Technology Letters*, vol.50, no.2, pp.269-271.

Farhey, D.N. 2006, 'Integrated virtual instrumentation and wireless monitoring for infrastructure diagnostics', *Structural Health Monitoring*, vol.5, no.1, pp.29–43.

Fink, M. 1999, 'Time-reversed acoustics', *Scientific American*, vol.281, no.5, pp.91-103.

Fu, Q., Wang, J., Zhou, D. and Luo, W. 2009, 'Passive wireless SAWR sensor system model including the effects of antenna distances', *Sensors and Actuators A: Physical*, vol.150, no.1, pp.151-155.

Garg, R., Bhartia, P., Bahl, I. and Ittipiboon, A. 2000, *Microstrip antenna design handbook*, 1st edn, England: Artech House.

Ghretli, M., Khalid, K., Grozescu, I.V., Sahri, M.H. and Abbas, Z. 2007a, 'Dual frequency microstrip antenna sensor for water content measurements independent of temperature variation', *Measurement Science and Technology*, vol.18, no.4, pp.1054-1060.

Ghretli, M.M., Khalid, K., Grozescu, I.V., Sahri, M.H. and Abbas, Z. 2007b, 'Dual-frequency microwave moisture sensor based on circular microstrip antenna', *IEEE Sensors Journal*, vol.7, no.12, pp.1749-1756.

Hadzic, R., John, S. and Herszberg, I. 1999, 'Structural integrity analysis of embedded optical fibres in composite structures', *Composite Structures*, vol.47, no.1-4, pp.759-765.

Huang, W. and Kishk, A.A. 2007, 'Compact dielectric resonator antenna array for microwave breast cancer detection', in: *IEEE Region 5 Technical Conference*, Apr, 2007, pp.9–12.

Huang, Y. and Boyle, K. 2008, *Antennas from theory to practice*, 1st edn, England: John Wiley & Sons Ltd.

James, J.R., Hall, P.S. 1989, *Handbook of microstrip antennas*, 1st edn, England: Peter Peregrinus Ltd.

Jia, Y., Sun, K., Agosto, F.J. and Quinones, M.T. 2006, 'Design and characterization of a passive wireless strain sensor', *Measurement Science and Technology*, vol.17, no.11, pp.2869–2876.

Jin, J.M., Riley, D.J. 2009, *Finite element analysis of antennas and arrays*, 1st edn, US: John Wiley & Sons Ltd.

Jones, R. and Galea, S. 2002, 'Health monitoring of composite repairs and joints using optical fibres', *Composite Structures*, vol.58, no.3, pp.397-403.

Jones, R. and Galea, S. 2002, 'Health monitoring of composite repairs and joints using optical fibres', *Composite Structures*, vol.58, no.3, pp.397-403.

Ju, T., Zhongrong, X., Xiaoxing, Z. and Caixin, S. 2007, 'GIS partial discharge quantitative measurements using UHF microstrip antenna sensors', in: *Annual Report Conference on Electrical Insulation and Dielectric Phenomena*, Vancouver, Canada, Oct, 2007, pp.116-119.

Kakoyiannis, C.G. and Constantinou, P. 2008, 'Co-design of antenna element and ground plane for printed monopoles embedded in wireless sensors', in: *The Second International Conference on Sensor Technologies and Applications*, Aug, 2008, pp.413-418.

Kerr, J. 1973, 'Short axial length broad-band horns', *IEEE Transactions on Antennas and Propagation*, vol.21, no.5, pp.710-714.

Kesavan, A. [S John- Supervisor] 2006, 'Embedded intelligence in structural health monitoring using artificial neural networks', *PhD Thesis*, School of Aerospace, Mechanical & Manufacturing Eng., RMIT University, Melbourne, Australia.

Kesavan, A., John, S. and Herszberg I. 2008a, 'Structural health monitoring of composite structures using artificial intelligence protocols', *Journal of Intelligent Material Systems and Structures*, vol.19, no.1, pp.63-72.

Kesavan, A., John, S. and Herszberg I. 2008b, 'Strain-based structural health monitoring of complex composite structures', *Structural Health Monitoring*, vol.7, no.3, pp.203-213.

Khedr, A.M. and Osamy, W. 2006, 'A topology discovery algorithm for sensor network using smart antennas', *Computer Communications*, vol.29, no.12, pp.2261-2268.

Kim, D., You, C. and Hwang, W. 2009, 'Effect of adhesive bonds on electrical performance in multi-layer composite antenna', *Composite Structures*, vol.90, no.4, pp.413–417.

Kucuk, K., Kavak, A. and Yigit, H. 2007, 'A smart antenna module using OMNeT++ for wireless sensor network simulation', in: *4th International Symposium on Wireless Communication Systems*, Trondheim, Norway, Oct, 2007, pp.747-751.

Kucuk, K., Kavak, A., Yigit, H. and Ozdemir, C. 2008, 'A new wireless sensor networks localization scheme with antenna arrays', in: *14th European Wireless Conference*, Prague, Czech Republic, Jun, 2008, pp.1-6.

Kumar, D. and Pourush, P.K.S. 2010, 'Circular patch microstrip array antenna on NiCoAl ferrite substrate in C-band', *Journal of Magnetism and Magnetic Materials*, vol.322, no.9-12, pp.1635-1638.

Li, H.C.H., Beck, F., Dupouy, O., Herszberg, I., Stoddart, P.R., Davis, C.E. and Mouritz, A.P. 2006, 'Strain-based health assessment of bonded composite repairs', *Composite Structures*, vol.76, no.3, pp.234-242.

Liao, W.H., Wang, D.H. and Huang, S.L. 2001, 'Wireless monitoring of cable tension of cable-stayed bridges using PVDF piezoelectric films', *Journal of Intelligent Material Systems and Structures*, vol.12, no.5, pp.331–339.

Mancini, S., Tumino, G. and Gaudenzi, P. 2006, 'Structural health monitoring for future space vehicles', *Journal of Intelligent Material Systems and Structures*, vol.17, no.7, pp.577-585.

Marques, R., Baena, D.J., Martel, J., Medina, F., Falcone, F., Sorolla, M. and Martin, F. 2003a, 'Novel small resonant electromagnetic particles for metamaterial and filter design', in: *Proc. ICEAA 03*, Torino, Italy, 2003, pp.439-442.

Marques, R., Martin, F., Sorolla, M. 2008, *Metamaterials with negative parameters*, 1st edn, US: John Wiley & Sons Ltd.

Marques, R., Medinaand, F., Rafi-El-Idrissi, R. 2002, 'Role of bi-anisotropy in negative permeability and left handed metamaterials', *Phys. Rev. B*, vol.65.

Marques, R., Mesa, F., Martel, J. and Medina, F. 2003b, 'Comparative analysis of edge and broad-side coupled split ring resonators for metamaterial design, theory and experiment', *IEEE Trans. Antennas Propag.*, vol.51, pp.2572-2581.

Matsuzaki, R. and Todoroki, A. 2006, 'Wireless detection of internal delamination cracks in CFRP laminates using oscillating frequency changes', *Composites Science and Technology*, vol.66, no.3-4, pp.407-416.

Matsuzaki, R. and Todoroki, A. 2007, 'Wireless flexible capacitive sensor based on ultra-flexible epoxy resin for strain measurement of automobile tires', *Sensors and Actuators A: Physical*, vol.140, no.1, pp.32-42.

Matsuzaki, R., Melnykowycz, M. and Todoroki, A. 2009, 'Antenna/sensor multifunctional composites for the wireless detection of damage', *Composites Science and Technology*, vol.69, no.15-16, pp.2507-2513.

Mehdizadeh, M. [S John- Supervisor] 2009, 'Curvature mode shape analyses of damage in structures', *MEng Thesis*, School of Aerospace, Mechanical & Manufacturing Eng., RMIT University, Melbourne, Australia.

Melik, R., Perkgoz, N.K., Unal, E., Puttlitz, C. and Demir, H.V. 2008, 'Bio-implantable passive on-chip RF-MEMS strain sensing resonators for orthopaedic applications', *Journal of Micromechanics and Microengineering*, vol.18, no.11, pp.115017.

Melik, R., Unal, E., Perkgoz, N.K., Puttlitz, C. and Demir, H.V. 2009, 'Metamaterial-based wireless strain sensors', *Applied Physics Letters*, vol.95, no.1.

Mendes, P.M., Bartek, M., Burghartz, J.N. and Correia, J.H. 2004, 'Novel very small dual-band chip-size antenna for wireless sensor networks', in: *IEEE Radio and Wireless Conference*, Sep, 2004, pp.419-422.

NASA 2003, *Columbia accident investigation board: report volume 1*, NASA, viewed 20 September 2009, < http://www.nasa.gov/columbia/home/index.html>

Oruganti, K., Mehdizadeh, M., John, S. and Herszberg, I. 2008, 'Damage detection in composites using vibration signatures and mode shapes', in: *Proceedings of the ASME 2008 Conference on Smart Materials, Adaptive Structures and Intelligent Systems (SMASIS2008)*, Ellicott City, USA, Oct, 2008, pp.79-90.

Ourir, A., Burokur, S.N., Yahiaoui, R. and Lustrac, A. 2009, 'Directive metamaterial-based subwavelength resonant cavity antennas – applications for beam steering', *Comptes Rendus Physique*, vol.10, no.5, pp.414-422.

Pell, B., Rowe, W., Sulic, E., Ghorbani, K., John, S., Gupta, R., Zhang, K. and Hughes, B. 2008, 'Experimental study of the effect of paint on embedded automotive antennas', in: *VTC Spring 2008 IEEE Vehicular Technology Conference*, May, 2008, vol.2, no.4, pp.3057–3061.

Pendry, J.B., Holden, A.J., Robbins, D.J. and Stewart, W.J. 1999, 'Magnetism from conductors and enhanced nonlinear phenomena', *IEEE Trans. Microwave Theory Tech*, vol.47, pp.2075-2084.

Petosa, A. 2007, *Dielectric Resonator Antenna Handbook*, 1st edn, England: Artech House.

Pires, E.S., Ferreira, P.I.L., Fontgalland, G., Melo, M.A.B., Valle, R.M. and Vuong, T.P. 2008, 'Design of a UWB antenna for sensor and wireless systems applications', in: *Proceedings of the IEEE International Conference on Ultra-Wideband (ICUWB2008)*, Hannover, Sep, 2008, pp.185-188.

Shams, K.M.Z. and Ali, M. 2007, 'Wireless power transmission to a buried sensor in concrete', *IEEE Sensors Journal*, vol.7, no.12, pp.1573-1577.

Shams, K.M.Z., Ali, M. and Miah, A.M. 2006, 'Characteristics of an embedded microstrip patch antenna for wireless infrastructure health monitoring', in: *IEEE International Symposium on Antennas and Propagation*, Albuquerque, USA, Jul, 2006, pp.3643-3646.

Silva-Munoz, R.A. and Lopez-Anido, R.A. 2009, 'Structural health monitoring of marine composite structural joints using embedded fiber Bragg grating strain sensors', *Composite Structures*, vol.89, no.2, pp.224-234.

Soontornpipit, P., Furse, C.M., Chung, Y.C. and Lin, B.M. 2006, 'Optimization of a buried microstrip antenna for simultaneous communication and sensing of soil moisture', *IEEE Transactions on Antennas and Propagation*, vol.54, no.3, pp.797–800.

Spencer Jr, B.F., Ruiz-Sandoval, M.E. and Kurata, N. 2004, 'Smart sensing technology: opportunities and challenges', *Structural Control and Health Monitoring*, vol.11, no.4, pp.349–368.

Staszewski, W.J. 2000, 'Monitoring on-line integrated technologies for operational reliability – monitor', *Air and Space Europe*, vol.2, no.4, pp.67–72.

Staszewski, W.J., Boller, C. and Tomlinson, G.R. 2004, *Health monitoring of aerospace structures: smart sensor technologies and signal processing*, 1st edn, England: John Wiley & Sons Ltd.

Takao, H., Kizuna, S., Sawada, K., Sudou, M. and Ishida, M. 2007, 'RF-powered silicon-MEMS microsensors for distributed and embedded sensing applications', in: *4th International Conference on Network Sensing Systems*, Braunschweig, Jun, 2007, pp.35-42.

Tan, E.L., Pereles, B.D., Shao, R., Ong, J. and Ong, K.G. 2008, 'A wireless, passive strain sensor based on the harmonic response of magnetically soft materials', *Smart Materials and Structures*, vol.17, no.2.

Tanner, N.A., Wait, J.R., Farrar, C.R. and Sohn, H. 2003, 'Structural health monitoring using modular wireless sensors', *Journal of Intelligent Material Systems and Structures*, vol.14, no.1, pp.43–56.

Tata, U., Huang, H., Carter, R.L. and Chiao, J.C. 2009, 'Exploiting a patch antenna for strain measurements', *Measurement Science and Technology*, vol.20, no.1.

Umbrecht, F., Wendlandt, M., Juncker, D., Hierold, C. and Neuenschwander, J. 2005, 'A wireless implantable passive strain sensor system', in: *IEEE Proceedings of Sensors Conference*, Oct-Nov, 2005, pp.20–23.

Vishay 2011, *Vishay Micro-Measurements™ strain indicator and recorder*, Intertechnology Inc, viewed 18 April 2011, < http://www.intertechnology.com/Vishay/pdfs/P3.pdf>

Volakis, J.L. 2007, *Antenna engineering handbook*, 4th edn, US: McGraw-Hill.

Wang, C.H, Rose, J.T. and Chang, F.K. 2004, 'A synthetic time-reversal imaging method for structural health monitoring', *Smart Materials and Structures*, vol.13, no.2, pp.415-423.

Watters, D.G., Jayaweera, P., Bahr, A.J. and Huestis, D.L. 2002, 'Design and performance of wireless sensors for structural health monitoring', *AIP Conference Proceedings*, vol.21, no.615, pp.969-976.

Wong, K.L. 2002, *Compact and broadband microstrip antennas*, 1st edn, US: John Wiley & Sons Ltd.

Wu, J., Yuan, S., Ji, S., Zhou, G., Wang, Y. and Wang, Z. 2009, 'Multi-agent system design and evaluation for collaborative wireless sensor network in large structure health monitoring', *Expert Systems with Applications*, vol.37, no.3, pp.2028-2036.

Yan, Y.J., Cheng, L., Wu, Z.Y. and Yam, L.H. 2007, 'Development in vibration-based structural damage detection technique', *Mechanical Systems and Signal Processing*, vol.21, no.5, pp.2198-2211.

Yang, W., Roggemann, M.C. and Cooper, K., Buller, W., Subotic, N., Middlebrook, C. and Boreman, G.D. 2008, 'The IR antenna pair coupled sensor element and its potential application in wavefront sensing', *Infrared Physics and Technology*, vol.51, no.6, pp.495-504.

You, C. and Hwang, W. 2007, 'Antenna integration with composite sandwich structures using gain enhancement methods', *Journal of Composite Materials*, vol.41, no.9, pp.1037-1049.

Zainud-Deen, S.H., Badr, M.E., Awadalla, K.H. and Sharshar, H.A. 2006, 'Microstrip antenna for detecting buried land mines', in: *IEEE International Symposium on Antennas and Propagation*, Albuquerque, Jul, 2006, pp.2609-2612.

Zhou, G. and Sim, L.M. 2009, 'Evaluating damage in smart composite laminates using embedded EFPI strain sensors', *Optics and Lasers in Engineering*, vol.47, no.10, pp.1063-1068.

Zivanovic, B., Weller, T.M., Melais, S. and Meyer, T. 2007, 'The effect of alignment tolerance on multilayer air cavity microstrip patches', in: *IEEE International Symposium on Antennas and Propagation Society*, Jun, 2007, pp.381–384.